UNIVERSITY OF
BIRMINGHAM

Lithium Amide Halides for Hydrogen Storage

by

Rosalind Davies

Supervisor: Dr. Paul Anderson

A thesis submitted to The University of Birmingham
for the degree of Doctor of Philosophy

Centre for Hydrogen and Fuel Cell Research
School of Chemical Engineering
University of Birmingham
B15 2TT

Abstract

The lithium amide halides are a promising series of materials for hydrogen storage as they release hydrogen at a lower temperature than lithium amide on reaction with lithium hydride. The amide chloride system has been studied in detail, and a phases with reduced chloride content, of stoichiometry $Li_7(NH_2)_6Cl$, was identified by powder X-ray diffraction and Raman spectroscopy. This phases was seen to release hydrogen on reaction with LiH at a lower temperature than observed for lithium amide, and ammonia release was suppressed. The material was also able to be cycled, with the chloride ions maintained within the structure during desorption and rehydrogenation. The rehydrogenation of the imide dehydrogenation products of the new phase occurred more readily under the conditions used than for the known phase $Li_4(NH_2)_3Cl$.

The hydrogen cycling properties of $Li_7(NH_2)_6Cl$ were investigated alongside the amide bromide $Li_7(NH_2)_6Br$ and the amide iodide $Li_3(NH_2)_2I$. The systems successfully cycled hydrogen, and the reversible structural changes that happened during cycling were studied. All three materials, however, showed a capacity loss on cycling under dynamic vacuum.

Bulk cation transport has been identified as a key factor in the release and uptake of hydrogen in the Li-N-H system. The conductivity of the amide and imide halides was studied using A.C. impedance and found to be higher than for $LiNH_2$ and Li_2NH, respectively. This supports kinetic analyses that indicate ion diffusion is not rate-limiting for the hydrogen cycling of these systems.

Contents

1 Introduction **8**

1.1 Hydrogen Production 9

1.1.1 Hydrocarbon Fuel Processing 9

1.1.2 Electrolysis of Water 10

1.1.3 Other methods 11

1.2 Hydrogen as a Fuel 11

1.2.1 Internal Combustion Engine 12

1.2.2 Fuel Cells 12

1.3 Hydrogen Storage 14

1.3.1 Molecular Hydrogen 15

1.3.1.1 Compressed Gas 15

1.3.1.2 Liquid 15

1.3.1.3 Cryo-compressed Hydrogen 16

1.3.1.4 Physisorption 16

1.3.2 Metal Hydrides 17

1.3.2.1 Magnesium hydride 18

1.3.2.2 Aluminium hydrides 19

1.3.2.3 Borohydrides 20

1.3.2.4 Amides 21
1.3.2.5 Mixed Lithium Magnesium Amide Systems 23
1.3.2.6 Other Mixed Complex Hydride Systems 25
1.3.2.7 Halide Doping in Hydrogen Storage 25
1.3.2.8 Challenges 27
1.4 Project Objectives 28

2 Experimental **30**

2.1 Solid state synthesis under inert gas 30
2.2 Crystallography and diffraction 31
2.2.1 Crystallography 31
2.2.1.1 Crystal structures 31
2.2.1.2 Lattice planes 32
2.2.2 X-ray diffraction 33
2.2.2.1 X-ray generation 34
2.2.2.2 Monochromation 34
2.2.2.3 Detection 35
2.2.2.4 Laboratory X-ray diffraction 35
2.2.2.5 Synchrotron X-ray diffraction 36
2.2.3 Neutron diffraction 36
2.2.4 Powder diffraction 38
2.3 Rietveld analysis 39
2.3.1 Quantitative phase analysis 41
2.4 Mass spectrometry 43
2.4.1 Ionisation 43
2.4.2 Separation 43

2.4.3 Detection 44
2.5 Temperature programmed desorption 44
2.5.1 Calibration 45
2.6 Hydrogenation 47
2.7 Raman spectroscopy 48
2.8 A.C. impedance spectroscopy 51
2.9 Volumetric analysis 53
2.10 Hydrogen cycling at the Diamond Light Source 54
2.11 Deuterium cycling on the POLARIS beamline at the ISIS neutron source . . 55
2.12 Gravimetric measurements during deuterium cycling on the POLARIS beamline at the ISIS neutron source 56

3 Structural investigation of $Li_4(NH_2)_{4-x}Cl_x$ **59**

3.1 Introduction 59
3.2 Experimental 61
3.3 The effect of composition on the kinetic product 62
3.4 Time dependence of the formation of $Li_4(NH_2)_3Cl$ 67
3.4.1 *In situ* monitoring of the effect of reaction time 68
3.5 Effect of changing the Cl^- composition: 12 hour reaction time 71
3.5.1 Unknown phase 74
3.5.2 Structural refinement of the new phase with lower chloride content . 75
3.5.3 Diamond and ISIS structural refinement 76
3.5.4 Raman spectroscopy 79
3.6 Time dependence of the formation of $Li_7(NH_2)_6Cl$ 80
3.7 Effect of magnesium on the structure 81
3.7.1 The effect of reaction time 82

3.7.2 Raman spectroscopy 84
3.8 Conclusions and further work 85

4 Hydrogen storage properties of $Li_7(NH_2)_6Cl$ and $Li_6Mg_{1/2}(NH_2)_6Cl$ 86

4.1 Introduction 86
4.2 Experimental 87
4.3 Dehydrogenation of $Li_7(NH_2)_6Cl$ and $Li_7Mg_{1/2}(NH_2)_6Cl$ on reaction with LiH 88
4.3.1 Characterisation of the dehydrogenated products 89
4.4 TPD-MS of a lithium amide/ lithium hydride/ lithium chloride mixture . . . 92
4.5 Rehydrogenation of the imide chlorides 94
4.5.1 Rehydrogenation under different pressures 97
4.6 Dehydrogenation of $Li_7(NH_2)_6Cl$ with a mixture of LiH and MgH_2. 101
4.6.1 Hydrogenation after reaction with a LiH/MgH_2 mixture 104
4.7 Cycling properties 105
4.7.1 TPD of rehydrogenated products 105
4.7.2 HTP of $Li_7(NH_2)_6Cl$ 107
4.7.3 Hydrogen cycling of $Li_7(NH_2)_6Cl$ studied using synchrotron powder X-ray diffraction on the I11 beamline 109
4.7.4 Deuterium cycling of $Li_{13}(ND)_6Cl$ measured by powder neutron diffraction 115
4.7.5 *Ex-situ* characterisation of the sample after cycling 123
4.7.6 Gravimetric cycling of $Li_7(ND_2)_6Cl$ studied using powder neutron diffraction 125
4.8 A.C. Impedance Spectroscopy 131
4.8.1 $Li_7(NH_2)_6Cl$ 131
4.8.2 $Li_{13}(NH)_6Cl$ 134

4.9 Conclusions and further work 136

5 Hydrogen storage properties of other amide halides 140

5.1 Introduction 140

5.2 Experimental 141

5.3 The lithium amide bromide, $Li_7(NH_2)_6Br$ 142

5.3.1 Structure 142

5.3.2 A.C. Impedance Spectroscopy 144

5.4 TPD-MS of a lithium amide/ lithium bromide mixture 148

5.4.1 Deuterium cycling of the bromide system measured by powder neutron diffraction 151

5.4.1.1 New Br phase 154

5.4.2 *Ex-situ* characterisation of the sample after cycling 155

5.4.3 Hydrogen cycling studied by synchrotron radiation 156

5.4.4 Deuterium cycling and gravimetric measurements 161

5.4.5 New phase in the lithium amide bromide system 165

5.5 The lithium amide iodide, $Li_3(NH_2)_2I$ 167

5.5.1 TPD-MS of a lithium amide/ lithium iodide mixture 167

5.5.2 Hydrogen cycling of $Li_3(NH_2)_2I$ studied by synchrotron radiation . 169

5.5.3 Deuterium cycling and gravimetric measurements 173

5.5.4 Further deuterium cycling and gravimetric measurements 178

5.6 Incorporation of fluoride 182

5.6.1 $LiNH_2 + LiF$ 182

5.6.2 $LiNH_2 + KF$ 182

5.6.3 BF_4^- 182

5.7 LiH_xF_{1-x} solid solution 184

5.7.1 Hydrogen desorption 184
5.8 Conclusions and further work 186

6 Conclusions 188

Chapter 1

Introduction

Currently, the majority of electrical and thermal energy is generated by the combustion of fossil fuels: coal, oil and natural gas.[1] Fossil fuels are highly calorific and convenient because they have been easy to mine, transport, store and burn. However, increasing concerns about the security and longevity of their supply and the pollution caused by their combustion are leading to the need for development of alternative technologies. Air quality is another motivator for alternative forms of energy production as the UK has breached the EU Air Quality Directive and, as a consequence, the Government is now subject to infraction proceedings.[2]

Hydrogen has the potential to form part of a renewable and sustainable energy system as an energy carrier. This is because it can be produced from renewable sources, stored and then used, with only water being emitted at the point of use. Electricity is the main alternative to hydrogen for this purpose, with batteries being used for storage. The dominance of one of these technologies over the other will depend on a number of factors. The method of hydrogen production will determine the overall efficiency of using hydrogen, as well as the economic and environmental costs of the process.

The automotive industry will also have a major influence on the technology adopted, as the preference for hydrogen- or battery-powered vehicles will lead to more widespread adoption of this technology for other uses, for example heating and large scale energy storage. The main barrier to implementation of either technology is currently the lack of an 'ideal' storage method, causing limitations to the amount of energy stored on board and therefore the range of the vehicle. Current state of the art battery technology has enabled the development of electric vehicles with ranges of over 300 miles, but these are still prohibitively expensive to the mass automobile market.[3]

1.1 Hydrogen Production

Although hydrogen is the most abundant element on the Earth, only 1% is found in the form required for use in a renewable energy system, as the majority of the hydrogen on Earth is chemically bound into H_2O, with some present in hydrocarbons.[4] There are a number of methods of producing hydrogen from different feedstocks, although not all produce hydrogen in a sustainable manner.

1.1.1 Hydrocarbon Fuel Processing

There are three main methods of processing hydrocarbon fuels to produce hydrogen: steam reforming, partial oxidation and autothermal reforming. Steam reforming is currently the preferred method for producing hydrogen for industrial use and is described by equation 1.1.[5]

$$\mathrm{C}_m\mathrm{H}_n + \mathrm{mH_2O} \longrightarrow \mathrm{mCO} + (\mathrm{m} + \frac{1}{2}\,\mathrm{n})\mathrm{H_2} \tag{1.1}$$

These fuel processing methods also produce carbon monoxide and the inclusion of the water-gas shift reaction, as described by equation 1.2, allows this carbon monoxide to be used to increase the amount of hydrogen produced.

$$CO + H_2O \longrightarrow CO_2 + H_2 \tag{1.2}$$

Although these methods are currently well developed, they rely on the use of fossil fuels. Producing hydrogen in this way therefore still leads to emissions of CO_2 and concerns about security and sustainability of supply. Widespread hydrogen production in this way could, however, lead to the development of an infrastructure and other components of an energy system, preventing a delay in these technologies being determined by the lack of a hydrogen supply.[6] Hydrogen filling station networks for fuelling fuel cell vehicles are starting to be installed around the world, but currently only 13% of these are supplied with hydrogen produced from a renewable source.[7]

Biomass could act as an intermediate feedstock as it is renewable, easy to use and could be grown in abundance. It can be processed *via* steam methane reforming and the CO_2 emissions over the life cycle are nearly zero due to the photosynthesis of the plants. Thermochemical pyrolysis and gasification hydrogen production methods are economically viable and have the potential to become competitive with the conventional natural gas reforming method.[8] However, use of biomass brings its own issues, as the capital equipment costs are high, and biomass feedstocks are also currently expensive.[9] Large-scale use of biomass also has implications for land use, as its growth competes with farming crops.[10]

1.1.2 Electrolysis of Water

The electrolysis of water produces oxygen and hydrogen via equations 1.3 and 1.4.

$$2\,H_2O_{(l)} \longrightarrow O_{2(g)} + 4\,H^+_{(aq)} + 4\,e^- \tag{1.3}$$

$$2\,\mathrm{H}^{+}_{(\mathrm{aq})} + 2\,\mathrm{e}^{-} \longrightarrow \mathrm{H}_{2(\mathrm{g})} \tag{1.4}$$

The splitting of water is thermodynamically unfavourable and therefore an electric potential is required to drive the reaction. By using electricity generated from renewable sources such as solar or wind, this process is a potential route to 'green' hydrogen: hydrogen produced with no CO_2 emissions. Efficiencies of 73% and 85% have been observed for water electrolysis on an industrial and laboratory scale, respectively.[11] High cost means that water electrolysis is only a small proportion of total hydrogen production in 2015, but it is forecast to become half of the total production capacity by 2020.[12]

1.1.3 Other methods

Other methods of hydrogen production from water have been explored, including thermochemical and photocatalytic splitting. Thermochemical cycles use heat in combination with a chemical catalyst to split water. This, and high temperature electrolysis, are being considered as a way of harnessing the excess heat generated from nuclear power plants. Photocatalytic splitting offers a sustainable hydrogen production method, with the energy coming directly from the sun. Further research and development is required to investigate how to implement existing systems of this type and also how to improve efficiency and reduce cost.[13]

1.2 Hydrogen as a Fuel

Hydrogen has the highest heating value per kilogram of any fuel, 120 MJ kg^{-1}, and has the potential to be a zero-emission fuel as it produces only water on combination with oxygen.[14] The energy from hydrogen can be used to produce mechanical energy by using an internal combustion engine, or electrical energy via a fuel cell.

1.2.1 Internal Combustion Engine

Hydrogen can be burnt in an internal combustion engine (ICE), producing near-zero emissions and running at higher efficiencies than ICEs powered by gasoline.[15] However, the efficiency of chemical to mechanical transformation is limited by the Carnot cycle to approximately 25% for hydrogen-air mixtures.[4] Hydrogen-powered ICEs could be used to aid the transition between conventional fuels and hydrogen as fuel cell systems are developed further.

1.2.2 Fuel Cells

A fuel cell generates electricity via a reaction between a fuel and an oxidising agent and, as long as the supply of both of these is maintained, can operate continuously, unlike a battery which requires recharging.[16] A hydrogen fuel cell uses hydrogen as the fuel and oxygen as the oxidising agent and consists of two electrodes separated by an electrolyte. There are a number of different types of fuel cells which use different electrolytes: most commonly used are polymer, alkaline, solid oxide, molten carbonate and phosphoric acid. For automobiles, polymer electrolyte fuel cells (PEMFCs) are used, due to their operating temperature being most appropriate to the application.

PEMFCs (figure 1.1) use a solid polymer in which protons are mobile in the electrolyte. They are able to be run at low temperatures but, to prevent slow reaction times, platinum is required as a catalyst. This increases the price of the fuel cell and also means that they are unable to tolerate the presence of contaminants such as ammonia in the input gas.[17] In a PEMFC, hydrogen is oxidised at the anode according to equation 1.5 and oxygen is reduced at the cathode, as shown in equation 1.6.

$$2\,H_2 \longrightarrow 4\,H^+ + 4\,e^- \tag{1.5}$$

$$O_2 + 4\,H^+ + 4\,e^- \longrightarrow 2\,H_2O \tag{1.6}$$

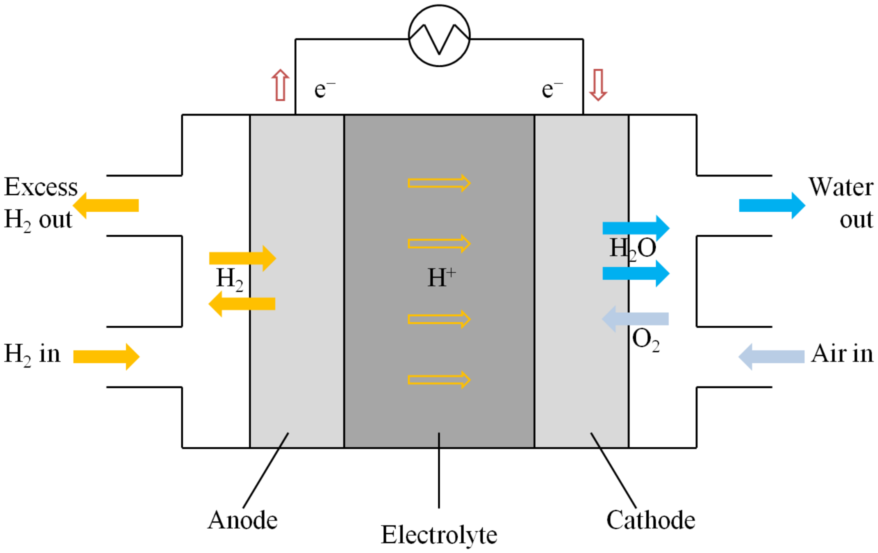

Figure 1.1: Schematic representation of a PEMFC.[18]

The main advantages of fuel cells are that they can achieve high efficiencies (a typical cell running at 0.7 V has an efficiency of 50%) and that they can be stacked to increase the overall voltage supplied. They also, unlike ICEs, do not emit NO_x gases. Most automotive companies agree that using fuel cells in combination with batteries in vehicles is the only option that enables zero-emission driving for a long range with refuelling times of between 3 and 5 minutes.[16,19] The first mass production hydrogen fuel cell cars are now available to purchase in the UK from manufacturers Toyota and Hyundai, with Honda due to release a model before 2017.[20]

1.3 Hydrogen Storage

For hydrogen to be considered as a viable energy vector, a suitable storage medium needs to be developed. The properties that need to be considered for a storage medium when considering an automotive application are the volumetric and gravimetric storage capacities, the ability to uptake and discharge hydrogen rapidly and conveniently, and the overall cost and efficiency.[21] The gravimetric capacities of different media are compared by looking at the weight of hydrogen released per unit weight of the material: the weight percent, or wt%. For an automotive application, it is more appropriate to consider the weight of the whole system, not just the storage medium. When considering this application, the US Department of Energy (DoE) has set targets for vehicular hydrogen storage systems, and they are shown in table 1.1.[22] When developing systems for storing hydrogen, these targets need to be taken into consideration.

Target	**2020**	**'Ultimate'**
System Gravimetric Density (% wt)	5.5 (1.8 kWh kg^{-1})	7.5 (2.5 kWh kg^{-1})
System Volumetric Density (g l^{-1})	40 (1.3 kWh l^{-1})	70 (2.3 kWh l^{-1})
System Fill Time for 5 kg fill (min)	3.3	2.5
Fuelling rate (kg min^{-1})	1.5	2.0
Operational cycle life (cycles)	1500	1500
Delivery pressure from storage system (bar)	5 (min) - 12 (max)	3 (min) - 12 (max)

Table 1.1: Table showing the US DoE targets for vehicular hydrogen storage.[22]

There are a number of methods of storing hydrogen, including:[23]

- High-pressure gas cylinders.
- Cryogenically cooled liquid hydrogen.
- Adsorbed onto materials with a large surface area, typically below 100 K.
- Absorbed onto interstitial sites in a host metal.

- Chemically bonded in ionic or covalent compounds.

Each of these methods has different benefits and challenges associated with it and they will be discussed in more detail below.

1.3.1 Molecular Hydrogen

1.3.1.1 Compressed Gas

Storing hydrogen as a compressed gas is the most well established form of hydrogen storage. High pressure cylinders made of composite materials are able to withstand pressures of up to 700 bar.[24] However, the ideal input into a fuel cell is at a lower pressure than this, leading to a need for additional systems to step down this pressure. There are also safety concerns amongst the general public, even though these composite tanks have undergone considerable safety testing to ensure they are as safe as petrol or diesel tanks.[25] Current hydrogen cars use compressed gas storage, with both the Toyota Mirai and the Hyundai ix35 storing hydrogen in two 700 bar tanks.[26,27] However, this form of storage does not meet the the DoE's 'Ultimate' volumetric targets, and the cost of the carbon fibres needed to maintain the pressure is becoming a major factor towards the overall cost of the car.[28]

1.3.1.2 Liquid

Hydrogen can also be stored as a liquid at cryogenic temperatures. The main advantage gained on moving from a compressed gas to storing hydrogen in a liquid form is the higher volumetric capacity. The pressure is also not as high, therefore there is no need for step down technology. The main disadvantage to storing hydrogen as a liquid is the high energetic cost of cryogenic cooling, which can be up to 30% of the stored hydrogen.[6] The tank also needs to be larger as a lot of insulation is needed, as is additional equipment for venting any boiloff. Cryogenically cooled hydrogen is only used where high storage density is essential, for example the aerospace industry.[29]

1.3.1.3 Cryo-compressed Hydrogen

The storage of hydrogen at cryogenic temperatures in a vessel that can be pressurized is referred to as cryo-compressed hydrogen. This method can benefit from the advantages of both liquid hydrogen and compressed gas storage. The time that the vehicle can remain dormant is extended from that of a liquid hydrogen tank due to the higher pressure of the system.[30] This method of storage can meet all of the 2015 targets apart from cost and efficiency.[28]

1.3.1.4 Physisorption

Van der Waals forces between hydrogen molecules and the surface of a material can bind a monolayer of hydrogen. Any additional hydrogen can only be bound to other hydrogen molecules and therefore this cannot occur over the boiling point. To adsorb a high weight percent of H_2, high surface area solids are needed. In general, the higher the apparent surface area, the higher wt% can be adsorbed. This high surface area can be achieved by smaller particles, or developing a high internal surface area.

Carbon nanostructures have promising structural and mechanical properties that make them attractive for hydrogen storage applications.[31] Graphene has also been investigated as a storage medium, as it can be hydrogenated, forming graphane, from which hydrogen can be released at $450°$C.[32] Contaminant gases are also absorbed more strongly by these materials and therefore they are not ideal as storage materials.

Porous frameworks, such as zeolites and metal organic frameworks, have a high surface area and so have been considered to have a high potential for storing large volumes of hydrogen. The capacities, however, have not been shown to be as high as initially anticipated.

These storage techniques also require very low temperatures to adsorb hydrogen, causing a large quantity of liquid nitrogen to be needed for cooling purposes.[21]

1.3.2 Metal Hydrides

Because viable storage of molecular hydrogen relies on energy intensive compression or liquefaction of hydrogen, these techniques do not have the potential to meet all of the targets for widespread automotive application. Solid state materials-based hydrogen storage has been identified as perhaps the only approach able to achieve performance and cost targets.[33] By storing hydrogen in a metal framework, more hydrogen can be stored per unit volume. Metal hydrides have been shown to have very high volumetric hydrogen storage densities, for example $LaNi_5H_6$ can store up to 115 kg m^3, and can deliver hydrogen at a constant pressure.[23]

For a typical interstitial metal hydride, the thermodynamic behaviour can be described using a pressure-composition isotherm, as shown in figure 1.2.[34] The diagram to the left shows the α-phase that occurs at small hydrogen to metal ratio, where a solid solution is formed as the hydrogen dissolves into the metal and the metal lattice expands. The hydride, or β-phase, is shown on the right and in this phase the hydrogen pressure rises steeply with concentration. The plateau region illustrates the coexistence of the two phases and ends at the critical temperature T_c. A Van't Hoff plot can be constructed to calculate the enthalpy of formation, ΔH, and the entropy of formation, ΔS, as shown in reaction 1.7.

$$\ln p = \frac{\Delta H}{RT} - \frac{\Delta S}{R} \tag{1.7}$$

Interstitial metal hydrides are not suitable for mobile applications due to very low gravimetric capacities.[35] To avoid this gravimetric penalty, lower atomic mass hydrides have

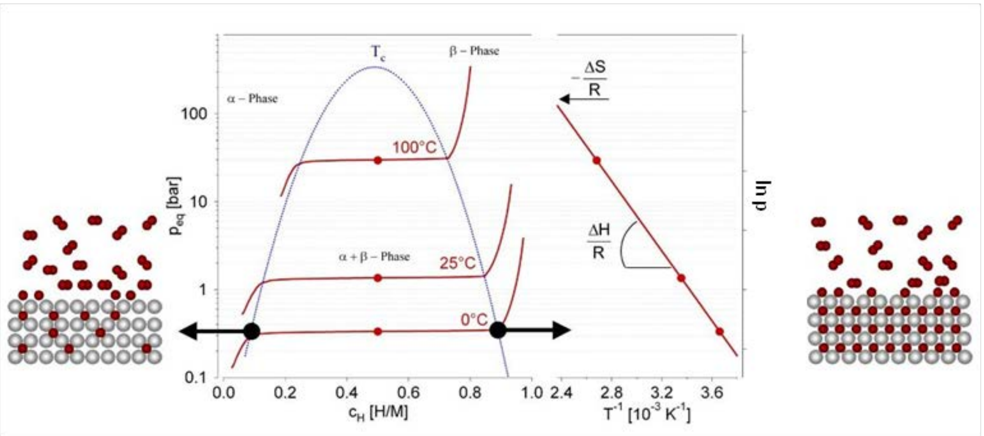

Figure 1.2: Graph showing the pressure-composition isotherm for hydrogen absorption in a typical intermetallic compound with the construction of the Van't Hoff plot shown on the right hand side. Adapted from Zϋttel *et. al.*[34]

been considered. The metal-hydrogen bonds in these compounds are usually strong, requiring higher temperatures for hydrogen desorption. As an alternative to conventional metal hydrides, a series of hydrogen-containing 'complex hydrides' of lighter metals have been gaining increasing levels of attention. These are compounds in which the hydrogen is covalently bonded to a central ion and encompasses the Group I and II salts of $[AlH_4]^-$, $[NH_2]^-$ and $[BH_4]^-$.[36] These compounds were initially not considered as hydrogen stores, as hydrogen desorption was thought not to be feasible, until work on alkali metal aluminium hydrides showed otherwise.[37] Lightweight complex metal hydrides have the potential to meet the Department of Energy targets, as they contain up to 13.7 wt% hydrogen.[38,39] Complex hydrides based on different lightweight metals have a variety of different properties and storage capacities, and are discussed in more detail below.

1.3.2.1 Magnesium hydride

MgH_2 has a high hydrogen storage capacity of 7.7 wt%, exhibits good reversibility, and has the advantage of being made of low cost materials.[40] The temperature needed for hydrogen discharge is, however, too high for practical applications due to a high desorption enthalpy.[41] Powdered MgH_2 is also susceptible to surface oxidation, and diffusion of hydrogen through the MgH_2 is slow. These properties can be improved by ball milling, introducing a catalyst and alloying with other metals.[42,43]

1.3.2.2 Aluminium hydrides

Complex aluminium hydrides have a high hydrogen content, for example $LiAlH_4$ can store over 10 wt% H_2, and therefore have the potential for meeting the DoE mobile hydrogen storage targets. Most decompose via a three step process, as shown by reactions 1.8, 1.9 and 1.10. The first two of these reactions proceed around 160-210°C and release 5.3 and 2.6 wt% of hydrogen, respectively.[44]

$$3\,\mathrm{LiAlH_4} \longrightarrow \mathrm{Li_3AlH_6} + 2\,\mathrm{Al} + 3\,\mathrm{H_2} \tag{1.8}$$

$$\mathrm{Li_3AlH_6} \longrightarrow 3\,\mathrm{LiH} + \mathrm{Al} + \frac{3}{2}\,\mathrm{H_2} \tag{1.9}$$

$$3\,\mathrm{LiH} \longrightarrow 3\,\mathrm{Li} + \frac{3}{2}\,\mathrm{H_2} \tag{1.10}$$

The high thermodynamic stability of the hydrides LiH and NaH means that the final decomposition step occurs only at very high temperatures. For $NaAlH_4$, this reduces the accessible hydrogen content to 3.6 wt%.[21] The low prices of the materials needed to produce these compounds (NaH and Al) is motivation for further investigation.

Metastable aluminium-based hydrides such as $Mg(AlH_4)_2$ exhibit a low heat of decomposition and rapid low temperature kinetics, making them another hydrogen storage candidate. For larger-scale applications, a number of key challenges need to be overcome: at practical pressures of hydrogen these materials do not show reversibility and the conventional synthesis routes are expensive.[45]

1.3.2.3 Borohydrides

$LiBH_4$ has high hydrogen storage capacity, with a gravimetric hydrogen density of 18.5 wt% and a volumetric hydrogen density of 121 kgH_2 m^3. Only three of the four hydrogen atoms per formula unit contained within the structure can be liberated, as the high stability of LiH causes it to remain as a decomposition product. The route to LiH occurs via three stages: the first is a structural transition at 108°C that releases a small amount, 0.9 wt%, of H_2 as shown in reaction 1.11. The high temperature phase releases up to 13.5 wt% of H_2, but in two stages, thought to proceed *via* an un-characterised intermediate '$LiBH_2$', as shown in reactions 1.12 and 1.13.[46] The end products, LiH and B, can be rehydrogenated under 35 bar at 400°C to form $LiBH_4$.[47]

$$\mathrm{LiBH_4} \longrightarrow \mathrm{LiBH}_{(4-x)} + \frac{1}{2}\,(\mathrm{x})\,\mathrm{H_2} \tag{1.11}$$

$$\mathrm{LiBH}_{(4-x)} \longrightarrow \text{`}\mathrm{LiBH_2}' + \frac{1}{2}\,(1{-}\mathrm{x})\,\mathrm{H_2} \tag{1.12}$$

$$\text{`}\mathrm{LiBH_2}' \longrightarrow \mathrm{LiH} + \mathrm{B} + \frac{1}{2}\,\mathrm{H_2} \tag{1.13}$$

Many other borohydrides have been studied as potential hydrogen storage materials, including $NaBH_4$ which can be hydrolysed to form $NaBO_2$ releasing 10.8 wt% H_2[48] and $Mg(BH_4)_2$ which has been shown to release 13.7 wt% H_2.[49] The challenges associated with recycling the $NaBO_2$ has led to the US Department of Energy declaring $NaBH_4$ a 'no-go' for automotive hydrogen storage.[50]

1.3.2.4 Amides

$LiNH_2$ has been known since 1894, and it was shown as early as 1933 that it can decompose to form the imide and then the nitride.[51,52] This decomposition releases ammonia but, on addition of LiH, it has been considered to have a great potential for hydrogen storage. Although a recent theoretical study has shown that it may be possible to pass directly from Li_3N to $LiNH_2$,[53] the reaction is observed to occur *via* a two step process, as shown in equation 1.14. Li_3N is able to absorb 9.3 wt% H_2.[54]

$$\mathrm{LiNH_2 + 2\,LiH \longleftrightarrow Li_2NH + LiH + H_2 \longleftrightarrow Li_3N + 2\,H_2} \tag{1.14}$$

Due to the stability of LiH, the second stage has been found to require temperatures higher than 320°C to release hydrogen and exhibits slow hydrogen uptake. The first stage alone has a high gravimetric storage capacity, of 6.5 wt%, and is reversible under conditions that could be practical for hydrogen storage applications.[55]

Considering the first stage: when heated, $LiNH_2$ decomposes to form Li_2NH and ammonia.[56] Addition of LiH not only lowers the temperature of decomposition, but also prevents ammonia release.[57,58] It is thought that this is due to the interaction between the $H^{\delta-}$ in the LiH and the $H^{\delta+}$ in $LiNH_2$. It has been shown that dehydrogenation temperature is reduced when metal hydrides containing negatively charged hydrogen, such as LiH, are combined with metal amides, which contain a positively charged hydrogen.[59] The mechanism of desorption in the $LiNH_2$-LiH system has been investigated, and it is thought to be dependent on the sample morphology and reaction conditions. When the ion migration is constrained, the amide and hydride particles are not in good contact, or the reaction temperature is high enough to allow NH_3 formation at a sufficient rate, the desorption is likely to be NH_3 mediated. This has been observed experimentally to occur *via* two reactions, shown in equations 1.15 and 1.16.[60,61] Reaction 1.16 is an ultra-fast surface reaction and therefore reaction 1.15 is proposed to be the rate determining step.[62]

$$2\,\mathrm{LiNH_2} \longrightarrow \mathrm{Li_2NH} + \mathrm{NH_3} \tag{1.15}$$

$$\mathrm{NH_3} + \mathrm{LiH} \longrightarrow \mathrm{LiNH_2} + \mathrm{H_2} \tag{1.16}$$

Reaction 1.16 has also been observed to occur in the opposite direction, under flowing H_2.[63] However, in a closed vessel, the reaction between $LiNH_2$ and H_2 will not proceed,[64] because even a low partial pressure of NH_3 will suppress the decomposition of $LiNH_2$ in this way.[65]

The mobility of Li^+ ions has been highlighted as a key factor in both reaction 1.15 and 1.16.[66] By considering the structures of $LiNH_2$ and Li_2NH (figure 1.3), the relationship between them can be easily observed. Their structural similarities allow for de/rehydrogenation to occur *via* a solid solution of $Li_{(1+x)}NH_{(2-x)}$ due to the diffusion of Li^+ and H^+ through the lattice. On dehydrogenation, this causes a Li-rich layer to form on the interface between the amide and the LiH phase.[67]

Intermediate phases in this solid solution have been observed using *in situ* powder synchrotron diffraction, and it is thought that these intermediate phases have higher ionic conductivity than $LiNH_2$ and Li_2NH due to their intrinsic disorder.[68] It has been thought, therefore, that improved ionic mobility could improve the desorption kinetics of a material.[69] The high ionic mobility of some of these complex hydride systems has also been investigated when considering these materials as solid electrolytes for lithium batteries.[70] Attempts have been made to increase the conductivity by stabilising defects within the $LiNH_2$ structure by doping with Si, leading to a reduction in hydrogen desorption time.[71]

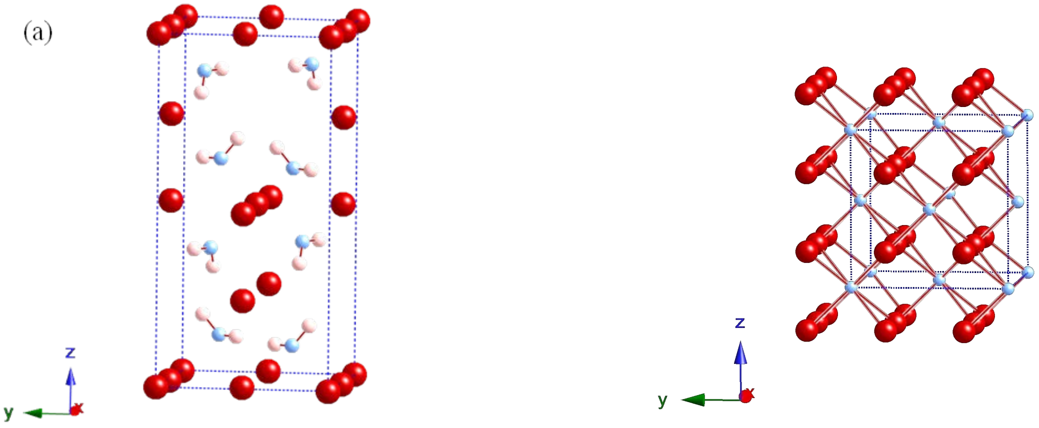

Figure 1.3: Structure of $LiNH_2$ (a, left),[72] and the anti-fluorite structure of Li_2NH (b, right)[56], with lithium ions represented by red spheres, nitrogen blue, hydrogen pink, and the unit cell shown by dotted lines. The hydrogen atoms in Li_2NH are distributed across the 48*h* sites and so have been emitted for clarity.

1.3.2.5 Mixed Lithium Magnesium Amide Systems

The Li-Mg-N-H system has been considered to be a very promising hydrogen storage medium for practical applications.[73] Theoretical calculations have shown that substituting Mg onto the Li sites increases the electron density around the Li and H atoms, weakening the bonds between Li-N and H-N.[74] There are two methods that have been investigated to introduce magnesium into the structure, described by reactions 1.17 and 1.18.

$$2\,\mathrm{LiNH_2} + \mathrm{MgH_2} \longrightarrow \mathrm{Li_2Mg(NH)_2} + \mathrm{H_2} \tag{1.17}$$

$$\mathrm{Mg(NH_2)_2} + 2\,\mathrm{LiH} \longrightarrow \mathrm{Li_2Mg(NH)_2} + \mathrm{H_2} \tag{1.18}$$

Reaction 1.17 has been studied using *in situ* powder XRD by reacting $LiNH_2$ with MgH_2, showing formation of the mixed imide $Li_2Mg(NH)_2$ and structural transformation of this imide at different temperatures.[75] The reaction of Li_3N with Mg under H_2 forms $Mg(NH_2)_2$ that is then seen to cycle H_2 according to equation 1.18.[76] A thermodynamic study into this system showed that substituting LiH with the less stable MgH_2 leading to partial substitution of Li by Mg, and the system can absorb hydrogen reversibly at 32 bar H_2 at 200°C.[77] However, due to the higher stability of $Mg(NH_2)_2$, the products of rehydrogenation are the starting materials of equation 1.18 rather than equation 1.17.[78] Adding $LiNH_2$ to the decomposition of $Mg(NH_2)_2$ has been seen to proceed *via* reaction 1.19, giving a pathway with better overall decomposition thermodynamics.[79]

$$\mathrm{Mg(NH_2)_2 + 4\,LiH + LiNH_2 \longrightarrow 2\,Li_2NH + LiMgN + 4\,H_2} \tag{1.19}$$

The mechanism of the reaction of $Mg(NH_2)_2$ ball-milled in the molar ratio 3 : 8 with LiH has been investigated and shows the existence of intermediate reactions during which the presence of Mg_3N_2 near the surface of $LiNH_2$ has been seen to be very important.[80,64]

As well as magnesium, addition of calcium to Li_2NH creates single phase materials that have been shown to have reduced hydrogen absorption/desorption temperatures.[81] The structure of the Li-Ca imide has been shown via X-ray diffraction to be of the form $Li_2Ca(NH)_2$, adopting a trigonal crystal structure.[82] The calcium and lithium systems have been combined, and been shown to release and uptake hydrogen reversibly, as shown in reaction 1.20.[83] The same is not the case for the sodium system and, although the Li-Na-N-H system releases hydrogen, it is considered non-reversible.[84]

$$\mathrm{CaH_2 + 2\,LiNH_2 \longrightarrow CaNH + Li_2NH + 2\,H_2 \longleftrightarrow Ca(NH_2)_2 + 2\,LiH} \tag{1.20}$$

1.3.2.6 Other Mixed Complex Hydride Systems

As the complex hydride systems have different advantages and disadvantages, they can be mixed to tune their properties. For example, it has been shown that addition of $LiBH_4$ to MgH_2 enhances the absorption/desorption kinetics.[35] Another mixed system that has been widely investigated is that of lithium amide and lithium borohydride. For $(LiNH_2)_x(LiBH_4)_{1-x}$, the compositions near $x = 0.667$ have been seen to release the least ammonia and the most hydrogen.[85] The structure at this composition has been investigated using X-ray diffraction, which found that the true composition is $Li_4(NH_2)_3(BH_4)$ and that it adopts a body centred cubic structure with the BH_4^- and NH_2^- ions in an ordered arrangement.[86,87] This is referred to as the α-phase. Replacement of the NH_2^- ions by BH_4^- (reduction in x) forms a β-phase observed with composition $Li_2(NH_2)(BH_4)$.[88] This β-phase has been refined to a hexagonal array of $(LiNH_2)_6$ clusters dispersed in a $LiBH_4$ matrix.[89] Gradual substitution of the BH_4^- ions with NH_2^- ions in $LiBH_4$ forms a solid solution of $Li(BH_4)_n(NH_2)_{4-n}$ tetrahedra.[90] Variable temperature X-ray diffraction has been used to create a phase diagram of the $LiNH_2$-$LiBH_4$ mixture.[91,88]

Hydrogen desorption from $Li_4BH_4(NH_2)_3$ has been observed to start at 260°C, with the relative amount of hydrogen to ammonia released dependent on the experimental set-up. Ammonia release is thought to be suppressed by long contact times between desorbed ammonia and the bulk material, favouring pathways that release hydrogen.[92] This is consistent with the ultra-fast hydrogen releasing reaction between LiH and ammonia observed in LiH - $LiNH_2$ systems.[60]

1.3.2.7 Halide Doping in Hydrogen Storage

Halide-containing compounds such as $TiCl_3$, $MoCl_3$ and TiF_3 have been shown to lower the desorption temperatures when added in catalytic amounts to lightweight complex hydrides such as $LiBH_4$ and $LiNH_2$.[93,94,95,96,97] For example, the addition of 1 mol.% $TiCl_3$ to a 1 : 1 mixture of $LiNH_2$ and LiH has been shown to desorb almost 80% of the total hydrogen content (5.5 wt%) within 30 minutes at 200°C, without emission of ammonia, for three cycles.[98] The $TiCl_3$ acts as a catalyst for the transfer of the NH_3 molecule from the $LiNH_2$ to LiH.[60] $TiCl_3$ has also been used in combination with $MgCl_2$ to bring the dehydriding starting temperature of $LiBH_4$ down to 60°C without losing boron.[99] It was shown that the $MgCl_2$ and $TiCl_3$ interacted with the $LiBH_4$ to form intermediate compounds such as TiB_2 and LiCl resulting in the lower dehydrogenation temperature.

Addition of halides to lightweight complex hydrides has been seen as early as 1983 to improve the lithium ion conductivity.[100] Improvements have also been observed to the ionic conductivity of $LiBH_4$ by addition of the halides LiX,[101] and by formation of mixed amide halides such as $Li_3(NH_2)_2I$.[102]

The concentration of the additive can determine the way that it alters the reaction mechanism: investigations into doping $MgCl_2$ into $LiNH_2$ found that, at low levels of addition (<4 mol%), the $MgCl_2$ acts as a NH_3 sorbent. For $MgCl_2$ addition of between 4 and 25 mol%, the $MgCl_2$ is thought to form a solid solution, further improving the hydrogen desorption properties. At levels higher than this, the $MgCl_2$ is thought to react with the $LiNH_2$ to form $Mg(NH_2)_2$ changing the Li-N-H system into the Li-Mg-N-H system LiH + 0.5 $Mg(NH_2)_2$.[103]

At the intermediate doping level, a solid solution of $Li(BH_4)_{1-x}I_x$ has also been seen to cycle hydrogen, maintaining 68% of the calculated hydrogen storage capacity after four cycles of hydrogen release, compared to only 25% after two cycles for $LiBH_4$.[104] Halides have also been added into the structure of $LiNH_2$, forming amide halides such as $Li_2Br(NH_2)$ and $Li_4(NH_2)_3Cl$.[105,69] These amide halides have been seen to have a lower temperature of hydrogen desorption when heated with LiH than $LiNH_2$ alone.[69,106] They are also seen to have high ionic conductivity thought, for $Li_3(NH_2)_2I$, to be due to structural features such as short Li-Li distances and abundant interstitial sites of large volume.[107]

The decomposition of $LiNH_2$ and Li_2NH without the presence of LiH has also been seen to occur at lower temperatures by addition of Cl^- ions by mixing with LiCl, and it is proposed that this occurs due to the weakening of the interaction between Li^+ and NH_2^-.[108] However, if not formed before addition, the formation of $Li_4(NH_2)_3Cl$ can have a detrimental effect, as its formation *in situ* could act as a competing reaction.[109] The addition of LiBr to $LiNH_2$ to form $Li_7(NH_2)_6Br$ is thought to weaken the N-H bond and promote the migration of Li^+ ions, suppressing ammonia emission and reducing the desorption temperature.[106] The effect of the addition of halides to the Li-Mg-N-H system has also been used to try and elucidate how the hydrogen de/rehydrogenation is improved on doping, although the exact mechanistic changes are still unclear.[110]

1.3.2.8 Challenges

Despite rapid advances in the field of complex metal hydrides, challenges still remain when considering their use as hydrogen stores. Many of the materials are expensive and, in some cases, show irreversible desorption or require high temperatures for hydrogen release.[111] Mechanical techniques can be used to optimise these materials: ball milling of the mixture of $LiNH_2$ and LiH has been shown to reduce the temperature of desorption and also the release of NH_3,[112] due to the reduction in particle size.[113] The same has also been observed for the system doped with lithium and calcium halides, and for other metal hydride systems.[114,115,40]

For a metal hydride system in an automotive application, the perfect store would have to store more than 6 wt% hydrogen near room temperature at a pressure of approximately 1 MPa. However, for such a system, 100 MJ of heat would be released when refilling with 6 kgH_2. It is therefore also crucial to manage the heat during this refilling process.[21] With fast charging times of three to five minutes, this heat problem will become even more of an issue.[116] Many of these lightweight complex metal hydrides are also hygroscopic and, in some cases, pyrophoric. This leads to additional engineering challenges, but they are relative cheap and easy to produce when compared to other possible hydrogen stores.[117]

1.4 Project Objectives

The project aim was to study the relationship between the structure of a hydrogen storage material and its physical properties, such as ionic conductivity, and the hydrogen uptake and release kinetics. The materials of focus were lithium and magnesium amide halides, with an emphasis on the lower halide doping limits, as this reduces the gravimetric hydrogen density penalty caused by halide addition.

The initial project objective was to determine the effect of chloride doping on lithium amide. Two phases had previously been observed after reaction under different conditions, and the details of the structure of these phases and the conditions for their production were to be determined. After characterisation on laboratory X-ray powder diffraction equipment, a more detailed structural analysis would be carried out by using synchrotron and neutron radiation.

After clarification of the structural details, the next stage of the project was to investigate and compare the physical properties of the different phases. Both the hydrogen uptake and release kinetics and the ionic conductivity would be investigated, and the relationship between these properties and the structure of the materials determined.

Mixed metal systems have been seen to show improvements in hydrogen storage properties, so the work was extended to consider the addition of magnesium into the system. Both the structural details and the hydrogen storage properties of any new phases were investigated and compared to the pure lithium system. The large range of possibilities of different reactant ratios gives this system huge scope for investigation.

The work was then be developed to consider the effect of the level of bromide doping on the structure of the lithium amide bromide system. A comparison of the structural results and the physical properties can then be made to the amide chloride.

This project has lead to greater knowledge of how the structure of how these materials change on cycling with hydrogen, and how the kinetics of these cycles can be used to gain insight into the reaction mechanisms.

Chapter 2

Experimental

2.1 Solid state synthesis under inert gas

The synthesis of the materials used in this project was carried out under inert conditions due to high reactivity towards oxygen and moisture. The reactants were weighed out on an analytical balance (with an accuracy of 0.1 mg) in an argon-filled glove box (MBraun, UniLab) and then ground together by hand using a pestle and mortar.

After grinding, the samples were transferred to a quartz reaction tube with an outer diameter of half an inch. This tube was then sealed with a Young's tap T-piece with Ultra-torr® fitting, removed from the glove box and clamped in such a way to ensure the sample sat in the centre of a vertical tube furnace (Lenton Furnaces, LTF 12/25/250 fitted with a Eurotherm 3216P1 controller). The T-piece was then connected to a flow of argon gas, purging the gas line. The Young's tap was then opened, causing the argon gas to flow over the sample, maintaining the inert atmosphere and removing any gaseous products of the reactions. The heating rate was varied from 2 to 10 °C min^{-1} and then the temperature held for a period of time after which the sample was allowed to cool. Once the sample was cool, the Young's tap was closed and the sample removed from the furnace and returned to the glove box.

2.2 Crystallography and diffraction

2.2.1 Crystallography

2.2.1.1 Crystal structures

All crystalline materials in the solid state are made up of a regular 3-dimensional arrangement of atoms. The smallest unit of the structure able to reconstruct the whole crustal structure through translational symmetry is described as the unit cell. A unit cell is described by 6 lattice parameters: the lengths of its edges (*a*, *b* and *c*) and the angles between them (α, β, γ). The symmetry of a structure can be described by using one of seven crystal systems, shown in table 2.1, determined by the combination of relationships between the different lattice parameters.[118,119]

Equivalent atomic positions are defined as lattice points, with the environment of an atom in one of these points being identical to if it were on any of the other lattice points. The translational symmetry of the structure is described by the location of these equivalent positions, giving rise to four types of lattice. The most simple is a primitive lattice (P), as this contains only one lattice point at the corners of the unit cell. Introducing a lattice point to the centre of the cell causes it to become body centred (I), and to the centre of each face gives a face-centred cell (F). If lattice points are located at the centre of just one unit cell face, in the centre of the *ab* plane, the lattice is a C lattice. Combining these possible lattice types with the seven crystal systems gives fourteen possible combinations, known as Bravais lattices, shown in table 2.1.

To describe the crystal structure of a material completely, it is necessary to know the lattice parameters that define the unit cell, the internal symmetry of the cell and the positions of the atoms within it. The atomic positions are the fractional coordinates from one corner along each direction of the unit cell. By defining atomic positions, additional symmetry

Crystal System	Unit Cell Dimensions	Essential Symmetry	Bravais Lattices
Cubic	$a = b = c$, $\alpha = \beta = \gamma = 90\,°$	Four threefold axes	P, I, F
Tetragonal	$a = b \neq c$, $\alpha = \beta = \gamma = 90\,°$	One fourfold axis	P, I
Orthorhombic	$a \neq b \neq c$, $\alpha = \beta = \gamma = 90\,°$	Three twofold axes	P, I, F, C
Hexagonal	$a = b \neq c$, $\alpha = \beta = 90\,°, \gamma = 120\,°$	One sixfold axis	P
Rhombohedral	$a = b = c$, $\alpha = \beta = \gamma \neq 90\,°$	One threefold axis	R
Monoclinic	$a \neq b \neq c$, $\alpha = \gamma = 90\,°, \beta \neq 90\,°$	One twofold axis	P, C
Triclinic	$a \neq b \neq c$, $\alpha \neq \beta \neq \gamma \neq 90\,°$	None	P

Table 2.1: Crystal systems and Bravais lattices

elements are required to describe the Bravais lattice. Once all possible three-dimensional symmetry elements are combined, 230 possible space groups can be derived, and these are able to describe the symmetry of the crystal structure.

2.2.1.2 Lattice planes

Lattice points that form a repeating three-dimensional arrangement can be connected to form a lattice plane. Each lattice plane has a lattice point within it, and the planes form a repeatable, equally placed set. For diffraction and crystallography, a formal description of these planes is required. For this purpose, the planes are described by Miller indices, determined by the points at which the lattice plane intersects the unit cell. The reciprocals of the fractional intercepts between the unit cell and the first plane are denoted by the Miller indices *h*, *k* and *l*. Any equivalent lattice plane will have the same *hkl* value. The distance between equivalent planes is the *d* spacing (d_{hkl}), which can be calculated for a cubic system by using equation 2.1.[118,119]

$$d_{hkl} = \frac{a}{\sqrt{h^2 + k^2 + l^2}} \tag{2.1}$$

2.2.2 X-ray diffraction

Using X-ray diffraction (XRD) experimentally involves shining a monochromatic beam of radiation onto a sample, and moving a detector at a defined geometry relative to the sample and the source of radiation. It is a usually non-destructive technique that can illicit information about the crystal structure and composition of a material. X-rays are used to investigate crystalline materials because they have a wavelength of a similar order to the distances between atoms in a solid. The X-rays interact with the electrons of the atoms in crystalline materials, giving a diffraction pattern. This pattern can be explained by using Bragg's analysis. He considered the crystals as layers of atoms, as described by the Miller indices introduced above. As shown in figure 2.1, some X-rays (labelled as 1) are reflected by the first plane of atoms. Others (labelled as 2) pass through and are reflected by another plane. If scattering of these two waves occurs at points A and D, it can be seen that the second wave travels further than the first.

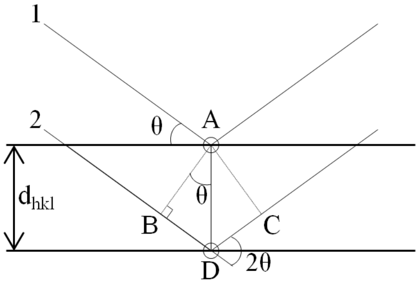

Figure 2.1: Geometry used in the derivation of Bragg's law.

Using the diagram enables the calculation of the difference in path length between the two waves:

$$\text{path length difference} = \text{BD} + \text{DC} = 2d_{hkl}\sin\theta \tag{2.2}$$

The reflections are only observed when completely constructive interference occurs between the two waves. This will only occur when the path difference is equal to an integer of the

X-ray wavelength ($n\lambda$):

$$\mathrm{n}\lambda = 2d_{hkl}\sin\theta \text{ where n = 0, 1, } 2\ldots \tag{2.3}$$

When this law is satisfied, a strong peak intensity is observed, whereas all other values of *n* give rise to destructive interference when summed over all scattering events. The angle of the observed diffracted beam gives the separation of the planes of the atoms (the *d* spacing). As the X-ray scattering occurs from the electron cloud, the intensity of the beam gives information on the properties of the scattering atoms.

2.2.2.1 X-ray generation

X-rays are generated in a laboratory setting when high energy electrons collide with a metal plate. This ejects an electron from a core orbital of the metal, forming a hole. The hole is filled *via* electron decay, a process accompanied by the emission of radiation of characteristic wavelengths. In the laboratory experiments in this study, copper was used as a target. The characteristic discrete wavelengths of copper are caused by the 2p to 1s and 3p to 1s relaxations (denoted K_α and K_β, respectively). For copper, the 2p electron has two possible spin states, and so the K_α transition is a doublet separated into $\mathrm{K}_{\alpha 1}$ (1.54056 Å) and $\mathrm{K}_{\alpha 2}$ (1.54433 Å). In addition to these emissions, a broad spectrum of background radiation is also observed, due to the release of kinetic energy in the form of photons as the electrons slow down on entering the metal target.

2.2.2.2 Monochromation

For XRD experiments, a single wavelength is required at high intensity and to achieve this, a monochromator is used. A crystal monochromator is used in the laboratory experiments in this project. This involves a single crystal set at a specific orientation, θ_m, satisfying the

Bragg equation below, where d_{hkl} is the d-spacing of an intense reflection. Using this set orientation, only one wavelength is diffracted, in the case of copper, the $K_{\alpha1}$ wavelength.

$$\lambda = 2d_{hkl}\sin\theta_m \tag{2.4}$$

2.2.2.3 Detection

The most common type of X-ray detector is a scintillation counter. When struck by the X-rays, a phosphorescent crystal emits a photon. This is then detected and amplified by a photomultiplier tube, producing a signal that is proportional to the number of photons hitting the crystal. The diffractometer detects the amount of X-rays at any given angle, 2θ.

2.2.2.4 Laboratory X-ray diffraction

Laboratory powder X-ray diffraction measurements were collected on a Bruker AXS D8 diffractometer in transmission mode. This uses a germanium monochromator to give copper $K_{\alpha1}$ radiation at a wavelength of 1.54056 Å. Samples were prepared in an argon-filled glovebox, sealed between two pieces of Scotch® Magic™ tape before being loaded onto the diffractometer. The samples were rotated perpendicularly to the X-ray beam whilst measurement took place. Samples were also measured on a Siemens D5000 diffractometer in transmission mode, again using a germanium monochromator to produce Cu $K_{\alpha1}$ radiation at a wavelength of 1.54056 Å. For this diffractometer, samples were loaded into Cole–Parmer polyimide tubing with 0.0340 inch internal diameter and sealed with vacuum grease. The samples were aligned and rotated perpendicular to the beam during measurement.

2.2.2.5 Synchrotron X-ray diffraction

A synchrotron uses synchronised magnetic and electric fields to generate a focussed beam of high energy particles. These are controlled by magnetic fields in a circular orbit. Radiation is emitted when the high energy particles change direction or speed over a wide range of wavelengths.[120]

Powder synchrotron X-ray data were collected on beam line I11 at the Diamond Light Source, Didcot, UK. A schematic of this beamline is shown in figure 2.2. Samples were measured using a wavelength of 0.826937 Å (September 2013), and 0.826205 Å (July 2015). Samples for single environment experiments were sealed into 0.5 mm borosilicate capillaries in an argon-filled glovebox using epoxy resin, aligned and rotated during measurement. A hot air blower was used to control the temperature of the sample.

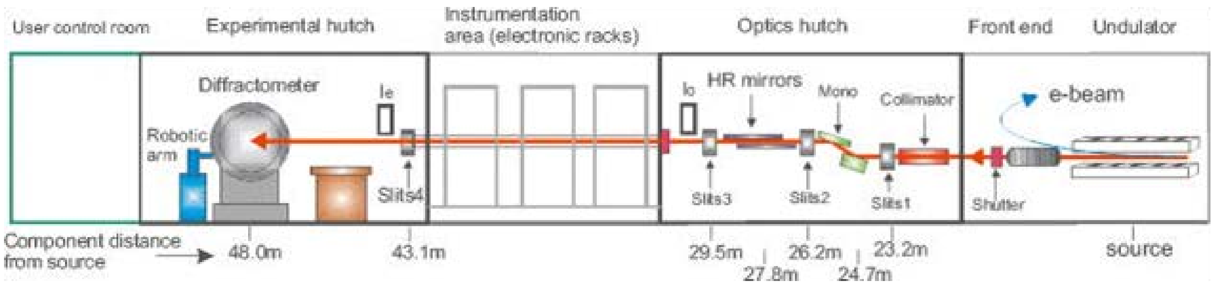

Figure 2.2: Schematic diagram of beamline I11 at the Diamond Light Source showing the main components and their approximate distances from the X-ray source.[121]

2.2.3 Neutron diffraction

In addition to X-rays, neutrons can also be used to investigate the structures of crystalline materials. Whereas X-rays are scattered by the electron clouds of the atoms, neutrons are predominantly scattered by the atomic nuclei, causing the neutron scattering factor of an atom to be different than for X-rays. This can cause higher relative sensitivity to lighter elements.

Neutrons can be generated using a nuclear reactor, or *via* spallation. The latter occurs when high energy protons are fired in pulses at a heavy metal target. This causes it to release neutrons with a broad range of wavelengths. Neutrons penetrate further into samples than X-rays, but also scatter more weakly. Neutron powder diffraction experiments therefore require larger samples and longer collection times.

Total neutron scattering is composed of a coherent part and an incoherent part. Hydrogen ^{1}H gives very strong incoherent scattering, leading to a large contribution to the background of the neutron diffraction pattern. The isotope deuterium ^{2}H gives mainly coherent scattering, and is so used instead of hydrogen for structural studies using neutron sources.[122]

Powder neutron diffraction experiments were carried out on the beamline POLARIS at the ISIS neutron source at the Rutherford Appleton Laboratory in Oxfordshire. A schematic of the POLARIS beamline is shown in figure 2.3. Instead of measuring at a fixed wavelength, as for X-ray diffraction, the time of flight method was used. The entire neutron wavelength spectrum is used, with a fixed diffraction angle θ. The de Broglie relationship shows the dependence of the neutron wavelength on its velocity. It is shown in equation 2.5, where m is the mass of the neutron (1.675×10^{-27} kg).

$$\lambda = \frac{m}{v} \tag{2.5}$$

With the detector a fixed distance from the sample, the time of flight is measured, enabling the wavelength to be measured, and the d-spacing calculated using Braggs law (equation 2.3). Samples for diffraction-only experiments were prepared in an argon-filled glove box and sealed inside a vanadium can with indium wire.

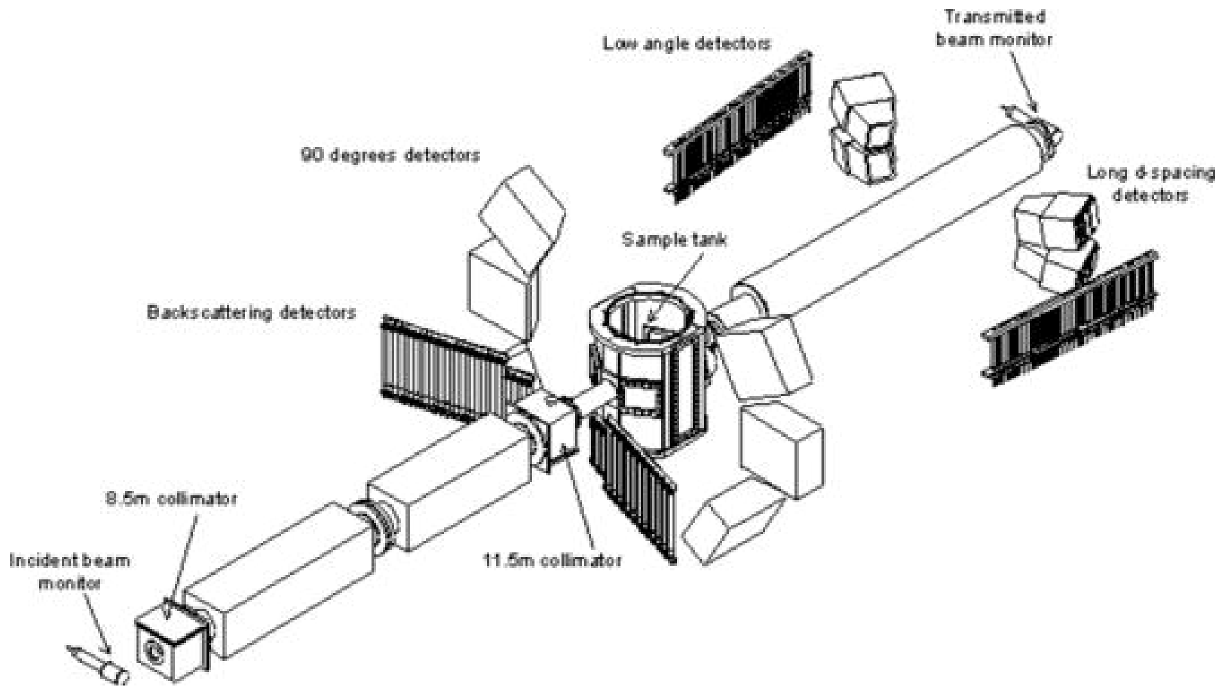

Figure 2.3: Schematic diagram of the POLARIS beamline at the ISIS neutron source showing the main components.[123]

2.2.4 Powder diffraction

Unlike for single crystal X-ray diffraction, a powder sample contains many small crystallites which are randomly orientated. This will also therefore be the case for the lattice planes within the structure and so the X-rays will be diffracted in all directions. As each crystalline material has a characteristic diffraction pattern, a powder diffraction pattern can be used to determine which phases are present within the powder sample. The position, shape and intensity of the peaks in the pattern are used for analysis.

Peak positions are determined by the unit cell parameters and symmetry and the wavelength used in the experiment. Using the Bragg law, shown in equation 2.1, the distances between the lattice planes in the unit cell correspond to the peak positions, although errors in the height of the sample can cause a change in the observed peak positions. The particle size and crystallinity predominantly determine the peak shapes of the pattern, as will instrumental factors. The Bragg law only truly applies for an infinite crystalline sample, and so for a finite crystal the intensity of a Bragg peak will be spread over an area. This enables the crystalline size to be calculated using the peak width. Although overall peak intensity is influenced by instrumental and experimental factors, the relative amount of each phase determines the relative peak intensities. Within a phase, the relative peak intensities give information on the positions and type of atoms in the unit cell. Scattering of X-rays depends on the electron cloud of the atoms: heavier atoms scatter X-rays more strongly than lighter ones.

The intensity of a Bragg peak is also determined by a number of other factors, including a thermal factor. Diffraction experiments take a snapshot of the atomic positions, but in reality the atoms move about these positions, causing a drop off in scattering power which the thermal parameter takes into account.

2.3 Rietveld analysis

Rietveld analysis was carried out to determine the structures of the phases present in the samples studied using the computer program TOPAS.[124] The Rietveld method constructs a powder diffraction pattern based on a structural model, and refines it against the experimental data. The simulated pattern is calculated from a combination of structural and experimental parameters. The structural factors taken into account include the unit cell parameters, the atomic positions and their occupancies. Experimental factors include the peak shape and background. The parameters within the simulated pattern are refined using a least squares method to find a solution with the minimum difference between the simulated and experimental patterns. During a least squares refinement, the function S_y, as shown in equation 2.6, is minimised. This function sums over all data points the difference between the observed intensity for the i^{th} step, y_i and the calculated intensity for the i^{th} step, y_{ci}, and weights them based on the estimated error in intensity, w_i.[125,126]

$$S_y = \sum\nolimits_i w_i(y_i - y_{ci})^2 \tag{2.6}$$

As the Rietveld method refines a structural model, the input needs to be the best possible starting model. When determining the structure of a material, the pattern will first be indexed to determine the crystal system and lattice parameters. The space group and an approximate structure can then be calculated, before the Rietveld method is used to refine this approximate structure. To determine the success of the Rietveld fit, initially a visual inspection is necessary. The refinement will produce a difference pattern, which would be a straight line if the observed and calculated structures were the same. Beyond a visual inspection, various numerical parameters are used to determine quantitatively the quality of the fit. The statistical comparison between the observed and calculated patterns is described as '*R*-weighted profile', or R_{wp}, equation 2.7.

$$R_{wp} = \sqrt{\frac{\sum_i w_i(y_i - y_{ci})^2}{\sum_i w_i y_i^2}} \tag{2.7}$$

As the calculation of R_{wp} includes the function S_y, it is a good indication of how well the model is fitting to the data. However, the value of R_{wp} can be artificially high if not all of the observed peaks are present in the calculated pattern. Conversely a high, well fitted, background in the pattern will produce a particularly low R_{wp} value. Because of this, other statistical measures, or a background-corrected R_{wp} value are also considered. For a given data set, the best possible statistical fit is described by '*R*-expected', or R_{exp}. As the refinement progresses, it is expected that the value for R_{wp} should approach that of R_{exp}. The quality of the data is what determines R_{exp}, as described by equation 2.8, where N is the number of observables, P is the number of parameters refined and C is the number of constraints.

$$R_{exp} = \sqrt{\frac{N-P-C}{\sum_i w_i y_i^2}} \tag{2.8}$$

The statistical significance of the difference between R_{wp} and R_{exp} can be calculated by the square of the ratio between them, χ^2, as shown in equation 2.9.

$$\chi^2 = [\frac{R_{wp}}{R_{exp}}]^2 \tag{2.9}$$

χ^2 can be a useful statistic, as it includes the number of parameters that are being refined. However, it is affected by the quality of the data, and so high quality data can produce an artificially high value of χ^2, while an artificially low value of χ^2 can be produced if poor quality data masks the errors associated with the structural model. In addition to a good statistical fit, it is important to consider the chemistry of the structural model. Atomic distances and bond angles must be sensible, and fractional occupancies in agreement with the chemical composition of the sample.

2.3.1 Quantitative phase analysis

Rietveld analysis can be used to give accurate values of the relative and/or absolute amounts of the phases present in a mixture. This technique of Quantitative Phase Analysis, or QPA, has been shown to be effective in both X-ray and neutron diffraction data.[127,128] QPA can be described by equation 2.10, where W_p is the relative weight fraction of phase p in a mixture of n phases, S is the Rietveld scale factor, and Z, M and V are the number of formula units per unit cell, the mass of the formula unit (in atomic mass units) and the unit cell volume (in Å^3), respectively.

$$W_p = \frac{S_p(ZMV)_p}{\sum\limits_{i=1}^{n} S_i(ZMV)_i} \tag{2.10}$$

Deviation of the determined weight factors from the true values can be influenced by any factor that affects the Bragg intensity of the peak, such as preferred orientation. This arises when the crystallites in a powder sample have a strong tendency to be oriented in one particular direction.

In this study, QPA has been used to study light metal hydrides and their reactions. Hand grinding was used to ensure that the samples were homogeneous before being measured using powder XRD, and the samples spun rapidly during data collection. The majority of QPA calculations were carried out using data collected using synchrotron radiation. During QPA, only lattice parameters, peak shapes and scale functions were refined for each phase. Atomic positions and thermal parameters were determined from a previous refinement of a pure phase.

2.4 Mass spectrometry

Mass spectrometry, or MS, is used as an analytical tool to measure the mass to charge ratio (*m/z*) of charged particles. The mass spectrometer will scan a range of *m/z* values to determine the relative abundances of the particles present. The sample gas stream is ionised, and the particles within it manipulated using an electromagnetic field to distinguish between the different *m/z* ratios. MS needs to be done at low gas pressures to prevent collisions between the charged particles.[129]

2.4.1 Ionisation

Ionisation converts particles or molecules into charged particles by removing or adding an electron or proton. In this study, electron impact (EI) ionisation was used. A tungsten filament is used to generate an electron beam, which removes an electron from the sample atoms to form charged particles. Singly charged species are preferable, as it is the *m/z* ratio that is being measured. Because of this, doubly charged cations are ignored by the analyser. The excess energy from this ionisation process may cause the molecules to fragment, forming smaller cations. These fragments will be detected at a smaller *m/z* ratio, and so a knowledge of the breakdown mechanisms of the molecules in a sample is crucial. A repeller electrode accelerates the cations towards the mass analyser.

2.4.2 Separation

Before detection, the ions are separated by their *m/z* ratio. In the past, mass spectrometers separated the ions using a curved electromagnet with a magnetic field of varying strength. At low magnetic fields, the particles with a lower *m/z* would be directed onto the detector, and then the magnetic field strength increased to direct those with larger *m/z* ratios. More commonly now, and in this study, quadrupole mass analysers are used. Instead of bending the ions around a curve, parallel electrodes oscillate at radio frequencies to produce an electric field. This stabilises the path to the detector of ions with a certain *m/z* ratio, whilst those with other *m/z* ratios are neutralised through collisions. The full range of *m/z* ratios are measured by varying the frequency.

2.4.3 Detection

On reaching the detector, the ions produce a current on collision with the surface which is then amplified. When a large ion current will be generated, a Faraday cup detector is used. This kind of detector is a conductive cap that emits an electron when a charged particle hits the surface. When greater sensitivity is required, a secondary electron multiplier (SEM) detector may be used. This amplifies the electrons produced by the collision using a series of electrodes at increasing potentials. By producing a cascade of electrons, this technique can increase the sensitivity by a factor of around 10^6.

2.5 Temperature programmed desorption

Temperature programmed desorption (TPD) is a technique that allows the desorption products of a sample to be monitored as it is heated.[92] In this work, a homebuilt TPD apparatus was used, enabling the gases given off when a sample is heated at a chosen rate to be monitored using mass spectrometry. This experimental set up, described by figure 2.4, occurs under an atmosphere of flowing argon gas and will be referred to as 'TPD-MS'. The argon flow was controlled by a mass flow controller (Hastings 200 series, Teledyne) to a constant flow of 100 ml min^{-1} and the gaseous products measured using a quadrupole mass spectrometer (HPR-20, Hiden Analytical). The gas is sampled through a narrow heated capillary which passes into the vacuum system of the mass spectrometer to restrict the amount of gas entering the MS. Multiple ion monitoring mode was used to detect only the ions of interest, and SEM detection used to measure both hydrogen and ammonia fragments.

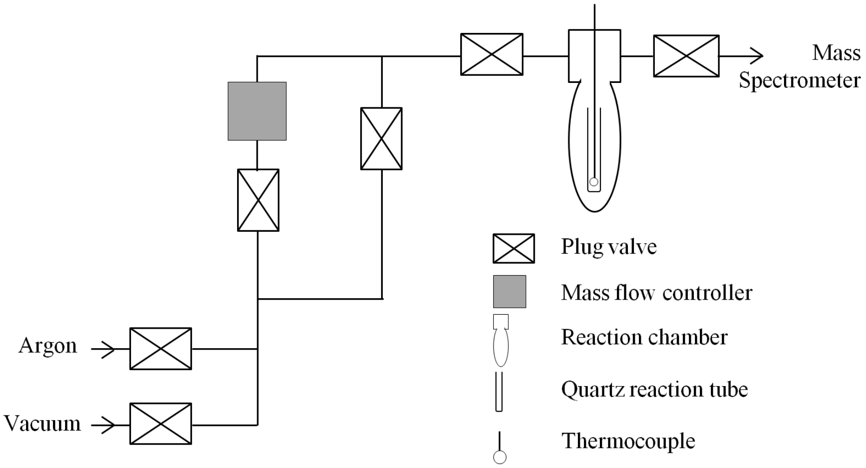

Figure 2.4: Schematic diagram of the TPD-MS set-up.

The sample to be studied was weighed inside an argon-filled glove box, placed into a quartz reaction tube (7 mm O/D, 4 mm I/D) and sealed within the reaction chamber. The weight of the samples studied ranged between 0.5 and 1 g. Exposure to the atmosphere was avoided by repeated evacuation and argon purging cycles of the connecting pipes before connecting the reaction chamber and opening the valves. A barrel heater was placed around the sample while a thermocouple directly in contact with the sample enabled accurate control over the heating, and an indication of any endothermic or exothermic events.

2.5.1 Calibration

To determine the relative sensitivity of the mass spectrometer to hydrogen and ammonia, a calibration gas was used (BOC Speciality Gases, 5000 ppm H_2, 5000 ppm NH_3 in Argon). This gas was flowed through the TPD apparatus in the way that argon is during the TPD-

MS experiments. The mass spectrometer was set up to measure the partial pressures for *m/z* values of 2 (H_2^+), 16 (NH_2^+), 17 (NH_3^+/OH^+), 18 (H_2O^+), 28 (N_2^+), 32 (O_2^+) and 40 (Ar^+). The mass flow was set to 45.8 ml min^{-1} and, once the gas traces had levelled off, the signals were recorded. Due to the main mass fragment of ammonia, NH_3^+, having the same *m/z* ratio as OH^+, the fragment NH_2^+ was used instead. The comparison of the NH_2^+ and NH_3^+ fractions can be used as an indication of the moisture level in the gas line.

The partial pressure of the gases H_2^+ and NH_2^+ were converted into a fraction of the total gases present, and the equivalent fractional signals from the pure argon carrier gas were subtracted from them. These background-subtracted fractional signals were then divided by the true molar fraction of H_2 and NH_3 in the calibration gas. For the calibration gas used, the molar fractions are 4.736×10^{-3} and 4.898×10^{-3} for H_2 and NH_3, respectively. This calculation yields relative sensitivity values for each species that were used to correct the observed signals obtained from TPD-MS experiments.

For each set of MS data, before heating, the signal was recorded for a short period of time to collect background signals for *m/z* values for 2 and 16. This background signal was then subtracted from the signals from the experiment. After this background subtraction, the fractional values were divided by the relative sensitivities calculated previously to give corrected molar fractions of H_2 and NH_3 present in the experimental gas flow.

2.6 Hydrogenation

Samples were hydrogenated under pressures of up to 90 bar H_2 in a stainless steel reactor connected to a gas manifold fitted with a pressure gauge and pressure release valve as shown in figure 2.5.

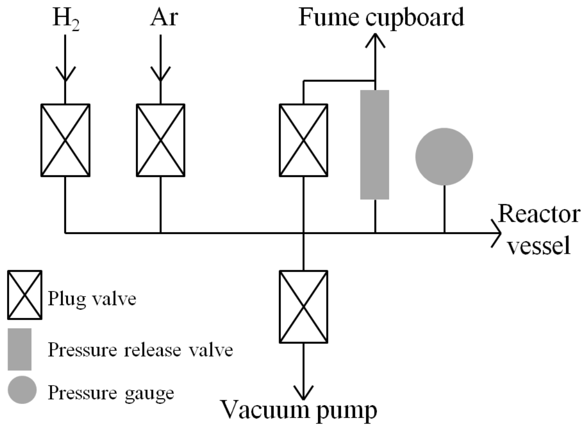

Figure 2.5: Schematic diagram of the gas manifold used for high pressure hydrogenation.

Samples were prepared in an argon-filled glove box due to their air sensitivity, loaded into quartz tubes and placed in the stainless steel reactor. The reactor was sealed using a torque wrench set to 90 Nm^2 before being removed from the glove box. The manifold was evacuated and then filled with argon multiple times, before the reactor was connected and then the whole system evacuated and purged with a low pressure of hydrogen.

The pressure of H_2 was then increased to the desired pressure for the reaction, to allow for the increase in pressure on increasing the temperature. A furnace was then fitted around the reactor and the heating regime set. Throughout the set-up and the reaction time, hydrogen detectors were used to check the system for leaks. Once the furnace program had finished, the system was emptied of hydrogen, evacuated and purged with argon. The reactor was then closed and disconnected from the system before being opened in an argon-filled glove box.

2.7 Raman spectroscopy

When a molecule is irradiated with electromagnetic radiation the energy can be transmitted, absorbed or scattered. In Raman spectroscopy the radiation scattered by the sample is analysed. A monochromatic source of radiation is used to irradiate the sample. If an elastic collision occurs between the incident photon and the molecule, it is referred to as Rayleigh scattering. In this case, the rotational and vibrational energy of the molecule is unchanged, and so the energy and frequency of the scattered photon is the same as that of the incident photon. Rayleigh scattering forms the strongest component of the scattered radiation.[130,131]

The Raman effect is observed when an inelastic collision occurs between the incident photon and the molecule. If the molecule gains energy and moves into a higher vibrational state, Stokes lines are observed in the spectrum (figure 2.6). Anti-Stokes lines are observed in the spectrum when the molecule loses energy during the scattering process. At room temperature, the majority of the molecules are in their lowest vibrational state (v=0, figure 2.6), meaning that Stokes scattering is the dominant form of Raman scattering. For a vibration of a molecule to be Raman active, the polarisability of the molecule must change during the vibration.

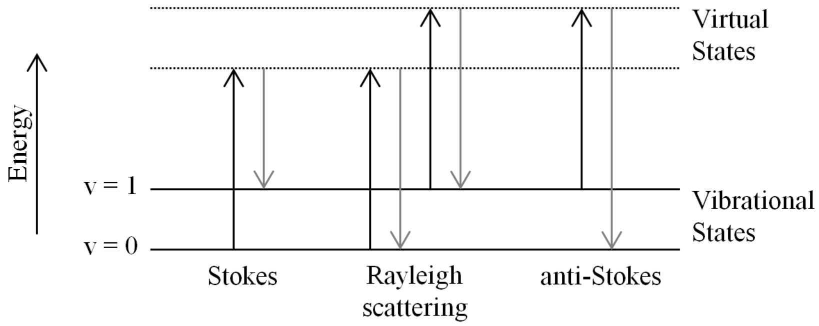

Figure 2.6: Diagram of the Rayleigh and Raman scattering processes.

Raman spectra were collected using a Renishaw InVia Raman microscope using an Ar laser at a wavelength of 488 nm. Samples were loaded into an Instec sample cell in an argon-filled glove box and then transferred to the Raman microscope.

Across all the samples, the active group of interest is the NH_2^- group. An ideal NH_2^- anion is bent, and has the point group C_{2v}. When the amide ion is in the structure of $LiNH_2$, it lies on a general position with point symmetry of C_s, although this symmetry reduction does not affect the number of vibrational modes that can be observed. The point group table for C_{2v} is shown in table 2.2.

	E	C_2 (z)	σ_v (xz)	σ_v (yz)	Linear, rotations	Quadratic
A_1	1	1	1	1	z	x^2, y^2, z^2
A_2	1	1	-1	-1	R_z	xy
B_1	1	-1	1	-1	x, R_y	xz
B_2	1	-1	-1	1	y, R_x	yz
Γ_{red}	9	-1	1	3		

Table 2.2: Point group table for C_{2v}

The reducible representation (Γ_{red}) can be reduced to an irreducible representation:

$$\Gamma_{irr} = 3\ A_1 + 1\ A_2 + 2\ B_1 + 3\ B_2.$$

By considering the point group table, it can be seen that translation and rotation have the symmetry properties:

$$\Gamma_{trans} = A_1 + B_1 + B_2$$

$$\Gamma_{rot} = A_2 + B_1 + B_2$$

From this information, the symmetry properties of the vibrational modes of the amide molecule can be determined:

$$\Gamma_{vib} = \Gamma_{tot} - \Gamma_{trans} - \Gamma_{rot} = 2\ A_1 + B_2$$

These three vibrational fundamentals are shown in figure 2.7 and represent the symmetric stretch (A_1), the bending vibration (A_1) and the asymmetric stretch (B_2). For a vibration to be Raman active, the polarisability must change during the vibration. To determine which modes are Raman active, the irreducible representations that correspond to the quadratic functions are cross checked with those for the vibrational modes. From table 2.2 it can be seen that all three of these vibrational modes are Raman active as they have the same symmetry as a quadratic function. The bending mode is observed at much lower wavenumber than the stretches, and the asymmetric stretch is observed to split into two bands in both the Raman and Infra-Red spectra.[132] The Raman spectra of $LiNH_2$ and the product of the first stage of dehydrogenation, Li_2NH, were measured and the observed peaks correlate well with those observed in the literature (table 2.3).

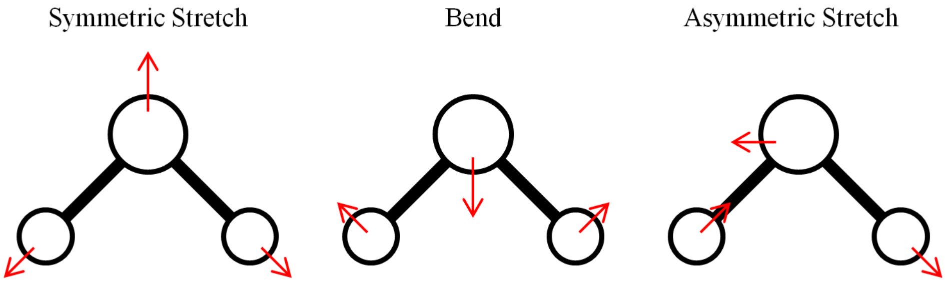

Figure 2.7: Schematic representation of the three Raman active modes of the NH_2^- molecule.

Reference	$LiNH_2$ sym	$LiNH_2$ a-sym	$LiNH_2$ a-sym	Li_2NH
Bohger *et. al.*[132]	3258	3310	3315	
Kojima *et. al.*[133]	3260	3315		3180
Chellappa *et. al.*[134]	3269	3321	3332	
Observed	3263	3313	3324	3183

Table 2.3: Observed Raman stretching modes for $LiNH_2$ and Li_2NH

2.8 A.C. impedance spectroscopy

In this work the conductivity of the samples was investigated using A.C. impedance spectroscopy. Measurements were made on a Solartron 1200 phase-sensitive multimeter with impedance analysis interface within the frequency range 1 Hz to 1 MHz. Powder samples were pressed into 7 mm pellets using a Specac mini-pellet press inside an argon-filled glove box by applying an axial force of 1 tonne. The pressed pellets were sintered in a quartz tube under flowing argon, at a temperature determined by the stability of the sample. After sintering, the large circular faces of the pellets were coated with silver-electrodag (Agar Scientific), to ensure good electrical contact at the surfaces, and attached to the silver electrodes of a custom-built rig that enables measurements under an inert atmosphere, shown in figure 2.8. After being left to dry the electrodag overnight, the rig was placed into a furnace, with the temperature monitored by a thermocouple next to the sample.

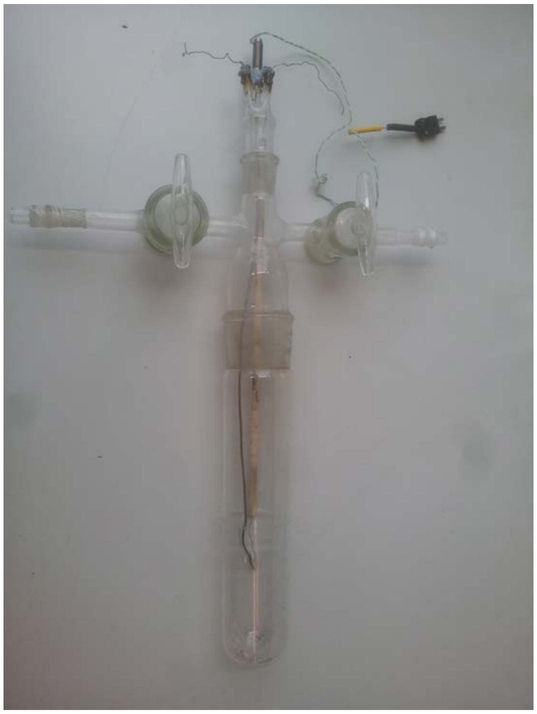

Figure 2.8: Photograph of the inert atmosphere rig used for A.C. impedance measurements.

This technique applies an AC voltage across a sample and a standard resistor which are in series with one another. The voltage across the sample causes the charge-carrying species to move towards its complementary pole and generate a current. If the sample does not behave as a perfect resistor, there is a phase difference between the sinusoidal applied voltage and the resulting current through the sample, due to capacitive or inductive effects. This phase difference is described by the phase angle, θ, and the impedance at time t, Z, is the ratio between the applied voltage (E_t) at frequency f (Hz) and the current (I_t), as defined in equation 2.11.[135]

$$Z = \frac{E_t}{I_t} = \frac{E_0 \sin(2\pi f)}{I_0 \sin(2\pi f t + \theta)} \tag{2.11}$$

Impedance is a vector quantity, as shown in equation 2.12, and impedance data are plotted as the real, Z' (resistive), against imaginary Z'' (capacitive) components.

$$Z(2\pi f) = Z_0(\cos\theta + i\sin\theta) = Z' + Z'' \tag{2.12}$$

The resistance and capacitance of the sample can be calculated from these semi-circular Nyquist plots by modelling an equivalent circuit for a resistor and a capacitor in parallel.[136] The resistance is used with the pellet dimensions to calculate the conductivity, σ, of the samples, as shown in equation 2.13.

$$\sigma = \frac{\text{Pellet thickness}}{\text{Pellet area} \times \text{Resistance}} \tag{2.13}$$

From the time dependence of the conductivity, the activation energy, E_a, for ion migration can be calculated using an Arrhenius relationship as described by equation 2.14.

$$\ln(\sigma) = \frac{-E_a}{R} \times \frac{1}{T} + \ln(\sigma_0) \equiv \log(\sigma) = \frac{-E_a}{2.303R} \times \frac{1}{T} + \log(\sigma_0) \tag{2.14}$$

2.9 Volumetric analysis

Volumetric analysis was carried out using a Hiden Isochema HTP volumetric analyser. The sample is accurately weighed and then inertly loaded into the reaction chamber using a portable glove box mounted onto the system. In addition to the reaction chamber, the HTP has an empty dose chamber inside whose pressure is varied. Once the pressure is stable, the connection between the two chambers is opened and the pressure change in the dose chamber measured. The same process is repeated over a range of pressures while the temperature is controlled by an external furnace, monitored by a thermocouple in direct contact with the sample.

This method, the Sieverts method, is used to create pressure composition isotherms which can then be used to calculate the thermodynamic properties of the sample.

2.10 Hydrogen cycling at the Diamond Light Source

As described by Parker *et. al.*,[137] gas cycling experiments were carried out on beamline I11 at Diamond Light Source, Oxfordshire. The samples were loaded into 0.5 mm borosilicate capillaries and then mounted into a low pressure capillary gas cell, as shown in figure 2.9. During data collection, the sample was rocked to improve the particle statistics. To control the temperature, an external hot air blower was used, and a gas control panel was used to control the gas supply to the sample. Before starting, the capillary was tested to 150 % of the pressure used during the experiment.

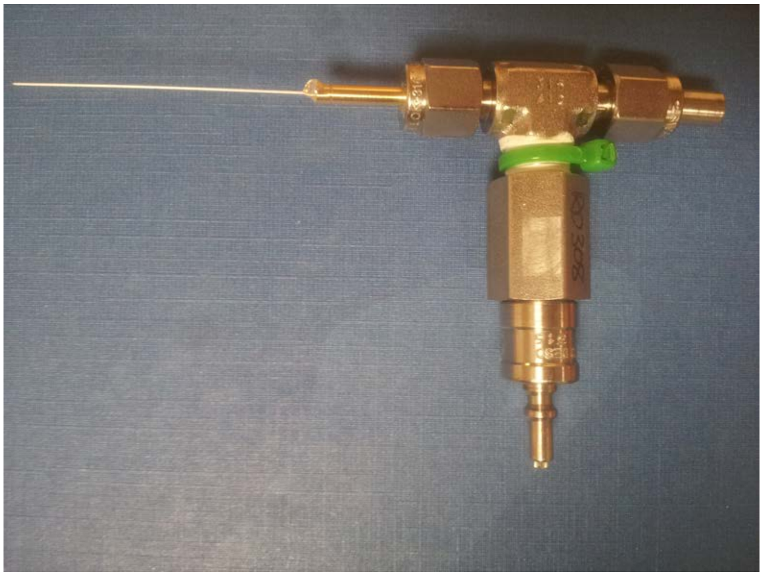

Figure 2.9: Photograph of the capillary gas cell used for hydrogen cycling measurements on the I11 beamline at Diamond Light Source.

2.11 Deuterium cycling on the POLARIS beamline at the ISIS neutron source

A gas cell, as illustrated in figure 2.10, was used to cycle samples under deuterium and vacuum on the POLARIS beamline at the ISIS neutron source. The cell was made of stainless steel with an 11 mm internal diameter and a wall thickness of 0.35 mm. The gas flowed into the cell through a pipe that extended 14.5 mm into the cell volume, and out through a hole in the top, minimising the likelihood of a blockage occurring. Samples were loaded into the cell and assembled with the remainder of the POLARIS *in situ* apparatus in an argon-filled glove bag. After sealing, a boron nitride collimation shell with gadolinium shielding was used to encase the cell, removing the diffraction signal of the steel from the data.

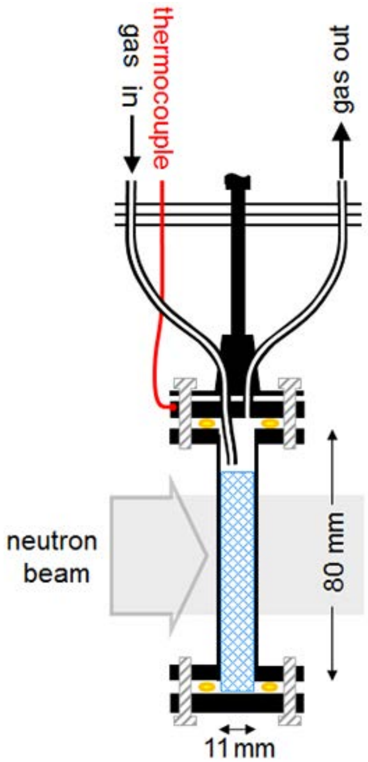

Figure 2.10: Experimental setup used for cycling samples under deuterium / vacuum on the POLARIS beamline at the ISIS neutron source, adapted from Makepeace *et. al.*[138]

2.12 Gravimetric measurements during deuterium cycling on the POLARIS beamline at the ISIS neutron source

An Intelligent Gravimetric Analyser (IGA, Hiden Analytical) is a thermo-gravimetric balance that can operate at constant pressure. A specialised IGA, an IGA^n, was used at the POLARIS beamline at the ISIS neutron source, Rutherford Appleton Laboratory, Oxfordshire. The samples were loaded inside a specialised argon-filled glove box, as shown in figure 2.11, into a quartz bucket which was loaded onto a microbalance, enabling accurate measurement of the mass of the sample. This enabled the change in weight of the sample to be monitored whilst the temperature and pressure were changed. The temperature of the sample was controlled by coiled heating wires above and below the sample and monitored using a sensor next to the sample, as shown in figure 2.12. The gas composition at the sample position was controlled remotely, with the sealed vessel able to reach pressures of up to 20 bar deuterium or be held under vacuum.

Figure 2.11: Photograph of the Intelligent Gravimetric Analyser used on the POLARIS beamline, in the argon-filled glove box used for sample loading next to the control system.

Figure 2.12: Photograph of a sample in a quartz bucket loaded onto the microbalance of the IGA^n.

Chapter 3

Structural investigation of $Li_4(NH_2)_{4-x}Cl_x$

3.1 Introduction

Previous investigations have looked in detail at the structures of a new series of amide halides. The amide halides have been shown to release hydrogen at a lower temperature on reaction with lithium hydride than $LiNH_2$.[69] The amide iodide $Li_3(NH_2)_2I$ was seen to adopt a double-layered hexagonal structure.[102] Two amide bromides were observed: Li_2NH_2Br taking an orthorhombic cell,[105] and $Li_7(NH_2)_6Br$ forming a rhombohedral structure with a hexagonal unit cell.[69] One amide chloride is reported, with stoichiometry $Li_4(NH_2)_3Cl$, and has been seen to take two structures depending on the reaction conditions of its formation.[69] After reaction of $3LiNH_2$ with LiCl for one hour, a rhombohedral phase is formed. After a reaction time of twelve hours, a cubic phase is observed.[69] Figure 3.1 shows the powder X-ray diffraction patterns of the two phases. The cubic phase, space group $I2_13$, has a unit cell that contains twenty-four NH_2^- ions on the 24*c* sites and eight Cl^- ions on the 8*a* sites.

The rhombohedral phase is in space group R$\bar{3}$ and has a slightly different stoichiometry: each cell contains sixteen NH_2^- ions and five Cl^- ions. Three of the Cl^- ions are located on the 3*a* sites and the remaining two are accommodated on the 18f NH_2^- ion positions ('Cl2 sites').[139] The two different unit cells are shown in figure 3.2.

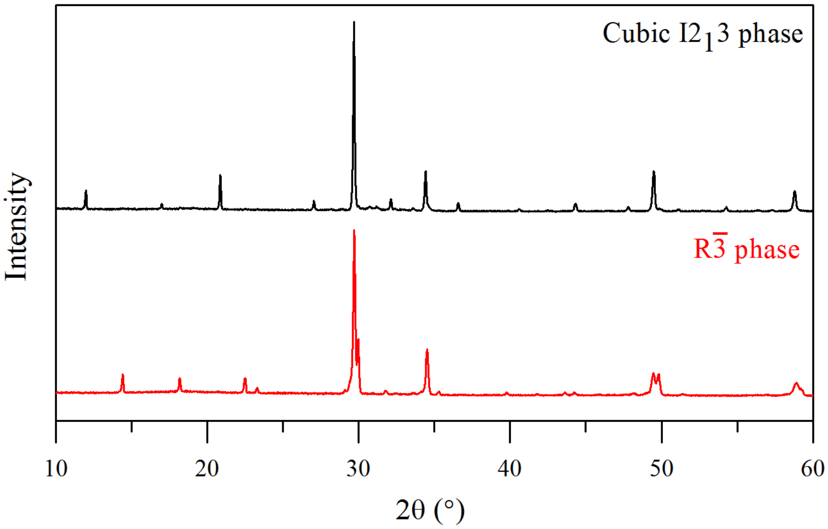

Figure 3.1: Powder X-ray diffraction patterns of the cubic and rhombohedral phases of $Li_4(NH_2)_3Cl$.

In this chapter I report the effect of composition and time on the structure of the amide chloride formed, with the aim of reducing the chloride content whilst maintaining the structure needed to exhibit the preferential hydrogen storage properties observed when comparing $Li_4(NH_2)_3Cl$ to $LiNH_2$. As magnesium has been seen to further reduce the hydrogen desorption temperature,[80] the investigation was extended to the structures formed on reaction of $LiNH_2$ with $MgCl_2$.

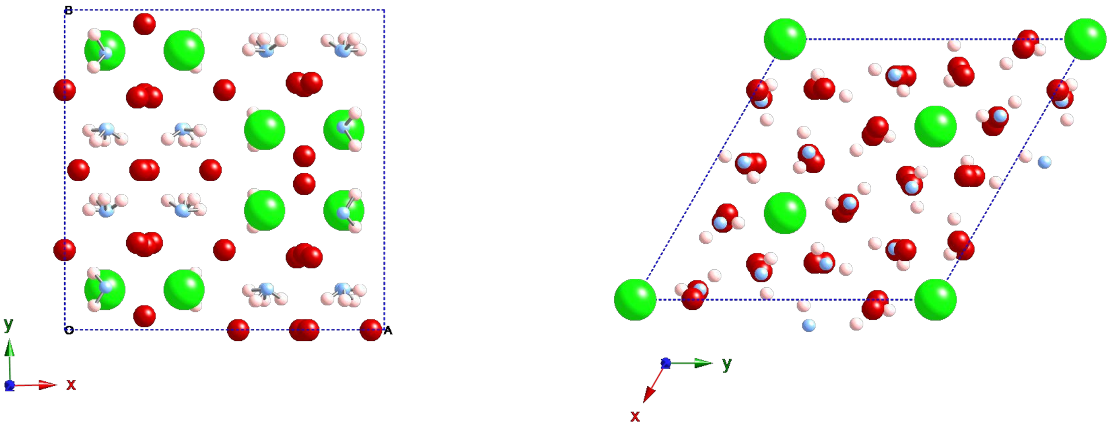

Figure 3.2: Left: The structure of one unit cell of the $I2_13$ phase of $Li_4(NH_2)_3Cl$. Right: The structure of one unit cell of the $R\bar{3}$ phase of $Li_4(NH_2)_3Cl$, with the 'Cl2' ions disordered on the nitrogen sites. Both structures are viewed down the z axis. Chloride ions are shown as green spheres, lithium red, nitrogen blue and hydrogen pink. Unit cells are marked with dotted lines.

3.2 Experimental

Samples of ground mixtures of lithium amide (Sigma–Aldrich, 95% purity) and either LiCl or $MgCl_2$ (Sigma–Aldrich, anhydrous beads, 10 mesh, 99.998% purity) were prepared in an argon-filled glove box. The samples were prepared in various stoichiometries across a range of amide to chloride ratios between 1.3 : 1 and 7 : 1 and heated in quartz tubes under flowing argon at temperatures up to 400°C for up to 12 hours, as described in section 2.1.

Powder X-ray diffraction data were collected in the laboratory as described in section 2.2.2.4 using a Bruker D8 instrument in transmission geometry with a wavelength of 1.54059 Å and a Siemens D5000 transmission geometry with a wavelength of 1.54059 Å. Powder synchrotron X-ray diffraction data were collected at Diamond Light Source on the I11 beamline with a wavelength of 0.826937 Å (September 2013), and 0.826205 Å (July 2015). Powder neutron diffraction data were collected at ISIS neutron source at the Rutherford Appleton Laboratory in Oxfordshire using the beamline POLARIS.

Raman spectroscopy, as described in section 2.7 was also performed on the samples and is discussed in this chapter. The hydrogen storage properties of these materials are reported later in this study.

3.3 The effect of composition on the kinetic product

Initially, the phase space of the amide chloride was investigated for the products of a one hour reaction time. The reaction in equation 3.1 was carried out over a range of Cl^- compositions between $x = 0.5$ and 1.75 at 400°C for one hour.

$$(4{-}\mathrm{x})\,\mathrm{LiNH_2} + x\,\mathrm{LiCl} \longrightarrow \mathrm{Li_4(NH_2)_{4-\mathit{x}}Cl_{\mathit{x}}} \tag{3.1}$$

For $x = 1$, a rhombohedral $R\bar{3}$ phase was observed, as reported previously.[69] As the chloride content, x, was increased, the $R\bar{3}$ phase was no longer present but instead a cubic $I2_13$ phase was observed. This phase has a structure similar to the $Li_4(NH_2)_3Cl$ product previously observed after a twelve hour reaction time. Increasing the chloride content to $x > 1.14$ leads to LiCl appearing alongside the cubic phase in the XRD pattern of the product, as shown for $x = 1.75$ in figure 3.3. Therefore, after a reaction time of one hour, additional Cl^- ions cannot be accommodated into the cubic structure beyond the amide to chloride ratio of approximately 5 : 2.

Accommodation of any additional Cl^- ions beyond the 3 : 1 ratio would only occur if they were to be positioned on the sites in the structure occupied by NH_2^- ions. The observation of a cubic phase at $x = 1.14$ indicates that the $Li_4(NH_2)_3Cl$ structure is able to accommodate a small amount of non-stoichiometry in this way, up to the 5 : 2 ratio. However, beyond this, excess chloride ions must not be able to be accommodated into the structure, causing the reagent LiCl to remain un-reacted in the product.

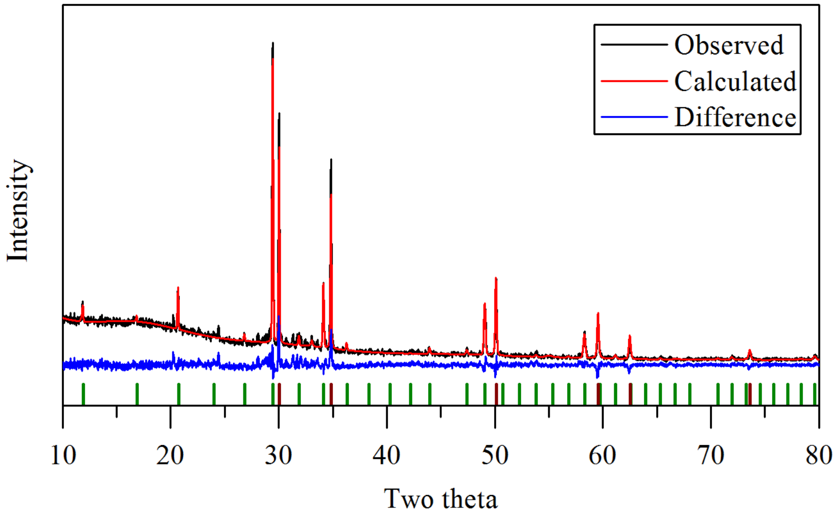

Figure 3.3: Powder X-ray diffraction pattern of the product of 2.25 $LiNH_2$ + 1.75 LiCl, showing lithium chloride (red tick marks) alongside the cubic phase (green tick marks).

Reducing the chloride content below the known stoichiometry of $Li_4(NH_2)_3Cl$, decreasing x below 1, causes the rhombohedral phase peaks in the XRD pattern to split, as shown in figure 3.4.

The patterns with split peaks can be refined to a mixture of two rhombohedral phases with different unit cell parameters, shown in figure 3.5. Because of the larger size of the Cl^- ion in comparison to NH_2^-, the phase with the larger parameters is likely to be that with a higher chloride content, while that with a smaller cell is likely to be more amide rich. Because of the presence of two phases, determination of exact stoichiometry of the phases present in these samples is challenging.

Decreasing x below 0.7 causes excess $LiNH_2$ to be observed in the diffraction pattern of the product. Therefore no more additional amide was accommodated within the structure,

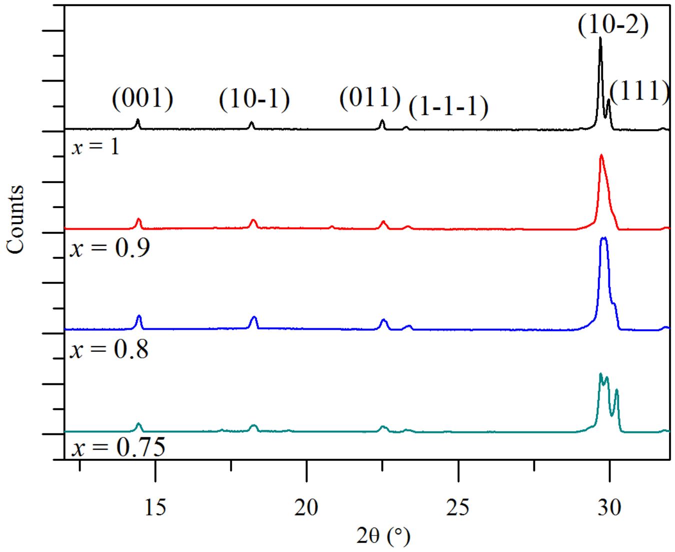

Figure 3.4: Powder X-ray diffraction patterns for the product of the reaction (4-x) $LiNH_2$ + x LiCl for $x = 1$ to $x = 0.75$ after one hour reaction time, with *hkl* values shown for the $x = 1$ pattern.

indicating that the lowest chloride content has been reached. The stoichiometry corresponding to $x = 0.7$ equates to an average unit cell content of 19.5 NH_2^- ions and 1.5 Cl^- ions. If this was accommodated within one phase, this ratio would correspond to half of the Cl^- 3a sites being occupied by NH_2^- ions. At $x < 0.7$, the peaks corresponding to this rhombohedral phase are split. This could either be due to the presence of two phases with varying chloride content, or some variation in the ordering of the amide ions on the chloride sites.

The Raman spectra of the same series are shown in figure 3.6 alongside the Raman spectrum for $LiNH_2$. As the chloride content decreases, the sample spectrum starts to resemble that for lithium amide, as it is present alongside the amide chloride at low chloride content.

A summary, shown in figure 3.7, shows the phases present over the range of x values for this reaction time. The weight percentage of each phase was calculated using quantitative phase analysis, as described in section 2.3.1.

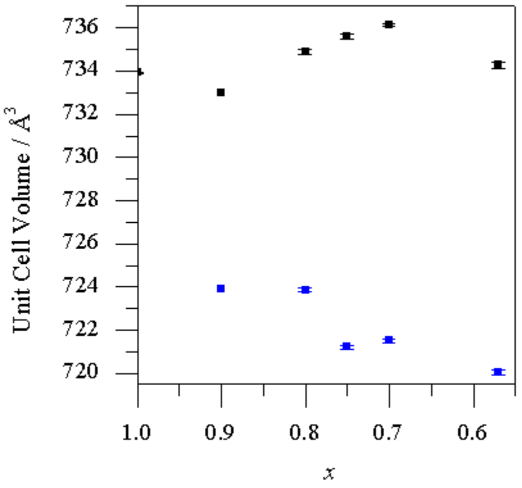

Figure 3.5: Unit cell volumes for the rhombohedral products observed in the XRD patterns of the products of a one hour reaction time. Black points correspond to the phase ‘R$\bar{3}$ phase 1’, the dominant phase at $x = 1$, and blue ‘R$\bar{3}$ phase 2’

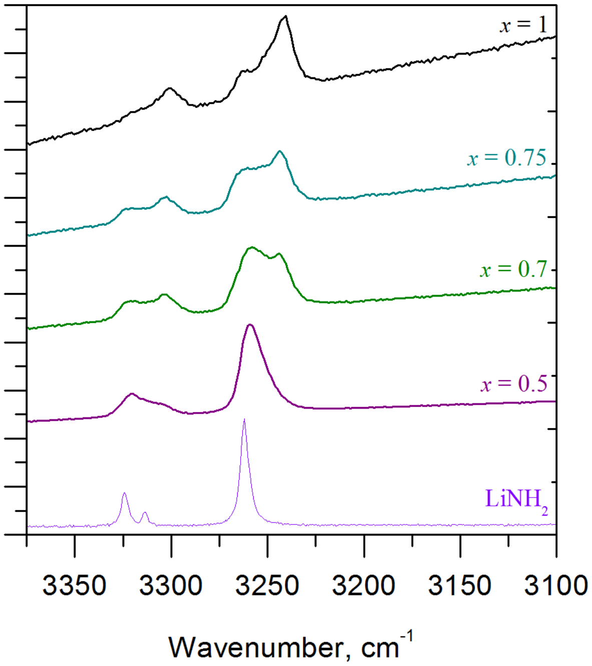

Figure 3.6: Raman spectra for the product of the reaction (4-x) $LiNH_2$ + x LiCl for $x = 1$ to $x = 0.5$ after one hour reaction time alongside that for $LiNH_2$.

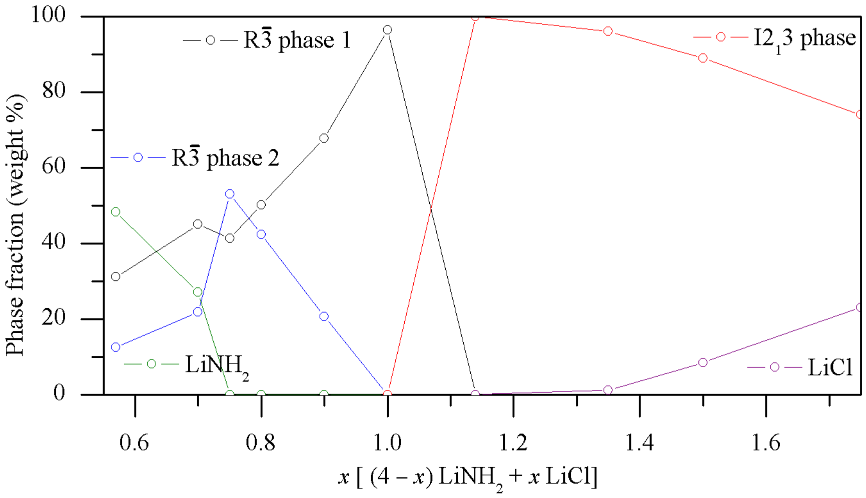

Figure 3.7: Diagram showing the phases present at different *x* values after a one hour reaction time for the product of the reaction (4-*x*) $LiNH_2$ + *x* LiCl.

3.4 Time dependence of the formation of $Li_4(NH_2)_3Cl$

A detailed time dependence study was carried out for the reaction of $3\,LiNH_2$ + LiCl at 400°C for reaction times ranging from one to twelve hours. For samples heated for one hour, a heating rate of 10°C min^{-1} was used, and those heated for twelve hours were heated at a rate of 2°C min^{-1}. A number of experiments were repeatable at different heating rates, showing that heating rate did not influence the product of the reaction.

The XRD patterns were analysed using quantitative phase analysis, as described in section 2.3.1, giving the weight percentages of each phase present in the pattern. Figure 3.8 shows these data, and it can be seen that for a reaction time of six or more hours, the cubic $I2_13$ phase of $Li_4(NH_2)_3Cl$ is formed. Shorter reaction times favour the formation of the rhombohedral $R\bar{3}$ phase, although sometimes the cubic phase was observed.

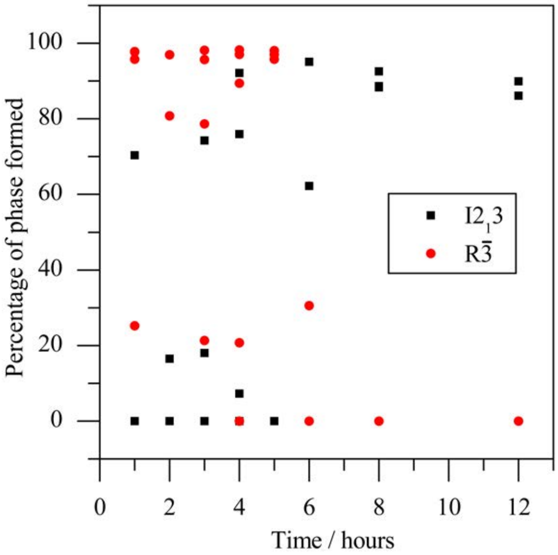

Figure 3.8: Graph showing the phase composition of the product of $3\,LiNH_2$ + LiCl against reaction time. Repeat experiments are shown by multiple data points.

The lattice parameters of the phases were calculated using model-independent fits to the data using TOPAS and are shown in figure 3.9. For a given reaction time, there was some variation in the observed unit cell volumes of the product phases between different experiments. The overall trend was a slight decrease in the unit cell volume in the rhombohedral phase with increasing reaction time, whereas for the cubic phase a slight increase in unit cell volume was observed with increasing reaction time.

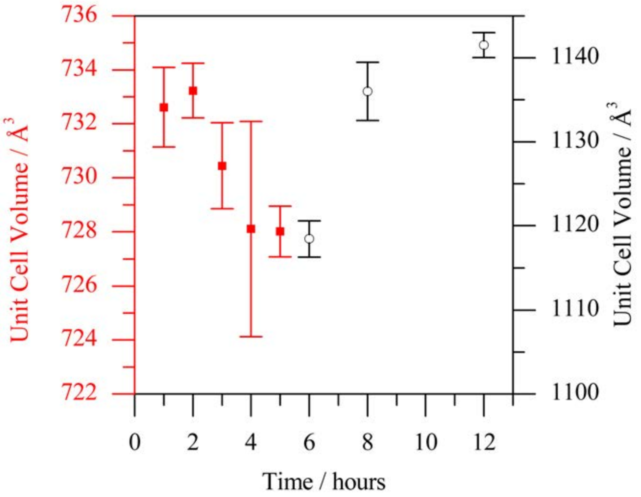

Figure 3.9: Graph showing the unit cell volumes of the reaction product of 3 $LiNH_2$ + LiCl against time, with error bars encompassing the results from repeated experiments. Red points and axis represent the $R\bar{3}$ phase, with black points and axis representing the $I2_13$ phase.

The Raman spectra of $Li_4(NH_2)_3Cl$ after a reaction time of one, three, four and twelve hours are shown in figure 3.10. They show the transition from one phase to another by the convergence of the peaks that are split in the initial rhombohedral phase into those representative of the cubic amide chloride.

3.4.1 *In situ* monitoring of the effect of reaction time

The transformation from the rhombohedral to the cubic phase was monitored using variable temperature powder synchrotron XRD. The rhombohedral phase was heated to 200°C and then held at this temperature, with patterns recorded at regular time intervals (figure 3.11).

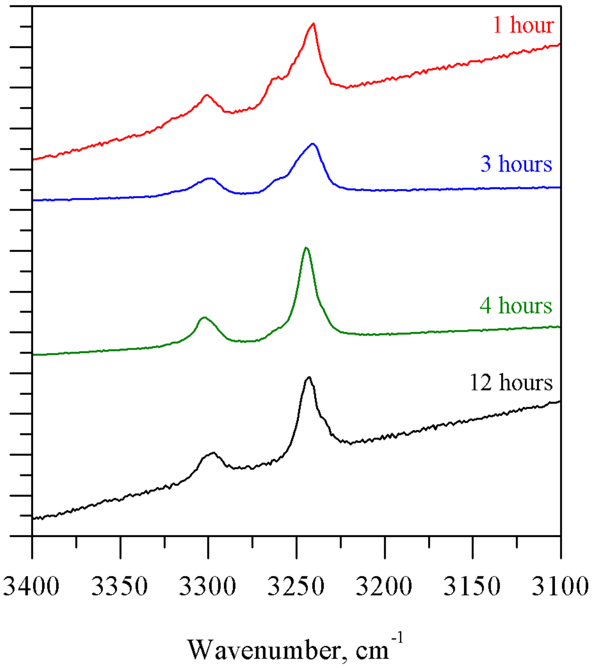

Figure 3.10: Raman spectra for the reaction products of 3 $LiNH_2$ + LiCl after different reaction times.

The patterns show a linear growth of peaks corresponding to the cubic phase and a corresponding reduction in intensity of those of the rhombohedral phase.

The results of these experiments suggest that the cubic phase can be considered to be the thermodynamic product at this reactant ratio, with the rhombohedral phase favoured kinetically. This is likely to be due to the chloride ions sharing the amide sites in the rhombohedral structure, making this phase thermodynamically disfavoured with respect to the cubic phase. The cubic phase is more dense than the rhombohedral phase, another factor that would favour its formation over longer reaction times.

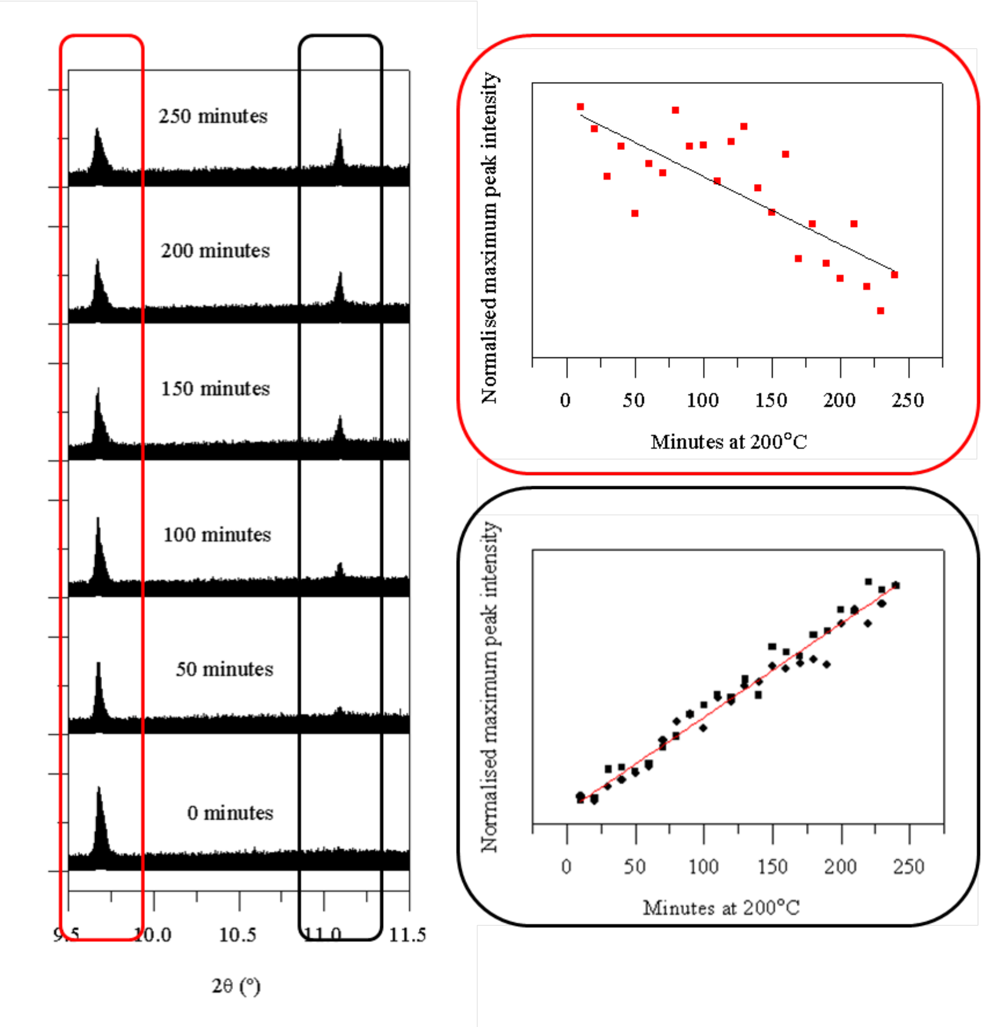

Figure 3.11: Powder synchrotron XRD patterns (a) of $Li_4(NH_2)_3Cl$ after heating at 200°C for increasing time periods, showing the reduction in height of the (110) peak corresponding to the rhombohedral $R\bar{3}$ phase (red, (b)) and the appearance and growth of the (211) peak representing the cubic $I2_13$ phase (black, (c)).

3.5 Effect of changing the Cl^- composition: 12 hour reaction time

As carried out for a one hour reaction, the reaction in equation 3.2 was carried out over a range of Cl^- compositions between x = 0.5 and 1.75 at 400°C, but this time for a twelve hour reaction time.

$$(4-\mathrm{x})\,\mathrm{LiNH_2} + x\,\mathrm{LiCl} \longrightarrow \mathrm{Li_4(NH_2)_{4-\mathit{x}}Cl_{\mathit{x}}} \tag{3.2}$$

For $x = 1$, a cubic $I2_13$ phase is observed, as reported previously.[69] Increasing the Cl^- content ($x > 1$) causes LiCl to be observed in the diffraction pattern of the product alongside the cubic phase. This suggests that, unlike for a one hour reaction time, after a reaction time of twelve hours no additional Cl^- ions can be accommodated into the structure beyond the amide to chloride ratio of 3 : 1. This is the ratio above which any additional chloride ions would need to be situated on amide ion sites. The comparison between reaction times suggests that accommodation of non-stoichiometry can happen to a limited extent (up to a 5 : 2 ratio) after a short reaction time but, given a longer reaction time to equilibrate, the structure no longer accommodates these additional Cl^- ions, and LiCl is formed.

Figure 3.12 shows the phases present over the range of x values studied after a reaction time of twelve hours. As the chloride content is reduced and x is decreased below 1, a new phase is observed alongside the cubic phase. This phase is observed with no other amide chloride phases at x = 0.57. All product diffraction patterns after a twelve hour reaction time show Li_2O in the product. Therefore, some oxidation is occurring during the reaction, despite the experimental setup being designed to reduce this as much as possible.

The x value of 0.57 corresponds to an amide to chloride ratio of 6 : 1, and would equate to an increase in the theoretical hydrogen storage capacity from 4.54 wt% to 5.28 wt% when compared to $Li_4(NH_2)_3Cl$. The structure of this new phase will be discussed in more detail

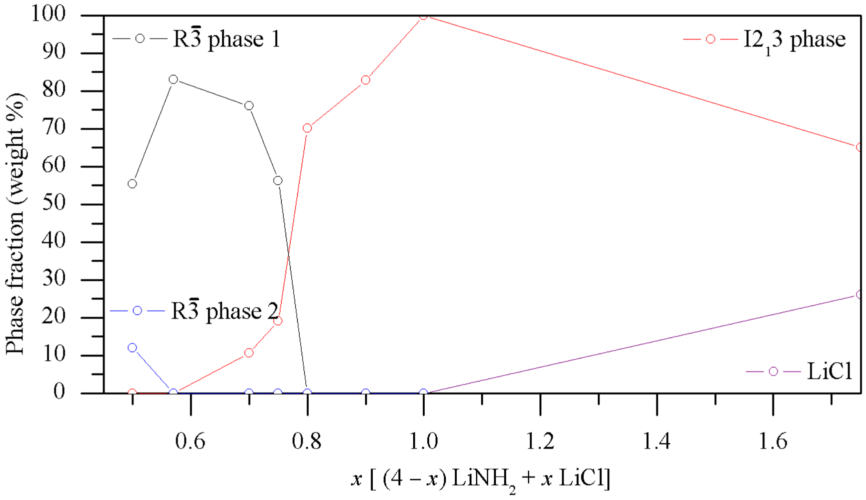

Figure 3.12: Diagram showing the non-oxide containing phases present at different x values after a twelve hour reaction time for the reaction (4-x) $LiNH_2$ + x LiCl.

below. Further reduction of the chloride level caused an additional rhombohedral phase to be observed in the powder XRD pattern alongside the new phase, indicating that the structure of the new phase cannot accommodate a lower level of chloride.

Raman spectroscopy of the *x* = 1 sample shows the peaks characteristic of the cubic phase. For *x* = 0.57, the new phase, the symmetric and antisymmetric peaks are seen to be split. Figure 3.13 shows both of these spectra, alongside that for *x* = 0.8 showing the transition between the two phases. In the Raman spectrum of $LiNH_2$, the asymmetric peak is split, but splitting of the symmetric peak indicates that there could be two different amide environments within the structure of the new phase.

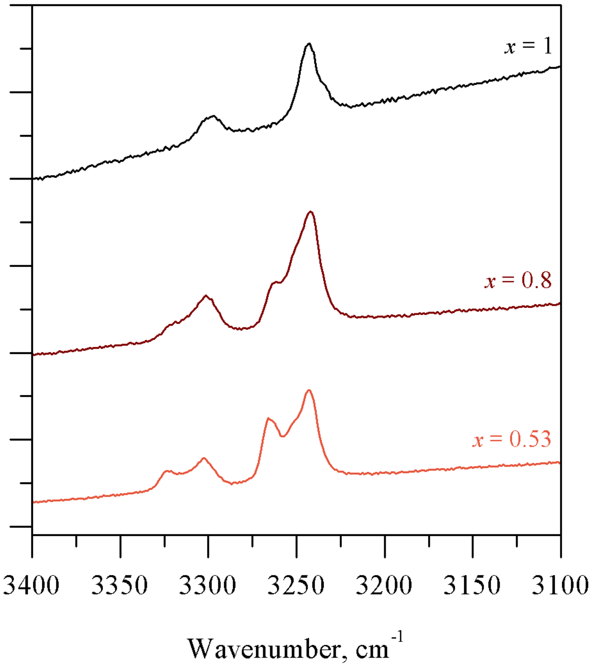

Figure 3.13: Raman spectra for *x* = 1, *x* = 0.8 and *x* = 0.53 after a twelve hour reaction time for the reaction (4-*x*) $LiNH_2$ + *x* LiCl.

3.5.1 Unknown phase

After all reactions that were carried out at 400°C for twelve hours, an additional phase was observed alongside the amide chloride and lithium oxide in the XRD patterns. This phase refined to a cubic Fm$\bar{3}$m unit cell with a = 4.6665(3) Å. Comparing this value with other lithium-containing cubic systems that could be observed in this system, in table 3.1, it can be seen that the value is in between that of lithium oxide and those of lithium imide and lithium chloride. The phase therefore could be a solid solution of lithium oxide with one, or both, of these other phases. The structures for Li_2O and Li_2NH are isostructural, and the anions are isoelectronic, making anionic substitution possible, but also very difficult to determine. As this phase is only observed when Cl^- is present in the starting material, it is likely that the phase is chloride-containing. Both Li_2O and LiCl take the space group Fm$\bar{3}$m, but the anions are not on the same site, although a simple structural transformation relates the two, making anionic substitution possible.

Phase	***a*, Å**
Li_2O	4.6120(3)
LiCl	5.1295(4)
Li_2NH	5.0742(2)
Unknown phase	4.6665(3)

Table 3.1: Cubic lithium phases and their unit cell sizes.

Reactions of Li_2O with Li_2NH and LiCl were carried out under the same conditions as for the amide chloride synthesis, but the unknown phase was not observed in the powder XRD patterns of the products. Rietveld refinements were attempted with a shared O/N, O/Cl and O/N/Cl site for Li_2O and LiCl, but substituted anion occupancies refined to zero. As the presence of this phase did not change throughout the series analysed in this study and the intensity of the peaks are of consistent intensity, it has been excluded from the QPAs used to calculate the weight percentages of the other phases present.

3.5.2 Structural refinement of the new phase with lower chloride content

The new phase was refined using a model-independent fit to a hexagonal unit cell with a = 9.7367(4) Å and c = 8.9307(3) Å in the space group $R\bar{3}$. There is a strong similarity between the XRD pattern of the new rhombohedral phase and that of the amide bromide $Li_7(NH_2)_6Br$. Therefore the published structure of $Li_7(NH_2)_6Br$ was used as a starting point for determining the structure of the new phase by Rietveld refinement. The initial refinement was run using the $Li_7(NH_2)_6Br$ structure, replacing the bromide ions by chloride ions. This gave a good fit to the data, with an R_{wp} of 9.383%, as shown in figure 3.14.

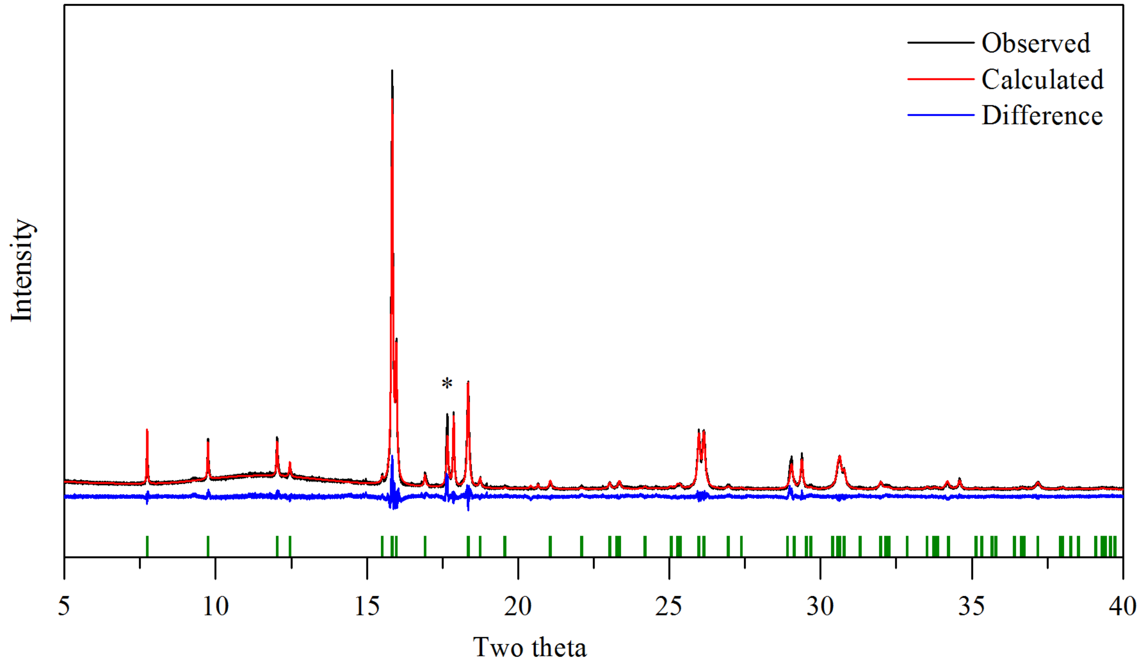

Figure 3.14: Powder synchrotron X-ray diffraction pattern of rhombohedral $Li_7(NH_2)_6Cl$ with a Rietveld refinement using the structure of $Li_7(NH_2)_6Br$ with a Cl placed on the Br sites (blue tick marks), showing observed (black), calculated Rietveld fit (red) and difference (blue) plots. Green tick marks show the peak positions of $Li_7(NH_2)_6Br$, and a star marks the peak position of Li_2O.

After this initial fit, the chloride position was refined and it remained on the 3a position, with an occupancy of 0.945 (R_{wp} of 9.274%). The nitrogen atoms were refined next, remaining on the same site but with refined atomic positions and with an R_{wp} of 9.192%. The lithium atoms also remained on the same sites, with refined positions and occupancies. The occupancies of the Li sites led to there being, on average, 6.5 Li atoms in each unit cell, whereas 7 would be expected for the ideal composition. Some lithium oxide is observed in the product XRD, potentially accounting for this discrepancy. Even at the ideal stoichiometry of $Li_7(NH_2)_6Cl$, the lithium sites would not be fully occupied. The atomic positions at this stage of the refinement are shown in table 3.2 and the diffraction data and fit shown in figure 3.15. Figure 3.16 shows a schematic representation of the new structure at this stage in the refinement.

Atom	**Site**	**x**	**y**	**z**	**Occ**
Cl	3a	0	0	0	1
N	18f	0.1922(2)	0.2237(1)	0.3480(1)	1
Li1	18f	0.2519(7)	0.1023(6)	0.3481(6)	0.5
Li2	18f	0.1448(6)	0.4198(6)	0.7621(4)	0.583

Table 3.2: Structure of $Li_7(NH_2)_6Cl$ after a preliminary structural refinement with R_{wp} = 11.338, R_{exp} = 5.531.

3.5.3 Diamond and ISIS structural refinement

Further structural refinement was carried out by combining the above structural model with data collected by neutron diffraction and pair distribution function data collected on beamline I15 at Diamond Light Source. Refinement of these data sets is in progress.

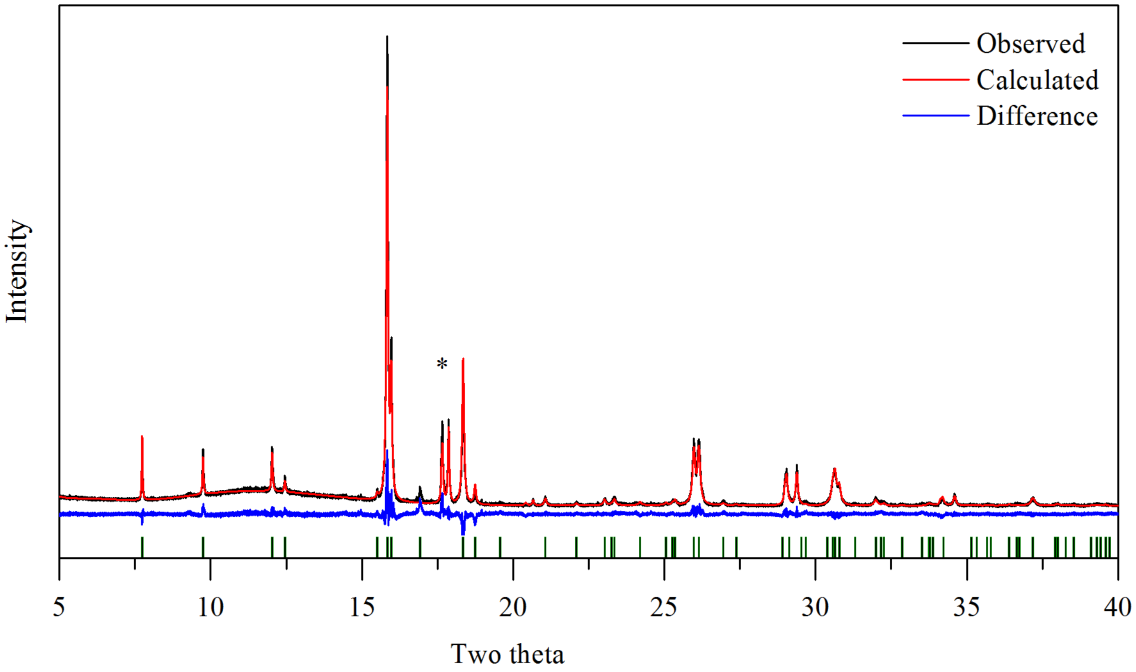

Figure 3.15: Powder X-ray diffraction pattern of the new phase, with the calculated Rietveld fit for the new structure of $Li_7(NH_2)_6Cl$. Tick marks show the peak positions of $Li_7(NH_2)_6Cl$, with a star marking the position of the peaks corresponding to Li_2O and the unknown phase.

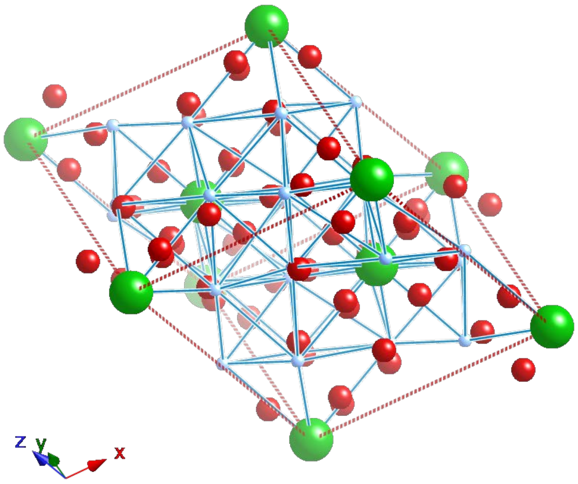

Figure 3.16: Schematic representation of the anion arrangement in rhombohedral $Li_7(NH_2)_6Cl$. Nitrogen is indicated by blue spheres and chloride by green spheres. The unit cell is shown by red dotted lines.

3.5.4 Raman spectroscopy

The reaction temperature for the synthesis of the amide chlorides (400°C) is above that at which $LiNH_2$ begins to decompose, slowly releasing ammonia (reaction 3.3).

$$2\,\mathrm{LiNH_2} \longrightarrow \mathrm{Li_2NH} + \mathrm{NH_3} \tag{3.3}$$

To confirm that the reaction products contained amide ions and not imide ions the Raman spectra of the amide chlorides were measured. The spectra of the new phase $Li_7(NH_2)_6Cl$ and $Li_4(NH_2)_3Cl$ and $Li_7(NH_2)_6Cl$ are shown in figure 3.17. The peaks that are present show that the new phases are amides and have not dehydrogenated to the imides during synthesis, as there are no peaks present in the spectra below 3200 cm^{-1}. The rhombohedral phases show two symmetric stretches alongside the two asymmetric stretches seen for $LiNH_2$. This splitting in the Raman spectra could be due to sample inhomogeneity, but the powder XRD patterns show only the amide chloride phases and lithium oxide. Therefore the splitting of the peaks must correspond to two different amide sites being present in the structure. Although there is only one nitrogen site in the structure, because the lithium sites are not fully occupied, rotational disorder of the hydrogen atoms on the amide ions could lead to different N-H bond environments, causing the splitting.

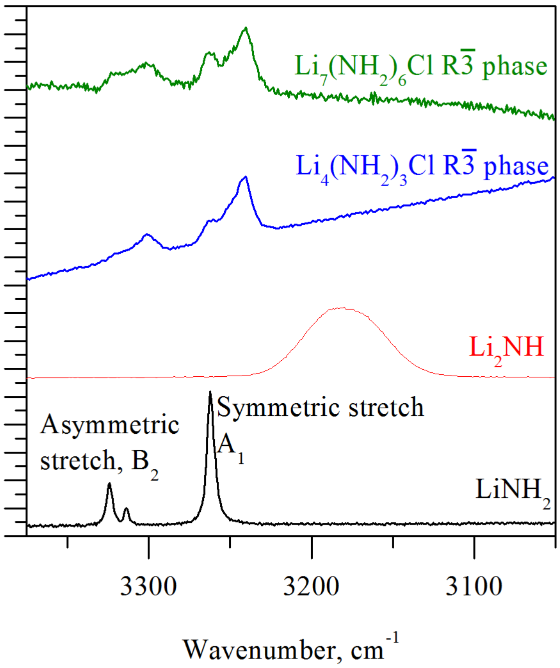

Figure 3.17: Raman spectra for the new amide chloride compared to the rhombohedral phase of $Li_4(NH_2)_3Cl$, alongside those for $LiNH_2$ and Li_2NH.

3.6 Time dependence of the formation of $Li_7(NH_2)_6Cl$

As for $Li_4(NH_2)_3Cl$, a study was undertaken to see the effect of reaction time on the phase of $Li_7(NH_2)_6Cl$ formed. As detailed above, a rhombohedral phase is observed on its own after a twelve hour reaction time of LiCl with 6 equivalents of $LiNH_2$ and after a one hour reaction time, a mixture is observed of two rhombohedral phases alongside $LiNH_2$ (figure 3.7). The same experiment was carried out by undergraduate project student Hilary Bartos for a four, six and eight hour reaction. It was found that increasing the reaction time decreases the quantity of $LiNH_2$ carried through to the product alongside the two rhombohedral phases, and for reaction times longer than ten hours, a single rhombohedral phase is observed.

3.7 Effect of magnesium on the structure

Magnesium chloride has been seen to lower the temperature of hydrogen desorption of $LiNH_2$, by forming a Li-Mg-N-H system when added at over 25%.[69,103] As for the lithium-only system, the level of added chloride needed to achieve this reduction was investigated, to reduce the gravimetric penalty due to the presence of a heavy halide ion.

The phase space of the system formed on replacement of LiCl by $MgCl_2$ in the reaction with $LiNH_2$ for twelve hours was investigated. As with the lithium only system, a cubic form of lithium magnesium amide chloride has previously been observed by carrying out reaction 3.4 and was assigned the formula $Li_3Mg_{1/2}(NH_2)_3Cl$.[139,114]

$$3\,\mathrm{LiNH_2} + \frac{1}{2}\,\mathrm{MgCl_2} \longrightarrow \mathrm{Li_3Mg_{1/2}(NH_2)_3Cl} \tag{3.4}$$

$Li_3Mg_{1/2}(NH_2)_3Cl$ showed a reduction in the temperature of the peak of hydrogen release on reaction with LiH by approximately 40°C when compared to $Li_4(NH_2)_3Cl$. The aim of this investigation was to reduce the chloride content to see if a new phase, with the same amide to chloride ratio as $Li_7(NH_2)_6Cl$, could be formed. The phases present as the chloride level was reduced are shown in figure 3.18.

As in the lithium-only system, a new rhombohedral phase was observed alone at the x value of 0.57. The formation of the new phase can be described by reaction 3.5 and has a unit cell volume of 737.4(5) Å^3, compared to 733.22(7) Å^3 for the lithium-only structure. As the Mg^{2+} ion is smaller than Li^+,[140] this unit cell expansion could be due to the introduction of defects into the structure. The powder XRD pattern and lattice parameters for the product are shown in figure 3.19 alongside those for the lithium-only phase.

$$6\,\mathrm{LiNH_2} + \frac{1}{2}\,\mathrm{MgCl_2} \longrightarrow \mathrm{Li_6Mg_{1/2}(NH_2)_6Cl} \tag{3.5}$$

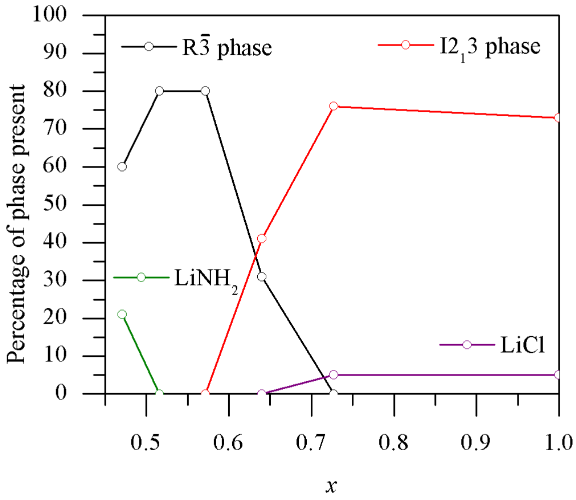

Figure 3.18: Phases present in the lithium magnesium amide chloride system for *x*, where the reaction taking place is (4-*x*) $LiNH_2$ + *x*/2 $MgCl_2$.

The presence of high levels of magnesium oxide, and the unexpected larger unit cell on addition of magnesium suggests that the magnesium ion may not have been incorporated into the amide chloride structure. It is therefore possible that the rhombohedral phase observed is that of a non-stoichiometric form of $Li_7(NH_2)_6Cl$. However, it was not possible to confirm this, and so for the remainder of this work the phase will be described as $Li_6Mg_{1/2}(NH_2)_6Cl$.

3.7.1 The effect of reaction time

An investigation was carried out by masters student Joseph Sheldrake into the effect of reaction time on the phase of the mixed lithium magnesium product formed at the two ratios at which a pure phase is observed: $Li_3Mg_{1/2}(NH_2)_3Cl$ and $Li_6Mg_{1/2}(NH_2)_6Cl$. Both reaction ratios were investigated for one, three, five, seven and nine hour reaction times. For $Li_3Mg_{1/2}(NH_2)_3Cl$ at all reaction times, a cubic phase was observed, although in some samples, mixed lithium magnesium imides were also seen in the product diffraction pattern. This could be due to the doping causing a lowering of the dehydrogenation temperature to

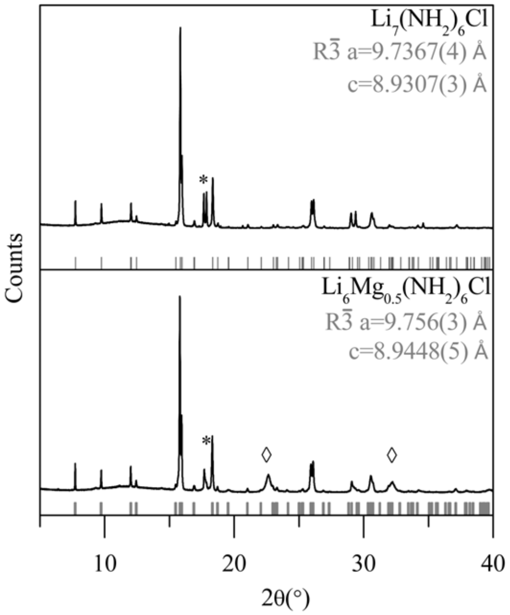

Figure 3.19: Powder X-ray diffraction patterns for $Li_7(NH_2)_6Cl$ and $Li_6Mg_{1/2}(NH_2)_6Cl$. Tick marks indicate peak positions for the observed phases. Stars mark peaks from Li_2O and diamonds those from MgO.

below that used for synthesis. For $Li_6Mg_{1/2}(NH_2)_6Cl$ a rhombohedral phase is observed for reaction times of less than nine hours. After longer reaction times, some cubic phase is observed in the product.

3.7.2 Raman spectroscopy

The spectra of the new phase $Li_6Mg_{1/2}(NH_2)_6Cl$ is shown in figure 3.20 alongside those for $Li_7(NH_2)_6Cl$, $LiNH_2$ and Li_2NH. The lack of peaks below 3200 cm^{-1} confirms the absence of an imide group, and therefore the new magnesium-containing phase has not decomposed to the imide on synthesis. The N-H stretches of the new phases occur at a slightly lower wavenumber than those for $LiNH_2$, suggesting the presence of a weaker N-H bonds in these phases than in $LiNH_2$.

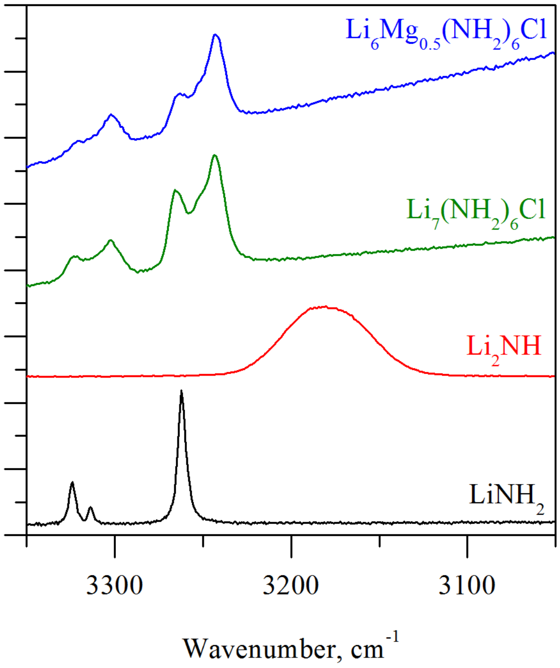

Figure 3.20: Raman spectra for the new amide chlorides alongside those for lithium amide and imide.

3.8 Conclusions and further work

The work discussed in this chapter was undertaken to investigate the effect of time and composition on the structure of the amide chlorides formed during the reaction between $LiNH_2$ and LiCl. Lowering the chloride content of the known phase $Li_4(NH_2)_3Cl$ saw a mixture of two phases form, except at the stoichiometry $Li_7(NH_2)_6Cl$ where a new phase is observed. This new phase shows a significant improvement in the theoretical gravimetric capacity of the system, as shown for the lithium-only system in figure 3.21. The investigation was extended into the mixed lithium magnesium system, but the magnesium content of the new phase formed in this system is unconfirmed.

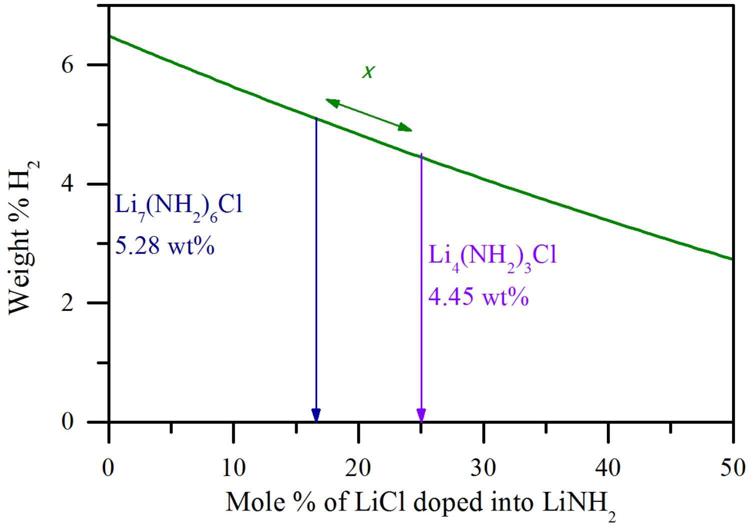

Figure 3.21: The effect on the weight percent of H_2 contained within the amide chloride, gained by reduction in the chloride content of the structure.

These improvements in gravimetric capacity will only be of interest if the new phases are able to undergo hydrogen cycling with the same properties as the starting phases. Structural properties such as a lower wavenumber for the N-H stretches, and lower than full occupancy of the Li^+ ion sites, will be favourable for more facile hydrogen desorption, and higher lithium ion mobility. These properties will be investigated experimentally in the next chapter.

Chapter 4

Hydrogen storage properties of $Li_7(NH_2)_6Cl$ and $Li_6Mg_{1/2}(NH_2)_6Cl$

4.1 Introduction

The addition of halides to lithium amide has been seen to decrease the temperature of decomposition in the presence of LiH,[69,106] and without.[108] The halides were also seen to inhibit the release of ammonia. This improvement in properties is thought to be due to the weakening of the N-H bonds,[69,106,108] although the exact mechanism is not fully understood.[110]

Recent structural investigations have shown that the dehydrogenation of $LiNH_2$ in the presence of LiH goes via a solid solution of $Li_{(1+x)}NH_{(2-x)}$.[66] It is thought that these intermediate phases have a higher ionic mobility than either $LiNH_2$ or Li_2NH, enabling Li^+ and H^+ ions to diffuse through the lattice.

After the synthesis of two new amide chloride phases in chapter 3, the dehydrogenation, rehydrogenation and ionic conductivity were investigated, to see whether the reduction in halide content had an effect on these properties.

4.2 Experimental

Sample preparation was carried out following the methods discussed in chapter 2. Desorption measurements were carried out using TPD-MS, as described in section 2.5, for ground mixtures of the prepared samples with LiH or MgH_2 (Sigma–Aldrich, $> 95\%$). These samples were prepared at the desired stoichiometry in an argon-filled glove box and heated in quartz tubes within the TPD apparatus at 2°C min^{-1} to 400°C.

Rehydrogenation was performed on the imide halide samples prepared as discussed in section 2.6. The samples were loaded into quartz tubes and sealed into the reactor vessel within an argon-filled glove box, before being pressurised to the specified pressure of H_2 under a specified heating regime. Volumetric cycling measurements were carried out using a Hiden Analytical HTP with inert loading as described in section 2.9.

Ionic conductivities were evaluated by the AC complex impedance method, as described in section 2.8, using a Solartron 1260 impedance analyser. Measurements were performed on pressed pellets (7 mm diameter, between 0.4 and 1.5 mm thickness) within a sealed glass rig designed for these measurements in-house. The surfaces of the pellets were coated with silver and attached to the electrodes also using silver, to ensure good electrical contact.

Cycling measurements were carried out using the flowing gas cell, and the IGA^n sample environment on the POLARIS beamline at ISIS neutron source, as described in sections 2.11 and 2.12, and on beamline I11 at the Diamond Light Source, as described in section 2.10.

4.3 Dehydrogenation of $Li_7(NH_2)_6Cl$ and $Li_7Mg_{1/2}(NH_2)_6Cl$ on reaction with LiH

Reactions of both $Li_7(NH_2)_6Cl$ and $Li_6Mg_{1/2}(NH_2)_6Cl$ with LiH were carried out by heating at 2° min^{-1} to 400°C and holding for an hour. The protic to hydridic ratio was maintained at 1 : 1 and the hydrogen desorption profiles are shown in figure 4.1, alongside the profiles for the same reaction for $LiNH_2$ and $Li_4(NH_2)_3Cl$.

For the reaction of $LiNH_2$ and LiH, hydrogen release at a low level was observed between 100 and 200°C before a steady increase in hydrogen desorption from around 210°C to over 300°C. This was followed by a second, faster, hydrogen release at 350°C, ultimately peaking at around 370°C. This second release occurred simultaneously with release of approximately 1.7 mol% of ammonia. For all of the amide chlorides studied, no ammonia was detected above the detection limit of the mass spectrometer, confirming that the presence of chloride within the amide structure suppresses ammonia release.

On addition of chloride, the onset of hydrogen release occurred at a similar temperature to that observed for $LiNH_2$, but the rate of release at lower temperatures was increased. The desorption profile for $Li_4(NH_2)_3Cl$ shows one broad hydrogen desorption, peaking at 320°C. The profile of the hydrogen desorption for $Li_7(NH_2)_6Cl$ is almost identical to that for $Li_4(NH_2)_3Cl$ despite the halving of the chloride content. Previous investigations indicated that the inclusion of magnesium reduces the temperature of hydrogen release.[80,77] It was seen here that the onset of release is slightly lower, but with not as dramatic an effect as seen in the literature. The effect of doping with magnesium is to create additional lithium ion vacancies within the structure to maintain a balanced charge. As the lithium sites in the structure of $Li_7(NH_2)_6Cl$ are not fully occupied, the addition of magnesium may not have much effect on the lithium diffusion and therefore the hydrogen desorption properties.

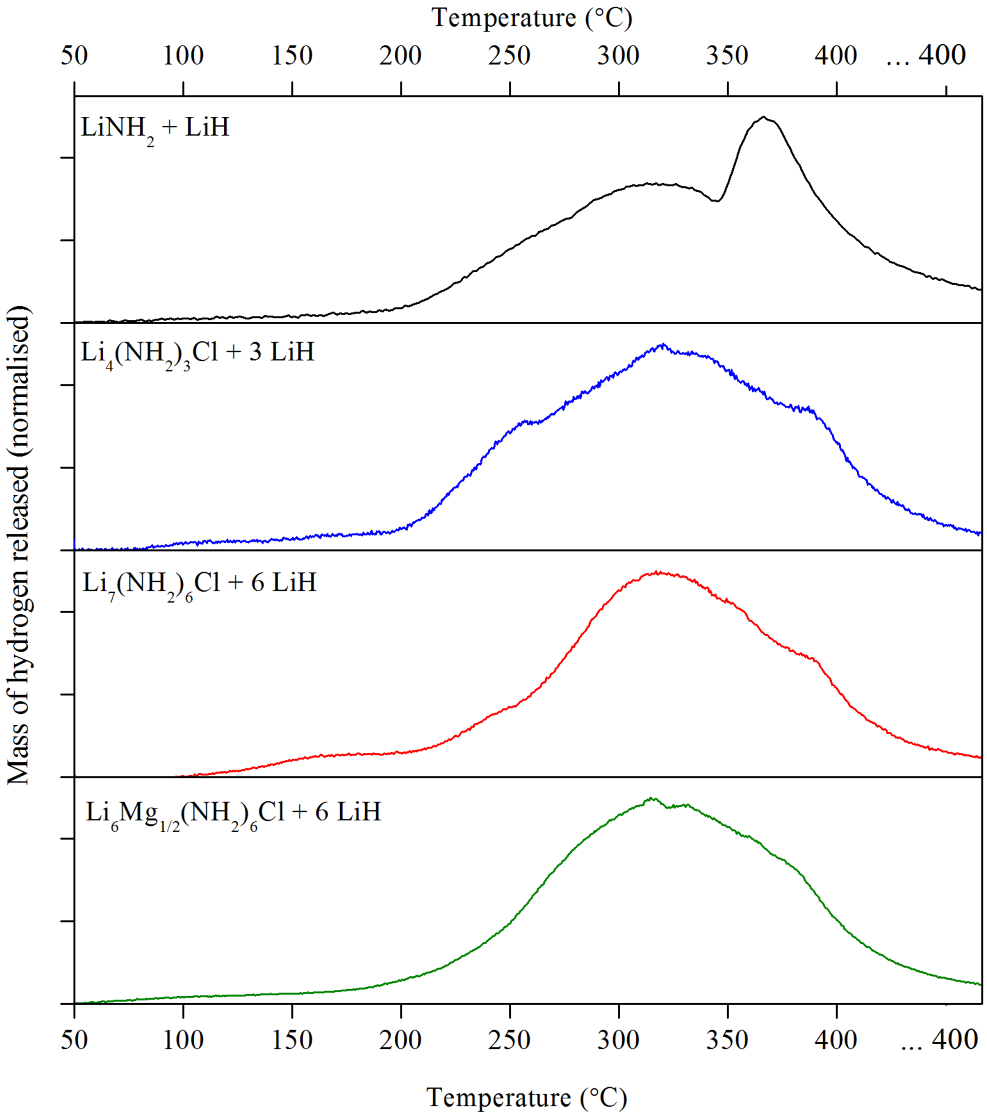

Figure 4.1: Hydrogen desorption profiles for the reactions of amide chlorides with LiH.

4.3.1 Characterisation of the dehydrogenated products

Raman spectra, shown in figure 4.2, confirm that the products are in the imide form, leading to a proposed decomposition reaction shown below in reaction 4.1. This reaction has a theoretical hydrogen weight loss of 5.28 wt%, compared to 4.45 wt% for the decomposition of $Li_4(NH_2)_3Cl$. During the TPD-MS experiments, the samples released approximately half of the theoretical weight percentage of hydrogen. Powder XRD patterns of the solid products of the reactions of $Li_7(NH_2)_6Cl$ and $Li_6Mg_{1/2}(NH_2)_6Cl$ with LiH are shown in figure 4.3. These patterns closely resemble those of the imide chlorides formed by reaction of Li_2NH with LiCl and $MgCl_2$.[69]

$$\mathrm{Li_7(NH_2)_6Cl + 6\,LiH \longrightarrow Li_{13}(NH)_6Cl + 6\,H_2} \tag{4.1}$$

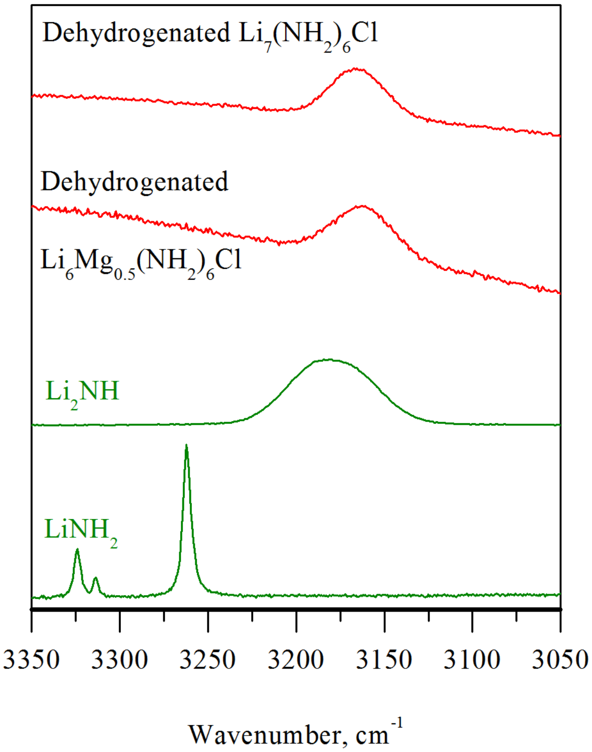

Figure 4.2: Raman spectra of the dehydrogenation product of the new amide chlorides alongside the spectra for lithium amide and lithium imide.

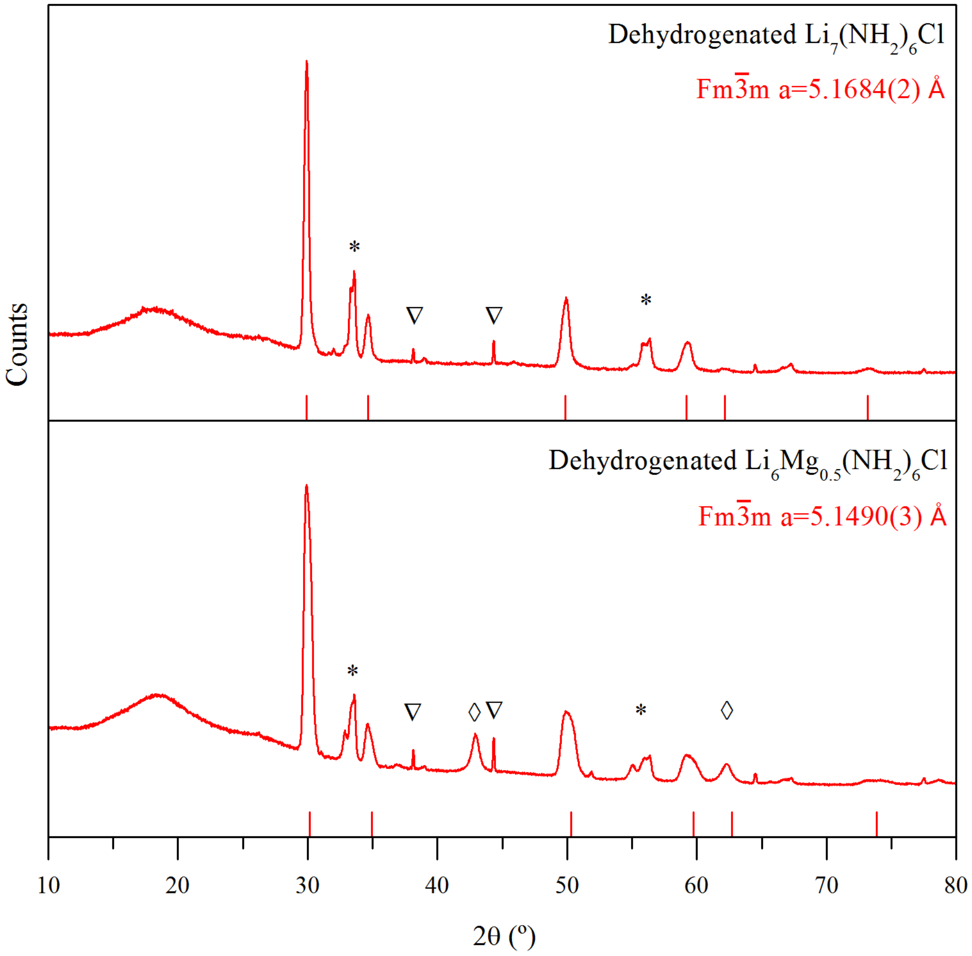

Figure 4.3: Powder XRD patterns for the dehydrogenation products of the new amide chlorides. Tick marks indicate peak positions for the observed phases. Stars mark peaks from Li_2O, triangles those for LiH and diamonds those from MgO.

4.4 TPD-MS of a lithium amide/ lithium hydride/ lithium chloride mixture

To determine whether the prior formation of the amide chloride is necessary for a reduction in hydrogen desorption temperature, an investigation was carried out using TPD-MS (section 2.5). Lithium amide and lithium hydride were hand ground with lithium chloride, heated at 2°C min^{-1} to 400°C and held for one hour. The gases given off were measured, and the hydrogen traces are shown alongside the halide-free system and the amide chloride in figure 4.4. No other gases were seen to be given off during the experiment. Therefore, even without initial formation of the amide chloride, the halide present prevents the release of ammonia. However, the hydrogen release profile is almost unchanged compared to $LiNH_2$-LiH when LiCl is present in the mixture. The formation of the amide chloride must therefore be necessary for the reduction in hydrogen release temperature to be observed.

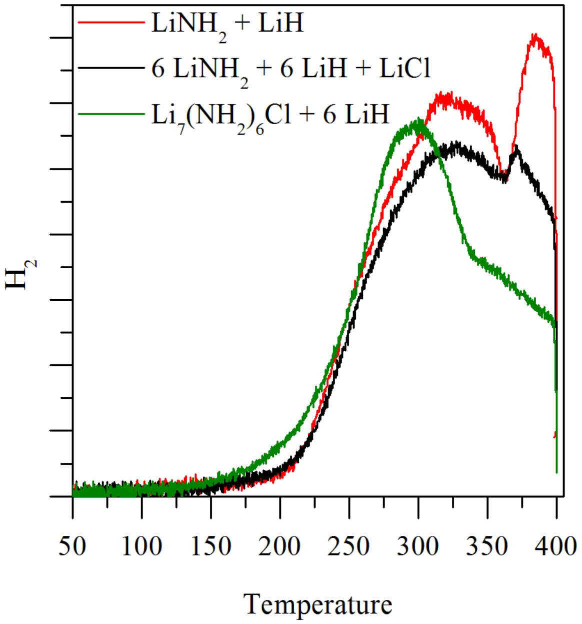

Figure 4.4: Hydrogen desorption profiles for the reaction with LiH for the chloride system with and without prior formation of an amide chloride.

4.5 Rehydrogenation of the imide chlorides

Once dehydrogenated, the rehydrogenation properties of these new phases were tested using a high pressure hydrogenator under 90 bar H_2 for 24 hours at 300°C. Powder XRD was used to the study the products of rehydrogenation for the two new compounds, along with the dehydrogenation products of $Li_4(NH_2)_3Cl$. For $Li_4(NH_2)_3Cl$, it had been previously reported that rehydrogenation resulted in a hexagonal phase with rhombohedral symmetry.[69] However, in this investigation, a cubic phase was formed. The same was true for the mixed lithium magnesium imide chloride, which rehydrogenated to form a cubic structure. In contrast, dehydrogenated $Li_7(NH_2)_6Cl$ hydrogenated to form a 4 : 1 mixture of cubic and rhombohedral phases (figure 4.5). The cubic phase formed on rehydrogenation of $Li_7(NH_2)_6Cl$ has a smaller unit cell size than that formed on rehydrogenation of $Li_4(NH_2)_3Cl$, most likely to be due to the substitution of large Cl^- ions by smaller $NH_2{}^-$ ions. The presence of the imide phase in the powder XRD rehydrogenation product of $Li_4(NH_2)_3Cl$, and not that of $Li_7(NH_2)_6Cl$, indicates that the lower chloride containing phase is easier to hydrogenate.

The products of rehydrogenation were characterised using Raman spectroscopy (figure 4.6) showing the presence of an amide phase and no imide, confirming that rehydrogenation had taken place. When comparing these Raman spectra to those of the as-synthesized rhombohedral phases, as shown in the previous chapter, the presence of the cubic phase after rehydrogenation becomes apparent. The Raman spectrum for the lithium-only phase after rehydrogenation was similar to that observed previously for the cubic $Li_4(NH_2)_3Cl$,[69] but with peaks at 3260 cm^{-1} and 3320 cm^{-1} present due to the small amount of the rhombohedral amide chloride present.

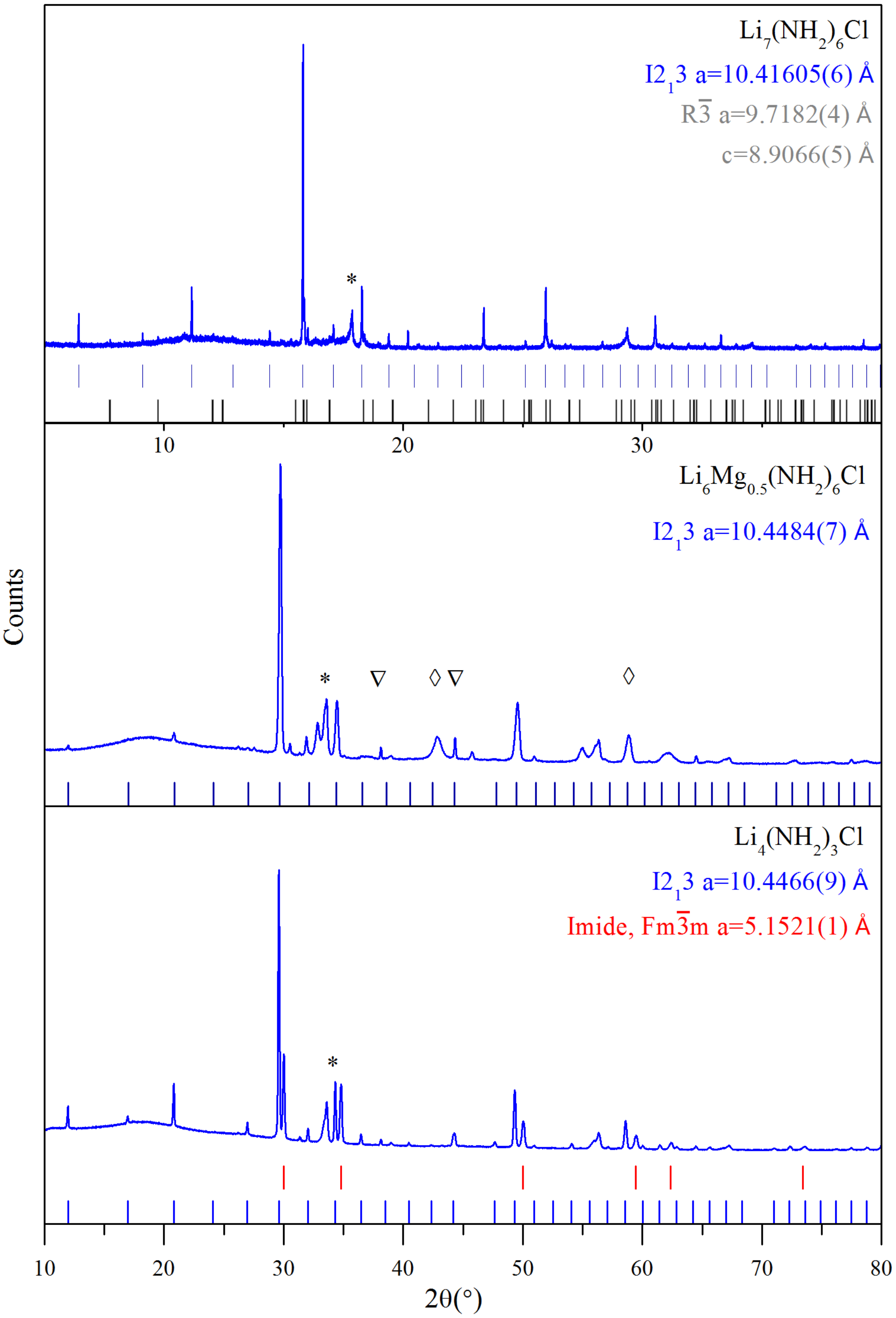

Figure 4.5: Powder X-ray diffraction patterns for the rehydrogenation products of the amide chlorides. Tick marks indicate peak positions for the observed phases: blue for the cubic amide chloride, black for the rhombohedral amide chloride and red for the imide chloride. Stars mark peaks from Li_2O, triangles those from LiH and diamonds those from MgO.

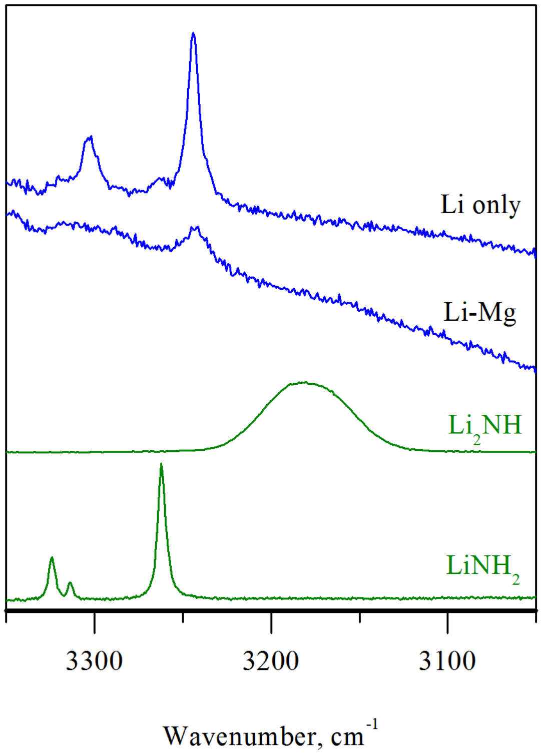

Figure 4.6: Raman spectra of the rehydrogenation products of $Li_{13}(NH)_6Cl$ and $Li_{12}Mg_{1/2}(NH)_6Cl$ alongside the spectra for $LiNH_2$ and Li_2NH.

4.5.1 Rehydrogenation under different pressures

As described in section 4.5, rehydrogenation of $Li_{13}(NH)_6Cl$ at 90 bar formed a mixture of the rhombohedral and cubic phases at a 1 : 4 ratio, as shown in figure 4.5. To investigate whether a pure phase could be formed by rehydrogenation at a different H_2 pressure, samples of $Li_{13}(NH)_6Cl$, formed by dehydrogenation of $Li_7(NH_2)_6Cl$ and LiH, were hydrogenated at pressures between 5 and 80 bar H_2. All samples were hydrogenated in the high pressure hydrogen rig described in section 2.6 at 300°C for 24 hours. Powder XRD was used to study the products and quantitative phase analysis, as described in section 2.3.1, to determine the relative percentages of each of the phases present. Lithium oxide was present in all samples, and so the values shown are the amount of each phase as a percentage of the total amide chloride formed.

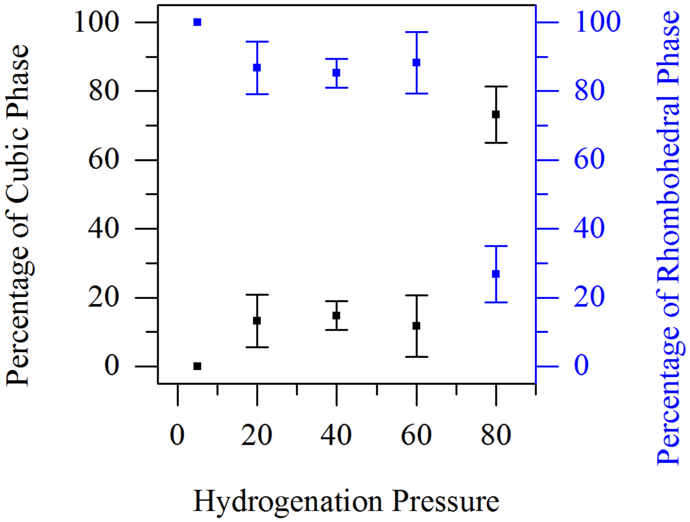

Figure 4.7: Plot of product phase vs hydrogenation pressure for a sample of $Li_{13}(NH)_6Cl$.

It was found that, as shown in figure 4.7, at lower pressures up to 60 bar H_2 the rhombohedral phase (blue points) was the dominant phase in the product. This is confirmed by the Raman spectra of the sample before and after rehydrogenation, as shown in figure 4.8. At

80 bar and above, the cubic phase was formed as a higher percentage of the product. By comparing the unit cell volumes and the atomic masses within them, it can be calculated that the rhombohedral phase is less dense than the cubic phase. This correlates with its preferential formation at lower pressures, and reduced prevalence at higher pressures.

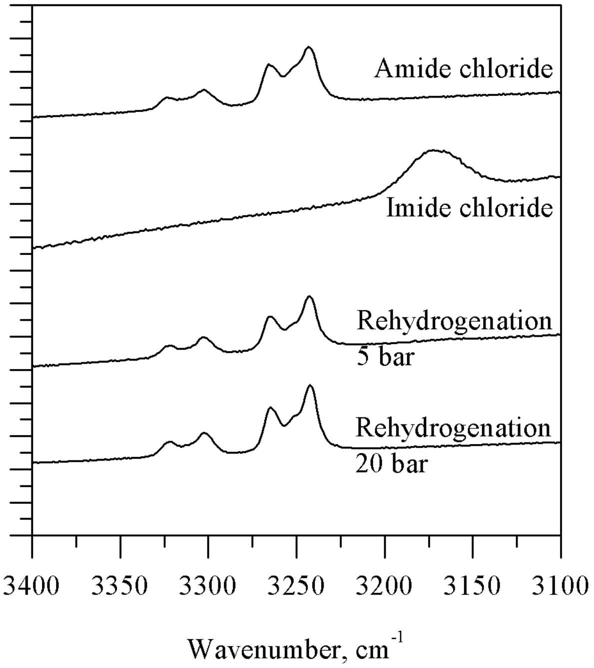

Figure 4.8: Raman spectra for samples of $Li_{13}(NH)_6Cl$ hydrogenated under different pressures.

The cubic and rhombohedral phases have different amide to chloride ratios, but both were shown in chapter 3 to accommodate different stoichiometries. To accommodate a specific chloride content within a mixture of phases, the relative ratios of the phases present may change, or the composition of those phases present. With both phases present in the rehydrogenation products of the 6 : 1 imide chloride it is likely that either, or both, phases are present with some variation in stoichiometry. As discussed in chapter 3, the relationship between lattice parameter and chloride content is not simple enough for the unit cell parameters of the products of rehydrogenation to be used to determine the chloride content of the phases present. As no LiCl or $LiNH_2$ is observed in the powder diffraction patterns of the products, it can be assumed that the stoichiometry of the starting imide is accommodated within the mixture of amide chloride phases present after rehydrogenation.

The effect of dehydrogenation and rehydrogenation at 10 bar H_2 on the structure is shown in figure 4.9. It can be seen that the structure is maintained on cycling. There is some LiH present in the powder XRD of the dehydrogenated product, suggesting that the dehydrogenation has not gone to completion.

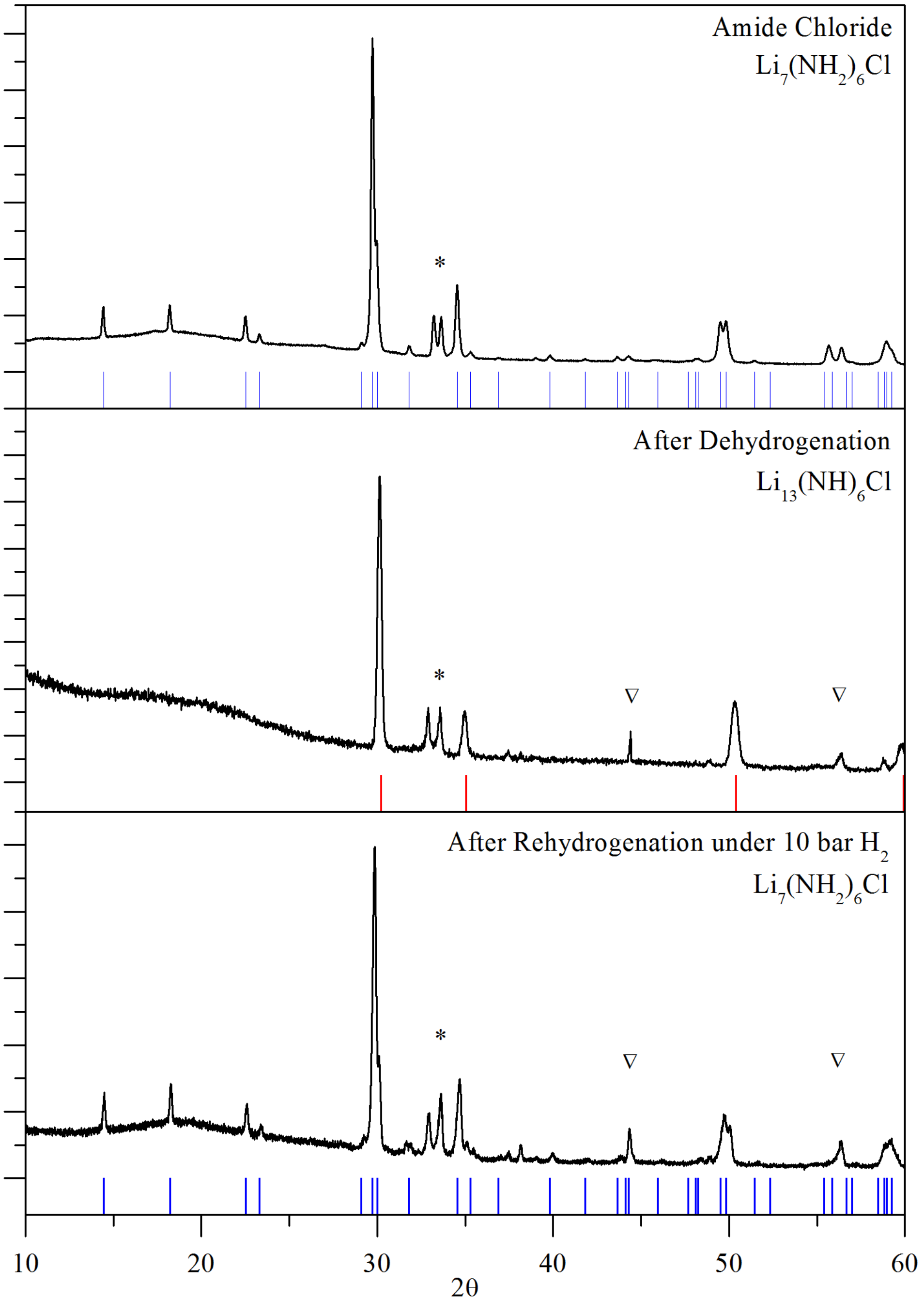

Figure 4.9: Powder XRD patterns for $Li_7(NH_2)_6Cl$, the product of dehydrogenation $Li_{13}(NH)_6Cl$, and the product of rehydrogenation at low pressure, where only the rhombohedral phase is observed. Blue tick marks show peak positions for rhombohedral $Li_7(NH_2)_6Cl$, and red tick marks show peak positions for $Li_{13}(NH)_6Cl$. Stars show the positions of Li_2O and triangles LiH.

4.6 Dehydrogenation of $Li_7(NH_2)_6Cl$ with a mixture of LiH and MgH_2.

Reaction 4.2 was examined for *y* = 0 to 6 using TPD-MS, according to the method described in section 2.5.

$$\mathrm{Li_7(NH_2)_6Cl + (6{-}y)\,LiH + \frac{1}{2}\,y\,MgH_2 \longrightarrow} \tag{4.2}$$

The hydrogen traces for the TPD-MS experiments are shown in figure 4.10; ammonia was not observed above the detection limit of the experiment. As the magnesium content (*y*) is increased, the hydrogen release trace changes from one broad peak into multiple desorption peaks. On moving from *y* = 4 to 6, the onset of hydrogen desorption occurs at a higher temperature, with the MgH_2 system exhibiting the highest onset temperature.

For the lithium-only system, as described above, an imide chloride is formed, as shown in reaction 4.3:

$$\mathrm{Li_7(NH_2)_6Cl + 6\,LiH \longrightarrow Li_{13}(NH)_6Cl + 3\,H_2} \tag{4.3}$$

The powder XRD patterns of the products were analysed using QPA, and the weight percentages of the non-oxide phases are shown in table 4.1. At low magnesium content when $y < 3$, the imide chloride was the main product but, as the magnesium content is increased (increasing *y*) the products were LiCl, Li_2NH and the nitride Mg_3N_2. The presence of the nitride suggests that the magnesium facilitates dehydrogenation beyond the imide.

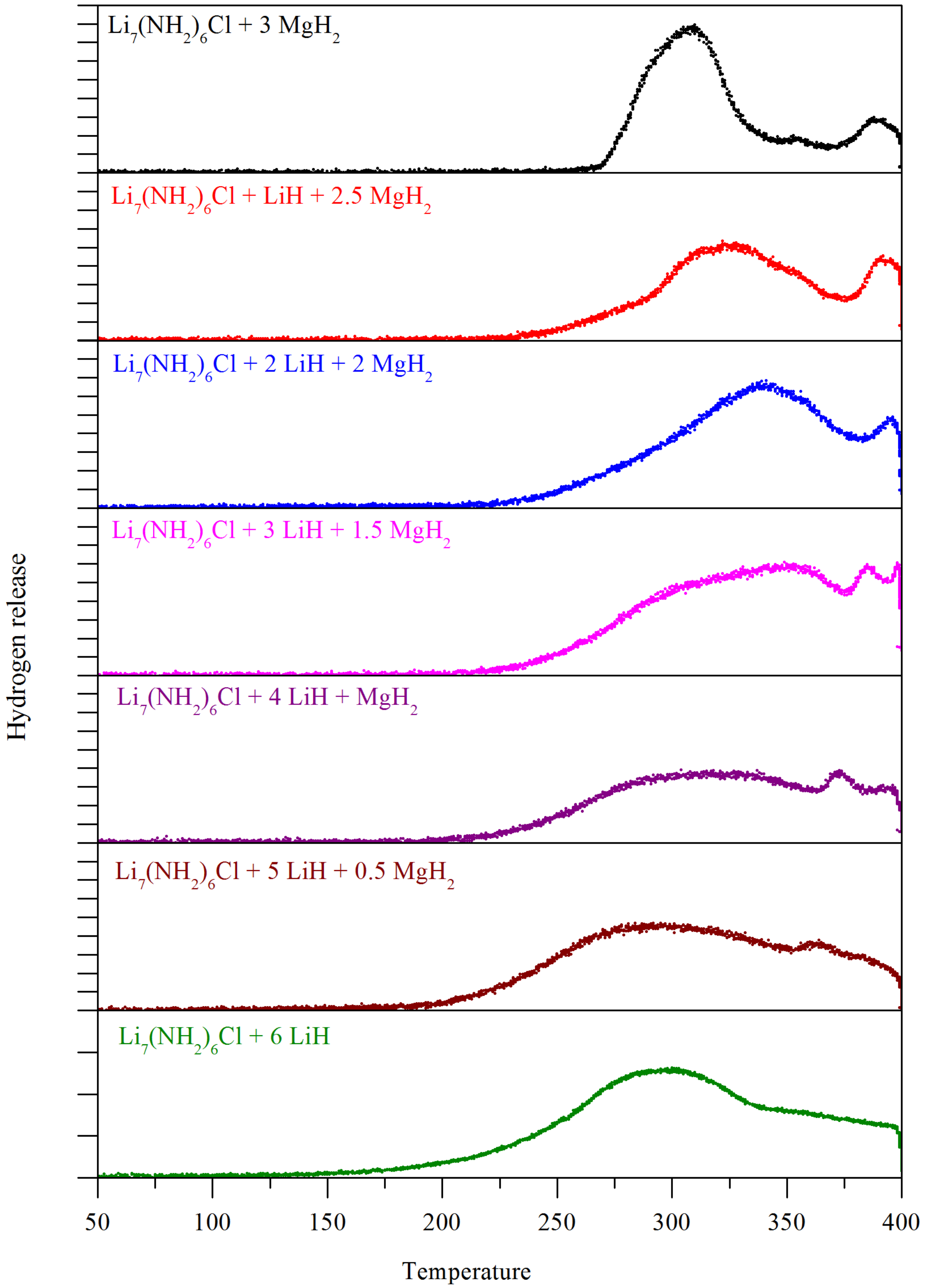

Figure 4.10: Hydrogen release traces from the TPD-MS experiments of $Li_7(NH_2)_6Cl$ with mixed LiH and MgH_2.

y	LiCl	Mg_3N_2	Li_2NH	Imide Chloride	LiH
6	24.4	32.4	43.2	-	-
5	26.0	28.5	45.5	-	-
4	24.8	28.4	46.8	-	-
3	-	32.3	-	60.8	6.9
2	-	-	-	96.1	3.9
1	-	-	-	91.0	9.0
0	-	-	-	91.7	8.3

Table 4.1: Phases present after dehydrogenation of $Li_7(NH_2)_6Cl$ with (6 - y) LiH + $\frac{1}{2}$ y MgH_2 as a weight percentage of the non-oxide content.

4.6.1 Hydrogenation after reaction with a LiH/MgH_2 mixture

After dehydrogenation on the TPD-MS, all six samples were hydrogenated together at 300°C for 24 hours, under 90 bar of H_2. Oxidation occurred to a small extent during the hydrogenation process, with both Li_2O and MgO observed in the powder XRD patterns of all of the hydrogenation products. Again, QPA was used to analyse the powder XRD patterns of the products, and the weight percentages of the non-oxide phases present are shown in table 4.2.

Even though LiCl was observed in the products of the TPD-MS experiments, amide chlorides were observed in the XRD patterns after hydrogenation. Some LiCl is observed in the products of hydrogenation, although this is less than that observed in the dehydrogenation products. The cubic amide chloride phase is observed in the patterns for all the samples, with the rhombohedral phase only observed in four of the samples. However, mixed imide phases are also present in the samples containing magnesium, and so the lithium-only sample is the only to be reversible under these conditions. The addition of both magnesium and chloride to the Li-N-H system makes it very complex, as many different decomposition and rehydrogenation pathways are now possible. It appears that different Li : Mg ratios cause different pathways to be favoured, as there is no clear trend in the phases formed during cycling.

y	MgH_2	$I2_13$ amide	$R\bar{3}$ amide	LiCl	LiH	$Li_2Mg_2(NH)_3$	$Li_2Mg(NH)_2$
6	1.32	32.1	-	4.7	2.7	32.9	26.2
5	-	43.2	25.1	5.7	-	13.1	13.0
4	-	64.0	-	-	4.6	27.8	10.1
3	-	62.3	-	-	9.7	25.3	6.1
2	-	29.6	57.0	-	11.7	4.0	9.6
1	-	40.9	54.1	-	4.4	2.4	9.9
0	-	62.5	17.0	-	20.5	-	-

Table 4.2: Phases present after rehydrogenation of the dehydrogenation products of $Li_7(NH_2)_6Cl$ with (6 - y) LiH + $\frac{1}{2}$ y MgH_2 as a weight percentage of the non-oxide content.

4.7 Cycling properties

4.7.1 TPD of rehydrogenated products

TPD-MS was carried out on some samples that had been rehydrogenated in the laboratory. All samples showed a reduced temperature of hydrogen release, as shown in figure 4.11. This is likely to be due to the LiH being more intimately mixed with the amide chloride within the samples, in agreement with research showing that ball milling of the amide halide with LiH before dehydrogenation causes hydrogen release to occur at a lower temperature.[114] The favourable micro structure produced when the LiH is formed on rehydrogenation is likely to reduce the diffusion lengths and improve the kinetics of the second desorption.

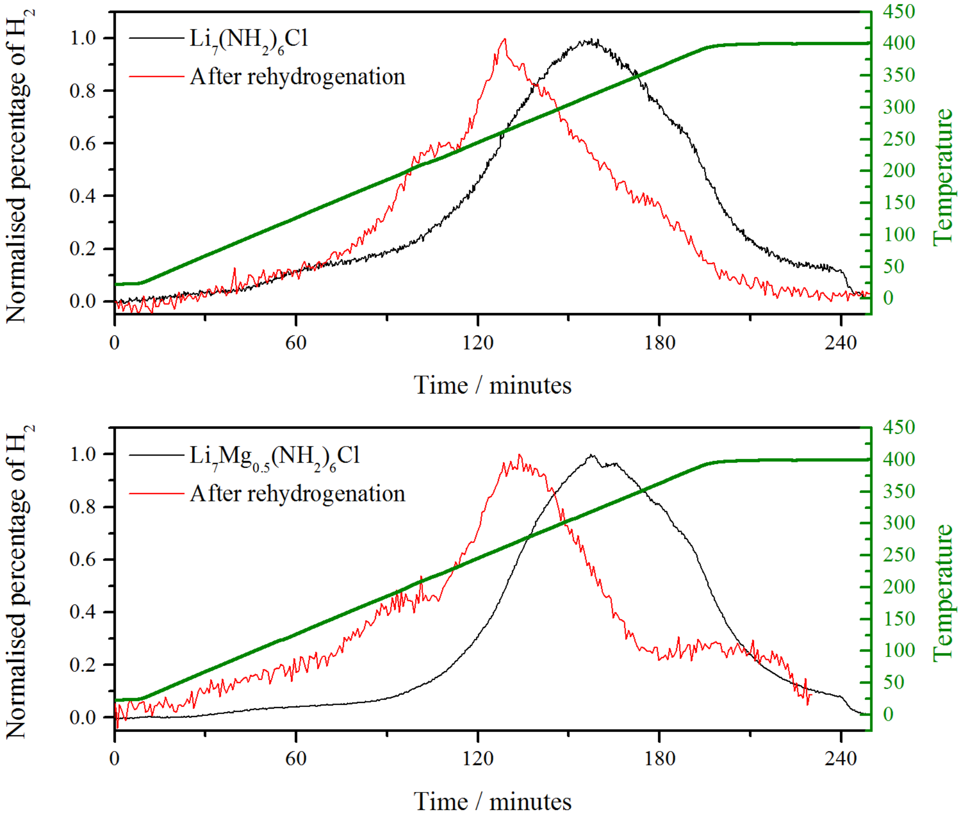

Figure 4.11: Hydrogen release traces from samples comparing initial and second dehydrogenations, normalised so that maxima are all equal to one.

4.7.2 HTP of $Li_7(NH_2)_6Cl$

When the temperature was fixed at 400°C and the pressure cycled between 1 and 50 bar, $Li_7(NH_2)_6Cl$ released and re-adsorbed 2.5 wt% of hydrogen, approximately half of the theoretical capacity. Reduction of the temperature caused the capacity of the material to decrease, with the compound reversibly storing 1.5 wt% at 300°C. When the temperature was increased back to 400°C, the imide chloride was able to take up 2.5 wt% of hydrogen, showing that the capacity is maintained during the experiment. Using the desorption isotherms shown in figure 4.12, equilibrium hydrogen pressures were determined from the plateaus. Producing a van't Hoff plot using these pressures gives values of $\Delta H = 47 \pm 3$ kJ mol^{-1} and $\Delta S = 87 \pm 4$ J K^{-1} mol^{-1}. This value of reaction enthalpy is slightly lower than that quoted for the reaction of lithium amide and lithium hydride of 51 kJ mol^{-1}.[77] It is also lower than that of $\Delta H = 65 \pm 5$ kJ mol^{-1} reported for the $Li_4(NH_2)_3Cl$ system.[114] This lower desorption enthalpy is consistent with the lower onset temperature for desorption observed by the temperature-programmed desorption experiments. The sloped isotherms have been observed for the $LiNH_2$-LiH system, and the $Li_4(NH_2)_3Cl$-LiH system, and could be due to the existence of phases with stoichiometries between that of the amide and the imide.[66,68,114]

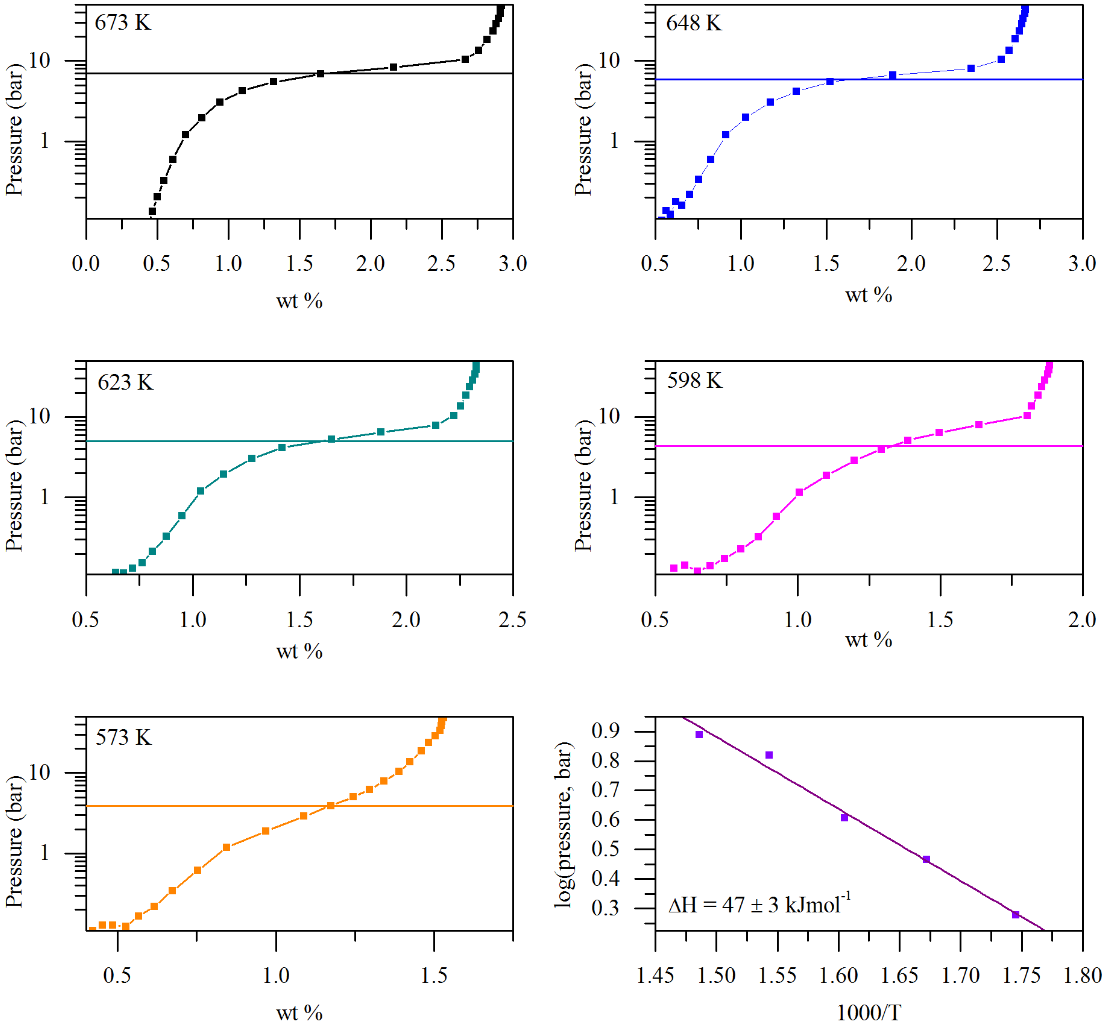

Figure 4.12: Desorption isotherms, with plateau pressures indicated, at a range of temperatures for $Li_7(NH_2)_6Cl$, alongside the van't Hoff plot used to calculate the thermodynamic properties.

4.7.3 Hydrogen cycling of $Li_7(NH_2)_6Cl$ studied using synchrotron powder X-ray diffraction on the I11 beamline

A sample of the lithium imide chloride, $Li_{13}(NH)_6Cl$ was studied under cycling with hydrogen using powder synchrotron X-ray diffraction. $LiNH_2$ was ground with LiCl to form the amide chloride by heating at 400°C for 18 hours, and then the sample was dehydrogenated by heating to 400°C for 18 hours with LiH. The sample was loaded into a borosilicate capillary and then onto the low pressure gas cell at beamline I11 at Diamond Light Source, as described in section 2.10. Scans were taken continuously, with a new scan taken every minute.

The sample was heated under vacuum and, once at 250°C, 20 bar H_2 was applied. Very little change was observed in the XRD pattern of the sample, and so the temperature was increased to 300°C and left for two hours. The gas was removed approximately 2.5 hours into the experiment and the sample held under vacuum at 350°C. Five hours into the experiment 20 bar H_2 was again applied to the sample. After ninety minutes, the gas was removed, and the sample held under vacuum for two hours. For the final hydrogenation, nine hours into the experiment, the temperature was decreased to 300°C and the sample left under 20 bar H_2 for eight hours to observe the structural change during hydrogenation more slowly. After this time, approximately 16 hours into the experiment, data was collected under vacuum for two hours, and then the temperature increased to 350°C. After another two hours, the sample was cooled under 1 bar of helium gas and removed.

A contour plot showing the diffraction patterns between 2θ = 5° and 17° of the sample collected during this experiment is shown in figure 4.13. It shows that, during the first hydrogenation, peaks corresponding to both the rhombohedral (labelled R) and cubic (labelled C) amide chlorides were seen to appear, grow in intensity, and then level off. When data were collected under vacuum at 350°C these peaks are no longer observed. On the second and

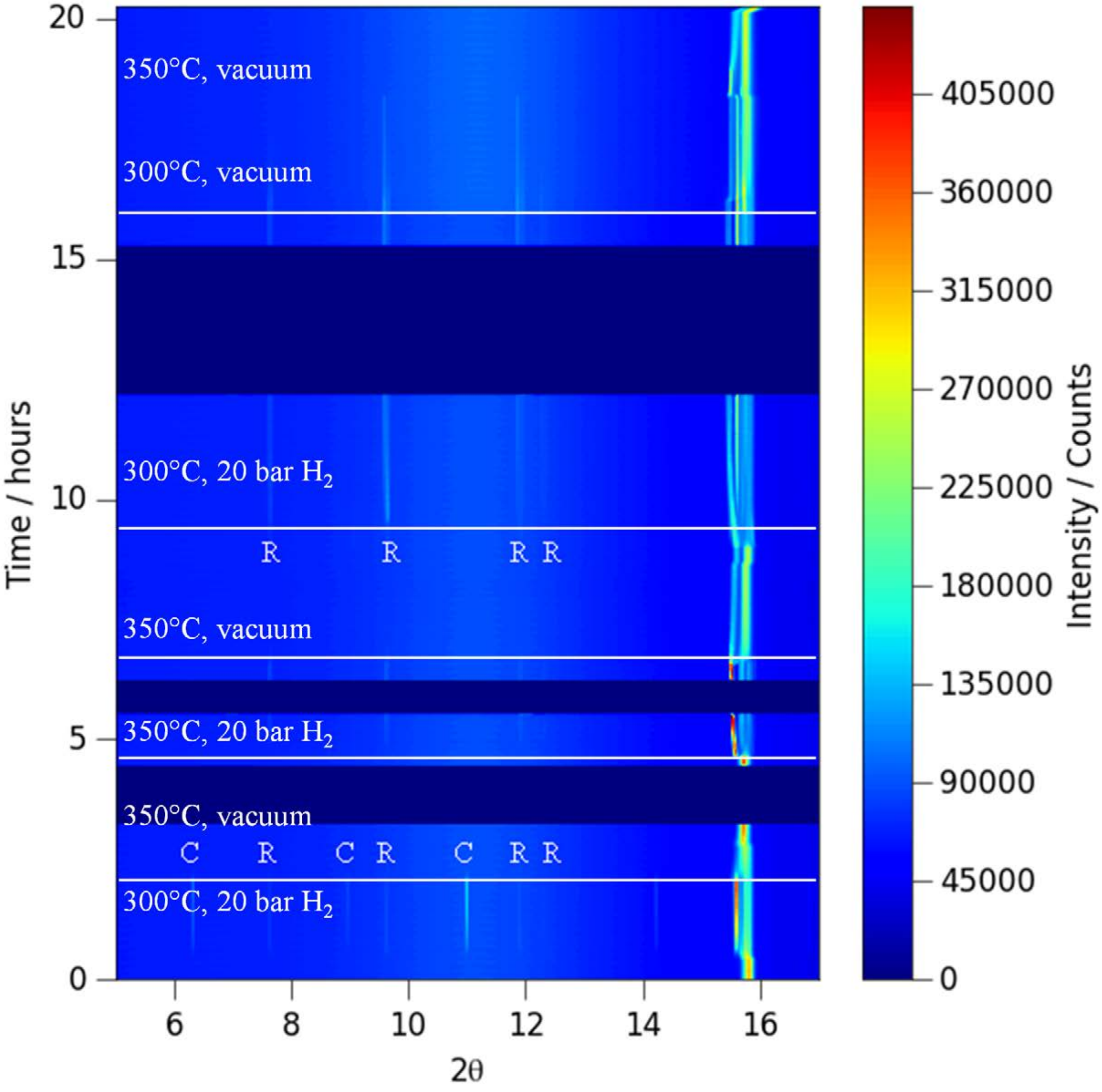

Figure 4.13: Contour plot of powder synchrotron XRD patterns for 2θ between 5° and 17° during the hydrogen cycling of $Li_{13}(NH)_6Cl$ at beamline I11. Dark blue strips represent periods of no synchrotron radiation.

third hydrogenations, only the peaks for the rhombohedral phase were seen in the diffraction pattern. It was seen on the final dehydrogenation that the peaks corresponding to the amide chloride were only removed from the diffraction pattern when the temperature was increased to 350°C, suggesting that 300°C is too low for dehydrogenation to occur on the timescale of the experiment.

During the hydrogenations, the shape of the peaks corresponding to the amide chloride was seen to change over time: in general they were complex, as illustrated by an example in figure 4.14. The large range of d-spacings observed for these peaks probably indicates the presence of multiple amide chloride phases of varying hydrogen and chloride content. The discontinuous nature of the peak distribution could be interpreted as a number of different preferred compositions. However, a more likely explanation is the inability to rapidly rotate the sample. Typically, samples would be spun to improve powder averaging. The gas cell environment only allowed the sample to be rocked through the relatively small angle of ±5°. This could lead to the data appearing more as a collection of small single crystals, rather than a randomly oriented powder. A single crystal of well defined composition temporarily oriented in the beam could give a strong reflection which then decreases as the orientation changes. This is illustrated by the way the peak shape changes over time, as shown by the contour plot of the powder diffraction data shown in figure 4.15.

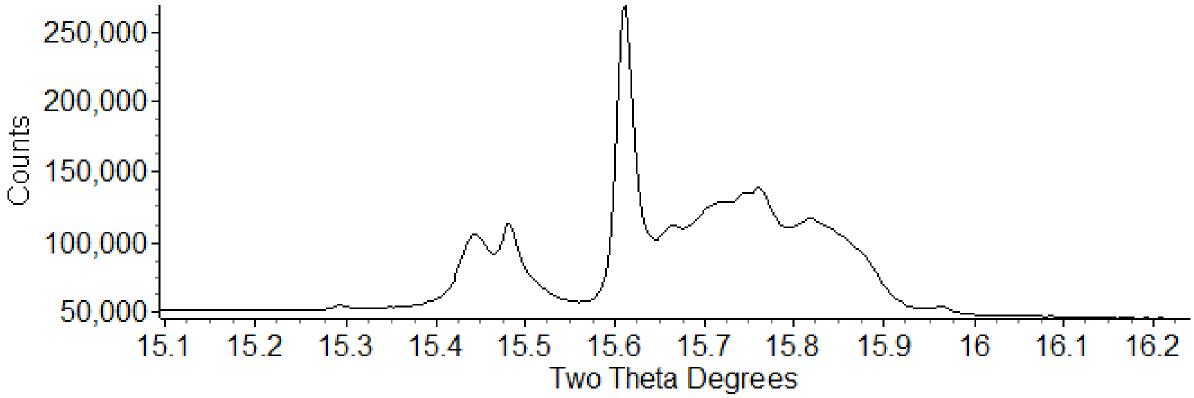

Figure 4.14: Example of the complex peak shape of a peak of the amide chloride phase.

A batch quantitative phase analysis (QPA) refinement was attempted using a template file containing the amide and imide chloride phases and LiH. Each raw file was fitted using

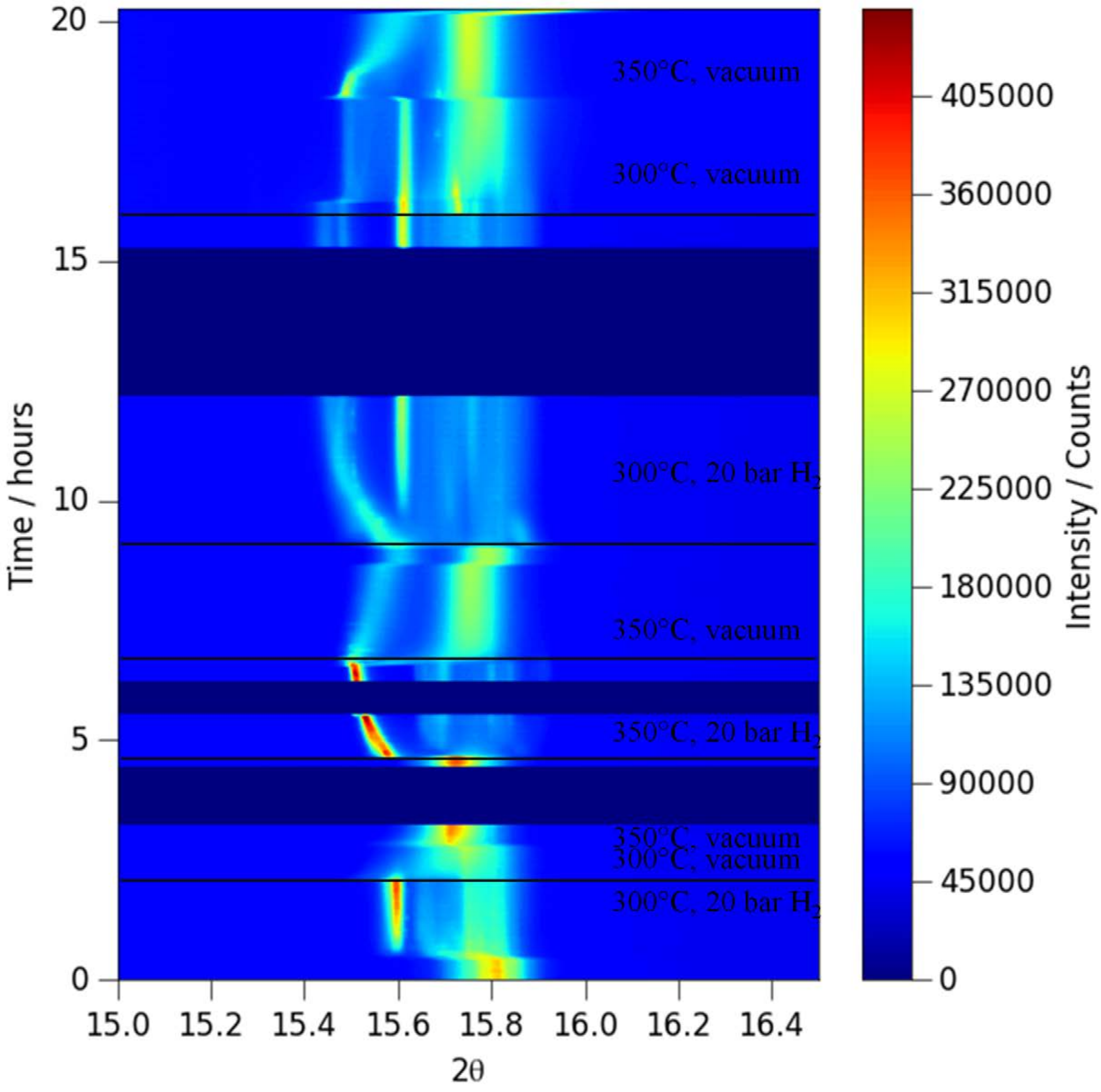

Figure 4.15: Contour plot of powder synchrotron XRD patterns for 2θ between 15° and 17° during the hydrogen cycling of $Li_{13}(NH)_6Cl$ at beamline I11 showing the complex peak shapes and how they change over time. Dark blue strips represent periods of no synchrotron radiation.

the technique described in section 2.3.1. However, because of the complex peak shapes, the QPA did not give an accurate representation of the relative weight percentages of the imide chloride and the amide chloride phases. The scale factor of the LiH phase, an output from the QPA, can be seen for the experiment in figure 4.16 and can be used as a guide to study amount of this phase present during cycling. The scale factor was seen to increase during the three hydrogenations, and decrease whilst the sample was under vacuum, as would be expected. A contour plot of the powder synchrotron XRD patterns in the region of the (002) peak of LiH is shown in figure 4.17.

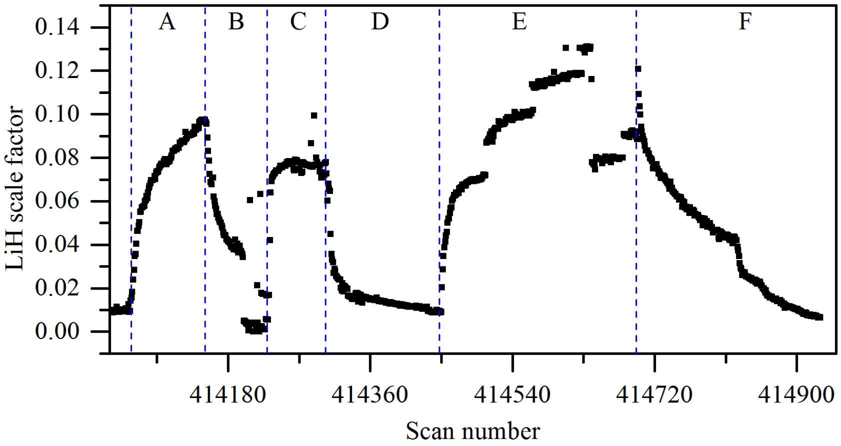

Figure 4.16: Scale factor of LiH formed during the cycling experiment on beamline I11. Blue dashed lines represent changes in hydrogen pressure, with regions A, C and E representing data collected under hydrogen, and regions B, D and F representing data collected under vacuum.

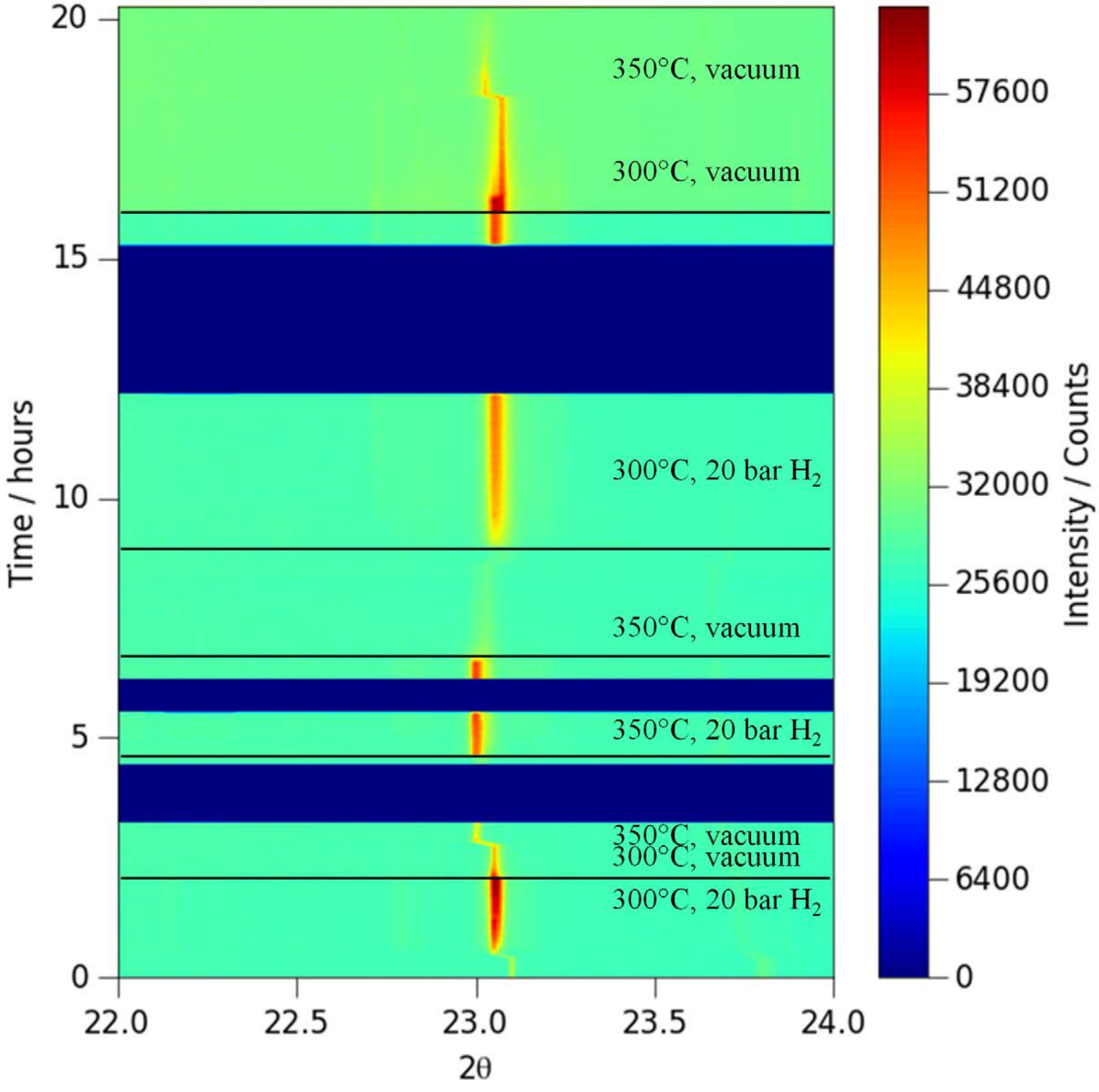

Figure 4.17: Contour plot of powder synchrotron XRD patterns for 2θ between 22° and 24° during the hydrogen cycling of $Li_{13}(NH)_6Cl$ at beamline I11, to focus on the (002) peak of LiH. Dark blue strips represent periods of no synchrotron radiation.

4.7.4 Deuterium cycling of $Li_{13}(ND)_6Cl$ measured by powder neutron diffraction

A sample of the deuterated lithium imide chloride $Li_{13}(ND)_6Cl$ was studied under cycling with deuterium using powder neutron diffraction. Studying the material in this way enabled the avoidance of the averaging problems leading to complex peak shapes in the synchrotron XRD experiment. To form the sample, $LiND_2$ was heated with LiCl at 400°C for 18 hours. The product of this reaction was confirmed using laboratory powder XRD to be the deutero-amide chloride, and it was then heated with LiD under flowing argon at 400°C for 18 hours to form the deutero-imide chloride. A number of samples made using the same procedure were combined to form a larger mass of sample to be measured on the POLARIS beamline, using the flowing gas cell described in section 2.11. Scans were taken continuously, with a new scan taken every two minutes.

The sample was heated to 100°C under 1 bar D_2 and, once the pressure had been increased to 3 bar D_2, the temperature was raised to 300°C. Once at 300°C, the temperature was kept constant and the sample left under these conditions for 6 hours. The scan time was increased from just under two minutes to five minutes, to improve the quality of the powder patterns collected. The temperature was reduced to 250°C and data collected under vacuum. After one hour the sample temperature was increased to 275°C and held for another hour. 3 bar of D_2 was introduced and the sample held under these conditions for six hours.

Little change was observed in the neutron powder diffraction patterns during cycling, as the high d-spacing (002) and (011) peaks of the amide chloride that are used in X-ray powder diffraction to distinguish between the amide and imide phases are not observed under these experimental conditions. The intensity of the peaks corresponding to the deutero-imide chloride, and the lattice parameter of this phase, were seen to change during the experiment, as shown in a contour plot of the neutron powder diffraction data in figure 4.18.

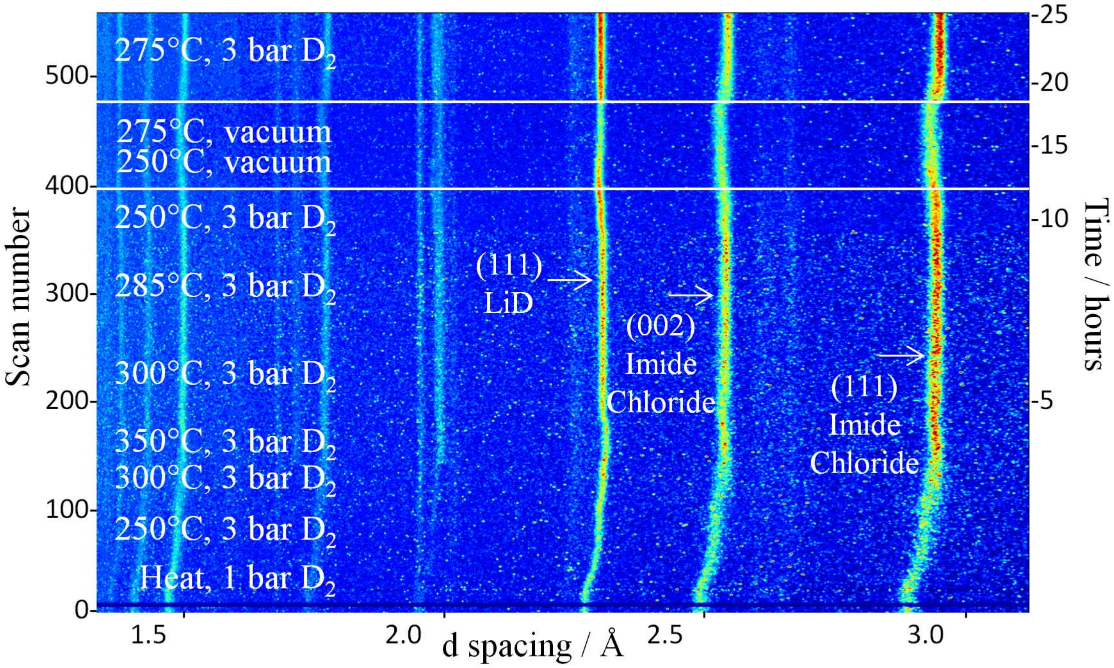

Figure 4.18: Contour plot of the powder neutron patterns for $Li_{13}(ND)_6Cl$ annotated with experimental conditions.

A batch QPA refinement was carried out using a template file containing a deutero-imide chloride phase and LiD. The weight percentages of the two phases are shown against scan number in figure 4.19. This shows the reduction in the deutero-imide chloride phase and the corresponding increase in LiD for the first 400 scans, approximately 15 hours, as expected when the sample is under deuterium. After this point, the data were collected under vacuum, and the opposite trend is seen: an increase in the deutero-imide chloride phase and a decrease in the lithium deuteride. The final change is observed when the sample was put back under deuterium, and the weight percent of the deutero-imide chloride is seen to decay while that for lithium deuteride increases.

The statistical parameters R_{wp} and R_{exp} are shown for the data set in figure 4.20, and show that the scans that appeared as anomalous points in figure 4.19 are outliers when considering the statistical fit. It is therefore reasonable to disregard these points. The plot also shows the improvement in statistics gained on increasing the scan time from 90 seconds to five minutes

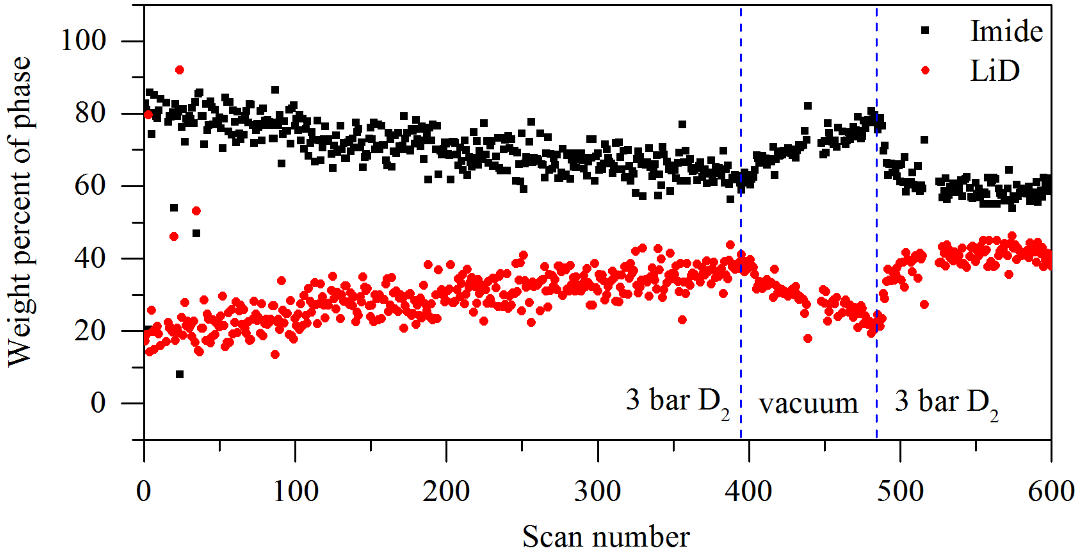

Figure 4.19: The weight percent of the deutero-imide chloride phase and the lithium deuteride phase calculated *via* batch QPA refinements of the neutron powder diffraction patterns of the sample cycled under deuterium on the POLARIS beamline.

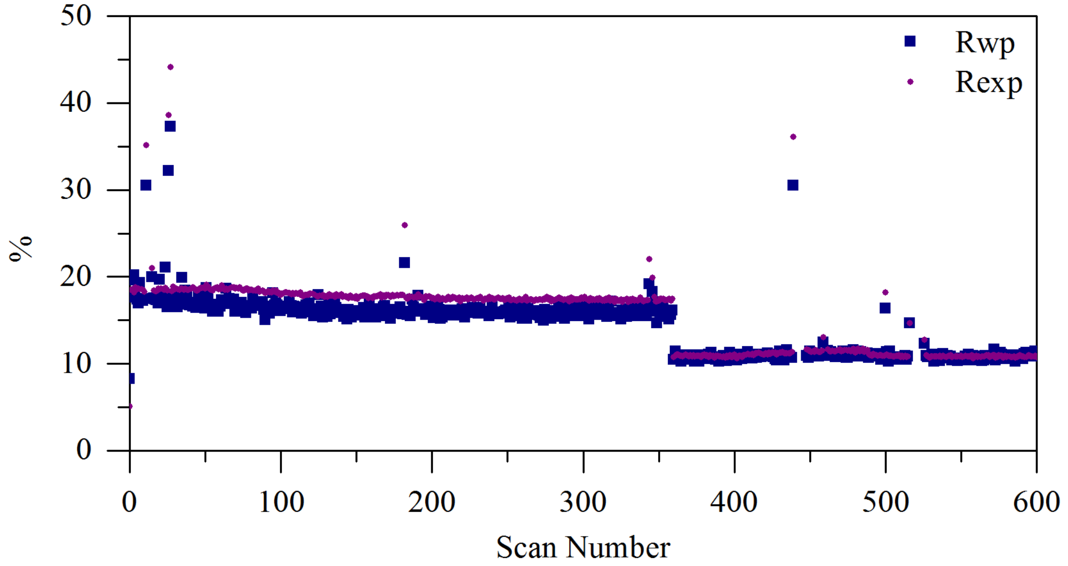

Figure 4.20: The statistical parameters R_{wp} and R_{exp} for the batch QPA refinements of the sample cycled under deuterium on the POLARIS beamline.

at scan number 360. The R_{exp} is greater than R_{wp}, most likely due to a high background in the neutron diffraction data. This could be due to the sample environment, or to residual H present because of incomplete deuteration, and causes an artificially low R_{wp} value. To prevent this, a background subtraction for each pattern would need to have been carried out but, as this would depend on the gas pressure and temperature, it was not practical for this experiment.

Using the weight percentages of the phases during the final deuteration, the kinetics of the reaction can be probed. There are a number of possible kinetic models that could be used to describe the behaviour of the system. If the data fit to an exponential function, either exponential decay, or an exponential function of the form shown in equation 4.4, the reaction is first order. In this case the reaction rate is proportional to the fraction of the reactant remaining.[141] Fitting (de)hydrogenation data in this way has been carried out previously to probe the kinetics of the halide-free system.[68] In this investigation, this model gave a reasonable fit to the data, as shown in figure 4.21, with an r^2 of 0.7876, and a half life of the chloride-containing phase of 46(5) minutes.

$$a = a_0 - Ae^{-kt} \tag{4.4}$$

An alternative model to describe the kinetics of a solid state system is a diffusion model, in which the rate of product formation decreases proportionally with the thickness of the product barrier layer.[141] This model can be described at the basic level in one dimension by equation 4.5 and, more similar to the systems studied in this investigation, in three dimensions, by equation 4.6, assuming spherical solid particles.[142] The datasets were also fitted using both of these kinetic models. The one-dimensional (1D) diffusion model gave an r^2 value of 0.5355 and is shown alongside the exponential model for LiD in figure 4.22. The three-dimensional (3D) model gave an r^2 value of 0.7153 and is shown alongside the expo-

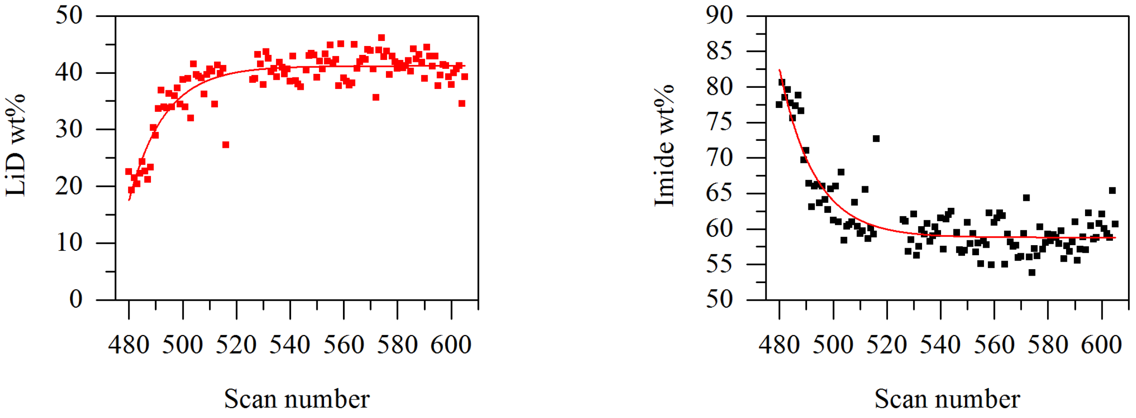

Figure 4.21: Weight percentages of LiD (left) and the chloride-containing phase (right) during the final deuteration at 275°C on the POLARIS beamline modelled using an exponential function.

nential model for the chloride-containing phase in figure 4.22.

$$a = (k't)^{\frac{1}{2}} + B \tag{4.5}$$

$$a = A - (B - (k't)^{\frac{1}{2}})^3 \tag{4.6}$$

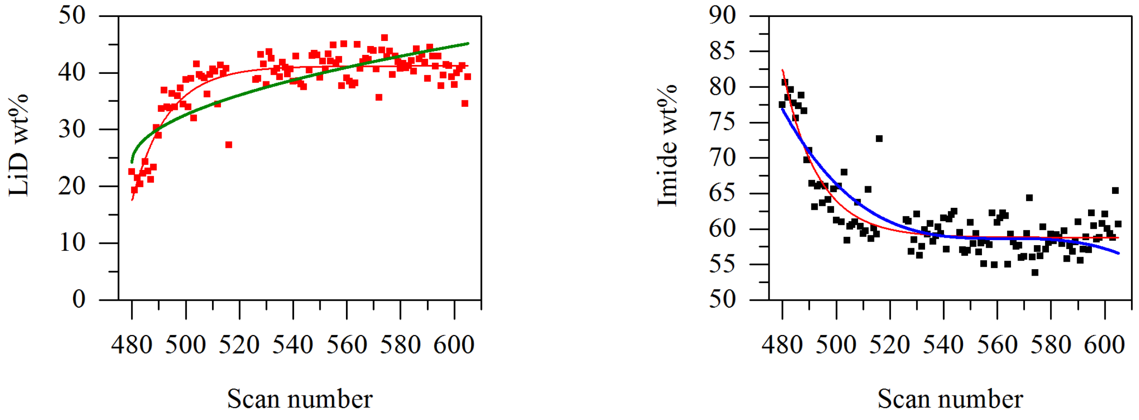

Figure 4.22: Weight percentages of LiD and the chloride-containing phase during the final deuteration at 275°C on the POLARIS beamline modelled using an exponential model (red lines) and diffusion models (1D: green, 3D: blue).

The QPA also gave the lattice parameter, a, for the deutero-imide chloride phase, which was seen to increase during the two deuterations. This increase is likely to be due to the increased size of the anion, on moving from imide to amide. Therefore the trend in lattice parameter is likely to be a good representation of the hydrogen content of the phase. Modelling a using the same exponential function as used for the weight percentage, equation 4.4, enabled a calculation of a half life, τ, for each stage of the cycling experiment. The data were also modelled using the 1D and 3D diffusion models which, in this example, gave very similar fits. The different models are compared in figure 4.23, showing that the fit to the exponential function model is better than that to either diffusion controlled model, and gave a half life of 76(15) minutes.

The lattice parameter was also plotted for the chloride-containing phase on dedeuteration, and fitted to an exponential decay model and the two diffusion controlled models. The fits are compared in figure 4.24 and show that the exponential function gives a better statistical fit to the data, outputting a half life, τ, of 104(14) minutes.

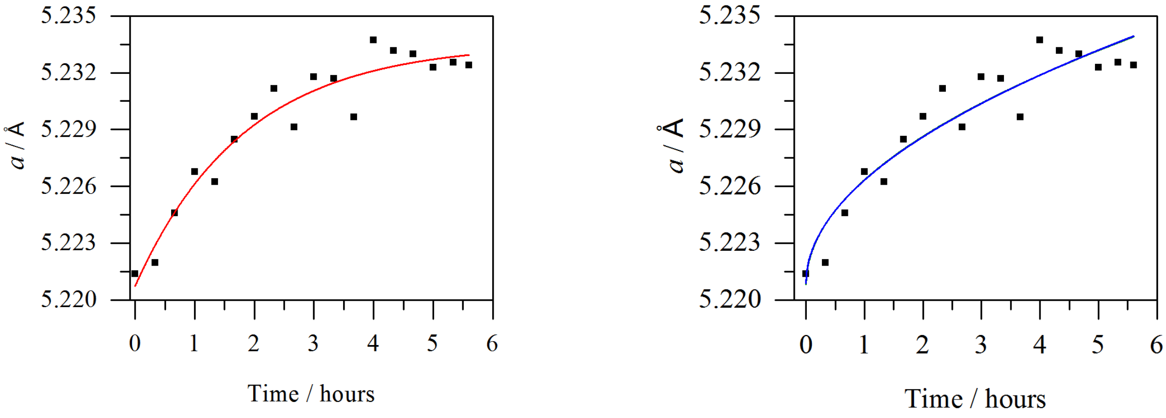

Figure 4.23: Lattice parameter of the imide chloride phase during the first deuteration at 300°C on the POLARIS beamline, along with an exponential function fit to the data (left, red, $r^2 = 0.9268$), and the 1D (right, green, $r^2 = 0.8899$) and 3D (right, blue, $r^2 = 0.8813$) diffusion models which, in this case, are indistinguishable.

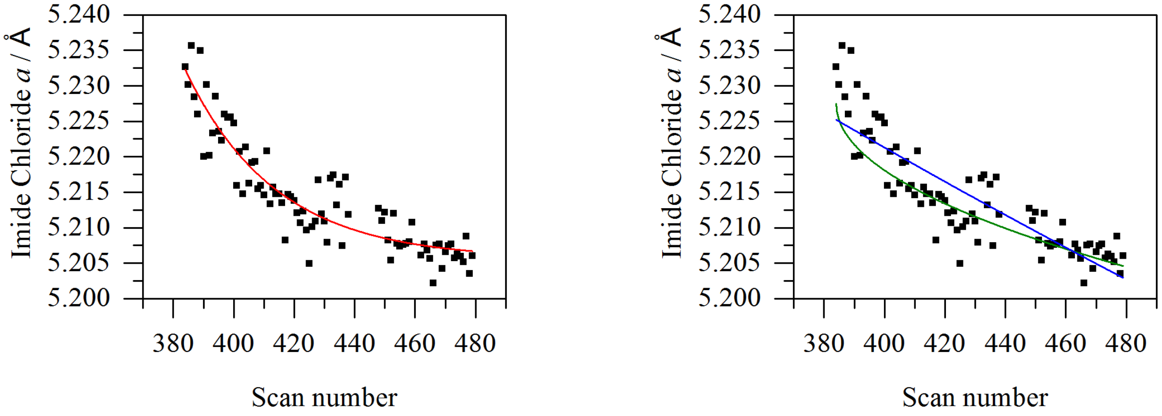

Figure 4.24: Lattice parameter of the deutero-imide chloride when under vacuum at 275°C on the POLARIS beamline, with an exponential function fit (left, red, $r^2 = 0.8400$), and 1D (right, green, $r^2 = 0.7459$) and 3D (right, blue, $r^2 = 0.7391$) diffusion models.

The same analysis was carried out for the second deuteration, at 275°C, and is shown in figure 4.25. Using the exponential function model, τ was calculated to be 56(10) minutes. This is consistent, within error, with the 46(5) minutes calculated from fitting the weight percentages of the phases. The *a* value towards which the lattice parameter is trending, a_0, is lower for the first deuteration at 300°C (5.2335(8) Å) than for the second at 275°C (5.2423(4) Å). This is not what would be expected due to thermal expansion, and so could be an indication that the sample is able to take up more deuterium at this lower temperature as the absorption is more thermodynamically favourable at lower temperatures. The half life is lower than that of the first deuteration, suggesting that subsequent cycles occur at a higher rate, as observed in the laboratory measurements discussed in section 4.7.1.

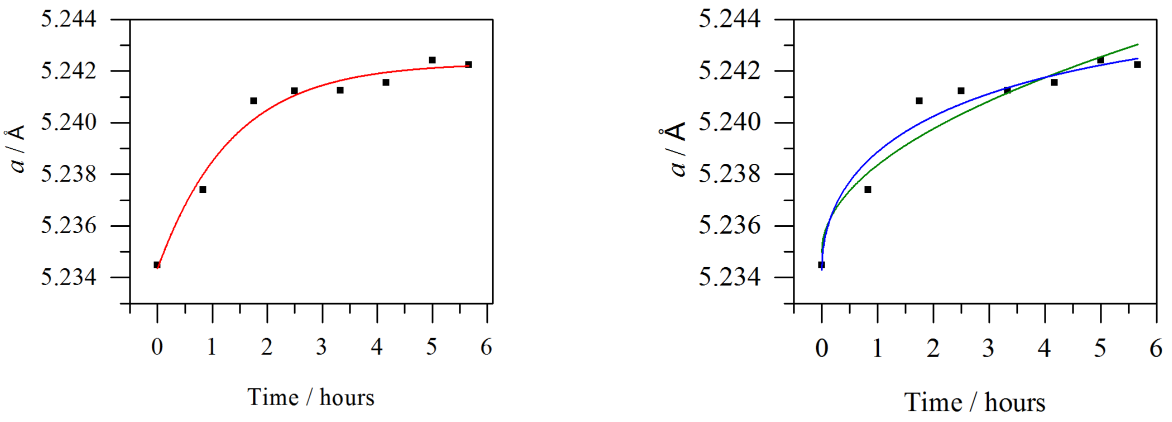

Figure 4.25: Lattice parameter of the imide chloride phase during the second deuteration at 275°C on the POLARIS beamline, along with an exponential function fit to the data left, red, $r^2 = 0.9663$), and 1D (right, green, $r^2 = 0.9098$) and 3D (right, blue, $r^2 = 0.9345$) diffusion models.

Throughout this analysis, both on deuteration and under vacuum, the data are modelled more favourably under a first order reaction model, rather than one that is diffusion controlled. This suggests that diffusion is not the rate-limiting step for this system, but instead the rate depends on the concentration of the reactant: the deutero-amide/imide chloride. This may be due to relatively high ionic mobility, making diffusion facile and therefore not the rate-determining step of the reaction. The ionic conductivity of both the amide and imide chloride will be investigated later in this study.

4.7.5 *Ex-situ* characterisation of the sample after cycling

After cycling the sample was measured using both powder XRD and Raman spectroscopy to investigate whether any structural change had occurred during the cycling process. Figure 4.26 shows the Raman spectra of the samples after cycling, and the deutero-imide chloride starting material. It can be seen by comparison to the original deutero-amide chloride that, after cycling, there was no imide peak observed at around 2340 cm^{-1} in the Raman spectrum and therefore the sample is present in the amide form.

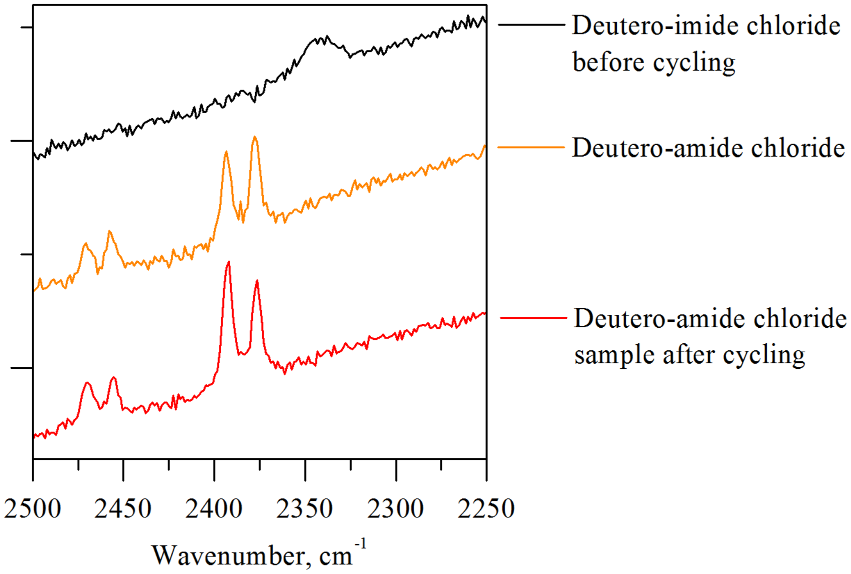

Figure 4.26: Raman spectra of samples before and after cycling on the POLARIS beamline.

Comparing the spectrum of $Li_7(ND_2)_6Cl$ with that of $Li_7(NH_2)_6Cl$ leads to the calculation of an isotope effect. For an N-H bond, modelling the bond as a harmonic oscillator and using Hooke's law gives the ratio between N-H stretching vibration vs N-D stretching vibration of 1.32. Table 4.3 shows the peak positions in the Raman spectra of both the amide and deutero-amide chloride species. The two lower wavenumber peak positions have a ratio of 1.36 and the two higher wavenumber peak positions have a ratio of 1.34.

Sample	Peak 1	Peak 2	Peak 3	Peak 4
$Li_7(NH)_6Cl$	3240	3262	3300	3321
$Li_7(ND)_6Cl$	2377	2393	2457	2471
Ratio	1.36	1.36	1.34	1.34

Table 4.3: Comparison of Raman peak positions for $Li_7(ND)_6Cl$ and $Li_7(NH)_6Cl$

Powder XRD was carried out on the sample after it had been cycled and the patterns are shown alongside that for $Li_7(ND_2)_6Cl$ in figure 4.27. In agreement with the Raman spectra, the pattern shows the presence of $Li_7(ND_2)_6Cl$, with some Li_2O. The relative intensities of the low angle peaks (101, 110, 012, 021) compared to those at higher angle is lower in the cycled sample. This may indicate that the sample is not quite so well ordered after cycling.

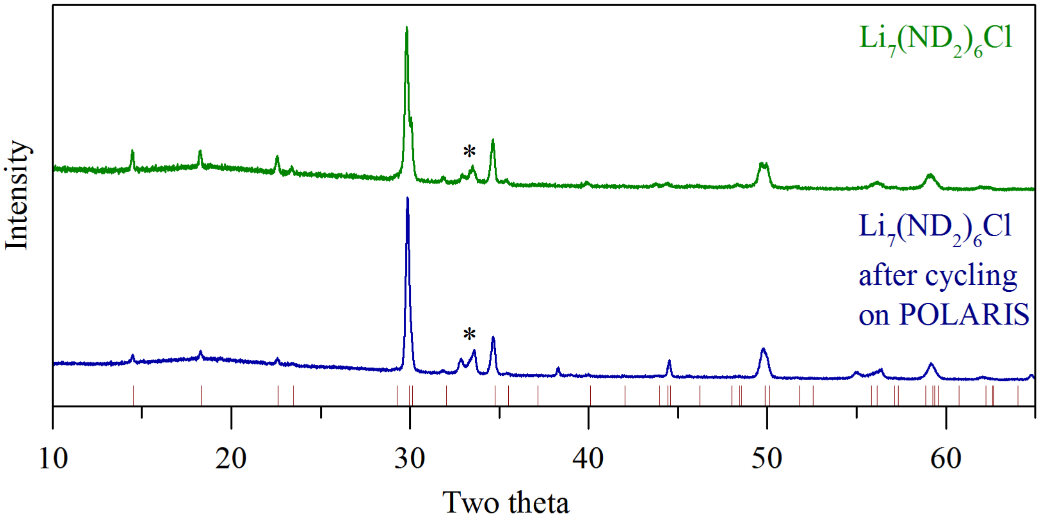

Figure 4.27: Powder XRD patterns for $Li_7(ND_2)_6Cl$ before (green) and after (blue) cycling on the POLARIS beamline. Tick marks show the peak positions for $Li_7(ND_2)_6Cl$ and asterisks mark the positions of peaks corresponding to Li_2O and the unknown phase described in section 3.5.1.

4.7.6 Gravimetric cycling of $Li_7(ND_2)_6Cl$ studied using powder neutron diffraction

During the *in situ* cycling measurements carried out on the I11 and POLARIS beamlines, it was not possible to measure the hydrogen content of the material whilst viewing the structural changes. A further experiment was carried out on the POLARIS beamline using the IGA^n sample environment, to simultaneously collect neutron powder diffraction data whilst measuring the mass of the sample. A 784 mg sample of the mixture of $Li_7(ND_2)_6Cl$ and LiD that had been previously cycled on the POLARIS beamline was loaded onto the microbalance of the IGA^n. Data were recorded continuously, with a new scan taken every five minutes.

The sample was put under vacuum and heated to 350°C. The temperature was set to 300°C and the D_2 pressure increased to 20 bar. A computational problem caused the temperature control to stop, and the temperature to drop to below 150°C. It was then reset to 300°C. After 30 minutes, the temperature of the sample was increased to 350°C and the sample put under vacuum. Once the mass loss had levelled, the sample temperature was reduced to 300°C and 10 bar of D_2 applied. After one hour, the pressure of D_2 was increased to 15 bar.

Again, there was an unintentional temperature drop down to 200°C, and the temperature was reset to 350°C. The D_2 pressure was then decreased and data collected under vacuum. Once the mass loss had stabilised, the temperature was decreased to 250°C and the pressure of D_2 increased to 10 bar. After four hours, the temperature was increased to 350°C. After one hour, the pressure was reduced and data collected under vacuum. The temperature was reduced to 300°C and 5 bar of D_2 applied.

The mass, pressure and temperature data, alongside a contour plot of the neutron powder diffraction patterns can be seen in figure 4.28. For complete conversion of $Li_7(ND_2)_6Cl$ to $Li_{13}(ND)_6Cl$, a mass loss of 9.79 wt% would be expected, roughly double the theoretical

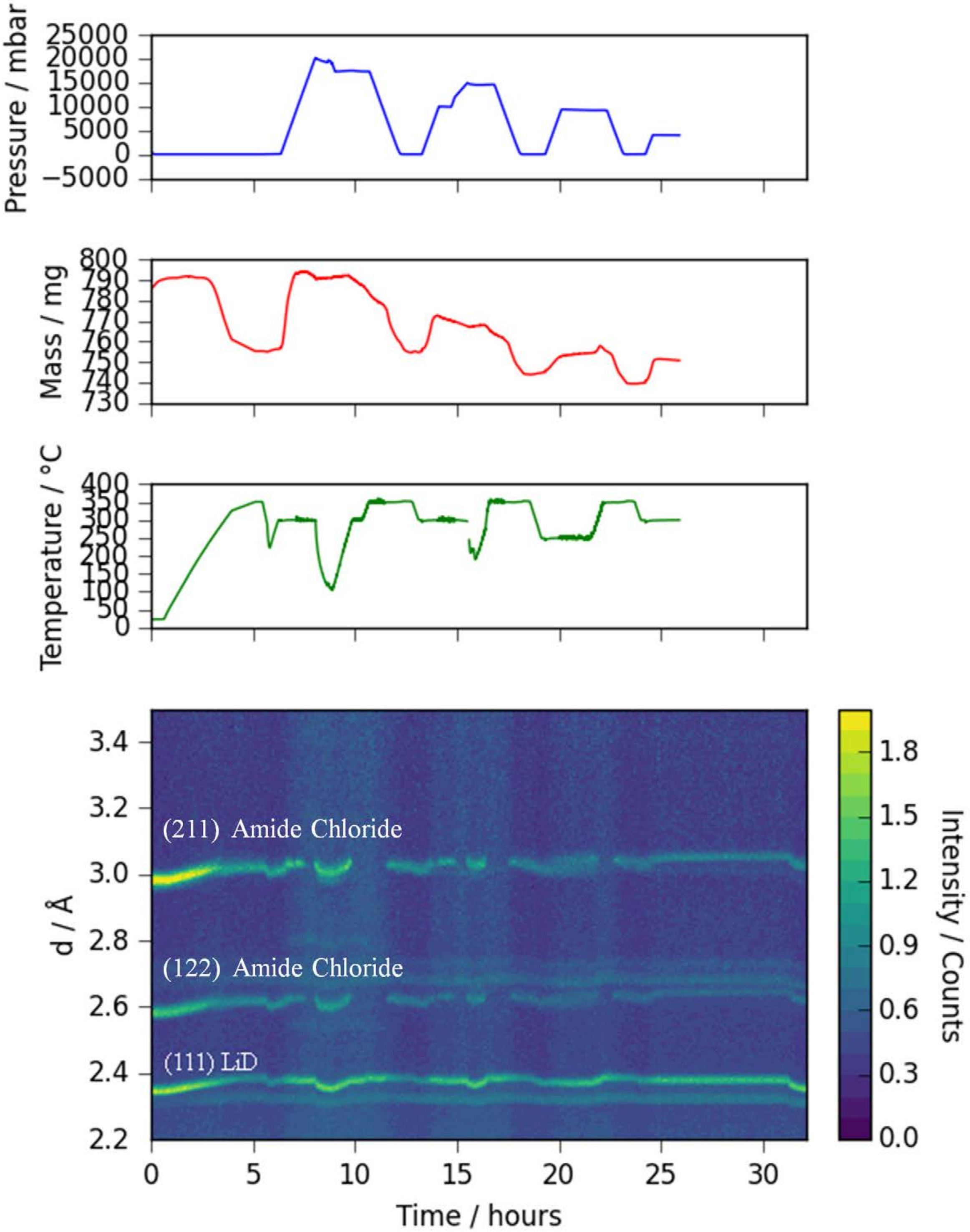

Figure 4.28: IGA^n and neutron powder diffraction data for the deuterium cycling of $Li_{13}(ND)_6Cl$ on the POLARIS beamline. All plots share the same universal x axis with the diffraction data.

dehydrogenation capacity due to the relative weights of D_2 and H_2. During the initial heating under vacuum, the sample lost 38.8 mg, corresponding to 4.55 wt%. The intensity of the deutero-amide chloride peaks in the neutron diffraction pattern was seen to decrease, along with those of LiD.

On application of 20 bar D_2 the sample regained the mass it had lost on dedeuteration, and the intensity of the LiD peaks was seen to increase. At this pressure, the deutero-amide chloride peak in the neutron powder pattern was no longer visible. However, when the temperature dropped, the deutero-amide chloride peak re-appeared in the diffraction pattern. Once the temperature had reached 300°C again, the peak was no longer present, suggesting that the phase becomes amorphous at higher temperatures.

During the second period of heating under vacuum the sample lost a similar mass as it had during the first dedeuteration, the equivalent of 4.61 wt%, and the peak corresponding to LiD increased in intensity in the neutron diffraction pattern. However, when put under 10 bar D_2, the sample took up 19.3 mg, compared to the 39.5 mg taken up on the previous deuteration. To attempt to recover the original mass, the pressure of D_2 was increased to 15 bar. The mass of the sample did not increase further. As observed after the initial deuteration, neither the peaks of the deutero-amide or deutero-imide chloride were present in the diffraction pattern. As before, when the temperature dropped, the deutero-amide chloride peaks re-appeared in the diffraction pattern. Increasing the temperature to 350°C caused the peaks to no longer be observed.

Taking the sample under vacuum caused the sample mass to decrease by 28.4 mg, bringing the sample mass 10 mg below the starting mass. During the third deuteration, at 10 bar, the LiD peaks in the diffraction pattern increased in intensity as the mass of the sample increased. However, the mass increase was again less than the previous cycle, although increasing the temperature to 350°C caused an additional 3 mg to be taken up by the sample.

During the final cycle under vacuum, the sample mass reduced by 18 mg to the lowest mass of the experiment: 739.3 mg. Application of 5 bar D_2 caused the sample to gain 13.3 mg, giving a final sample mass of 752.6 mg.

Due to the mass losses occurring under non-isothermal and non-isobaric conditions, it was not possible to fit a kinetic model to the mass loss data accurately. The sample was successfully cycled, retaining its capacity, for one vacuum / 20 bar D_2 / vacuum cycle but did not regain its original mass on subsequent hydrogenation at 10, and then 15 bar. This could be due to the sample morphology as, if the sample is no longer a powder, diffusion will be restricted preventing hydrogenation going to completion. Morphology would cause capacity loss, but it would not cause the mass of the system to decrease on subsequent hydrogenations, just for the cycling to be of a smaller quantity of deuterium.

The loss of capacity could also be due to loss of ND_3 from the system. Loss of ND_3 could occur either on dedeuteration, due to incomplete mixing, or on deuteration, forming LiD. The loss of ammonia on hydrogenation is due to the balance of equilibrium in reaction 4.7. A contour plot of the neutron diffraction data in the region of the (111) peak of LiD is shown in figure 4.29. The peak intensity does not appear to increase during the hydrogenation cycles. Due to the disappearance of the amide chloride peaks from the neutron diffraction patterns, it is not possible to carry out a bulk QPA for the data, preventing a quantitative measure of the relative amount of LiD present in the system.

$$\mathrm{LiNH_2} + \mathrm{H_2} \longleftrightarrow \mathrm{LiH} + \mathrm{NH_3} \tag{4.7}$$

During the first cycle, there is no ammonia lost on either dedeuteration or deuteration, as the mass returns to the starting mass. For all cycles, the sample was dedeuterated under the same conditions, but on redeueteration, the conditions were different for each cycle. Reaction 4.7 has been shown to be influenced by sample conditions, as even a low partial pressure of ammonia will suppress amide decomposition.[65] The IGA^n is a flowing system and so, under lower pressures of deuterium (used on subsequent cycles of the sample in this experiment), it may be more likely that the ND_3 can escape from the surface, preventing further hydrogenation and leading to capacity loss.

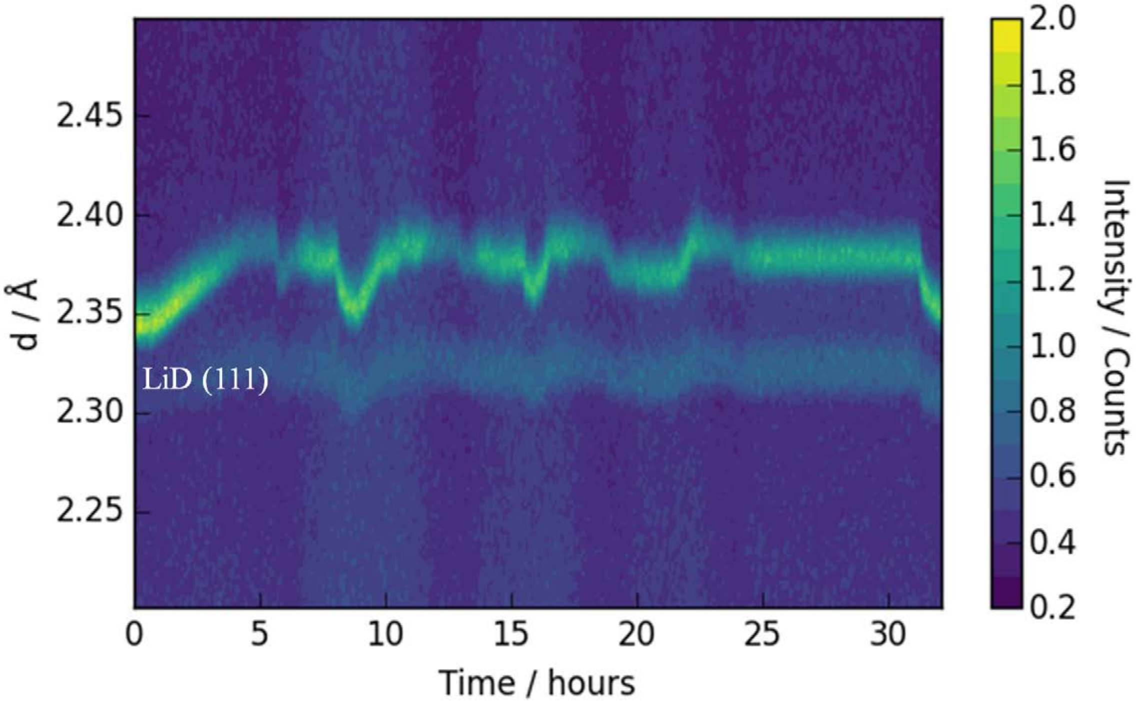

Figure 4.29: Neutron powder diffraction data for the deuterium cycling of $Li_{13}(ND)_6Cl$ on the POLARIS beamline, focussing in on the d spacing range of the (111) peak for LiD.

Proposing ND_3 loss as the cause of the capacity reduction in the system, the mass losses of the sample during cycling, as shown in figure 4.30, are tabulated in table 4.4. After separating into components due to reversible mass loss due to D_2 cycling and capacity loss due to ND_3 release, the two are converted to molar fractions using the formula masses and the sample mass before the dehydrogenation. For full capacity loss of D_2 from the sample, a molar fraction of six for D_2 would be expected to be lost. The data show that, on the first cycle, approximately half of the theoretical deuterium loss is observed, and regained on deuteration. The TPD-MS and HTP experiments detailed earlier in this chapter show an equivalent ability to cycle half of the theoretical capacity of hydrogen. Without a mass spectrometer, splitting the mass loss in this manner is purely speculative, but it shows a significant loss in the capacity of the system on cycling.

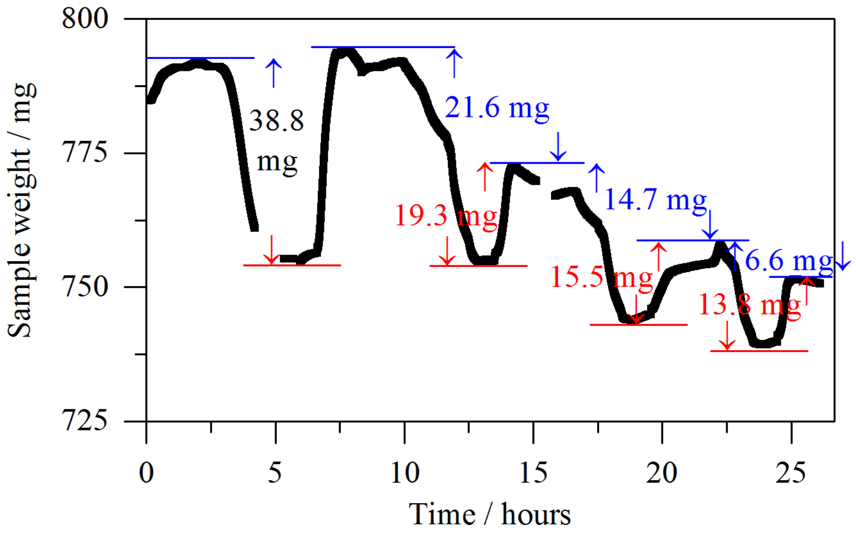

Figure 4.30: Mass of the sample for the deuterium cycling of $Li_{13}(ND)_6Cl$ on the POLARIS beamline, separated into capacity loss due to release of ND_3 (blue) and reversible release of D_2 (red).

Cycle number	Total Mass Loss / mg	Mass loss due to D_2 / mg	Relative molar fraction of D_2	Mass loss due to ND_3 / mg	Relative molar fraction of ND_3
1	38.8	38.8	3.0		
2	40.9	19.3	1.5	21.6	0.33
3	30.2	15.5	1.2	14.7	0.23
4	20.4	13.8	1.1	6.6	0.11

Table 4.4: Mass losses and molar fractions for a sample of $Li_7(ND_2)_6Cl$ + 6 LiD for four dehydrogenation cycles on the IGA^n measured on the POLARIS beamline.

4.8 A.C. Impedance Spectroscopy

4.8.1 $Li_7(NH_2)_6Cl$

Samples of $Li_7(NH_2)_6Cl$ were pressed into 7 mm diameter pellets, approximately 1 mm thick, sintered at 150°C for 12 hours, and connected to a custom-built inert atmosphere rig, as described in section 2.8. A.C. impedance measurements of the pellets were taken as the temperature was increased to just below 200°C, and also on cooling. The samples were kept below 200°C to prevent decomposition to the imide during the experiment. An example Nyquist plot of the amide chloride sample can be seen in figure 4.31. The resistance values given by the Nyquist plots were used to calculate the conductivity of the sample.

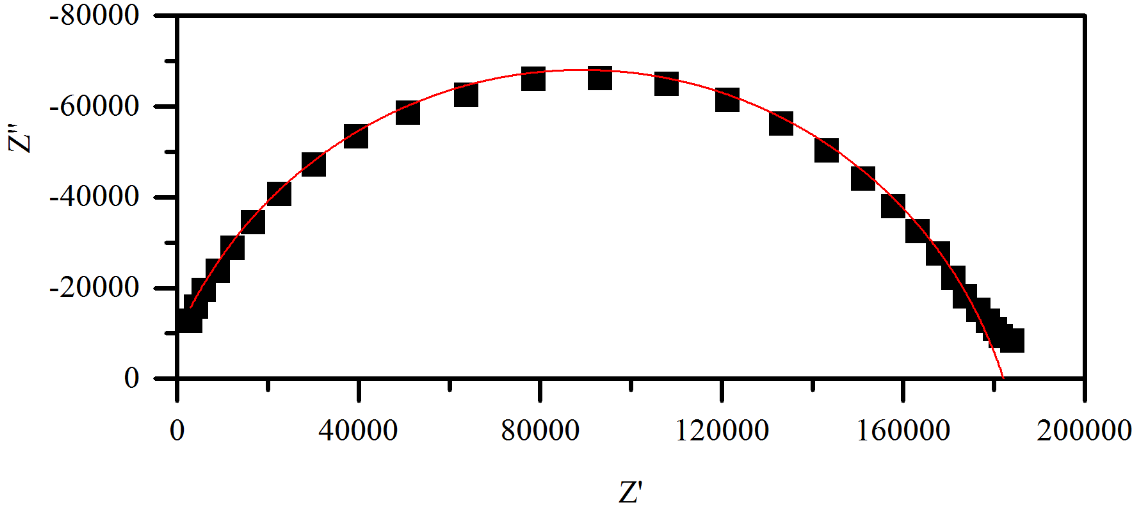

Figure 4.31: Experimental (circles) and calculated (line) Nyquist plot for $Li_7(NH_2)_6Cl$ at 156°C.

In a pellet modelled using the 'brickwork' method, as described by West *et. al.*,[136] the Nyquist plot would be expected to show two semicircles: corresponding to the bulk and grain boundary contributions, observed at higher and lower frequencies, respectively. For the amide chloride pellets, it was not possible to distinguish a second semicircle from the plots. To determine whether the values calculated corresponded to conductivity due to resistance to movement through the bulk of the material or across the grain boundaries, the capacitance was considered. Resistance to movement through the bulk material is usually characterised by a capacitance of the order of 10^{-12} F whereas that across the grain boundary is characterised by a lower capacitance of between 10^{-11} and 10^{-9} F.[136] The impedance results for the amide chloride showed capacitance values above 2×10^{-11} F. This is on the borderline between the two regions, but comparison with Nyquist plots for other similar samples that exhibit two semicircles indicates that those measured for the amide chloride represent the conductivity due to the resistance to movement of the ions through the bulk of the material.

Reported values for the conductivity of amide halides are for pellets measured using a different experimental setup, and with different pellet sizes.[69,102] To enable a comparison of the conductivity reported in this study with other materials, pellets of $LiNH_2$ and Li_2NH were measured. Pellets of $LiNH_2$ and Li_2NH were made using the procedure described above, with sintering temperatures of 150°C and 400°C, respectively. As with the amide chloride measurements, it was not possible to distinguish a second semi-circle in the Nyquist plots. The capacitance values were of a similar order to that of the $Li_7(NH_2)_6Cl$ samples and therefore the results were able to be used for comparison. Repeat experiments were carried out and were in agreement with the single set of results for each sample reported here. Temperature-dependent Arrhenius plots of the conductivity of three pellets of $Li_7(NH_2)_6Cl$ and those for $LiNH_2$ and Li_2NH are shown in figure 4.32 along with linear fits to the data. These plots show that a change in the gradient of the amide chloride plots occurs at approximately 100°C.

These results show that the conductivity of $Li_7(NH_2)_6Cl$ is greater than that of $LiNH_2$, but not as high as that of Li_2NH. The addition of Cl^- ions therefore leads to an increase in ionic

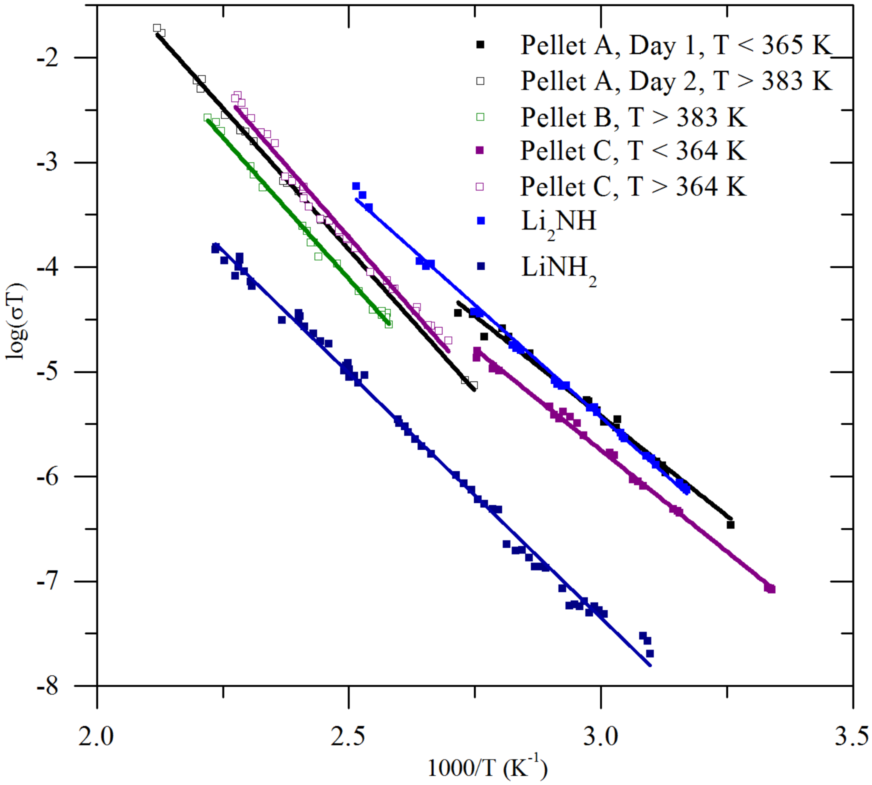

Figure 4.32: Plot of log(σT) against 1/T for samples of $Li_7(NH_2)_6Cl$ alongside those for $LiNH_2$ and Li_2NH.

conductivity in the amide. As there have been mechanisms proposed for dehydrogenation that involve lithium ion conduction,[69,66] this improvement in conductivity correlates with the lower desorption temperature of $Li_7(NH_2)_6Cl$ when compared to $LiNH_2$. The gradient of these plots can be used to calculate the activation energy of ionic conduction, as shown in table 4.5.

Sample	Gradient	Activation Energy (kJ mol $^{-1}$)
Pellet A, T < 110 °C	-3.8(1)	8.8(3)
Pellet A, T > 110 °C	-5.4(1)	12.4(1)
Pellet B	-5.4(1)	12.5(2)
Pellet C, T < 91 °C	-3.87(5)	8.9(1)
Pellet C, T > 91 °C	-5.5(1)	12.7(3)
$LiNH_2$	-4.67(4)	10.7(1)
Li_2NH	-4.28(5)	9.8(1)

Table 4.5: Gradients and calculated activation energies of ionic conduction for pellets of $Li_7(NH_2)_6Cl$ compared to those for $LiNH_2$ and Li_2NH.

4.8.2 $Li_{13}(NH)_6Cl$

When a sample of $Li_7(NH_2)_6Cl$ loses hydrogen, the initial dehydrogenation will occur on the surface of the material, leaving an outer layer of the imide phase, according to the model proposed by Cao *et. al.*[143] If the conductivity of lithium ions is important in hydrogen desorption, it will not only be important for the amide phase to have a high lithium ion conductivity, but also the imide phase. To investigate whether this was the case for the chloride-containing system, A.C. impedance was used to measure the conductivity of $Li_{13}(NH)_6Cl$ formed by the dehydrogenation of $Li_7(NH_2)_6Cl$. This sample was also measured to investigate whether the change in activation energy observed in the amide chloride system is due to dehydrogenation occurring.

Samples of $Li_{13}(NH)_6Cl$ were pressed into 7 mm diameter pellets, approximately 1 mm thick, sintered at 400°C for 12 hours, and connected using silver paint to a custom-built inert atmosphere rig, as described in section 2.8. A.C. impedance measurements of the pellets were taken as the temperature was increased to just below 200°C, and also on cooling. The resistance values given by the Nyquist plots were used to calculate the conductivity of the sample. For these samples, more than one semi-circle was observed in the Nyquist plots, and assigned as conductivity due to the bulk material (capacitance of 3×10^{-11} F) and the boundaries between the grains in the sample (capacitance of 8×10^{-10} F). The conductivities associated with these two properties are of similar magnitudes: approximately 2×10^{6} S cm^{-1} at 100°C.

To enable comparison between $Li_{13}(NH)_6Cl$ and previous samples measured, the resistance value used was that of comparable capacitance ($\times 10^{-11}$ F). Temperature-dependent plots of the conductivity of two pellets of $Li_{13}(NH)_6Cl$ are shown in figure 4.33 along with linear fits to the data alongside equivalent plots for $LiNH_2$, Li_2NH and one of the $Li_7(NH_2)_6Cl$ samples.

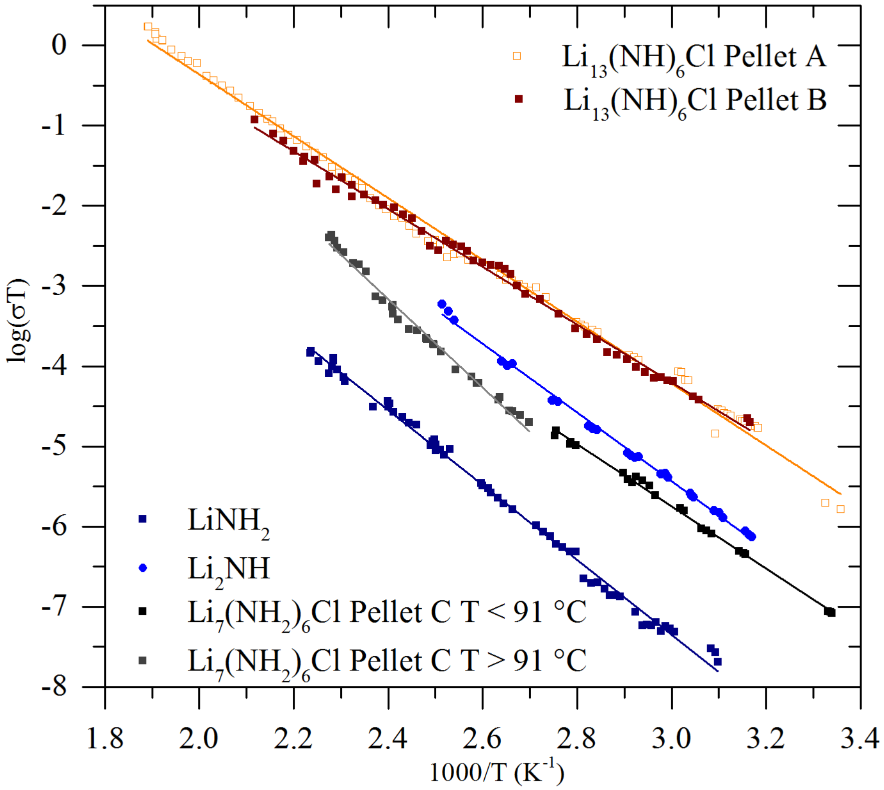

Figure 4.33: Plot of log(σT) against 1/T for samples of $Li_{13}(NH)_6Cl$ alongside those for $LiNH_2$, Li_2NH and $Li_7(NH_2)_6Cl$.

These plots show that, as with the amide system, the addition of chloride increases the conductivity of the material. This is consistent with a decreased hydrogen desorption temperature. The activation energies for pellets A and B of $Li_{13}(NH)_6Cl$ were 8.88(7) and

8.30(9) kJ mol^{-1}, respectively. These are similar values to those seen for the amide chloride pellets at low temperatures, and lower than those of both $LiNH_2$ and Li_2NH. These plots also show that the behaviour of the amide chloride above 100°C does not match that of the imide, indicating that the structural change that occurs is not dehydrogenation to the imide.

4.9 Conclusions and further work

This chapter investigated the hydrogen storage properties of the new, low chloride-content, amide chloride phases. It was found that both $Li_7(NH_2)_6Cl$ and $Li_6Mg_{1/2}(NH_2)_6Cl$ released hydrogen on reaction with LiH at a lower temperature than $LiNH_2$. The reduction in chloride content when compared with $Li_4(NH_2)_3Cl$ and $Li_3Mg_{1/2}(NH_2)_3Cl$ has not had a detrimental effect on the desorption temperature. The new phases also form imide chlorides on dehydrogenation, and can be rehydrogenated back to the amide chlorides. However, no improvement in properties due to the presence of magnesium in the amide chloride was observed. When the lithium only amide chloride was reacted with MgH_2 instead of LiH, the desorption temperature was reduced slightly, but this complex system did not show improvements on rehydrogenation.

Desorption measurements under flowing argon using a TPD-MS did not detect the release of ammonia, however, cycling experiments under dynamic vacuum showed a loss of capacity in the system, potentially due to ammonia release on deuteration. A detailed laboratory IGA study in combination with a mass spectrometer, with structural characterisation between cycles, would be of great help when considering what causes the capacity loss of the system on cycling. A capacity loss due to ammonia release has been observed in the $LiNH_2$/LiH system under similar conditions, and can be reduced by the introduction of N_2 into the hydrogen gas used for rehydrogenation.[144] It is proposed that the N_2 present reacts with liquid lithium, preventing the build up of LiH in the system, as observed by synchrotron radiation in this study. A gravimetric cycling experiment with this gas composition could be undertaken for $Li_7(NH_2)_6Cl$ to see if this reduces the capacity loss of the system.

Structural measurements taken during the cycling of $Li_7(NH_2)_6Cl$ were carried out to gain an insight into the de/rehydrogenation mechanism. The kinetic analysis of the cycling data show that they fit well to a first order kinetic model, indicating that the rate of the reaction is determined by the concentration of one reagent. An ammonia-mediated mechanism for the dehydrogenation of $LiNH_2$ with LiH has, as discussed in section 1.3.2.4, been observed experimentally as two reactions, shown in equations 1.15 and 1.16.[60,61]

$$2\,\mathrm{LiNH_2} \longrightarrow \mathrm{Li_2NH} + \mathrm{NH_3} \tag{4.8}$$

$$\mathrm{NH_3} + \mathrm{LiH} \longrightarrow \mathrm{LiNH_2} + \mathrm{H_2} \tag{4.9}$$

It has been proposed that reaction 4.9 is an ultra-fast surface reaction and therefore reaction 4.8 is the rate determining step.[62] The results of this investigation support this proposal for the amide chloride system, as reaction 4.8 involves just one reagent, supporting a first order kinetic model. For the rehydrogenation of the imide chloride, shown by reaction 4.10, the hydrogen concentration can be considered constant, again supporting first order reaction kinetics.

$$\mathrm{Li_{13}(NH)_6Cl} + 6\,\mathrm{H_2} \longrightarrow \mathrm{Li_7(NH)_6Cl} + 6\,\mathrm{LiH} \tag{4.10}$$

The half lives of the different cycling processes of this system have been measured, and are shown in table 4.6. The results are only preliminary findings, but suggest that this system will need to be improved to meet the US Department of Energy filling target of 5 minutes for automotive fuelling. The effect of physical manipulations, such as ball milling, could be investigated to see how the kinetics could be improved. It can be seen from the table that the half life decreases with the number of cycles. This was also observed in the laboratory, with a lower hydrogen release temperature observed for a sample that had previously undergone one cycle. This is encouraging that physical manipulations may be successful in improving the kinetics of (de)hydrogenation.

Process	Temperature / °C	Half life / minutes
Deuteration	300	76(15)
Dedeuteration	275	104(14)
Deuteration	275	56(10)
Deuteration	275	46(5)

Table 4.6: Half lives for different stages of cycling of a sample of $Li_{13}(ND)_6Cl$ with D_2.

During dehydrogenation using the variety of techniques studied in this investigation, it was only possible to release approximately 50% of the theoretical hydrogen capacity. It is possible that is due to the reaction pathway proceeding via a higher-chloride (and therefore lower-hydrogen) state, possibly the originally synthesised amide chloride $Li_4(NH_2)_3Cl$. The TPD-MS for $Li_4(NH_2)_3Cl$, however, also showed release of less than 50% of the theoretical capacity, and so this is unlikely to be the case. The inability to release the full capacity could be due to sample preparation techniques, but as the complex mechanism of dehydrogenation is still not fully understood, it is difficult to be certain as to why this is the case. If these materials are to be used in automotive, or other, applications then this is an issue that would need to be mitigated.

The difference in the phases formed during each cycling experiment is an indication of the complexity of this system. Varying hydrogen and chloride content, and the formation of an amorphous phase, makes determination of the exact structural changes challenging.

The ionic conductivities of the amide and imide chloride were measured, and were higher than those of the chloride-free system for both the amide and imide forms. Considering that the rehydrogenation kinetics suggest that diffusion is not rate-limiting, it may be that improvement in the ionic conductivity prevents ionic diffusion hindering the reaction process. It would be interesting to see how the conductivity is affected by the presence of magnesium, and whether the difference between the 3 : 1 amide chlorides $Li_4(NH_2)_3Cl$ and $Li_3Mg_{1/2}(NH_2)_3Cl$ is larger than that between the new, low-chloride, amide chlorides $Li_7(NH_2)_6Cl$ and $Li_6Mg_{1/2}(NH_2)_6Cl$ to correlate with the difference in hydrogen desorption properties.

It has been shown in preliminary investigations that the conductivity, and hydrogen storage properties, are improved on moving from the chloride system to those containing bromide and iodide.[69,139] Investigations were carried out to see if this was the case for the new amide chloride, and the results of these will be discussed in the following chapter.

Chapter 5

Hydrogen storage properties of other amide halides

5.1 Introduction

The phase space of the amide bromide and amide iodide systems have previously been investigated to find the lower halide doping limit of the structures.[139,145] Although at stoichiometries with lower bromide content than $Li_7(NH_2)_6Br$, $LiNH_2$ was observed alongside the amide bromide, a change in lattice parameter suggested that some sub-stoichiometry could be accommodated. The structure of the amide iodide $Li_3(NH_2)_2I$ was not seen to accommodate any other stoichiometries.

The hydrogen desorption properties of these amide halides has been reported, with the reaction of $Li_7(NH_2)_6Br$ and LiH giving rise to two distinct hydrogen desorption events at 285°C and 325°C. The desorption of the amide iodide was also complex, with hydrogen release observed as low as 140°C.[69]

Given the similarity of the structure of the new amide chloride $Li_7(NH_2)_6Cl$ to the amide bromide $Li_7(NH_2)_6Br$, the properties of the two were compared using A.C. Impedance spectroscopy and diffraction techniques during hydrogen cycling. The hydrogen cycling properties of the amide iodide were also studied in the same way to enable comparison of this system with its lower hydrogen release temperature to the other amide halides.

5.2 Experimental

Samples of ground mixtures of lithium amide (Sigma–Aldrich, 95% purity) and LiBr or LiI (Sigma–Aldrich, anhydrous beads, 99.998% purity) were prepared in an argon-filled glove box. The samples were prepared in various stoichiometries and heated under flowing argon at temperatures up to 250°C (LiBr) or 150°C (LiI) for 12 hours, as described in section 2.1.

Powder X-ray diffraction data were collected in the laboratory as described in section 2.2.2.4 using a Bruker D8 instrument in transmission geometry with a wavelength of 1.54059 Å and a Siemens D5000 in transmission geometry with a wavelength of 1.54059 Å.

Desorption measurements were carried out using TPD-MS as described in section 2.5, for ground mixtures of the prepared samples with LiH (Sigma–Aldrich, $> 95\%$). These samples were prepared at the desired stoichiometry in an argon-filled glove box and heated in quartz tubes within the TPD apparatus at 2°C min^{-1} to 400°C.

Ionic conductivities were evaluated by the AC complex impedance method (section 2.8) using a Solartron 1260 impedance analyser. Measurements were performed on pressed pellets (7 mm diameter, between 0.4 and 1.5 mm thickness) within a sealed glass rig designed for these measurements in-house. The surfaces of the pellets were coated with silver and attached to the electrodes also using silver, to ensure good electrical contact.

Cycling measurements were carried out using an IGA^n on the beam line POLARIS at ISIS neutron source, as described in section 2.12 and on beamline I11 with a wavelength of 0.826205 Å at Diamond light source, as described in section 2.10.

5.3 The lithium amide bromide, $Li_7(NH_2)_6Br$

5.3.1 Structure

Lithium amide reacts with lithium bromide to form a rhombohedral phase of stoichiometry $Li_7(NH_2)_6Br$.[69] The unit cell of this phase has an NH_2^- : Br^- ratio of 18:3, space group $R\bar{3}$. Reaction 5.1 was carried out at 250°C over a range of y values for a reaction time of twelve hours. Previous investigation had shown that decreasing the bromide level formed the rhombohedral phase, but that excess $LiNH_2$ was formed, suggesting that the structure was not able to accommodate any additional NH_2^- ions.[139] The X-ray diffraction pattern for the 18 : 3 phase ($y = 0$) is shown in figure 5.1.

$$(7-y)\,LiNH_2 + y\,LiBr \longrightarrow Li_7(NH_2)_{7-y}Br_y \tag{5.1}$$

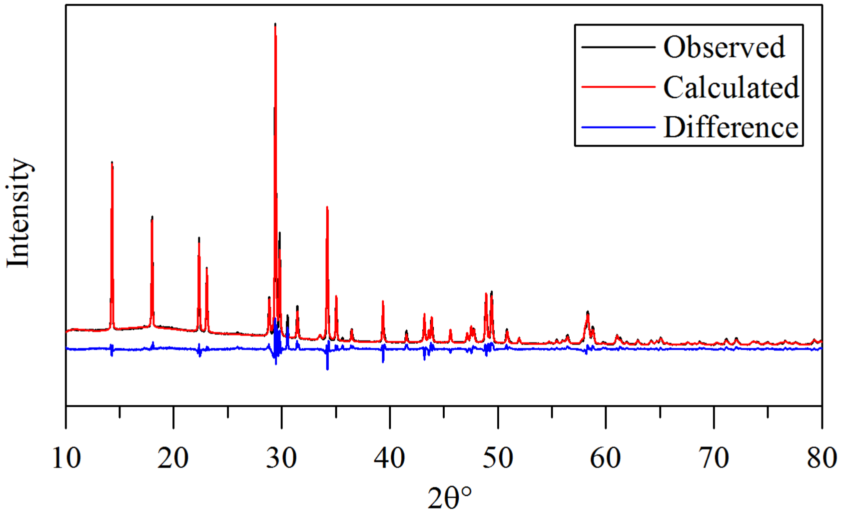

Figure 5.1: Powder X-ray diffraction pattern for $Li_7(NH_2)_6Br$, with the calculated and difference patterns for a Rietveld fit to the data.

This work increased the bromide level, by investigating *y* values greater than one, and looking at the structures formed by using powder X-ray diffraction. Increasing the bromide level decreased the yield of the amide bromide and large peaks for LiBr were observed, indicating that the structure cannot accommodate any additional Br^- ions. The product from the reaction at the 14 $NH_2{}^-$: 7 Br^- ratio is seen to contain mainly un-reacted starting materials. Therefore it can be concluded that the amide bromide system cannot accommodate any variation in stoichiometry in the bromide rich region.

There is therefore no equivalent of $Li_4(NH_2)_3Cl$ formed in the bromide system, even though both systems exhibit similar structures at the amide to halide ratio of 6 : 1. This suggests that both the cubic and rhombohedral structures of $Li_4(NH_2)_3Cl$ must be of a form that cannot accommodate larger bromide ions on the sites occupied by Cl^-. This can be explained by considering the distances between the Hal^- and $NH_2{}^-$ ions in the different structures. Table 5.1 shows the different bond distances, and it can be seen from these data that the distances in both the $I2_13$ and $R\bar{3}$ form of $Li_4(NH_2)_3Cl$ are much shorter than those observed in the amide bromide. It can also be seen by comparing the N-Cl distances for the two different Cl^- sites in the $R\bar{3}$ structure that the addition of chloride ions onto the amide sites (Cl2) results in Cl^- being closer to the amide ions. This could explain why a similar structure is not observed in the bromide system, due to the larger ions.

Sample	Shortest Hal-N bond distance (Å)
$Li_7(NH_2)_6Br$	3.769
$Li_7(NH_2)_6Cl$	3.644
$Li_4(NH_2)_3Cl$, $I2_13$	3.635
$Li_4(NH_2)_3Cl$, $R\bar{3}$, N-Cl1	3.763
$Li_4(NH_2)_3Cl$, $R\bar{3}$, N-Cl2	3.454

Table 5.1: Distances between the halide ions and nitrogen atoms in the amide ions in the amide halide structures.

5.3.2 A.C. Impedance Spectroscopy

Samples of $Li_7(NH_2)_6Br$ and $Li_{13}(NH)_6Br$ were pressed into 7 mm diameter pellets, approximately 1 mm thick, sintered at 100°C and 400°C, respectively, for 12 hours and connected using silver paint to a custom-built inert atmosphere rig, as described in section 2.8. A.C. impedance measurements of the pellets were taken as the temperature was increased to just below 200°C, and also on cooling. The samples were kept below 200°C to prevent decomposition during the experiment. The resistance values given by Nyquist plots were used to calculate the conductivity of the samples at each temperature value. Repeat experiments were carried out on different pellets and were in agreement with the single set of results for each sample reported here.

Examples of the conductivity values at approximately 100°C are shown in table 5.2 and show that, at this temperature, the conductivity of $Li_7(NH_2)_6Br$ is lower than that of $LiNH_2$, but that the imide bromide has a higher conductivity than Li_2NH. Figure 5.2 shows the temperature dependence and fitted Arrhenius plots of the conductivity of the amide and imide bromide alongside those for $LiNH_2$ and Li_2NH.

Sample	Temperature / °C	Conductivity / S cm^{-1}
$Li_7(NH_2)_6Br$	100	3.21×10^{-9}
$LiNH_2$	102	4.37×10^{-9}
$Li_{13}(NH)_6Br$	103	1.21×10^{-6}
Li_2NH	101	1.97×10^{-7}

Table 5.2: Conductivity values at approximately 100°C for $Li_7(NH_2)_6Br$ and $Li_{13}(NH)_6Br$ compared to those for $LiNH_2$ and Li_2NH.

As the hydrogen desorption temperature of the bromide system is lower than that for $LiNH_2$, this result suggests that it is not the amide conductivity that determines the hydrogen release properties. However, the higher conductivity for the imide bromide when compared to Li_2NH suggests that the conductivity of this phase could be correlated to the improvement in release properties. On dehydrogenation, initial decomposition occurring on the surface of the material will form a layer of a lithium rich, hydrogen poor, imide-like phase which the lithium ions must flow through in order for further dehydrogenation to occur. In this way, a layered intermediate stage has been proposed both for the halide-free system,[67] and with a $TiCl_3$ catalyst,[146] and is possible due to the structural similarity between $LiNH_2$ and Li_2NH. The structure of the amide bromide can be compared to the imide bromide, figure 5.3, and can be seen to be similar, giving the potential for an equivalent topotactic transformation.

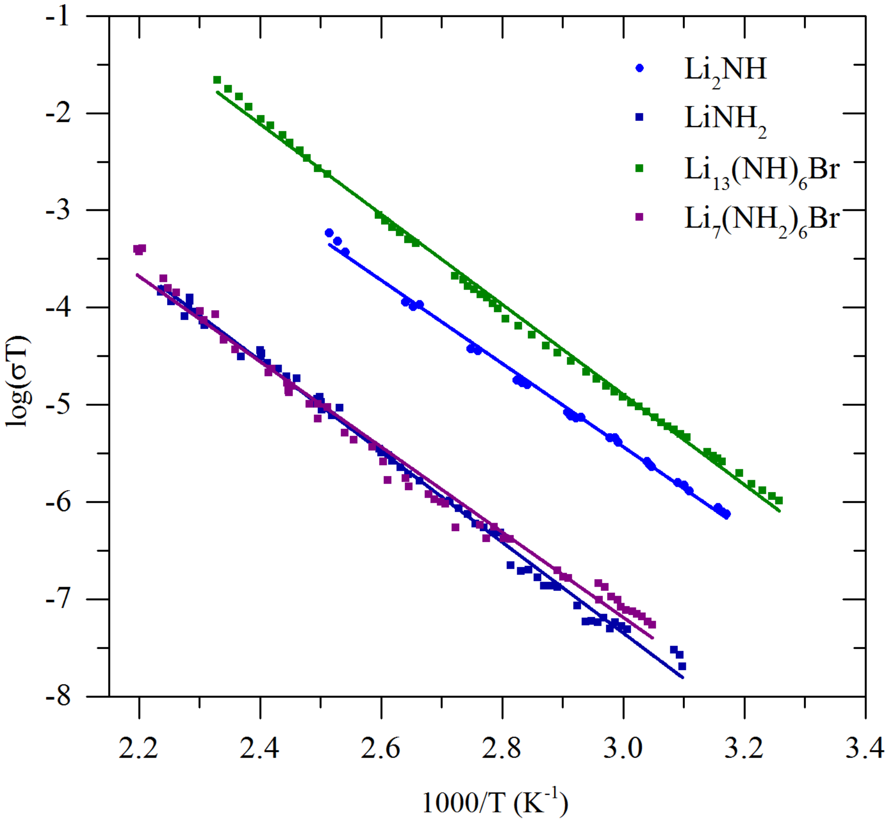

Figure 5.2: Arrhenius plots for $Li_7(NH_2)_6Br$ and $Li_{13}(NH)_6Br$ alongside those for $LiNH_2$ and Li_2NH.

The Arrhenius plots for the amide and imide bromide samples are also shown alongside those for the chloride equivalents and the non-halogenated system in figure 5.4. The activation energies calculated from the gradients of these plots are shown in table 5.3. The

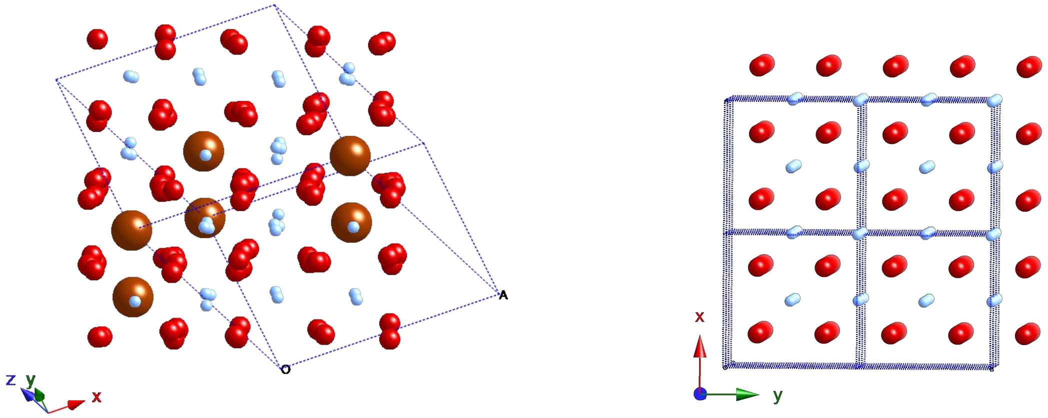

Figure 5.3: Left: Section of the structure of $Li_7(NH_2)_6Br$, displayed to be compared to that for the imide bromide. Right: structure of Li_2NH: in the imide bromide, bromide ions are present evenly distributed on the NH^{2-} sites. Lithium ions are shown as red spheres, nitrogen blue and bromide brown. Unit cells are marked with dotted lines.

chloride and bromide systems have the same structure in both the amide and imide phases, as described previously in this study. Therefore any difference in conductivity must be due to the halide ion that is present. As the conductivity of the imide and amide chloride are greater than that of the bromide equivalents, the presence of the larger bromide ion could inhibit the movement of the lithium ions through the lattice if the pathway of the lithium ions moves past the halide. The difference could also be due to the level of disorder within the structures of the amide and imide bromide compared to that within the chloride-containing equivalents. More disorder within the chloride structure would correlate with the chloride system being more able to accommodate non-stoichiometry within the structure.[145]

As shown in figure 5.4, at higher temperatures, the conductivity of the imide bromide starts to be higher than that of the imide chloride. As these temperatures are comparable with the conditions required for hydrogen desorption, this could be why the bromide system has a lower temperature onset of hydrogen desorption than the chloride system.[69]

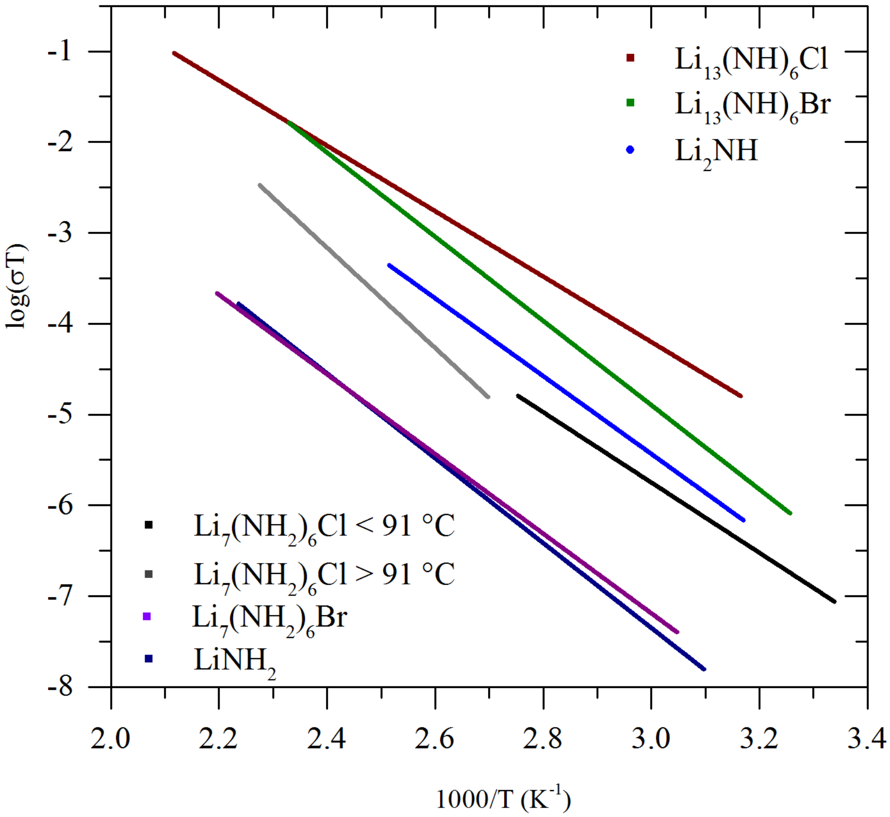

Figure 5.4: Arrhenius plots for $Li_7(NH_2)_6Br$ and $Li_{13}(NH)_6Br$ alongside those for $LiNH_2$, Li_2NH, $Li_7(NH_2)_6Cl$ and $Li_{13}(NH)_6Cl$.

Sample	Activation Energy (kJ mol $^{-1}$)
$Li_{13}(NH)_6Cl$	8.30(9)
$Li_{13}(NH)_6Br$	10.67(7)
Li_2NH	9.8(1)
$LiNH_2$	10.7(1)
$Li_7(NH_2)_6Cl$, $T < 91$ °C	8.9(1)
$Li_7(NH_2)_6Cl$, $T > 91$ °C	12.7(3)
$Li_7(NH_2)_6Br$	10.1(2)

Table 5.3: Activation energy of ionic conduction for samples measured in this study.

5.4 TPD-MS of a lithium amide/ lithium bromide mixture

To determine whether the formation of the amide halide is necessary for a reduction in hydrogen desorption temperature, an investigation was carried out using TPD-MS (section 2.5). Lithium amide and lithium hydride were hand ground with lithium bromide at different NH_2^- to Br^- ratios, heated at 2°C min^{-1} to 400°C and held for one hour. The gases given off were measured, and the hydrogen traces are shown alongside the halide-free system and the amide bromide in figure 5.5. No other gases were seen to be given off during the experiment. Therefore, even without initial formation of the amide, the halide present prevents the release of ammonia.

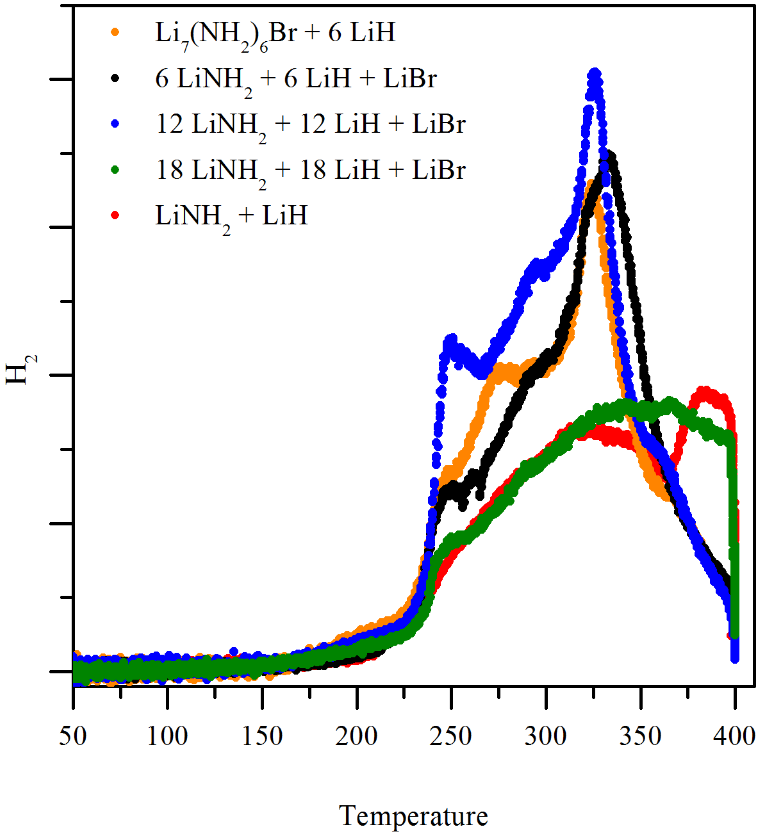

Figure 5.5: Hydrogen traces of different ratios of lithium amide, lithium hydride and lithium bromide, heated on the TPD-MS.

Addition of lithium bromide at both the 6 : 1 and 12 : 1 ratios increases the amount of hydrogen given off at lower temperatures. The effect of the bromide addition is minimal at the 18 : 1 ratio, as the hydrogen release profile is similar to that for $LiNH_2$. At the 6 : 1 ratio, the effect of pre-forming the amide bromide can be seen by comparing the black and orange traces: the shapes of the release profiles are slightly different, with an additional shoulder present in the dehydrogenation of $Li_7(NH_2)_6Br$. Apart from this small shoulder, the peak profiles are very similar. As the amide bromide is formed at 250°C, and this is only just above the lowest temperature of hydrogen release, it is reasonable to assume that the amide bromide is formed *in situ* during the TPD-MS experiment. The increased release of hydrogen for the 12 : 1 ratio is likely to be due to the greater theoretical hydrogen capacity of 5.26%, compared to 4.42% for the 6 : 1 system, because less bromide is present in the system. The similar peak shape suggests that the sample does not need to be present fully as $Li_7(NH_2)_6Br$ for the desorption properties to be affected, unlike the analogous chloride system.

The multiple peaks in the desorption trace was investigated in more detail for the 12 : 1 system by running the same experiment at different temperatures, chosen to match the series of peaks in the release profile. The hydrogen release profiles of these experiments are shown in figure 5.6. Both the sample heated to 350°C and that to 310°C showed only the imide bromide in the diffraction pattern, although the peaks were much broader in the sample taken to 310°C. The product of heating to 250°C showed peaks for the amide bromide, with some broadening towards the imide bromide positions, and also $LiNH_2$ peaks. Therefore after this time at 250°C, not all of the $LiNH_2$ has reacted to form the amide bromide.

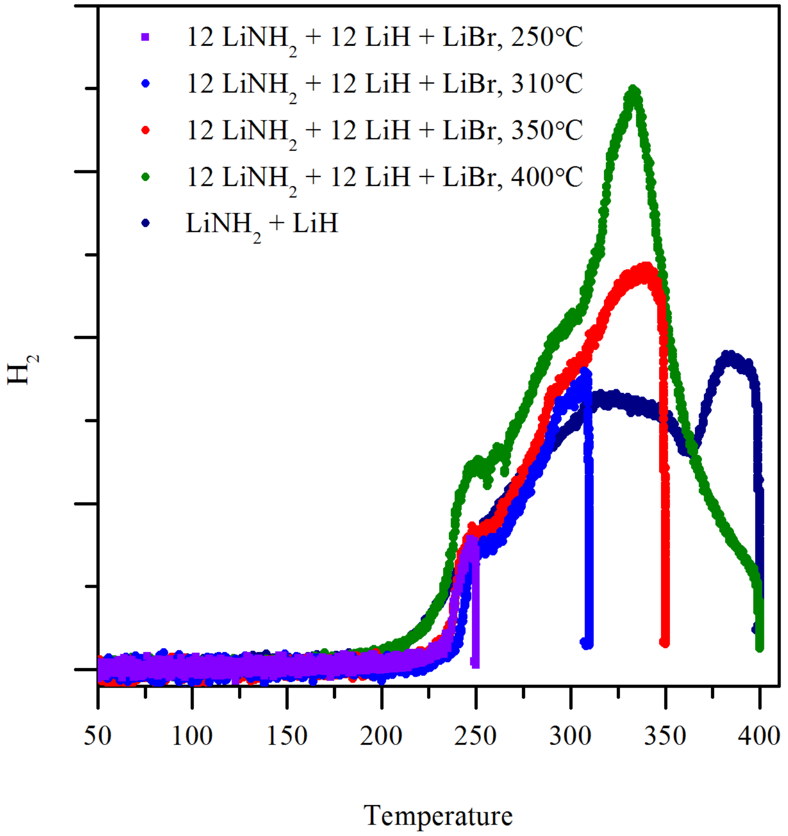

Figure 5.6: Hydrogen traces for the amide bromide system heated to different temperatures on the TPD-MS.

5.4.1 Deuterium cycling of the bromide system measured by powder neutron diffraction

A sample of the deuterated lithium amide bromide, $Li_7(ND_2)_6Br$, was studied under cycling with deuterium using powder neutron diffraction. To make the sample, $LiND_2$ was ground with LiBr and heated at 250°C for 12 hours. The product was confirmed using powder XRD to be the deutero-amide bromide and hand ground with LiD. The sample was loaded inside an argon-filled glove bag into a vanadium can which was sealed with indium wire. Data were recorded continuously, with a new scan taken every five minutes.

The sample was heated to 250°C under D_2 and, once at temperature, the gas was removed and data collected under vacuum. After one hour, the temperature was increased to 275°C. After eight hours under vacuum, the sample was put under 3 bar D_2 for five hours. The sample was again put under vacuum and, after three hours, 3 bar D_2 was applied. After four hours, with the temperature still at 275°C, the sample was again put under vacuum for three hours. The temperature was decreased to 250°C and 3 bar D_2 was applied for the remainder of the experiment.

A contour plot of the neutron diffraction patterns collected in the experiment is shown in figure 5.7. It shows that, when the sample was initially put under vacuum, it was only as the temperature is increased that the deutero-amide bromide peaks merged, showing the formation of the deutero-imide bromide phase. Dedeuteration of this system therefore did not occur at 250°C, but was facile at 275°C.

On application of 3 bar D_2 the neutron powder diffraction data showed the presence of an unknown phase. This was converted back to the deutero-imide bromide as the sample was again put under vacuum. On the second application of 3 bar D_2, the new phase was again observed, but after approximately three hours, the peaks corresponding to the newly observed phase decreased in intensity until they were no longer observed, and those of the

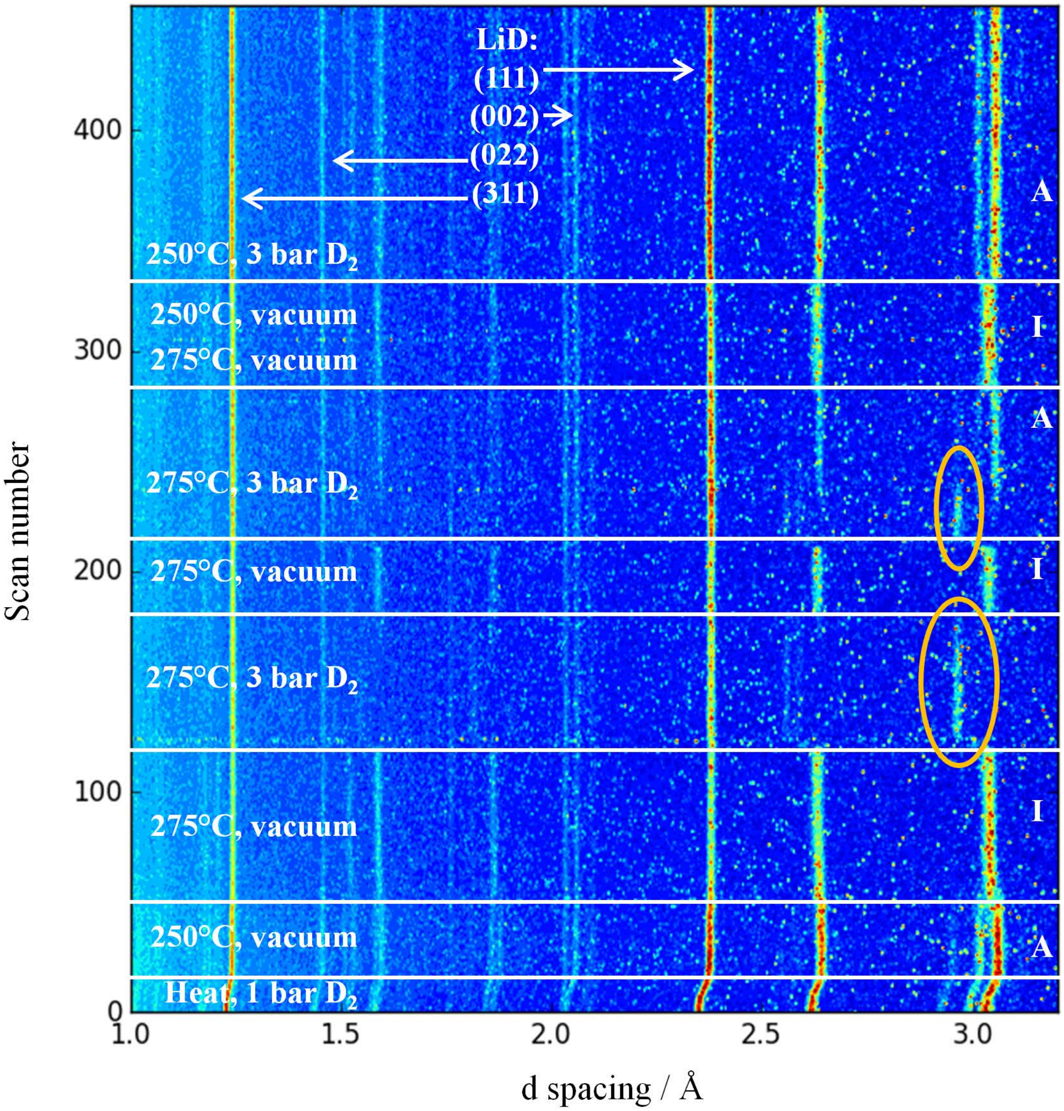

Figure 5.7: Contour plot of the neutron powder diffraction patterns collected during deuterium cycling of $Li_7(NH_2)_6Br$ on the POLARIS beamline. Peaks for the deutero-amide bromide (A), deutero-imide bromide (I) and LiD are labelled, and that of the new phase observed circled.

deutero-amide bromide were seen.

When data were collected under vacuum for a third time, the deutero-imide bromide was again seen to be formed. When D_2 was applied at the lower temperature of 250°C, the new phase was not observed, but instead peaks corresponding to the deutero-amide bromide were observed in the neutron powder diffraction pattern.

The lattice parameters of the bromide-containing phases were calculated from a bulk QPA of the neutron powder diffraction pattern and enabled analysis of the rate of deuterium release. During the initial dedeuteration, the lattice parameter of the deutero-amide bromide phase was seen to decrease linearly, as the deuterium is removed from the lattice. A linear fit to the data is shown in figure 5.8.

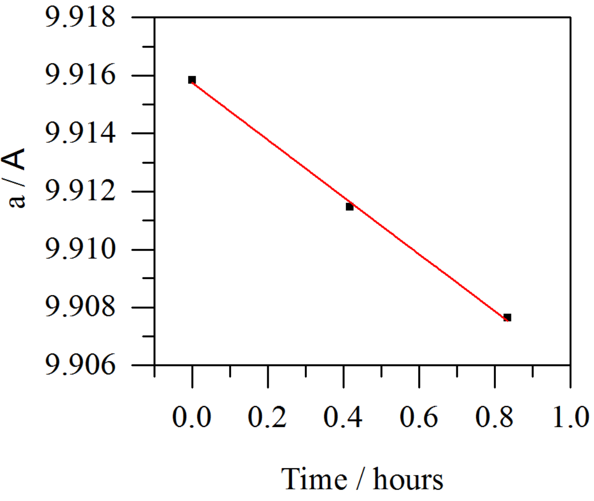

Figure 5.8: Linear fit to the lattice parameter, a for $Li_7(NH_2)_6Br$ when data was collected under vacuum at 250°C on the POLARIS beamline.

Once the temperature was increased to 275°C, and the deutero-imide bromide formed, the lattice parameter of this phase was seen to decrease. This decrease was modelled with both an exponential function, with a half life, τ, of 47(2) minutes, and the 1D and 3D diffusion models discussed in the previous chapter, as shown in figure 5.9. As for the chloride system, the fit was better to the exponential function than either of the diffusion models. The rate was higher than that of the chloride system, where τ was calculated to be 104(14) minutes.

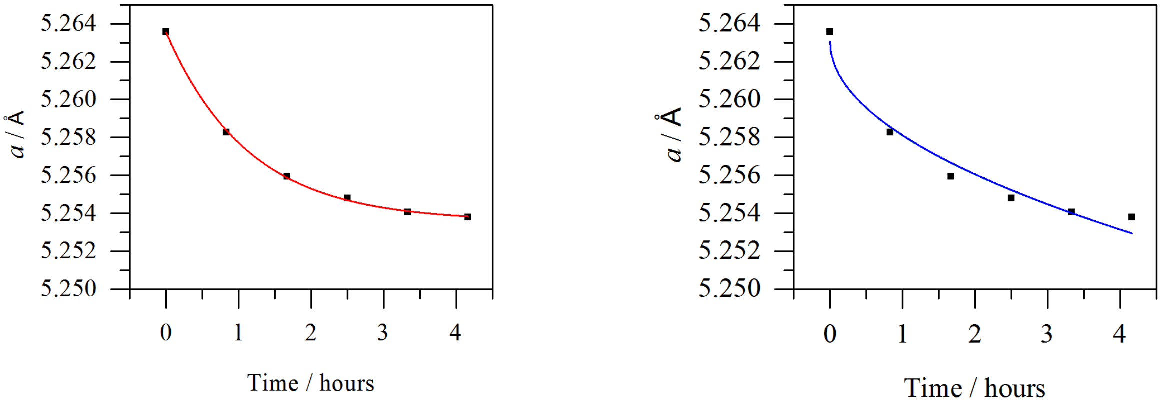

Figure 5.9: Lattice parameter of the Li$_{13}$(NH)$_6$Br during the initial dedeuteration at 275°C on the POLARIS beamline, along with an exponential function fit to the data (left, red, $r^2 = 0.9992$), and the 1D (right, green, $r^2 = 0.9684$) and 3D (right, blue, $r^2 = 0.957$) diffusion models which, in this case, are indistinguishable.

5.4.1.1 New Br phase

As described above, after deuterating at a D$_2$ pressure of 3 bar at 275°C, on redeuteration a new phase was observed in the neutron powder diffraction pattern, as circled in figure 5.7. In the d-spacing range visible using this experimental setup, only three peaks were seen for this new phase, at d-spacings of 2.56, 2.59 and 2.97 Å. Indexing these peaks to determine a structure was attempted, but unsuccessful and, because of this, attempts were made to synthesise this new phase in the laboratory.

A sample of Li$_{13}$(NH)$_6$Br was hydrogenated at 275°C under 5 bar H$_2$ (the lowest measurable pressure accessible using the hydrogenator described in section 2.6) for one, two and three hours. After one hour, peaks corresponding to the amide bromide were seen at a low intensity in the powder XRD pattern, with the imide bromide still the dominant phase. After two hours, the hydrogenation was complete, and the amide bromide was observed alone in the powder XRD pattern. The phase observed while cycling on POLARIS is not observed in the powder XRD patterns for any of these three experiments. To characterise this new phase, the effect of cycling on the structure of the sample was carried out using synchrotron radiation.

5.4.2 *Ex-situ* characterisation of the sample after cycling

After cycling the sample was measured using Raman spectroscopy to investigate whether any structural change had occurred during the cycling process. Figure 5.10 shows the Raman spectra of the sample after cycling, and the deutero-amide bromide starting material. It can be seen by comparison to the original deutero-amide bromide that, after cycling, there is no imide peak observed at around 2340 cm^{-1} in the Raman spectrum and therefore the sample is present in the deuterated form. The powder XRD pattern of the product after cycling confirms that the deutero-amide bromide is present, alongside lithium deuteride and a small percentage (≈5 wt%) of lithium oxide.

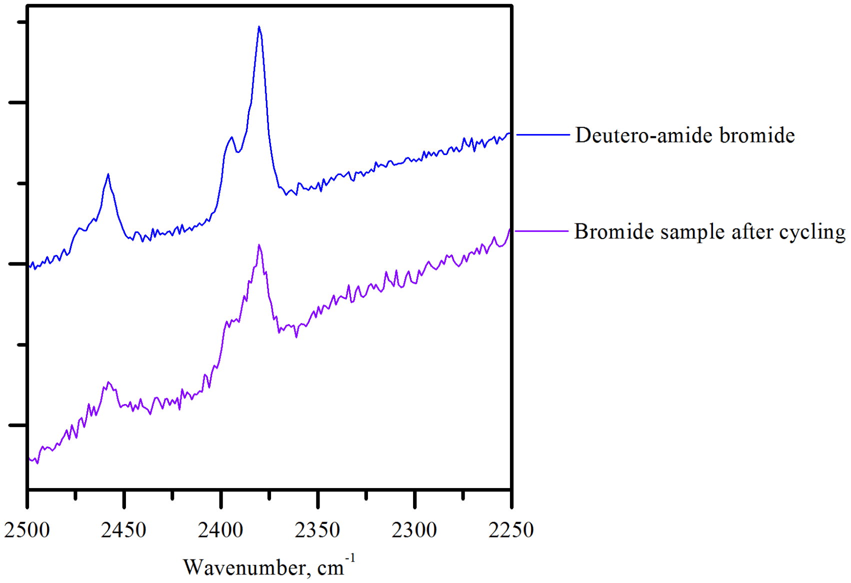

Figure 5.10: Raman spectra of samples of $Li_7(NH_2)_6Br$ before and after cycling on the POLARIS beamline.

5.4.3 Hydrogen cycling studied by synchrotron radiation

A sample of the lithium imide bromide $Li_{13}(NH)_6Br$ was studied under cycling with hydrogen using powder synchrotron X-ray diffraction. To form the sample, $LiNH_2$ was mixed with LiBr to form the amide bromide by heating at 250°C for 24 hours, and then the sample was dehydrogenated by heating to 400°C for 18 hours with LiH. The sample was loaded into a borosilicate capillary and then onto the low pressure gas cell at beamline I11. Scans were taken continuously, with a new scan taken every minute. Conditions were used to replicate those under which the new phase had been observed during cycling at the beamline POLARIS.

The sample was heated to 250°C under vacuum and once at temperature, 20 bar H_2 was applied. At t = 110 minutes, the sample was put under vacuum. After 45 minutes, the temperature was increased to 275°C, and then 350°C for 20 minutes. The sample was then returned to 275°C and at, t = 5 hours, 3 bar H_2 was applied. At t = 7.5 hours, the sample was put under vacuum for 80 minutes. The temperature was increased to 350°C and another of these cycles was then performed: the sample was taken under H_2 at 3 bar for 1 hour at 275°C (at t $\approx$ 9 hours) and then put under vacuum at 350°C (at t $\approx$ 10 hours). The temperature was increased further to 400°C for a short period, returned to 275°C and the sample hydrogenated under 3 bar H_2 once again (at t $\approx$ 15 hours) before being cooled and removed under 1 bar of helium.

A contour plot of the powder diffraction patterns taken during the experiment is shown in figure 5.11. It shows that, during the first hydrogenation under 20 bar H_2, the peaks corresponding to the amide bromide phase (labelled as ‘a’) were observed almost immediately and continued to grow in intensity over time. When data were collected under vacuum, the peaks for the amide bromide phase were seen to decrease in intensity. However, the peaks did not reduce to background level until the temperature was increased to 350°C.

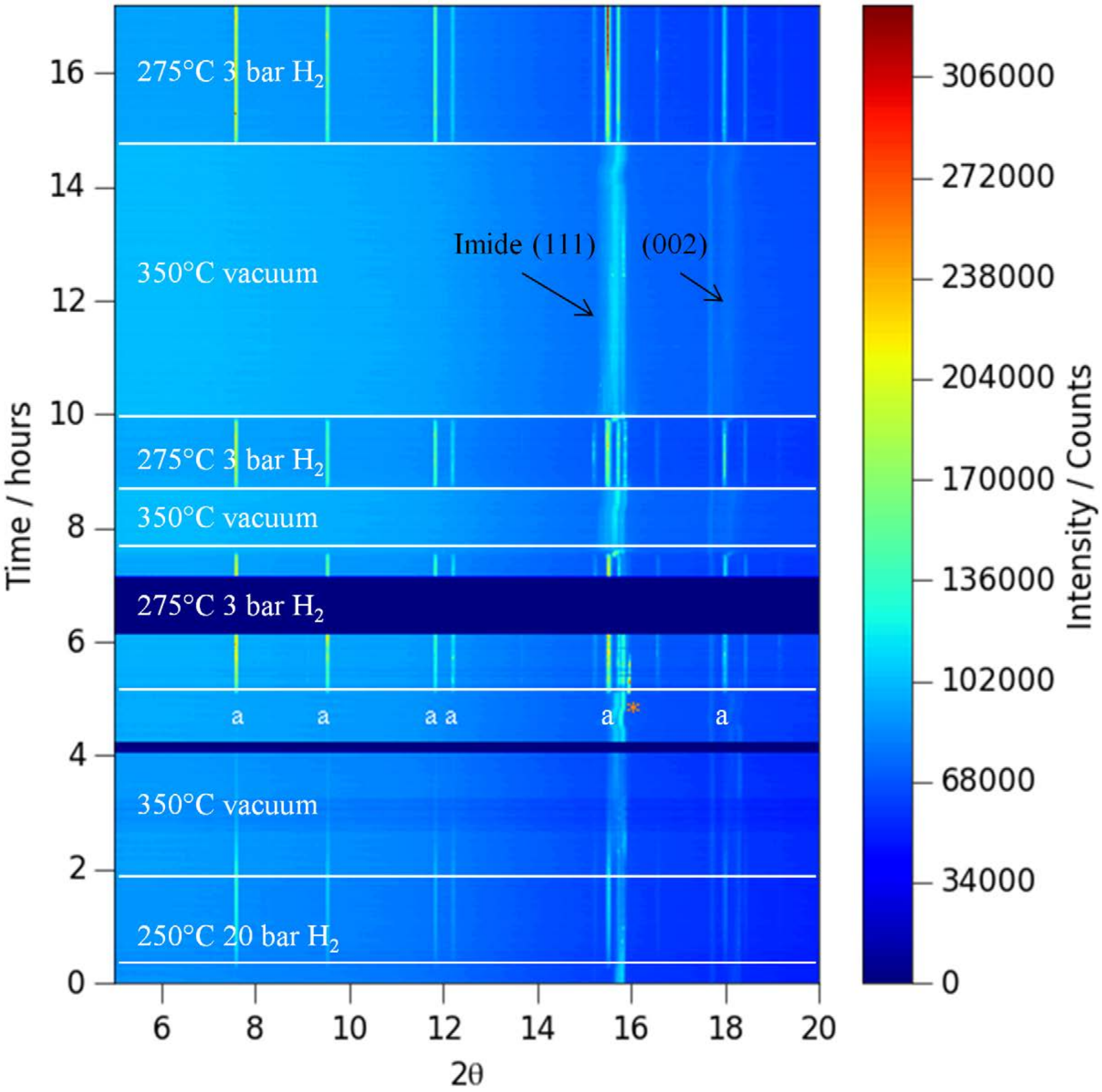

Figure 5.11: Contour plot of powder synchrotron XRD patterns for 2θ between 5° and 20° during the hydrogen cycling of $Li_{13}(NH)_6Br$ at beamline I11. An orange asterisk marks the peak observed for the unknown phase and 'a's label the (101), (110), (012), (021), (12-1) and (122) peaks of the amide bromide.

A lower pressure of 3 bar H_2 was then applied at 275°C, and the amide bromide peaks are again seen in the diffraction pattern. For a short period of time immediately after the hydrogen gas was applied, a peak is seen in the pattern that corresponds to the new phase observed during the experiment on the POLARIS beamline, shown in figure 5.11 by an asterisk. During the second cycle under the same conditions, the new phase was not observed, but the peaks of the amide bromide were seen to reduce and then grow in intensity as expected.

During the cycling experiment, the peaks for the imide bromide were seen to be very broad when compared to those of the amide bromide. A contour plot of the powder synchrotron patterns in the region of the (111) peak of the imide bromide and the (202), (211) and (003) peaks of the amide bromide is shown in figure 5.12. Compared to the chloride system, the peaks for the amide bromide are much more well defined, whereas the imide peaks are broad. The breadth of the peaks is determined by the variation in composition of the phases present. This observation therefore correlates with less compositional variation in the amide bromide system when compared to the amide chloride system and indicates a similar level of stoichiometric variation could be possible within the imide bromide structure.

In a similar way to the chloride system, a batch quantitative phase analysis (QPA) refinement was carried out using a template file containing the amide and imide bromide phases. Each raw file was fitted using the technique described in section 2.3.1 and the refined lattice parameters, weight percentages and statistical R_{wp} and R_{exp} were the outputs. The weight percentages of the two phases are shown against scan number in figure 5.13. This shows the cycling between the two phases during the changing conditions. One peak of an unknown phase was observed at a d-spacing of 2.98 Å during cycling, but a lack of a structure prevented its inclusion in this refinement.

The statistical parameters R_{wp} and R_{exp} are shown for the same data set in figure 5.14, and show that the anomalous points in figure 5.13 are outliers when considering the statistical fit. The quality of the fit is lower when the amide phase is the dominant phase, shown by the higher R_{wp} and R_{exp} values when this phase is present at a higher percent. This could be due to the complex peak shapes observed for the amide phase reducing the quality of the fit.

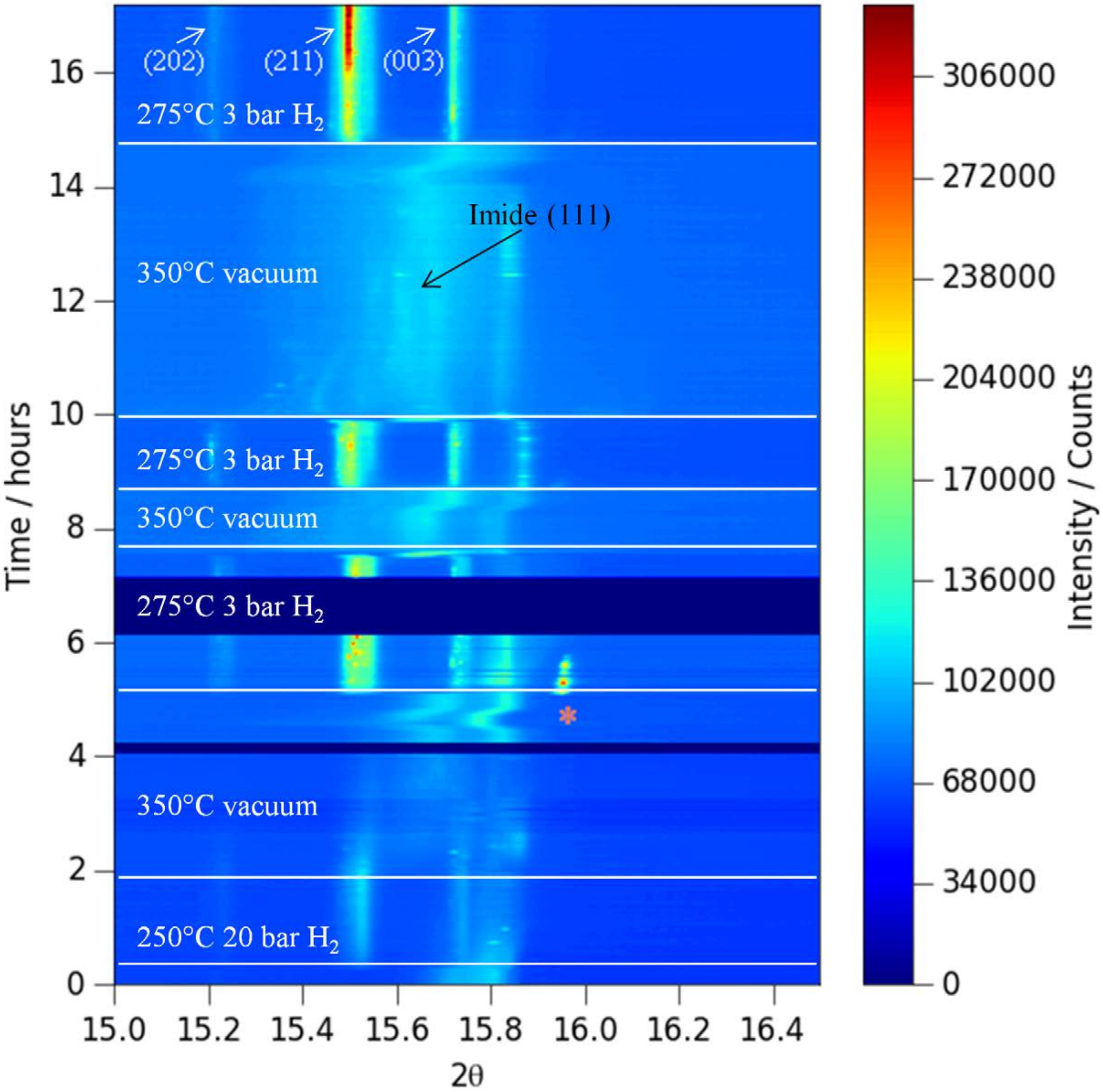

Figure 5.12: Contour plot of powder synchrotron XRD patterns for 2θ between 15° and 16.5° during the hydrogen cycling of $Li_{13}(NH)_6Br$ at beamline I11 showing how the peak shapes change over time.

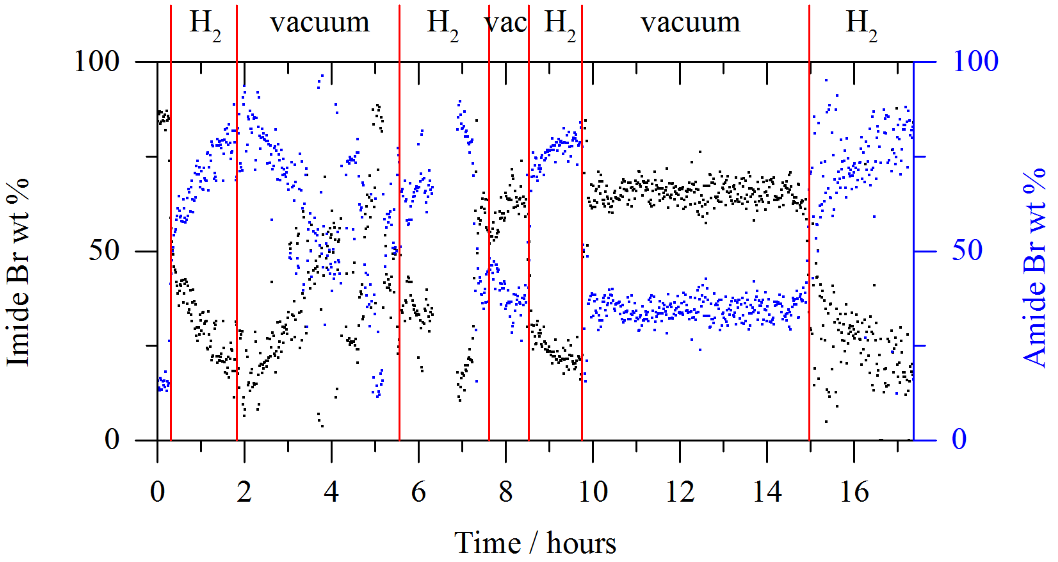

Figure 5.13: Weight percentages of the amide and imide bromide phases during hydrogen cycling on the I11 beamline.

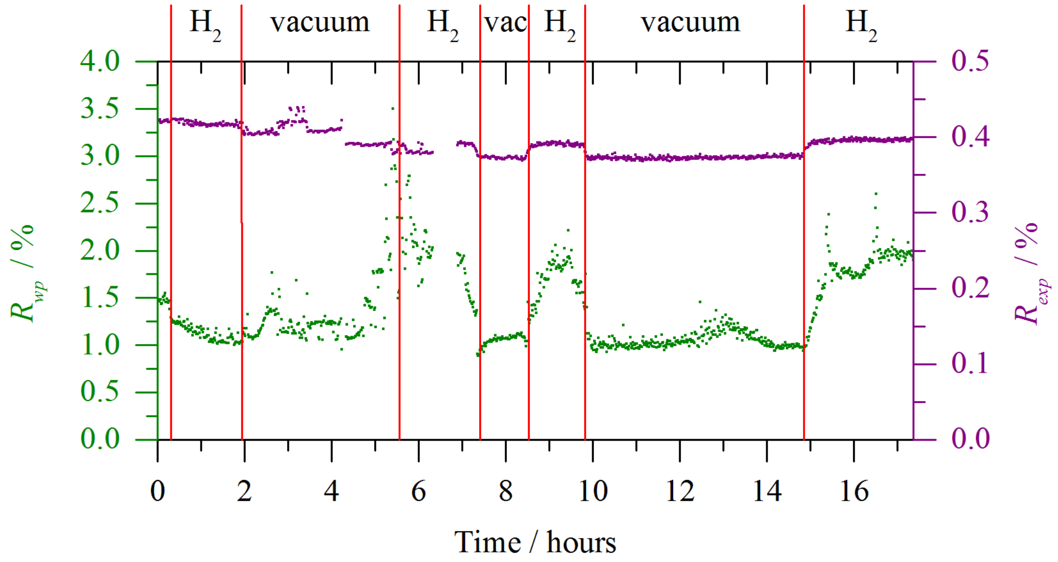

Figure 5.14: Statistical parameters for the batch QPA of the amide and imide bromide phases during hydrogen cycling on the I11 beamline.

5.4.4 Deuterium cycling and gravimetric measurements

The IGA^n sample environment was used simultaneously with neutron powder diffraction to measure the hydrogen content of the phases observed. A 612 mg sample of the mixture of $Li_7(ND_2)_6Br$ and LiD, previously cycled on the POLARIS beamline, was loaded onto the microbalance of the IGA^n and put into the POLARIS beamline. Data were recorded continuously, with a new scan taken every five minutes.

The sample was heated to 325°C under vacuum although, after reaching this temperature, a failure of the computer system caused the temperature to drop. It was then re-set to 275°C and the D_2 pressure set to 10 bar, at 100 mbar min^{-1}. After six hours, a restart of the system was required, causing the temperature to drop to 210°C. The temperature and pressure were reset to 250°C and 10 bar D_2. After another three hours, the sample was put under vacuum, and after another three hours, the temperature was increased to 300°C.

After another two hours under vacuum, the temperature was reduced to 250°C and 10 bar D_2 was applied. The sample was left for an hour under these conditions and then cooled and removed from the beamline. The temperature, pressure and mass data recorded by the IGA^n are shown alongside a contour plot of the neutron diffraction data in figure 5.15. The period between approximately six to twelve hours, in which no IGA^n data was collected, appears a straight line between the values on either side.

Dehydrogenation of the sample to $Li_{13}(ND)_6Br$ would equate to a D_2 loss of 8.29 wt% of the sample. During the initial dehydrogenation, the sample mass decreased by 72.6 mg, equivalent to 11.9 wt%. The neutron powder diffraction patterns show the deutero-amide peaks merging as the imide bromide is formed.

On application of deuterium, the mass of the sample began to increase. After six hours, the sample weight had increased by 16.8 mg, just over 20% of the weight lost on dedeuteration. The diffraction patterns show the appearance of a new phase. However, a problem

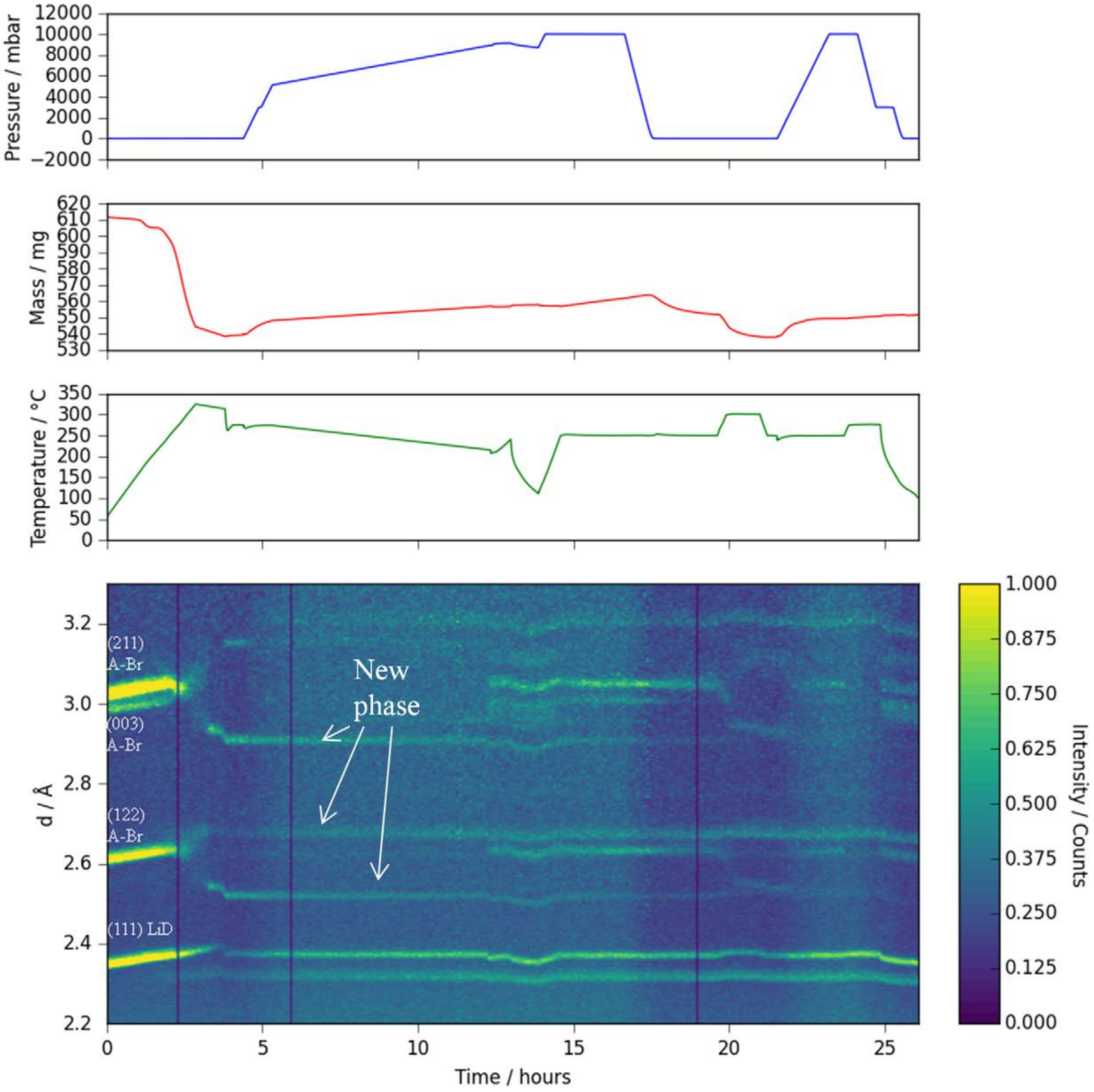

Figure 5.15: IGA^n data and contour plot of neutron diffraction patterns collected on the POLARIS beamline with peaks for LiD and the deutero-amide bromide (A-Br) labelled.

with the computer system caused the IGA^n data for this period not to be collected. After this period, the sample mass continued to increase slowly.

After taking the sample under vacuum at 250°C, the mass decreased by 12 mg, stabilising at 552 mg. This was not as low as had been observed during the previous cycle and so the temperature was increased to 300°C, prompting a further mass loss of 13.6 mg. The first stage of this dedeuteration was modelled using an exponential decay model and 1D and 3D diffusion models, as shown in figure 5.16. The 1D diffusion model did not converge for this data set, and the exponential function gave a marginally better fit to the data than the 3D diffusion model. The calculated half life for the deutero-amide bromide at 250°C was 30.5(1) minutes. Analysis of the unit cell parameter of the deutero-imide bromide on dedeuteration at 275°C during the previous cycling experiment on the POLARIS beamline gave a half life of 47(2) minutes. The faster rate observed during this experiment is likely to be due to the fact that the sample had been previously cycled.

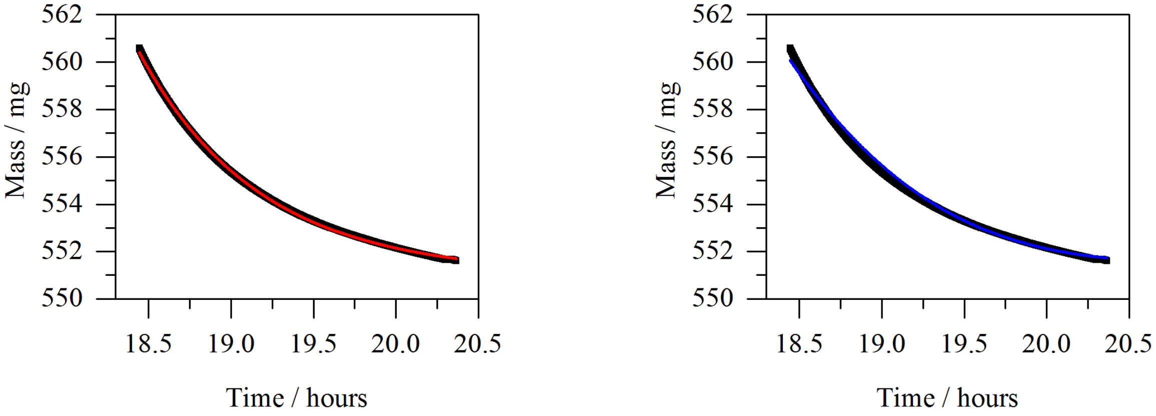

Figure 5.16: Sample weight for sample of $Li_7(ND_2)_6Br$ + 6 LiD during dedeuteration on the IGA^n on the POLARIS beamline, along with an exponential function fit to the data (left, red, $r^2 = 0.9994$), and the 3D (right, blue, $r^2 = 0.9955$) diffusion model.

Under 10 bar D_2 at 250°C, the sample mass increased by 11.1 mg to 549 mg. After stabilisation, attempts were made to further the deuteration by using higher temperatures and lower pressures, but the final mass achieved was 551 mg, 61 mg lower than the starting mass of the sample. This capacity loss could be due to ammonia loss or sample morphology, as in the chloride system, and is not recoverable under application of a higher pressure of D_2. Unlike the first cycle in the chloride system, however, the full mass was never regained on deuteration. Loss of ND_3 could therefore be occurring on either dedeuteration, deuteration, or both. Using the same method as applied to the chloride system in the previous chapter, the sample mass loss was separated into reversible mass loss, assumed to be D_2 and irreversible mass loss, assumed to be ND_3, as shown in figure 5.17.

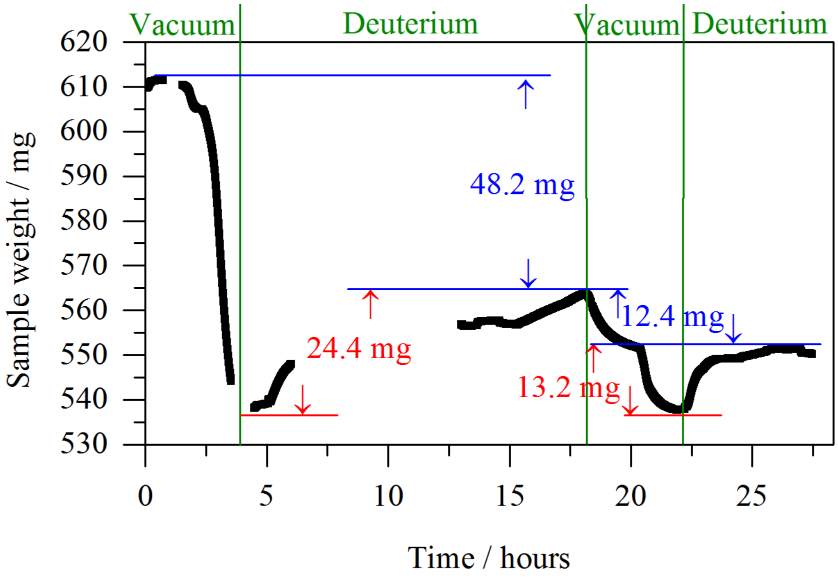

Figure 5.17: Sample weight for sample of $Li_7(ND_2)_6Br$ + 6 LiD during cycling with D_2 on the IGA^n on the POLARIS beamline.

Once separated, these mass losses were converted to relative molar fractions, displayed in table 5.4. The molar fraction of D_2 would be expected to be six on each dehydrogenation, but only half this was achieved, with a simultaneous loss of 1.7 moles of ND_3. The second cycle shows an even smaller release, of a quarter of the expected D_2 loss, with an accompanying loss of approximately one third of a mole of ND_3. A detailed IGA^n investigation coupled with a mass spectrometer would prevent the need for this kind of speculative analysis and would be a crucial piece of further work.

Total Mass Loss / mg	Mass loss due to D_2 / mg	Relative molar fraction of D_2	Mass loss due to ND_3 / mg	Relative molar fraction of ND_3
72.6	24.4	2.9	48.2	1.7
25.6	13.2	1.6	12.4	0.32

Table 5.4: Mass losses and molar fractions for a sample of $Li_7(ND_2)_6Br$ + 6 LiD for the dehydrogenation cycles on the IGA^n measured on the POLARIS beamline.

5.4.5 New phase in the lithium amide bromide system

A new phase was observed in the diffraction pattern of the bromide system during all of the three beamline cycling experiments. In the initial neutron diffraction experiment on the POLARIS beamline, peaks at d-spacings of 2.56, 2.59 and 2.97 Å were observed when the sample was exposed to 3 bar deuterium at 275°C. Under the same conditions on the second cycle, the same phase was observed in the diffraction pattern. However on this occasion, after three hours, the peaks of this phase decreased and those of the amide bromide phase were seen to appear and grow in intensity. It was also observed at a low intensity in the starting materials used for the experiment.

During the experiment on the synchrotron beamline I11, a peak of the new phase at a d-spacing of 2.98 Å was observed alongside the amide bromide when 3 bar H_2 was applied at 275°C. The peak then decreased in intensity until it was no longer observed in the pattern after approximately 30 minutes. The similar d-spacing suggests that this is the same phase that was observed during the first experiment.

For the experiment carried out using the IGA^n on the POLARIS beamline, peaks at d-spacings of 3.15, 2.91, 2.68 and 2.52 Å were first observed under vacuum when the temperature dropped suddenly from 350°C to below 275°C after a significant (11 wt%) mass loss from the sample had occurred. After the temperature equilibrated to 275°C and 10 bar D_2 applied, these peaks remained present in the neutron diffraction pattern. The intensity of the peaks were seen to decrease, coinciding with an increase in intensity for the peaks corresponding to LiD. A sudden temperature drop caused the deutero-amide bromide peaks to become visible in the pattern, although the peaks of the new phase remained present. They remained throughout the experiment, until data was collected under vacuum and the temperature raised to 300°C.

By considering the d-spacings of the peaks and the conditions under which they are observed, it appears as though the phase observed in the first two experiments is the same phase: formed on low pressure hydrogenation and transforms to the amide bromide over time. However, the peaks observed in the final experiment did not have the same d-spacings and were present throughout almost all of the experiment. These results suggest that this is a different phase than that observed in the previous two experiments, and could be formed by loss of ND_3 from the sample. A thorough laboratory gravimetric analysis combined with mass spectrometry and structural characterisation after each half cycle would be very informative, and could help to determine the structure and hydrogen content of these new phases.

5.5 The lithium amide iodide, $Li_3(NH_2)_2I$

5.5.1 TPD-MS of a lithium amide/ lithium iodide mixture

An equivalent set of TPD-MS experiments to those described in section 5.4 were carried out using lithium iodide, and the hydrogen release traces are shown in figure 5.18. As observed for the chloride and bromide systems, no ammonia was observed. For the only known amide iodide, $Li_3(NH_2)_2I$, the stoichiometric amide to iodide ratio is two to one. The hydrogen release traces for this experiment show that addition of lithium iodide at both a 12 : 1 and 18 : 1 ratio had a small effect on the desorption when compared to $LiNH_2$, with the peak of hydrogen release occurring at lower temperature. However, it was at the 6 : 1 ratio where the shape of the release profile changed dramatically, with hydrogen release starting at just over 100°C. For the other halide systems, the improvements were seen at a lower halide level than for this system. The need for higher halide content in this system before an improvement in the desorption properties is observed correlates with the stoichiometry of the amide iodide being more halide rich than for the other halides. However, it does show improvements to the hydrogen release properties below the level that is seen to be accommodated within the amide iodide structure.

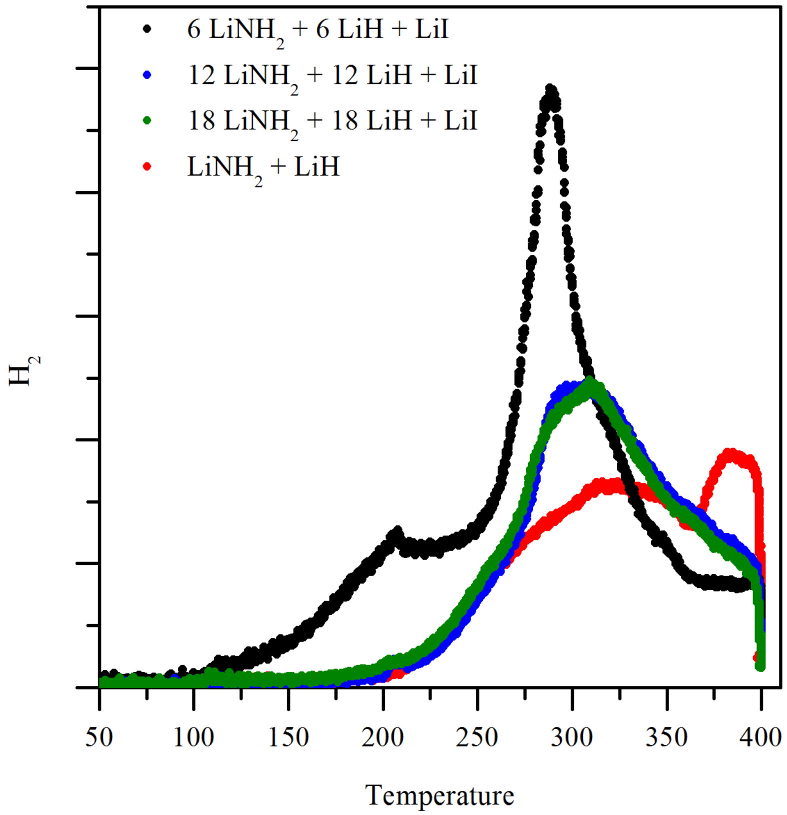

Figure 5.18: Hydrogen traces of different ratios of lithium amide, lithium hydride and lithium iodide, heated on the TPD-MS.

5.5.2 Hydrogen cycling of $Li_3(NH_2)_2I$ studied by synchrotron radiation

A sample of the lithium amide iodide, $Li_3(NH_2)_2I$, was studied under cycling with hydrogen using powder synchrotron X-ray diffraction. To form the sample, $LiNH_2$ was heated with LiI at 150°C for twelve hours. The sample was ground with LiH and loaded into a borosilicate capillary and then onto the low pressure gas cell at beamline I11. Scans were taken continuously, with a new scan taken every minute.

The sample was heated under vacuum to 400°C and held until t = 6 hours. After this time, the sample temperature was reduced to 250°C and 20 bar of H_2 applied. After 30 minutes, the sample was cycled once more: under vacuum for one hour at 400°C, under 20 bar H_2 for 40 minutes at 250°C and then data collected under vacuum again at 400°C. The pressure of hydrogenation was reduced to 3 bar at t = 10 hours and the sample left for 150 minutes. For the final dehydrogenation, at t = 13.5 hours the temperature was set to 300°C and the sample left for 270 minutes before the temperature was increased to 400°C to complete the dehydrogenation.

A contour plot of the powder diffraction patterns taken during the experiment is shown in figure 5.19. Initially, an impurity was observed in the powder XRD pattern, but this was not present after heating. Preliminary refinement of this phase was carried out by Dr. Phil Chater, and thought to be a C2221 structure with lattice parameters a = 14.533(3) Å, b = 4.5231(5) Å and c = 6.097(1) Å.

The XRD patterns show that, during the first dehydrogenation, the amide iodide peaks decreased until they were no longer present, and were replaced with peaks due to the imide iodide. The peak in the imide iodide pattern at approximately $2\theta = 13°$ was seen to change over time as new satellite type peaks appeared in the pattern and then merged into the (110) peak, as shown in figure 5.20. These satellite peaks appear in the diffraction pattern from the direction of the amide iodide, and so could be due to a less dehydrogenated part of the

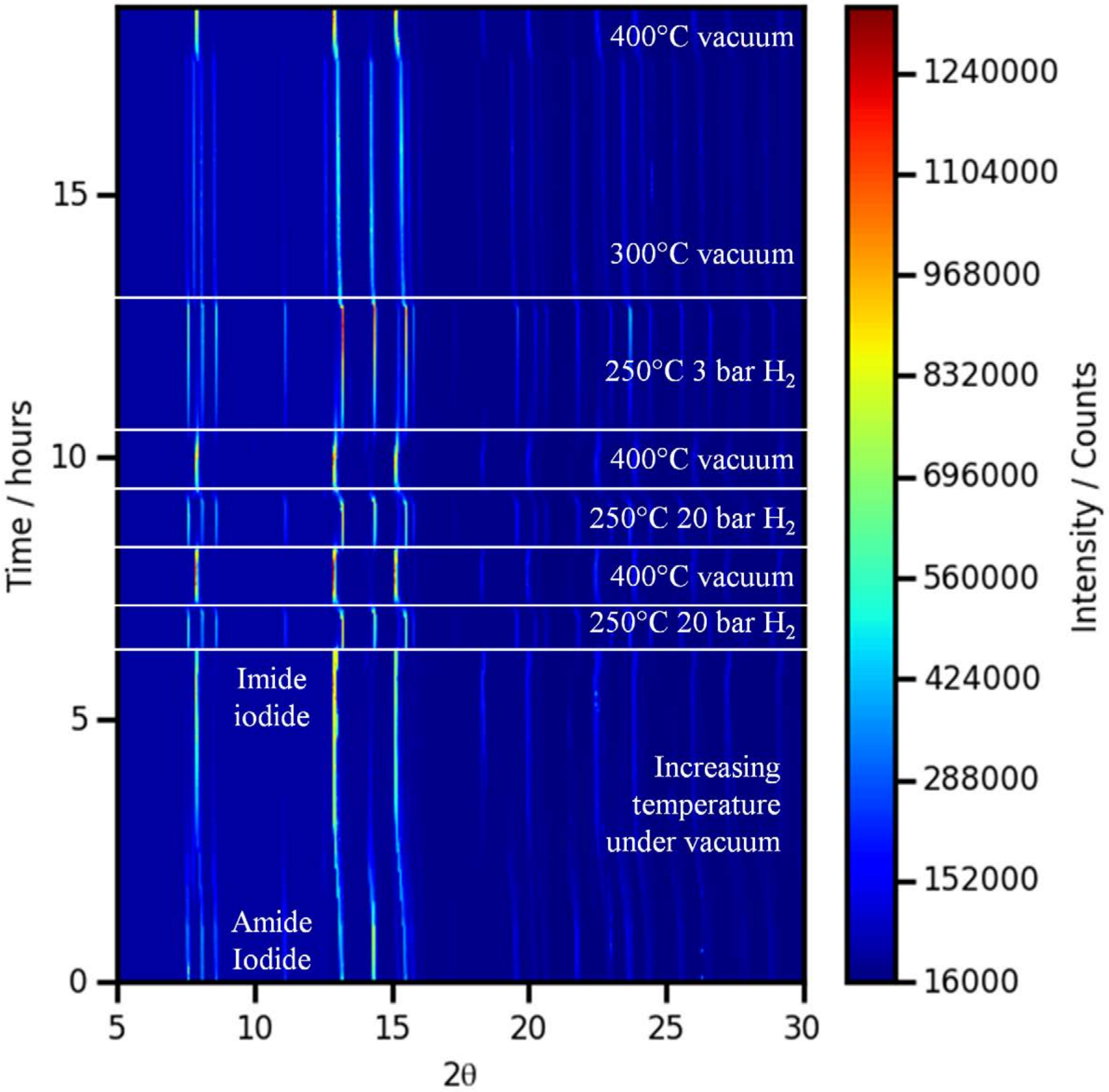

Figure 5.19: Contour plot of synchrotron powder diffraction patterns during hydrogen cycling of $Li_3(NH_2)_2I$ on beamline I11.

sample coming into the beam. On application of H_2, the amide iodide peaks were almost immediately observed in the diffraction pattern. During further cycles, the imide iodide and amide iodide peaks changed intensity as expected.

As for the chloride and bromide equivalents, a batch quantitative phase analysis (QPA) re-

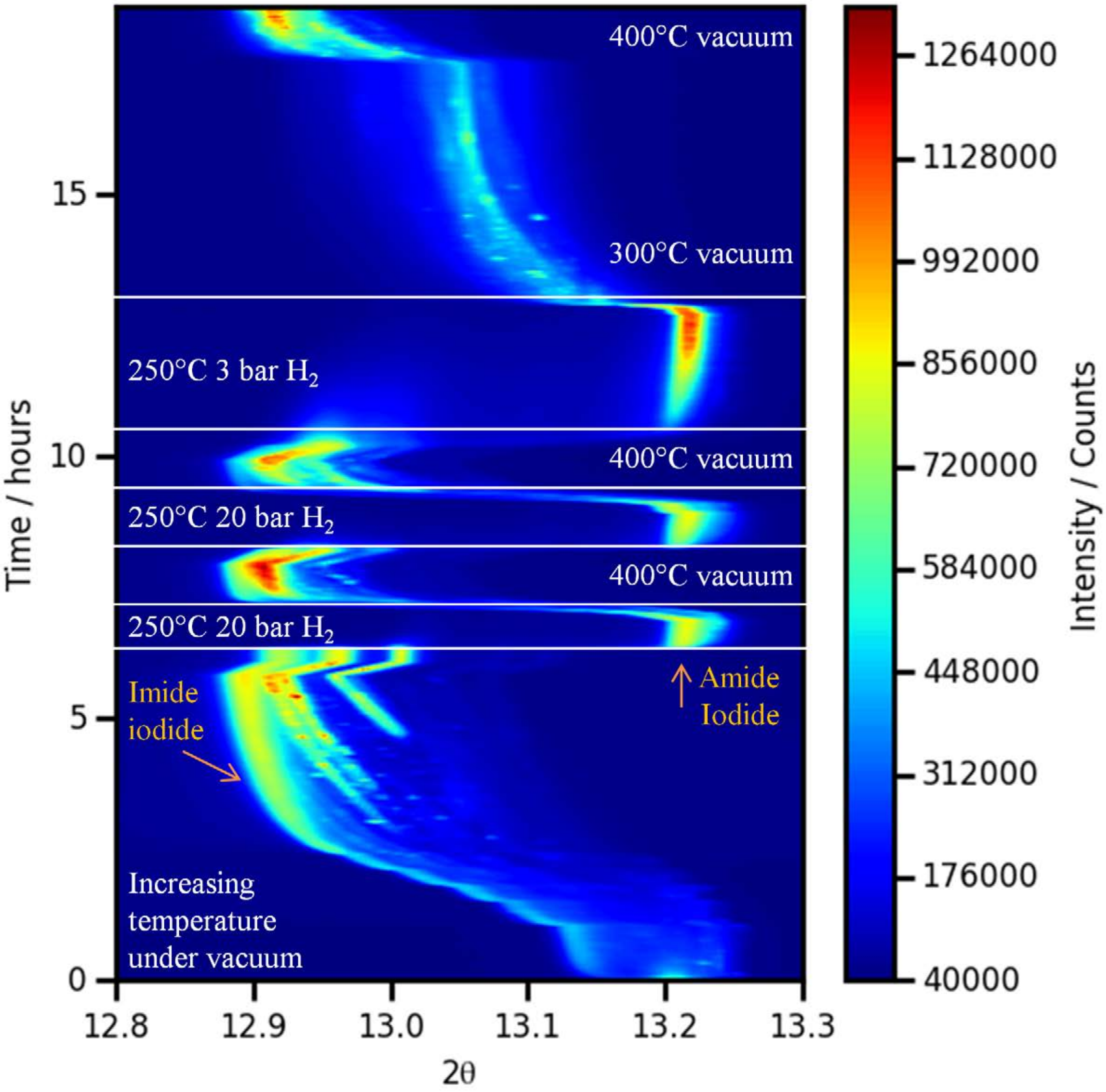

Figure 5.20: Contour plot of synchrotron powder diffraction patterns for 2θ between 12.8° and 13.3° during hydrogen cycling of $Li_3(NH_2)_2I$ on beamline I11 showing the merging of satellite peaks into the imide iodide (110) peak.

finement was carried out using a template file containing the amide and imide iodide phases. The weight percentages of the two phases are shown against scan number in figure 5.21. This shows the cycling between the two phases during the changing conditions. The statistical parameters R_{wp} and R_{exp} are shown for the same data set in figure 5.22.

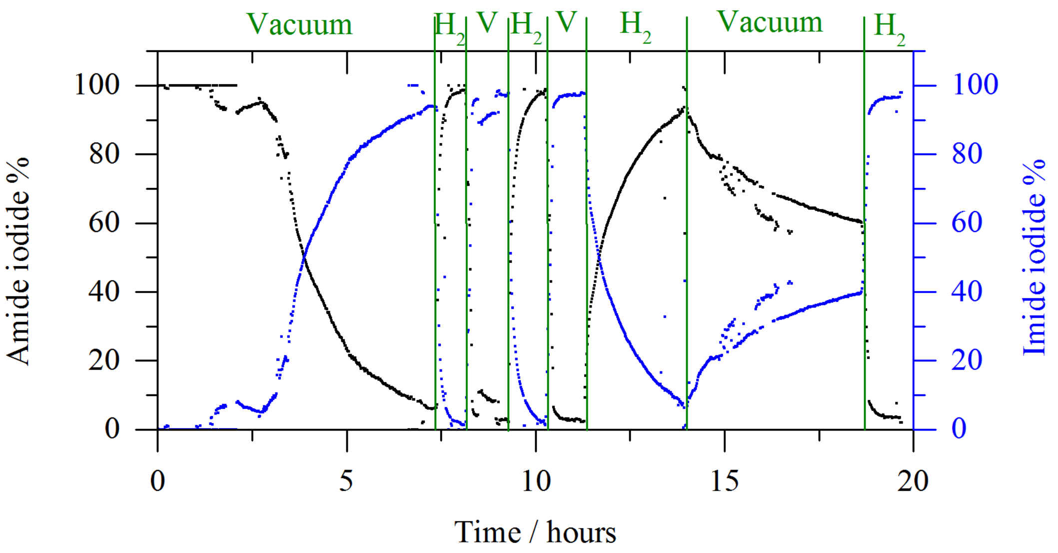

Figure 5.21: Weight percentages of the amide and imide iodide phases present during cycling of $Li_3(NH_2)_2I$ under hydrogen and vacuum on beamline I11.

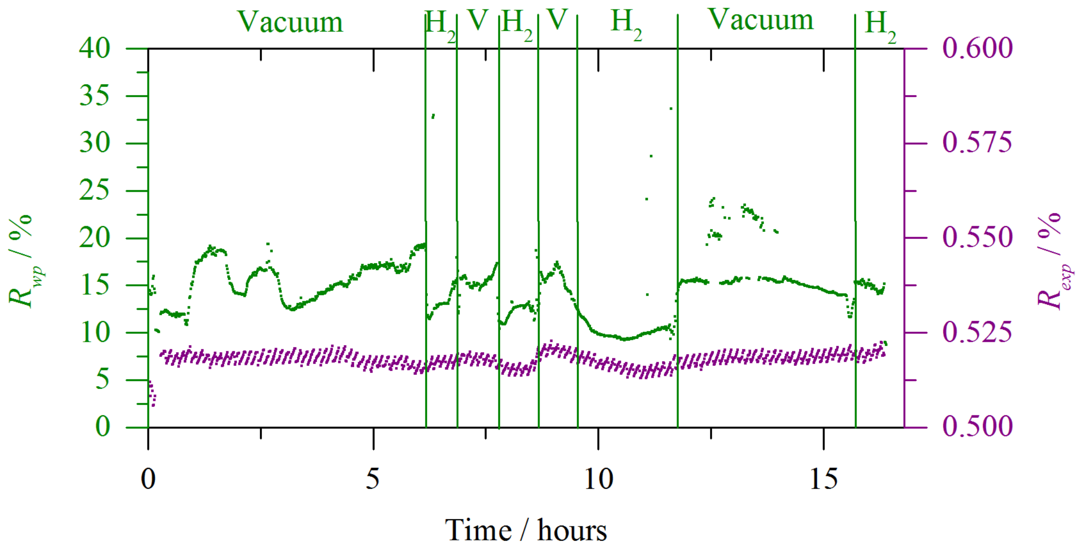

Figure 5.22: Statistical parameters for the batch QPA of the amide and imide iodide phases during hydrogen cycling on the I11 beamline.

5.5.3 Deuterium cycling and gravimetric measurements

The IGA^n sample environment was used simultaneously with neutron powder diffraction to understand the hydrogen content of the phases observed during cycling with deuterium. Data were recorded continuously, with a new scan taken every five minutes. The sample was heated to 250°C under vacuum, exposed to 3 bar of D_2 at a rate of 200 mbar min^{-1} and left at this pressure for three hours before data were collected under vacuum. After 30 minutes, the temperature was increased to 400°C for two hours and then cooled to 250°C. Once at temperature, the D_2 pressure was set to 3 bar and the sample left for eight hours. Data were then collected under vacuum, and the temperature increased in stages to 275, 300 and then 400°C. After an hour at 400°C, the D_2 pressure was set to 10 bar and the temperature reduced to 200°C. After an hour, the pressure was removed, the sample cooled and removed from the beamline. The temperature, pressure and mass data recorded by the IGA^n are shown alongside a contour plot of the neutron powder diffraction data in figure 5.23.

Complete deuteration of $Li_5(ND)_2I$ would equate to a gain of 3.65 wt%. During the first deuteration, the sample mass increased from 781 mg to 862 mg, the equivalent of 10.4 wt%. The neutron diffraction pattern showed the deutero-imide iodide peaks decreasing in intensity, and then the appearance of both the deutero-amide iodide phase and another, unknown, phase with peaks observed at d-spacings of 2.54 and 2.94 Å. When data were collected under vacuum, the mass decreased to below that of the starting sample, stabilising at 746 mg. The neutron diffraction pattern showed the deutero-amide iodide peaks, and those of the unknown phase, decreasing in intensity and those of the deutero-imide iodide appearing.

The second deuteration caused the sample to gain 32 mg, bringing it up to 778 mg, a gain of 4.3 wt% bringing the mass close to the starting mass of the sample. This time, the deutero-amide iodide peaks are seen to appear without the presence of the unknown phase. When data were collected under vacuum for a second time, the sample mass decreased to 757 mg and

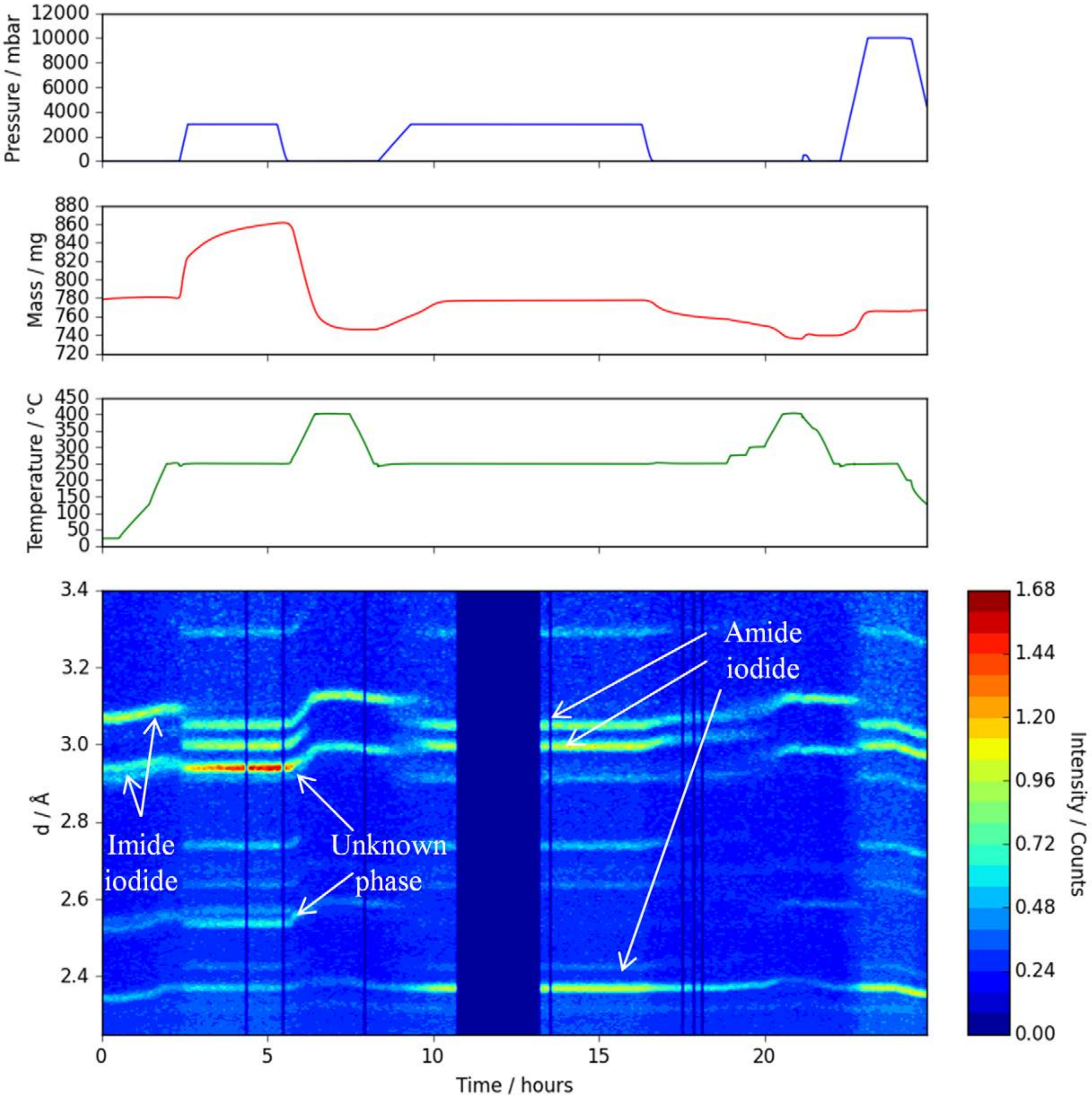

Figure 5.23: IGA^n data and contour plot of neutron diffraction data of $Li_3(NH_2)_2I$ collected on the POLARIS beamline.

the deutero-amide iodide peaks were still weakly visible in the neutron powder diffraction pattern. During this time, the mass loss was modelled using an exponential decay function and the 1D and 3D diffusion models, and the fits are shown in figure 5.24. The exponential function gives a half life of 31.5(1) minutes although, for the first time in this investigation, the fit to the 3D diffusion model has slightly better statistics than the exponential.

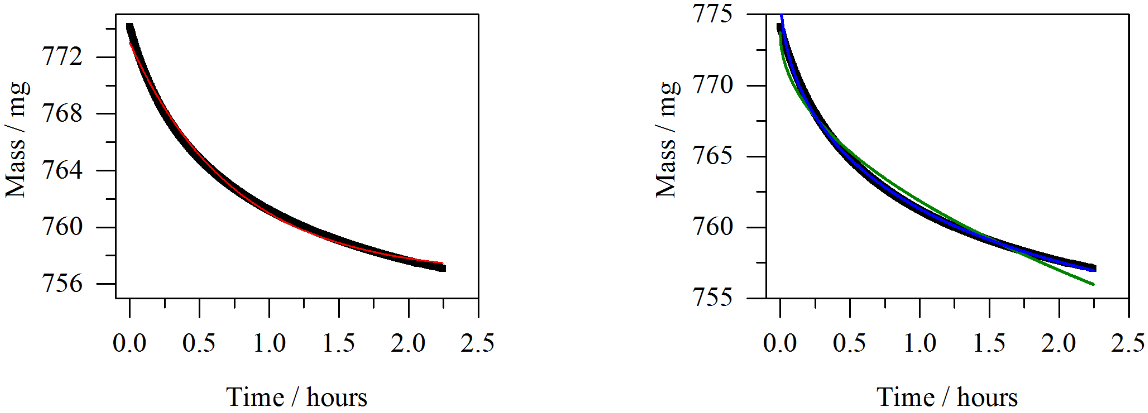

Figure 5.24: Sample weight for sample of $Li_3(NH_2)_2I$ during dedeuteration on the IGA^n on the POLARIS beamline, along with an exponential function fit to the data (left, red, $r^2 = 0.9965$), and the 1D (left, green, $r^2 = 0.9784$) and 3D (right, blue, $r^2 = 0.9983$) diffusion models.

After the temperature was increased, the mass decreased to 736 mg and the deutero-imide iodide was again seen in the diffraction pattern. Attempts to regain the original sample mass by applying 10 bar of D_2 resulted in a gain of 4.1 wt%, giving a final mass of 766 mg. The deutero-amide iodide was observed in the diffraction pattern, but the unknown phase was not seen under these conditions.

The initial uptake of more than the theoretical maximum D_2 uptake could be due to either the initial sample being in a more dehydrogenated form than the imide, or the application of D_2 causing over-deuteration, possibly by the formation of a phase containing ND_3. Ammoniates have been observed in metal borohydride systems of the form $M(BH_4)_m(NH_3)_n$,[147] and are formed by ball milling under ammonia.[148] The uptake of ammonia by lithium halides has been studied by pressure-composition isothermal measurements, although LiI was not studied.[149] LiCl, LiBr and NaI were all seen to take up ammonia and it was found that materials with a smaller electronegativity difference between the cation and anion exhibited a much lower equilibrium pressure, although NaI did not follow this trend. It is, therefore, possible that deuteration of the amide iodide led to ND_3 to be produced and subsequently captured by the amide iodide, rather than reacting with LiD. This would suggest that the unknown phase present after this mass uptake is of the form $LiI(NH_3)_n$. However, with only one peak present in the powder neutron diffraction pattern, structural characterisation of this phase is not possible.

A batch quantitative phase analysis (QPA) refinement was carried out using a template file containing the deutero-amide and deutero-imide iodide phases and LiD. Each raw file was fitted using the technique described in section 2.3.1 and the refined lattice parameters, weight percentages and statistical R_{wp} and R_{exp} were the outputs. The weight percentages of the two phases are shown against scan number in figure 5.25, showing the cycling between the phases during the changing conditions. The statistical parameters R_{wp} and R_{exp} are shown for the same data set in figure 5.26.

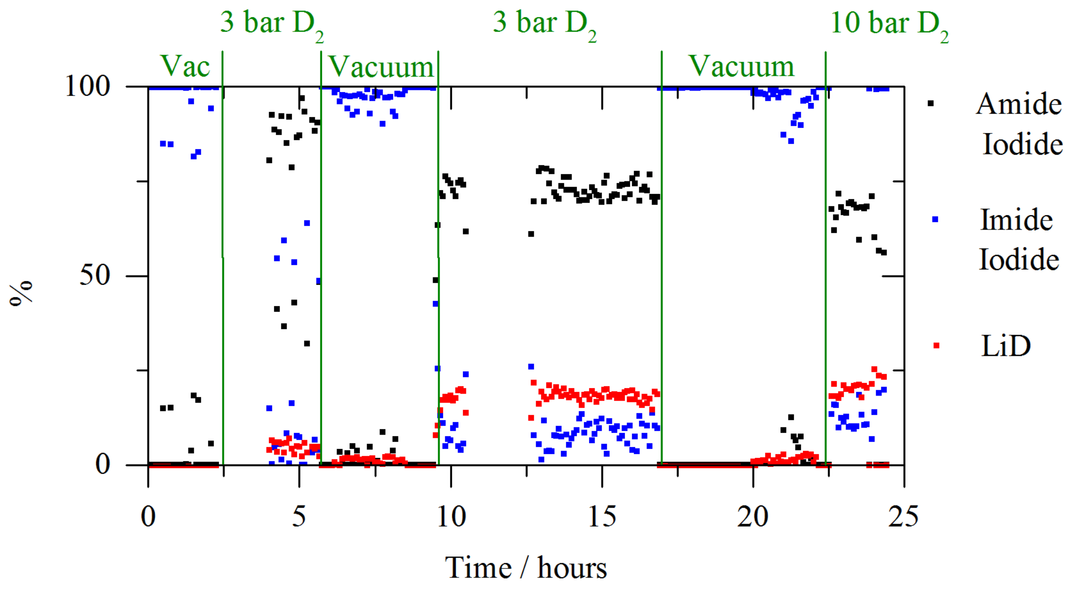

Figure 5.25: Weight percentages of the deutero-amide and deutero-imide iodide phases during hydrogen cycling on the POLARIS beamline during cycling in the IGA^n sample environment.

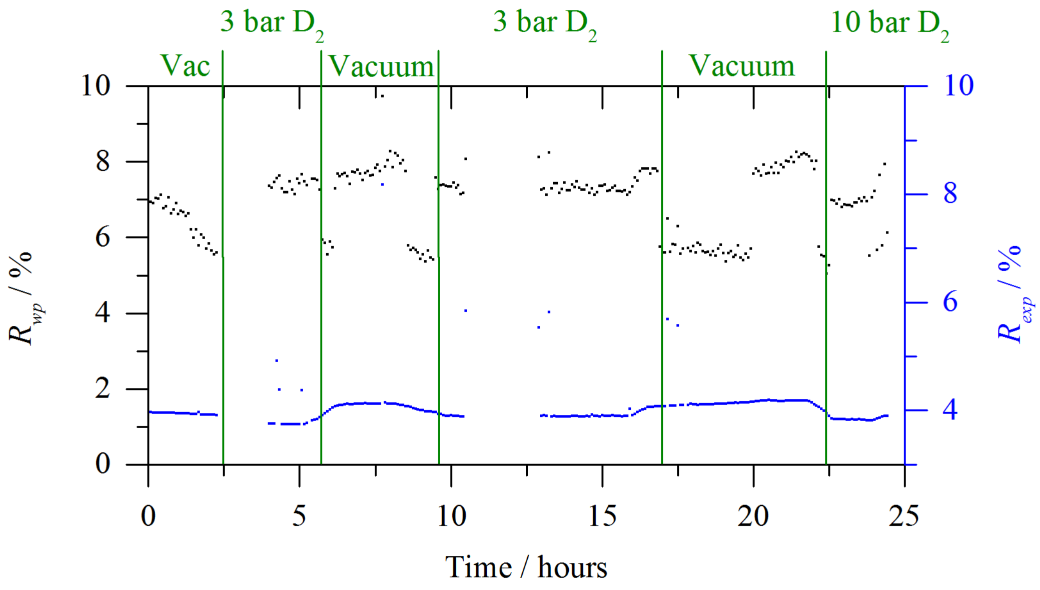

Figure 5.26: Statistical parameters for the batch QPA of the deutero-amide and deutero-imide bromide phases during cycling on the POLARIS beamline during cycling in the IGA^n sample environmen.

5.5.4 Further deuterium cycling and gravimetric measurements

Due to the unexpected mass uptake in the gravimetric experiment on the POLARIS beamline, a second experiment was carried out. A 455 mg sample of the deutero-imide iodide $Li_5(ND)_2I$ was loaded onto the microbalance of the IGA^n and heated to 250°C under vacuum. Data were recorded continuously, with a new scan taken every five minutes. The sample was exposed to 3 bar of D_2 at a rate of 50 mbar min^{-1}. After two hours under these conditions, the pressure was then reduced and data collected under vacuum for five hours. 3 bar of D_2 was applied to the sample at a rate of 200 mbar min^{-1} and maintained for four hours before the sample was cooled and removed from the beamline. The temperature, pressure and mass data recorded by the IGA^n are shown alongside a contour plot of the neutron powder diffraction data in figure 5.27.

A batch quantitative phase analysis (QPA) refinement was carried out, and the scale factor of the deutero-amide iodide phase is shown in figure 5.28. It can be seen to increase and decrease on application of deuterium and vacuum, respectively.

Complete deuteration of $Li_5(ND)_2I$ to $Li_3(ND_2)_2I$ + 2 LiD would equate to a 4.14% weight gain of the sample. On the initial deuteration, the sample weight was seen to increase by 13.7 mg, 3% of the initial weight. Unlike the first experiment, this sample was not seen to uptake more than the theoretical mass of deuterium. Peaks corresponding to the deutero-amide iodide were seen to appear in the neutron diffraction pattern. When data were collected under vacuum, the mass of the sample was seen to slowly decrease down to a level below that of the starting material: a loss of 20.3 mg, 4.3 wt%. The peaks in the neutron diffraction pattern were seen to decrease in intensity and shift in position as the sample dedeuterated. The phase observed in the neutron diffraction pattern during the first gravimetric cycling experiment was not observed during dedeuteration on this occasion, suggesting that the sample has not lost its full deuterium capacity. During the second deu-

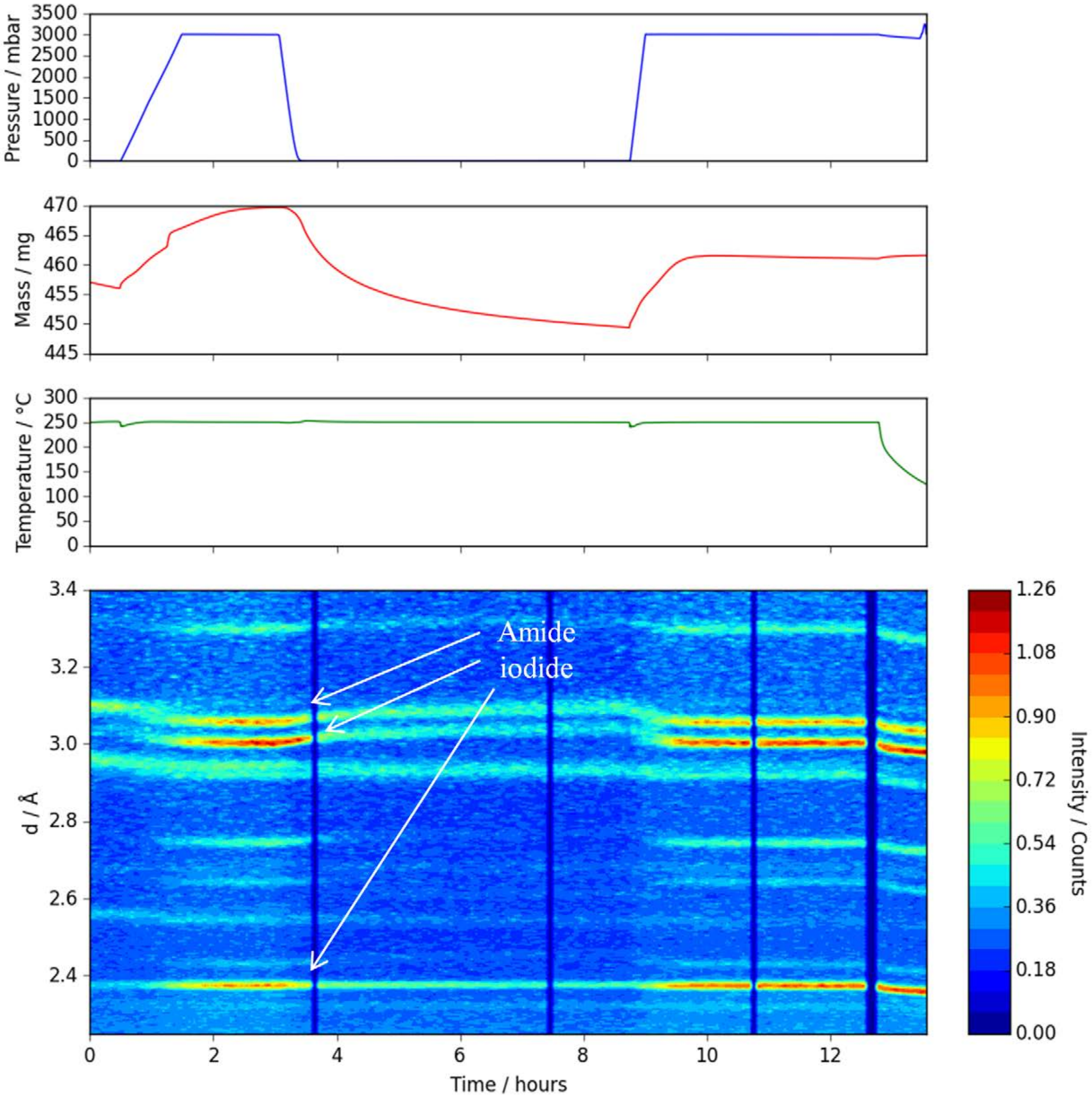

Figure 5.27: IGA^n data and contour plot of neutron diffraction data for $Li_3(NH_2)_2I$ collected on the POLARIS beamline.

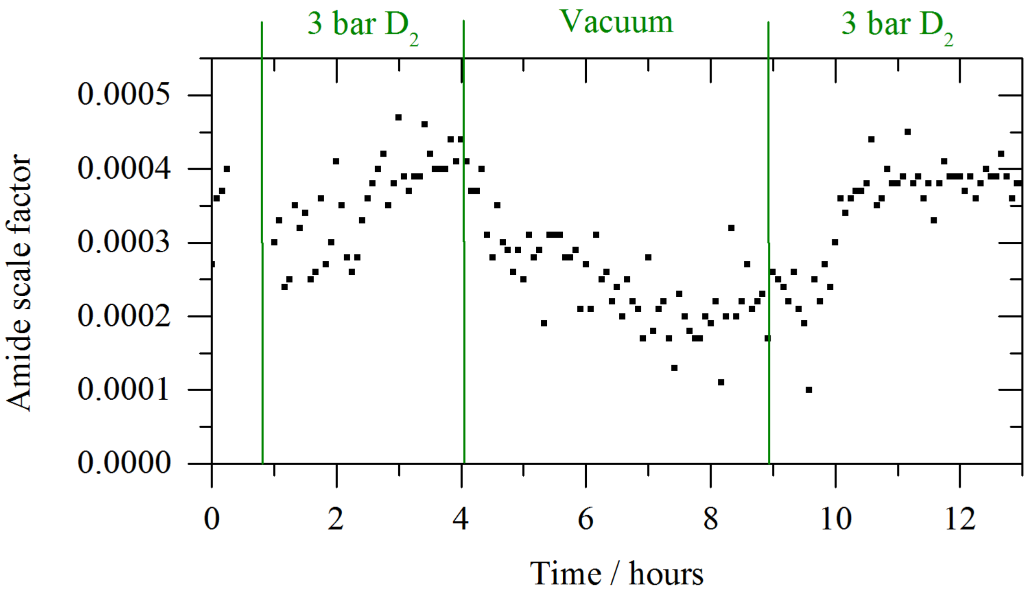

Figure 5.28: Scale factor of $Li_3(NH_2)_2I$ during cycling under hydrogen and vacuum on the POLARIS beamline.

teration, the mass of the sample was seen to increase by 12.1 mg. The peaks corresponding to the deutero-amide iodide phase were again observed in the neutron diffraction pattern. The mass loss was modelled using an exponential decay model and the 1D and 3D diffusion models, and the fits to the data are shown in figure 5.29. The exponential fit gives a half life of 55.8(1) minutes although, as with the previous gravimetric iodide cycling experiment, the fit to the 3D diffusion model is better, suggesting that it is ionic diffusion that is part of the rate determining step for the dedeuteration in the system.

The initial mass gain of 3 wt% is closer to the theoretical maximum of 4.14 than the weight percentages measured in the chloride and bromide systems where adsorption reached approximately half of the theoretical maximum. On desorption, the mass decreases below that of the starting mass. Unlike the chloride and the bromide, in the iodide system there is a stoichiometric nitride, Li_7N_2I, which could be formed on loss of 7.3 wt% D_2 from the amide. However, under the conditions in this experiment, the full mass loss on dehydrogenation was

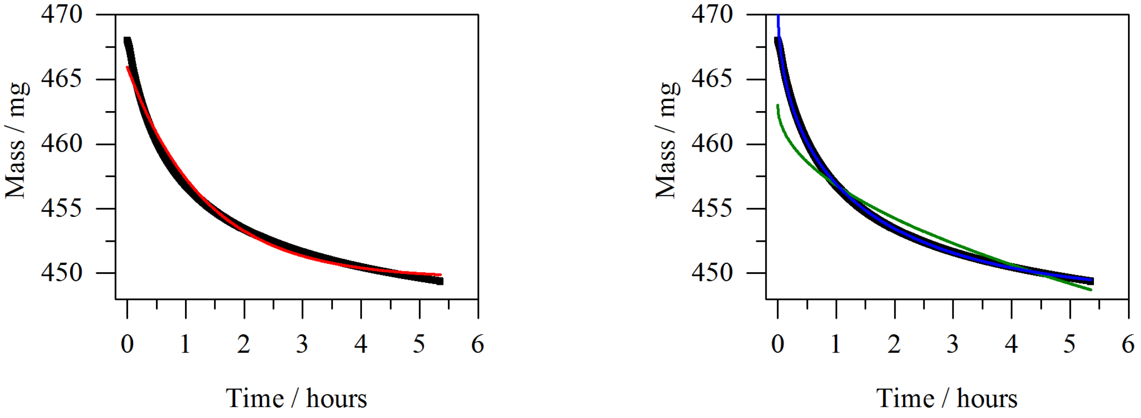

Figure 5.29: Sample weight for sample of $Li_3(NH_2)_2I$ during dedeuteration on the IGA^n on the POLARIS beamline, along with an exponential function fit to the data (left, red, $r^2 = 0.9902$), and the 1D (right, green, $r^2 = 0.9124$) and the 3D (right, blue, $r^2 = 0.9990$) diffusion models.

not regained under pressure of D_2, suggesting that, as in the chloride and bromide systems, there is capacity loss due to sample morphology and/or ND_3 loss.

5.6 Incorporation of fluoride

5.6.1 $LiNH_2$ + LiF

The reaction of lithium amide with lithium fluoride was carried out over a range of ratios and reaction conditions using solid state synthesis, as described in section 2.1, during a summer project by Emma Korkiakoski. It was found that, at temperatures up to 450°C, no change was observed to the diffraction pattern of the starting materials across the range of NH_2^- to F^- ratios after reaction and, above this, $LiNH_2$ was seen to decompose. A lack of solid solution formation is likely to be due to the high stability of LiF.

5.6.2 $LiNH_2$ + KF

Potassium fluoride was dried under vacuum, hand ground with $LiNH_2$ at a 1 to 6 ratio and heated for 12 hours at 400°C (the same conditions used for forming $Li_7(NH_2)_6Cl$). The reactants underwent a metathesis to form LiF and $KLi_3(NH_2)_4$, with some $LiNH_2$ remaining. Therefore it can be concluded that the reaction occurring is the one shown in reaction 5.2. $KLi_3(NH_2)_4$ has been investigated by others, by adding KH and KNH_2 to $LiNH_2$, and found to release ammonia at a much lower temperature than $LiNH_2$ alone.[150,151]

$$6\,\mathrm{LiNH_2} + \mathrm{KF} \longrightarrow \mathrm{KLi_3(NH_2)_4} + \mathrm{LiF} + 2\,\mathrm{LiNH_2} \tag{5.2}$$

5.6.3 BF_4^-

TPD-MS was carried out for the reaction $6\,LiNH_2$ + 6LiH + $LiBF_4$ with a heating rate of 2°C min^{-1} to 400°C. Ammonia and hydrogen were released, as shown in figure 5.30, and LiF and Li_2NH are present in the powder XRD patterns of the products. BN is likely to also be present, but not visible in the XRD pattern due to being in an amorphous state. The same reaction was carried out for $NaBF_4$, and a sudden release of hydrogen and ammonia occurred at 320°C, as shown in figure 5.30. A proposed reaction is shown in reaction 5.3, and the simultaneous release of H_2 and NH_3 suggests this is likely to be true for the sodium system, but NH_3 release precedes H_2 release for the lithium system. Addition of LiH to $LiNH_2$ is known to prevent the release of ammonia, but these results suggest that the presence of $LiBH_4$ stops this from happening, possibly driven by the formation of LiF.

$$12\,LiNH_2 + 12\,LiH + 2\,NaBF_4 \longrightarrow 9\,Li_2NH + 6\,LiF + 2\,NaF + 2\,BN + NH_3 + 12\,H_2 \quad (5.3)$$

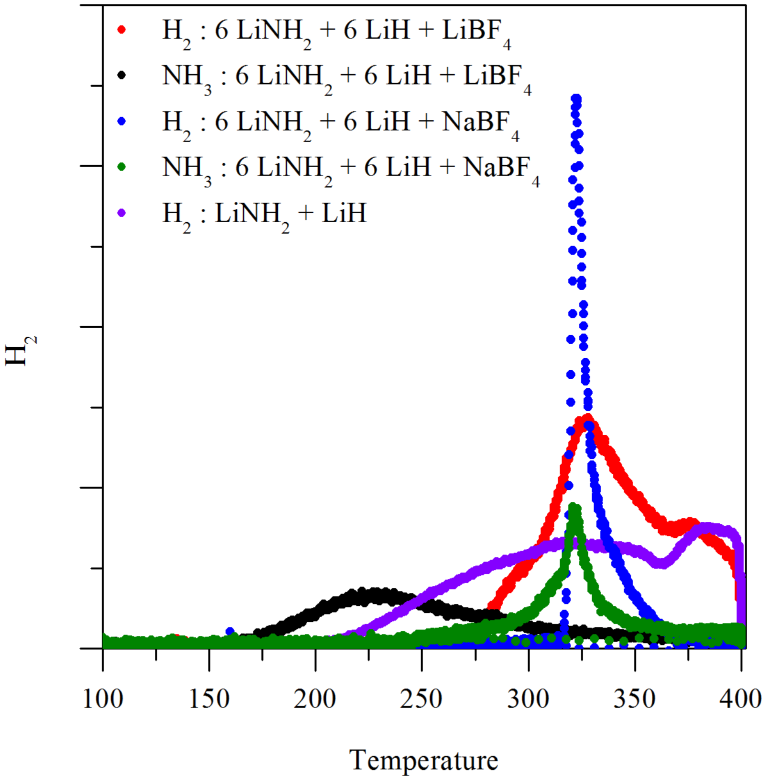

Figure 5.30: Hydrogen and ammonia traces for $LiBF_4$ and $NaBF_4$ added to $LiNH_2$ and LiH, collected on the TPD-MS.

5.7 LiH_xF_{1-x} solid solution

LiF and LiH are isostructural, as both are face-centred cubic with lattice constants that differ only by 1.5% (for LiH, a = 4.083 Å and for LiF a = 4.027 Å).[152] Alkali halide salts with lattice parameters that differ by less than 5% should form solid solutions and, above 321°C, LiH-LiF has been observed as a single phase.[153] At room temperature, a single phase of LiH_xF_{1-x} has been reported above $x = 0.6$.[154] Another group has observed a single phase for $x = 0$ to 0.6, with two phases observed at higher x with a values of 4.085 Å and 4.048 Å.[155]

Masters student Rachel London found that, for LiH_xF_{1-x}, at $x < 0.5$, a single phase is formed, with a lattice parameter that increases with LiH content, although not in accordance with Vegard's law. For $x = 0.5$ and above, two phases were formed: with lattice parameters a = 4.036 Å, and a = 4.048 Å. As the LiH content was increased, the fraction of the phase with larger lattice parameter increased relative to that with the smaller unit cell. At $x = 0.8$, the phase with a = 4.048 Å was formed alongside another with a = 4.078 Å.

5.7.1 Hydrogen desorption

An investigation was carried out to determine the effect of the introduction of LiF into LiH on the hydrogen desorption of the $LiNH_2$-LiH system. Reaction 5.4 was investigated by heating to 400°C with a heating rate of 2°C min^{-1} for x values between 1 and 4. The gases given off were measured by mass spectrometry. Figure 5.31 shows that, when compared to $LiNH_2$ reacting alone with LiH (black traces), addition of LiF into the mixture caused a reduction in the onset of hydrogen desorption (blue traces). In all cases, pre-treatment and formation of a fluoride-hydride hindered the hydrogen desorption (green traces).

$$\mathrm{LiNH_2} + \frac{1}{\mathrm{x}}\left(\mathrm{x\,LiH} + (5-\mathrm{x})\,\mathrm{LiF}\right) \longrightarrow \tag{5.4}$$

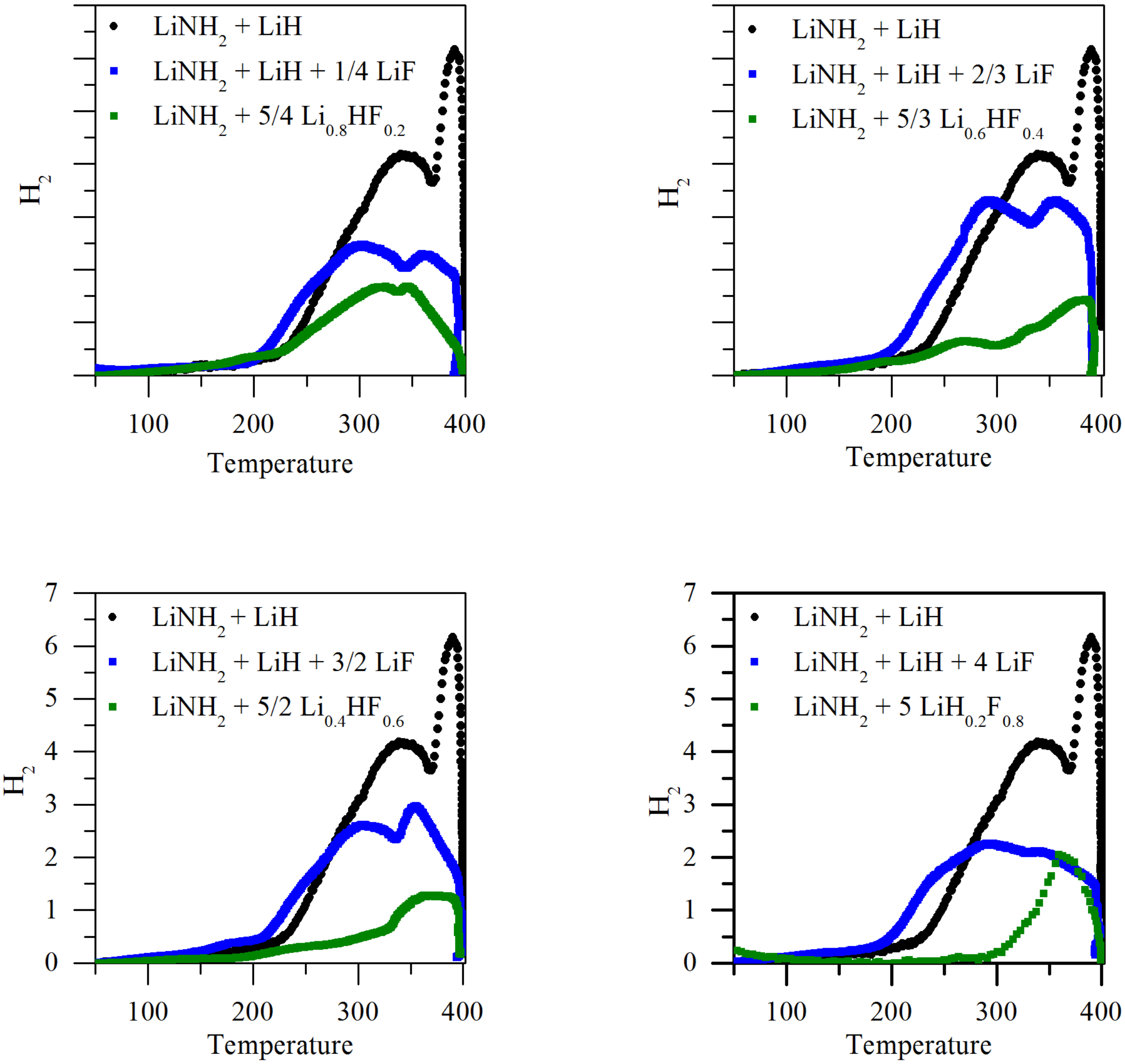

Figure 5.31: TPD-MS hydrogen traces for the reaction of $LiNH_2$ with Li_xF_{1-x} and LiH and LiF mixtures, scaled to the LiH content.

5.8 Conclusions and further work

This chapter investigated other halide ions, and their effect on the lithium amide system. Although equivalent structures were observed in the amide chloride and amide bromide systems at the amide to halide ratio of 6 : 1, the same was not observed at other ratios. This can be rationalised by considering the size of the halide ions, and the sites that would need to be occupied for other stoichiometries to be accommodated.

Hydrogen and deuterium cycling of the bromide and iodide systems showed that both systems are able to cycle hydrogen although, as observed in the chloride system, both showed a reduction in capacity on cycling. This could be due to a release of ammonia, and further cycling experiments coupled to a mass spectrometer would be extremely useful to determine the composition of the gases released. For the iodide system, which was able to be cycled at a fixed temperature, it would be useful for a similar study to be undertaken but with more cycles, to see how the cycling capacity is affected. During the beamline cycling experiments of both the bromide and iodide systems, new phases were observed. More detailed information of the structure and hydrogen content of these phases would aid the mechanistic investigation, although the fact they have only been observed *in situ* makes this especially challenging.

Although the structures of $Li_7(NH_2)_6Cl$ and $Li_7(NH_2)_6Br$ are very similar, the amide chloride was seen to have a higher ionic conductivity than the bromide equivalent, which was comparable to $LiNH_2$. The imide bromide also had lower ionic conductivity than the imide chloride although both were higher than that for the non-halogenated system. At temperatures where hydrogen cycling occurs, however, the conductivity of the imide chloride and imide bromide phases are comparable.

Analysis of the kinetics of hydrogen uptake and release has been carried out and, for the bromide system, comparison of a first order kinetic model and diffusion-controlled models indicated clearly that the rate-determining step of the reaction is first order and that the rate is not limited by diffusion. This is the same as observed for the chloride system, and can be rationalised by considering the ammonia-mediated mechanism as discussed previously. The fact that the rate is not determined by diffusion may be why the correlation between amide halide ionic conductivity and hydrogen desorption properties is not as clear as might have been expected. Both systems show good conductivity when compared to the halide-free system, enabling diffusion not to be the rate-determining step.

For the iodide system the analysis was not so clear, with both first order and 3D diffusion kinetic models fitting well to the data. Useful further work would be to measure the conductivity of the amide and imide iodide, to see if these values are lower, leading to diffusion being the rate-determining step. This is unexpected, as the layered structure of the iodide is reported for having high ionic conductivity between the layers.[102]

As observed in the chloride system, neither the bromide nor the iodide systems exhibit a half life of (de)hydrogenation that could meet the US Department of Energy target for a refuelling station.[22] Further work into mechanical processing methods could determine whether these materials would be suitable for commercial applications.

Chapter 6

Conclusions

The project aim was to study the relationship between the structure of a hydrogen storage material and its physical properties, such as ionic conductivity, and the hydrogen uptake and release kinetics. The materials of focus were lithium and magnesium amide halides, with an emphasis on the lower halide doping limits, as this reduces the gravimetric hydrogen density penalty caused by halide addition.

The effects of time and composition on the structure of the amide chlorides formed during the reaction between $LiNH_2$ and LiCl were investigated, and lowering the chloride content of the known phase $Li_4(NH_2)_3Cl$ resulted in the formation of a mixture of two phases, except at the stoichiometry $Li_7(NH_2)_6Cl$ where a new phase was observed. This new phase showed a significant improvement in the theoretical gravimetric capacity of the system, and was found to release hydrogen on reaction with LiH at a lower temperature than $LiNH_2$ whilst suppressing release of ammonia. Therefore the reduction in chloride content had no detrimental effect on the desorption temperature. On dehydrogenation $Li_7(NH_2)_6Cl$ formed an imide chloride and was able to be rehydrogenated back to $Li_7(NH_2)_6Cl$.

Extending the investigation to the magnesium-containing system a new phase was also observed at the same lower chloride stoichiometry. However, the magnesium content of this phase was not confirmed, and no improvement was seen in the dehydrogenation temperature on reaction with LiH when compared to $Li_7(NH_2)_6Cl$. When the lithium-only amide chloride $Li_7(NH_2)_6Cl$ was heated with MgH_2 instead of LiH, the desorption temperature was reduced slightly, but this complex system did not show improvements on rehydrogenation.

The amide chloride, amide bromide and amide iodide systems were studied on cycling under hydrogen and vacuum. All systems were able to cycle hydrogen, but showed a reduction in capacity on cycling, most likely due to release of ammonia. Ammonia was not seen to be lost during experiments under flowing argon, but only those cycling experiments that involved a dynamic vacuum. It is therefore likely that the environment immediately surrounding the sample is important in determining the progress and pathway of de/rehydrogenation. Across all measurements, the chloride system was seen to release half the theoretical hydrogen storage capacity.

Structural measurements were also taken during cycling of all three systems to gain an insight into the mechanism operating on de/rehydrogenation. Kinetic analysis showed that a first order model fitted better to the data than a diffusion model for all three systems indicating that the rate of the reaction is determined by the concentration of one reagent. As described, this supports the proposed ammonia-mediated mechanism.[60,61,62] During the beamline cycling experiments of both the bromide and iodide systems, new phases were observed. More detailed information of the structure and hydrogen content of these phases would aid the mechanistic investigation, although the fact they have only been observed *in situ* makes this challenging.

The half lives calculated during this investigation show that, currently, none of the systems could meet the refuelling targets set by the US Department of Energy.[22] However, the rate of de/rehydrogenation was seen to increase on subsequent cycles, so it is possible that physical manipulations could be successful in improving the kinetics of the systems.

The ionic conductivities of the amide and imide chloride and bromide were measured, and were higher than those of the chloride-free system. Considering that the rehydrogenation kinetics suggest that diffusion is not rate-limiting, it may be that improvement in the ionic conductivity prevents ionic diffusion hindering the reaction process. Although the structures of $Li_7(NH_2)_6Cl$ and $Li_7(NH_2)_6Br$ are very similar, the amide chloride was seen to have a higher ionic conductivity than the bromide equivalent, which was comparable to $LiNH_2$. The imide bromide also had lower ionic conductivity than the imide chloride although both were higher than that for the non-halogenated system. At temperatures where hydrogen cycling occurs, however, the conductivity of the imide chloride and imide bromide phases were comparable.

This study has produced a detailed examination of the phase space of the amide chloride system, and shown that the amide halides can be successfully cycled under hydrogen. The kinetic analyses and ionic conductivity measurements have given an insight into the mechanism involved in de/rehydrogenation, which will aid others in the future when investigating these, and other, materials for hydrogen storage.

Bibliography

[1] Department of Energy and Climate Change Energy Trends Technical report, National Statistics, December 2015.

[2] European Commission, Environment: Commission takes action against UK for persistent air pollution problems Press Release, 2004.

[3] Tesla Motors UK, Model S.

[4] L. Schlapbach and A. Züttel, *Nature*, 2001, **414**, 353–358.

[5] J. D. Holladay, J. Hu, D. L. King, and Y. Wang, *Catal. Today*, 2009, **139**, 244–260.

[6] P. P. Edwards, V. L. Kuznetsov, and W. I. F. David, *Philos. T. Roy. Soc. A*, 2007, **365** (1853), 1043–56.

[7] J. Alazemi and J. Andrews, *Renew. Sust. Energ. Rev.*, 2015, **48**, 483–499.

[8] M. Ni, D. Y. Leung, M. K. Leung, and K. Sumathy, *Fuel Process. Technol.*, 2006, **87** (5), 461–472.

[9] Office of Energy Efficiency & Renewable Energy, U. S. Department of Energy, Hydrogen Production: Biomass Gasification energy.gov.

[10] M. Wise, K. Calvin, A. Thomson, L. Clarke, B. Bond-Lamberty, R. Sands, S. J. Smith, A. Janetos, and J. Edmonds, *Science*, 2009, **324** (5931), 1183–6.

[11] P. Wan and X. J. Yang, *ChemSusChem*, 2012, **5** (8), 1381–2.

[12] UK H2 Mobility Phase 1 results Technical report, UK Government, 2013.

[13] F. Yilmaz, M. T. Balta, and R. Selbas, *Renew. Sust. Energ. Rev.*, 2016, **56**, 171–178.

[14] J. Zumerchik, *Macmillan Encyclopedia of Energy, Volume 2*, 2001.

[15] C. White, R. Steeper, and A. Lutz, *Int. J. Hydrogen Energy*, 2006, **31** (10), 1292–1305.

[16] K. Saravanan, N. Stalin, S. Rajalakshmi, and G. Giftson Samuel In *IEE P-Commun.*, p. 586, 2012.

[17] J. Larminie and A. Dicks, *Fuel Cell Systems Explained*, Wiley, 2003.

[18] S. Gottesfeld, *Advances in Electrochemical Science and Engineering*, Vol. 5, John Wiley & Sons, 2008.

[19] U. Eberle, B. Muller, and R. von Helmolt, *Energy Environ. Sci.*, 2012, **5**, 8780.

[20] A. Vaughan, The future is here: mass-market hydrogen cars take to Britain's roads The Guardian, 2015.

[21] M. Felderhoff, C. Weidenthaler, R. von Helmolt, and U. Eberle, *Phys. Chem. Chem. Phys.*, 2007, **9** (21), 2643–53.

[22] L. Klebanoff and J. Keller Final Report for the DOE Metal Hydride Center of Excellence Technical report, 2012.

[23] A. Züttel, *Die Naturwissenschaften*, 2004, **91** (4), 157–72.

[24] D. Ross, *Vacuum*, 2006, **80**, 1084–1089.

[25] S. Aceves, G. Berry, J. Martinezfrais, and F. Espinosaloza, *Int. J. Hydrogen Energy*, 2006, **31** (15), 2274–2283.

[26] A. Yamashita, M. Kondo, S. Goto, and N. Ogami, *SAE Technical Paper*, 2015, **1**, 1169.

[27] T. Lim and B.-K. Ahn, *ECS Transactions*, 2013, **50** (2), 3–10.

[28] R. Ahluwalia, T. Hua, and J. Peng, *Int. J. Hydrogen Energy*, 2012, **37** (3), 2891–2910.

[29] S. Sherif, F. Barbir, and T. Veziroglu, *Solar Energy*, 2005, **78** (5), 647–660.

[30] R. Ahluwalia, T. Hua, J.-K. Peng, S. Lasher, K. McKenney, J. Sinha, and M. Gardiner, *Int. J. Hydrogen Energy*, 2010, **35** (9), 4171–4184.

[31] T. Heine, L. Zhechkov, G. Seifert, and S. Patchkovskii, *SPIE Newsroom*, 2007.

[32] D. C. Elias, R. R. Nair, T. M. G. Mohiuddin, S. V. Morozov, P. Blake, M. P. Halsall, A. C. Ferrari, D. W. Boukhvalov, M. I. Katsnelson, A. K. Geim, and K. S. Novoselov, *Science*, 2009, **323** (5914), 610–3.

[33] J. Yang, A. Sudik, C. Wolverton, and D. J. Siegel, *Chem. Soc. Rev.*, 2010, **39** (2), 656–75.

[34] A. Züttel, *materialstoday*, 2003, **6** (9), 24–33.

[35] S. R. Johnson, P. A. Anderson, P. P. Edwards, I. Gameson, J. W. Prendergast, M. Al-Mamouri, D. Book, I. R. Harris, J. D. Speight, and A. Walton, *ChemInform*, 2005, **36** (39).

[36] S.-I. Orimo, Y. Nakamori, J. R. Eliseo, A. Zuettel, and C. M. Jensen, *ChemInform*, 2007, **38** (51).

[37] B. Bogdanović and M. Schwickardi, *J. Alloys Compd.*, 1997, **253-254**, 1–9.

[38] I. Jain, P. Jain, and A. Jain, *J. Alloys Compd.*, 2010, **503** (2), 303–339.

[39] D. Pukazhselvan, V. Kumar, and S. Singh, *Nano Energy*, 2012, **1** (4), 566–589.

[40] B. Sakintuna, F. Lamari-Darkrim, and M. Hirscher, *Int. J. Hydrogen Energy*, 2007, **32** (9), 1121–1140.

[41] B. Bogdanović, K. Bohmhammel, B. Christ, A. Reiser, K. Schlichte, R. Vehlen, and U. Wolf, *J. Alloys Compd.*, 1999, **282** (1-2), 84–92.

[42] J. Huot, G. Liang, S. Boily, A. Van Neste, and R. Schulz, *J. Alloys Compd.*, 1999, **293-295**, 495–500.

[43] W. Oelerich, T. Klassen, and R. Bormann, *J. Alloys Compd.*, 2001, **315** (1-2), 237–242.

[44] J. Chen, N. Kuriyama, Q. Xu, H. T. Takeshita, and T. Sakai, *J. Phys. Chem. B*, 2001, **105** (45), 11214–11220.

[45] J. Graetz, *ISRN Materials Science*, 2012, **2012**, 1–18.

[46] A. Züttel, P. Wenger, S. Rentsch, P. Sudan, P. Mauron, and C. Emmenegger, *J. Power Sources*, 2003, **118** (1-2), 1–7.

[47] S. Orimo, Y. Nakamori, G. Kitahara, K. Miwa, N. Ohba, S. Towata, and A. Züttel, *J. Alloys Compd.*, 2005, **404-406**, 427–430.

[48] H. I. Schlesinger, H. C. Brown, A. E. Finholt, J. R. Gilbreath, H. R. Hoekstra, and E. K. Hyde, *J. Am. Chem. Soc.*, 1953, **75** (1), 215–219.

[49] H.-W. Li, K. Kikuchi, Y. Nakamori, K. Miwa, S. Towata, and S. Orimo, *Scr. Mater.*, 2007, **57** (8), 679–682.

[50] U. Demirci, O. Akdim, and P. Miele, *Int. J. Hydrogen Energy*, 2009, **34** (6), 2638–2645.

[51] A. W. Titherley, *J. Chem. Soc., Trans.*, 1894, **65**, 504.

[52] F. W. Bergstrom and W. C. Fernelius, *Chem. Rev.*, 1933, **12** (1), 43–179.

[53] S. Zaginaichenko, Z. Matysina, D. Schur, and A. Zolotarenko, *Int. J. Hydrogen Energy*, 2012, **37** (9), 7565–7578.

[54] P. Chen, Z. Xiong, J. Luo, J. Lin, and K. Lee Tan, *Nature*, 2002, **420** (6913), 302–304.

[55] D. H. Gregory, *J. Mater. Chem.*, 2008, **18** (20), 2321.

[56] R. Juza and K. Opp, *Z. Anorg. Allg. Chem.*, 1951, **266** (6), 325–330.

[57] P. Chen, Z. Xiong, J. Luo, J. Lin, and K. Lee Tan, *J. Phys. Chem. B*, 2003, **107** (39), 10967–10970.

[58] Y. H. Hu and E. Ruckenstein, *J. Phys. Chem. A*, 2003, **107** (46), 9737–9739.

[59] J. Lu, Z. Z. Fang, and H. Y. Sohn, *Inorg. Chem.*, 2006, **45** (21), 8749–54.

[60] T. Ichikawa, N. Hanada, S. Isobe, H. Leng, and H. Fujii, *J. Phys. Chem. B*, 2004, **108** (23), 7887–7892.

[61] S. Hino, T. Ichikawa, N. Ogita, M. Udagawa, and H. Fujii, *Chem. Commun.*, 2005, (24), 3038–40.

[62] A. Borgschulte, M. O. Jones, E. Callini, B. Probst, S. Kato, A. Züttel, W. I. F. David, and S.-i. Orimo, *Energy Environ. Sci.*, 2012, **5** (5), 6823–6832.

[63] H. Leng, T. Ichikawa, S. Hino, and H. Fujii, *J. Alloys Compd.*, 2008, **463** (1-2), 462–465.

[64] H. Leng, T. Ichikawa, S. Hino, T. Nakagawa, and H. Fujii, *J. Phys. Chem. B*, 2005, **109** (21), 10744–8.

[65] S. Hino, N. Ogita, M. Udagawa, T. Ichikawa, and Y. Kojima, *J. Appl. Phys.*, 2009, **105** (2), 023527.

[66] W. I. F. David, M. O. Jones, D. H. Gregory, C. M. Jewell, S. R. Johnson, A. Walton, and P. P. Edwards, *J. Am. Chem. Soc.*, 2007, **129** (6), 1594–1601.

[67] H. Cao, J. Wang, Y. Chua, H. Wang, G. Wu, Z. Xiong, J. Qiu, and P. Chen, *J. Phys. Chem. C*, 2014, **118** (5), 2344–2349.

[68] J. W. Makepeace, M. O. Jones, S. K. Callear, P. P. Edwards, and W. I. F. David, *Phys. Chem. Chem. Phys.*, 2014, **16** (9), 4061–4070.

[69] P. A. Anderson, P. A. Chater, D. R. Hewett, and P. R. Slater, *Faraday Discuss.*, 2011, **151**, 271.

[70] M. Matsuo and S.-I. Orimo, *Adv. Energy Mater.*, 2011, **1** (2), 161–172.

[71] S. Nayebossadri and K.-F. Aguey-Zinsou, *Phys. Chem. Chem. Phys.*, 2011, **13** (39), 17683–8.

[72] H. Jacobs and R. Juza, *Z. Anorg. Allg. Chem.*, 1972, **391** (3), 271–279.

[73] C. Liang, Y. Liu, H. Fu, Y. Ding, M. Gao, and H. Pan, *J. Alloys Compd.*, 2011, **509** (30), 7844–7853.

[74] H. M. Jin and P. Wu, *Appl. Phys. Lett.*, 2005, **87** (18), 181917.

[75] J. Rijssenbeek, Y. Gao, J. Hanson, Q. Huang, C. Jones, and B. Toby, *J. Alloys Compd.*, 2008, **454** (1-2), 233–244.

[76] Z.-N. Li, H.-C. Qiu, S.-M. Wang, L.-J. Jiang, J. Du, J.-X. Zhang, M. Latroche, and F. Cuevas, *Rare Metals*, 2015.

[77] W. Luo, *J. Alloys Compd.*, 2004, **381**, 284–287.

[78] W. Luo and S. Sickafoose, *J. Alloys Compd.*, 2006, **407** (1-2), 274–281.

[79] B. Paik, H.-W. Li, J. Wang, and E. Akiba, *Chem. Commun.*, 2015, **51** (49), 10018–21.

[80] H. Y. Leng, T. Ichikawa, S. Hino, N. Hanada, S. Isobe, and H. Fujii, *J. Phys. Chem. B*, 2004, **108** (26), 8763–8765.

[81] Z. Xiong, G. Wu, J. Hu, and P. Chen, *Adv. Mater.*, 2004, **16** (17), 1522–1525.

[82] G. Wu, Z. Xiong, T. Liu, Y. Liu, J. Hu, P. Chen, Y. Feng, and A. T. S. Wee, *Inorg. Chem.*, 2007, **46** (2), 517–21.

[83] K. Tokoyoda, S. Hino, T. Ichikawa, K. Okamoto, and H. Fujii, *J. Alloys Compd.*, 2007, **439** (1-2), 337–341.

[84] L. H. Jepsen, P. Wang, G. Wu, Z. Xiong, F. Besenbacher, P. Chen, and T. R. Jensen, *Phys. Chem. Chem. Phys.*, 2015.

[85] G. P. Meisner, M. L. Scullin, M. P. Balogh, F. E. Pinkerton, and M. S. Meyer, *J. Phys. Chem. B*, 2006, **110** (9), 4186–92.

[86] Y. E. Filinchuk, K. Yvon, G. P. Meisner, F. E. Pinkerton, and M. P. Balogh, *Inorg. Chem.*, 2006, **45** (4), 1433–5.

[87] P. A. Chater, W. I. F. David, S. R. Johnson, P. P. Edwards, and P. A. Anderson, *Chem. Commun.*, 2006, **4** (23), 2439–41.

[88] J. P. Singer, M. S. Meyer, R. M. Speer, J. E. Fischer, and F. E. Pinkerton, *J. Phys. Chem. C*, 2009, **113** (43), 18927–18934.

[89] P. A. Chater, W. I. F. David, and P. A. Anderson, *Chem. Commun.*, 2007, (45), 4770–2.

[90] H. Wu, W. Zhou, T. J. Udovic, J. J. Rush, and T. Yildirim, *Chem. Mater.*, 2008, **20** (4), 1245–1247.

[91] P. A. Anderson, P. A. Chater, and B. David In *Mater Rese Soc*, 2009.

[92] P. Chater, P. Anderson, J. Prendergast, A. Walton, V. Mann, D. Book, W. David, S. Johnson, and P. Edwards, *J. Alloys Compd.*, 2007, **446-447**, 350–354.

[93] M. Au, A. R. Jurgensen, W. A. Spencer, D. L. Anton, F. E. Pinkerton, S.-J. Hwang, C. Kim, and R. C. Bowman, *J. Phys. Chem. C*, 2008, **112** (47), 18661–18671.

[94] G.-l. Xia, H.-y. Leng, N.-x. Xu, Z.-l. Li, Z. Wu, J.-l. Du, and X.-b. Yu, *Int. J. Hydrogen Energy*, 2011, **36** (12), 7128–7135.

[95] W. Lohstroh and M. Fichtner, *J. Alloys Compd.*, 2007, **446-447**, 332–335.

[96] C. Price, J. Gray, R. Lascola, and D. L. Anton, *Int. J. Hydrogen Energy*, 2012, **37** (3), 2742–2749.

[97] I. Malka, T. Czujko, and J. Bystrzycki, *Int. J. Hydrogen Energy*, 2010, **35** (4), 1706–1712.

[98] T. Ichikawa, S. Isobe, N. Hanada, and H. Fujii, *J. Alloys Compd.*, 2004, **365** (1-2), 271–276.

[99] M. Au, W. Spencer, A. Jurgensen, and C. Zeigler, *J. Alloys Compd.*, 2008, **462** (1-2), 303–309.

[100] A. Gotoh, H. Obayashi, R. Nagai, S. Mochizuki, and T. Kudo, Lithium halide-lithium imide compounds, solid electrolyte, cell, 1983.

[101] H. Maekawa, M. Matsuo, H. Takamura, M. Ando, Y. Noda, T. Karahashi, and S.-i. Orimo, *J. Am. Chem. Soc.*, 2009, **131** (3), 894–5.

[102] M. Matsuo, T. Sato, Y. Miura, H. Oguchi, Y. Zhou, H. Maekawa, H. Takamura, and S.-i. Orimo, *Chem. Mater.*, 2010, **22** (9), 2702–2704.

[103] H. Leng, Z. Wu, W. Duan, G. Xia, and Z. Li, *Int. J. Hydrogen Energy*, 2012, **37** (1), 903–907.

[104] H. Barlage and H. Jacobs, *Z. Anorg. Allg. Chem.*, 1994, **620** (3), 479–482.

[105] H. Barlage and H. Jacbobs, *ChemInform*, 1994, **42** (38).

[106] B. Li, Y. Liu, C. Li, M. Gao, and H. Pan, *J. Mat. Chem. A*, 2014.

[107] A. V. Skripov, R. V. Skoryunov, A. V. Soloninin, O. A. Babanova, M. Matsuo, and S.-i. Orimo, *J. Phys. Chem. C*, 2015, **119** (24), 13459–13464.

[108] J. Zhang and Y. H. Hu, *Ind. Eng. Chem. Res.*, 2011, **50** (13), 8058–8064.

[109] N. S. Gamba, P. Arneodo Larochette, and F. C. Gennari, *RSC Adv.*, 2015, **5** (84), 68542–68550.

[110] H. Cao, H. Wang, T. He, G. Wu, Z. Xiong, J. Qiu, and P. Chen, *RSC Adv.*, 2014, **4** (61), 32555.

[111] K. L. Lim, H. Kazemian, Z. Yaakob, and W. R. W. Daud, *Chem. Eng. Technol.*, 2010, **33** (2), 213–226.

[112] L. L. Shaw, R. Ren, T. Markmaitree, and W. Osborn, *J. Alloys Compd.*, 2008, **448** (1-2), 263–271.

[113] H. Miyaoka, Y. Wang, S. Hino, S. Isobe, K. Tokoyoda, T. Ichikawa, and Y. Kojima, *Materials*, 2015, **8** (7), 3896–3909.

[114] N. S. Gamba, P. Arneodo Larochette, and F. C. Gennari, *RSC Adv.*, 2016, **6**, 15622.

[115] R. F. Bill, D. Reed, D. Book, and P. A. Anderson, *J. Alloys Compd.*, 2015, **645** (Supplement 1), S96–99.

[116] J. Graetz, *Chem. Soc. Rev.*, 2009, **38** (1), 73–82.

[117] D. H. Gregory, *Imides and amides as hydrogen storage materials, Solid-state hydrogen storage*, Woodhead publishing limited, 2008.

[118] A. R. West, *Basic Solid State Chemistry*, Wiley, 2000.

[119] L. E. Smart and E. A. Moore, *Solid State Chemistry: An Introduction*, 2005.

[120] C. J. Rhodes, *Sci. Prog.*, 2015.

[121] S. P. Thompson, J. E. Parker, J. Potter, T. P. Hill, A. Birt, T. M. Cobb, F. Yuan, and C. C. Tang, jul , 2009, **80** (7), 075107.

[122] B. C. Hauback, *Structural characterisation of hydride materials, Solid-state hydrogen storage*, Woodhead publishing limited, 2008.

[123] User guide for the polaris powder diffractometer at isis. H. S. Smith, R.; Rutherford Appleton Laboratory, 1994.

[124] A. A. Coelho, TOPAS, General Profile and Structure Analysis Software for Powder Diffraction Data Bruker AXS GmbH: Karlsruhe, 2006.

[125] H. M. Rietveld, *J. Appl. Crystallogr.*, 1969, **2**, 65.

[126] R. A. Young, *The Rietveld Method*, Oxford University Press, 1993.

[127] D. L. Bish and S. A. Howard, *J. Appl. Crystallogr.*, 1988, **21** (2), 86–91.

[128] R. J. Hill and C. J. Howard, *J. Appl. Crystallogr.*, 1987, **20** (6), 467–474.

[129] S. Becker, *Inorganic Mass Spectrometry: Principles and Applications*, John Wiley & Sons, 2008.

[130] N. B. Colthup, L. H. Daly, and S. E. Wiberley, *Introduction to Infrared and Raman Spectroscopy*, Elsevier, 1990.

[131] D. C. Harris and M. D. Bertolucci, *Symmetry and Spectroscopy: An Introduction to Vibrational and Electronic Spectroscopy*, Courier Corporation, 1978.

[132] J.-P. Bohger, R. Eßmann, and H. Jacobs, *J. Mol. Struct.*, 1995, **348**, 325–328.

[133] Y. Kojima and Y. Kawai, *J. Alloys Compd.*, 2005, **395** (1-2), 236–239.

[134] R. S. Chellappa, D. Chandra, M. Somayazulu, S. A. Gramsch, and R. J. Hemley, *J. Phys. Chem. B*, 2007, **111** (36), 10785–9.

[135] E. Barsoukov and J. R. Macdonald, *Impedance Spectroscopy Theory, Experiment and Applications.*, Wiley, second ed., 2005.

[136] J. T. S. Irvine, D. C. Sinclair, and A. R. West, *Adv. Mater.*, 1990, **2** (3), 132–138.

[137] J. Parker, J. Potter, S. Thompson, A. Lennie, and C. Tang, *Mater. Sci. Forum*, 2012, **706-709**, 1707–1712.

[138] J. W. Makepeace, T. J. Wood, H. M. A. Hunter, M. O. Jones, and W. I. F. David, *Chem. Sci.*, 2015, **6** (7), 3805–3815.

[139] D. R. Hewett *Mixed anion amides for hydrogen storage* PhD thesis, 2012.

[140] A. F. Wells, *Structural Inorganic Chemistry*, OUP Oxford, 2012.

[141] A. Khawam and D. R. Flanagan, *J. Phys. Chem. B*, 2006, **110** (35), 17315–28.

[142] W. Jander, *Z. Anorg. Allg. Chem.*, 1927, **163** (1), 1–30.

[143] H. Cao, Y. Zhang, J. Wang, Z. Xiong, G. Wu, and P. Chen, *Progress in Natural Science: Materials International*, 2012, **22** (6), 560–550.

[144] J. Lamb, D. Chandra, W.-M. Chien, D. Phanon, N. Penin, R. Cerny, and K. Yvon, *J. Phys. Chem. C*, 2011, **115** (29), 14386–14391.

[145] R. A. Davies, D. R. Hewett, E. Korkiakoski, S. P. Thompson, and P. A. Anderson, *J. Alloys Compd.*, 2014, **645** (Supplement 1), S343–346.

[146] T. Zhang, S. Isobe, Y. Wang, N. Hashimoto, and S. Ohnuki, *RSC Adv.*, 2013, **3** (18), 6311.

[147] L. H. Jepsen, M. B. Ley, Y.-S. Lee, Y. W. Cho, M. Dornheim, J. O. Jensen, Y. Filinchuk, J. E. Jørgensen, F. Besenbacher, and T. R. Jensen, *Materials Today*, 2014, **17** (3), 129–135.

[148] Y. Yang, Y. Liu, Y. Zhang, Y. Li, M. Gao, and H. Pan, *J. Alloys Compd.*, 2014, **585**, 674–680.

[149] T. Aoki, T. Ichikawa, H. Miyaoka, and Y. Kojima, *J. Phys. Chem. C*, 2014, **118** (32), 18412–18416.

[150] B.-X. Dong, Y.-l. Teng, J. Ge, L. Song, and S.-y. Zhang, *RSC Adv.*, 2013, **3**, 16977–16980.

[151] B.-X. Dong, L. Song, J. Ge, Y.-L. Teng, and S.-Y. Zhang, *RSC Adv.*, 2014, **4** (21), 10702.

[152] C. Messer, *J. Solid State Chem.*, 1970, **2** (2), 144–155.

[153] C. E. Messer and J. Mellor, *J. Phys. Chem. B*, 1960, **64** (4), 503–505.

[154] Z.-Z. Fang, X.-D. Kang, Z.-X. Yang, G. S. Walker, and P. Wang, *J. Phys. Chem. C*, 2011, **115** (23), 11839–11845.

[155] H. Hahn and G. Strick, *Z. Anorg. Allg. Chem.*, 1970, **372** (2), 248–251.

List of Figures

1.1 Schematic representation of a PEMFC.[18] 13

1.2 Graph showing the pressure-composition isotherm for hydrogen absorption in a typical intermetallic compound with the construction of the Van't Hoff plot shown on the right hand side. Adapted from Z*ü*ttel *et. al.*[34] 18

1.3 Structure of $LiNH_2$ (a, left),[72] and the anti-fluorite structure of Li_2NH (b, right)[56], with lithium ions represented by red spheres, nitrogen blue, hydrogen pink, and the unit cell shown by dotted lines. The hydrogen atoms in Li_2NH are distributed across the 48*h* sites and so have been emitted for clarity. 23

2.1 Geometry used in the derivation of Bragg's law. 33

2.2 Schematic diagram of beamline I11 at the Diamond Light Source showing the main components and their approximate distances from the X-ray source.[121] 36

2.3 Schematic diagram of the POLARIS beamline at the ISIS neutron source showing the main components.[123] 38

2.4 Schematic diagram of the TPD-MS set-up. 45

2.5 Schematic diagram of the gas manifold used for high pressure hydrogenation. 47

2.6 Diagram of the Rayleigh and Raman scattering processes. 48

2.7 Schematic representation of the three Raman active modes of the ${NH_2}^-$ molecule. 50

2.8 Photograph of the inert atmosphere rig used for A.C. impedance measurements. 51

2.9 Photograph of the capillary gas cell used for hydrogen cycling measurements on the I11 beamline at Diamond Light Source. 54

2.10 Experimental setup used for cycling samples under deuterium / vacuum on the POLARIS beamline at the ISIS neutron source, adapted from Makepeace *et. al.*[138] 55

2.11 Photograph of the Intelligent Gravimetric Analyser used on the POLARIS beamline, in the argon-filled glove box used for sample loading next to the control system. 57

2.12 Photograph of a sample in a quartz bucket loaded onto the microbalance of the IGA^n. 58

3.1 Powder X-ray diffraction patterns of the cubic and rhombohedral phases of $Li_4(NH_2)_3Cl$. 60

3.2 Left: The structure of one unit cell of the $I2_13$ phase of $Li_4(NH_2)_3Cl$. Right: The structure of one unit cell of the $R\bar{3}$ phase of $Li_4(NH_2)_3Cl$, with the ‘Cl2’ ions disordered on the nitrogen sites. Both structures are viewed down the *z* axis. Chloride ions are shown as green spheres, lithium red, nitrogen blue and hydrogen pink. Unit cells are marked with dotted lines. 61

3.3 Powder X-ray diffraction pattern of the product of 2.25 $LiNH_2$ + 1.75 LiCl, showing lithium chloride (red tick marks) alongside the cubic phase (green tick marks). 63

3.4 Powder X-ray diffraction patterns for the product of the reaction (4-x) $LiNH_2$ + x LiCl for $x = 1$ to $x = 0.75$ after one hour reaction time, with *hkl* values shown for the $x = 1$ pattern. 64

3.5 Unit cell volumes for the rhombohedral products observed in the XRD patterns of the products of a one hour reaction time. Black points correspond to the phase ‘R$\bar{3}$ phase 1’, the dominant phase at $x = 1$, and blue ‘R$\bar{3}$ phase 2’ . 65

3.6 Raman spectra for the product of the reaction (4-x) $LiNH_2$ + x LiCl for $x = 1$ to $x = 0.5$ after one hour reaction time alongside that for $LiNH_2$. 65

3.7 Diagram showing the phases present at different x values after a one hour reaction time for the product of the reaction (4-x) $LiNH_2$ + x LiCl. 66

3.8 Graph showing the phase composition of the product of 3 $LiNH_2$ + LiCl against reaction time. Repeat experiments are shown by multiple data points. 67

3.9 Graph showing the unit cell volumes of the reaction product of 3 $LiNH_2$ + LiCl against time, with error bars encompassing the results from repeated experiments. Red points and axis represent the R$\bar{3}$ phase, with black points and axis representing the $I2_13$ phase. 68

3.10 Raman spectra for the reaction products of 3 $LiNH_2$ + LiCl after different reaction times. 69

3.11 Powder synchrotron XRD patterns (a) of $Li_4(NH_2)_3Cl$ after heating at 200°C for increasing time periods, showing the reduction in height of the (110) peak corresponding to the rhombohedral R$\bar{3}$ phase (red, (b)) and the appearance and growth of the (211) peak representing the cubic $I2_13$ phase (black, (c)). 70

3.12 Diagram showing the non-oxide containing phases present at different x values after a twelve hour reaction time for the reaction (4-x) $LiNH_2$ + x LiCl. 72

3.13 Raman spectra for $x = 1$, $x = 0.8$ and $x = 0.53$ after a twelve hour reaction time for the reaction (4-x) $LiNH_2$ + x LiCl. 73

3.14 Powder synchrotron X-ray diffraction pattern of rhombohedral $Li_7(NH_2)_6Cl$ with a Rietveld refinement using the structure of $Li_7(NH_2)_6Br$ with a Cl placed on the Br sites (blue tick marks), showing observed (black), calculated Rietveld fit (red) and difference (blue) plots. Green tick marks show the peak positions of $Li_7(NH_2)_6Br$, and a star marks the peak position of Li_2O. 75

3.15 Powder X-ray diffraction pattern of the new phase, with the calculated Rietveld fit for the new structure of $Li_7(NH_2)_6Cl$. Tick marks show the peak positions of $Li_7(NH_2)_6Cl$, with a star marking the position of the peaks corresponding to Li_2O and the unknown phase. 77

3.16 Schematic representation of the anion arrangement in rhombohedral $Li_7(NH_2)_6Cl$. Nitrogen is indicated by blue spheres and chloride by green spheres. The unit cell is shown by red dotted lines. 78

3.17 Raman spectra for the new amide chloride compared to the rhombohedral phase of $Li_4(NH_2)_3Cl$, alongside those for $LiNH_2$ and Li_2NH. 80

3.18 Phases present in the lithium magnesium amide chloride system for x, where the reaction taking place is $(4-x)$ $LiNH_2$ + $x/2$ $MgCl_2$. 82

3.19 Powder X-ray diffraction patterns for $Li_7(NH_2)_6Cl$ and $Li_6Mg_{1/2}(NH_2)_6Cl$. Tick marks indicate peak positions for the observed phases. Stars mark peaks from Li_2O and diamonds those from MgO. 83

3.20 Raman spectra for the new amide chlorides alongside those for lithium amide and imide. 84

3.21 The effect on the weight percent of H_2 contained within the amide chloride, gained by reduction in the chloride content of the structure. 85

4.1 Hydrogen desorption profiles for the reactions of amide chlorides with LiH. 89

4.2 Raman spectra of the dehydrogenation product of the new amide chlorides alongside the spectra for lithium amide and lithium imide. 90
4.3 Powder XRD patterns for the dehydrogenation products of the new amide chlorides. Tick marks indicate peak positions for the observed phases. Stars mark peaks from Li_2O, triangles those for LiH and diamonds those from MgO. 91
4.4 Hydrogen desorption profiles for the reaction with LiH for the chloride system with and without prior formation of an amide chloride. 93
4.5 Powder X-ray diffraction patterns for the rehydrogenation products of the amide chlorides. Tick marks indicate peak positions for the observed phases: blue for the cubic amide chloride, black for the rhombohedral amide chloride and red for the imide chloride. Stars mark peaks from Li_2O, triangles those from LiH and diamonds those from MgO. 95
4.6 Raman spectra of the rehydrogenation products of $Li_{13}(NH)_6Cl$ and $Li_{12}Mg_{1/2}(NH)_6Cl$ alongside the spectra for $LiNH_2$ and Li_2NH. 96
4.7 Plot of product phase vs hydrogenation pressure for a sample of $Li_{13}(NH)_6Cl$. 97
4.8 Raman spectra for samples of $Li_{13}(NH)_6Cl$ hydrogenated under different pressures. 98
4.9 Powder XRD patterns for $Li_7(NH_2)_6Cl$, the product of dehydrogenation $Li_{13}(NH)_6Cl$, and the product of rehydrogenation at low pressure, where only the rhombohedral phase is observed. Blue tick marks show peak positions for rhombohedral $Li_7(NH_2)_6Cl$, and red tick marks show peak positions for $Li_{13}(NH)_6Cl$. Stars show the positions of Li_2O and triangles LiH. 100
4.10 Hydrogen release traces from the TPD-MS experiments of $Li_7(NH_2)_6Cl$ with mixed LiH and MgH_2. 102

4.11 Hydrogen release traces from samples comparing initial and second dehydrogenations, normalised so that maxima are all equal to one. 106

4.12 Desorption isotherms, with plateau pressures indicated, at a range of temperatures for $Li_7(NH_2)_6Cl$, alongside the van't Hoff plot used to calculate the thermodynamic properties. 108

4.13 Contour plot of powder synchrotron XRD patterns for 2θ between 5° and 17° during the hydrogen cycling of $Li_{13}(NH)_6Cl$ at beamline I11. Dark blue strips represent periods of no synchrotron radiation. 110

4.14 Example of the complex peak shape of a peak of the amide chloride phase. . 111

4.15 Contour plot of powder synchrotron XRD patterns for 2θ between 15° and 17° during the hydrogen cycling of $Li_{13}(NH)_6Cl$ at beamline I11 showing the complex peak shapes and how they change over time. Dark blue strips represent periods of no synchrotron radiation. 112

4.16 Scale factor of LiH formed during the cycling experiment on beamline I11. Blue dashed lines represent changes in hydrogen pressure, with regions A, C and E representing data collected under hydrogen, and regions B, D and F representing data collected under vacuum. 113

4.17 Contour plot of powder synchrotron XRD patterns for 2θ between 22° and 24° during the hydrogen cycling of $Li_{13}(NH)_6Cl$ at beamline I11, to focus on the (002) peak of LiH. Dark blue strips represent periods of no synchrotron radiation. 114

4.18 Contour plot of the powder neutron patterns for $Li_{13}(ND)_6Cl$ annotated with experimental conditions. 116

4.19 The weight percent of the deutero-imide chloride phase and the lithium deuteride phase calculated *via* batch QPA refinements of the neutron powder diffraction patterns of the sample cycled under deuterium on the POLARIS beamline. 117

4.20 The statistical parameters R_{wp} and R_{exp} for the batch QPA refinements of the sample cycled under deuterium on the POLARIS beamline. 117

4.21 Weight percentages of LiD (left) and the chloride-containing phase (right) during the final deuteration at 275°C on the POLARIS beamline modelled using an exponential function. 119

4.22 Weight percentages of LiD and the chloride-containing phase during the final deuteration at 275°C on the POLARIS beamline modelled using an exponential model (red lines) and diffusion models (1D: green, 3D: blue). 120

4.23 Lattice parameter of the imide chloride phase during the first deuteration at 300°C on the POLARIS beamline, along with an exponential function fit to the data (left, red, $r^2 = 0.9268$), and the 1D (right, green, $r^2 = 0.8899$) and 3D (right, blue, $r^2 = 0.8813$) diffusion models which, in this case, are indistinguishable. 121

4.24 Lattice parameter of the deutero-imide chloride when under vacuum at 275°C on the POLARIS beamline, with an exponential function fit (left, red, $r^2 = 0.8400$), and 1D (right, green, $r^2 = 0.7459$) and 3D (right, blue, $r^2 = 0.7391$) diffusion models. 121

4.25 Lattice parameter of the imide chloride phase during the second deuteration at 275°C on the POLARIS beamline, along with an exponential function fit to the data left, red, $r^2 = 0.9663$), and 1D (right, green, $r^2 = 0.9098$) and 3D (right, blue, $r^2 = 0.9345$) diffusion models. 122

4.26 Raman spectra of samples before and after cycling on the POLARIS beamline. 123

4.27 Powder XRD patterns for $Li_7(ND_2)_6Cl$ before (green) and after (blue) cycling on the POLARIS beamline. Tick marks show the peak positions for $Li_7(ND_2)_6Cl$ and asterisks mark the positions of peaks corresponding to Li_2O and the unknown phase described in section 3.5.1. 124

4.28 IGA^n and neutron powder diffraction data for the deuterium cycling of $Li_{13}(ND)_6Cl$ on the POLARIS beamline. All plots share the same universal x axis with the diffraction data. 126

4.29 Neutron powder diffraction data for the deuterium cycling of $Li_{13}(ND)_6Cl$ on the POLARIS beamline, focussing in on the d spacing range of the (111) peak for LiD. 129

4.30 Mass of the sample for the deuterium cycling of $Li_{13}(ND)_6Cl$ on the POLARIS beamline, separated into capacity loss due to release of ND_3 (blue) and reversible release of D_2 (red). 130

4.31 Experimental (circles) and calculated (line) Nyquist plot for $Li_7(NH_2)_6Cl$ at 156°C. 131

4.32 Plot of $\log(\sigma T)$ against 1/T for samples of $Li_7(NH_2)_6Cl$ alongside those for $LiNH_2$ and Li_2NH. 133

4.33 Plot of $\log(\sigma T)$ against 1/T for samples of $Li_{13}(NH)_6Cl$ alongside those for $LiNH_2$, Li_2NH and $Li_7(NH_2)_6Cl$. 135

5.1 Powder X-ray diffraction pattern for $Li_7(NH_2)_6Br$, with the calculated and difference patterns for a Rietveld fit to the data. 142

5.2 Arrhenius plots for $Li_7(NH_2)_6Br$ and $Li_{13}(NH)_6Br$ alongside those for $LiNH_2$ and Li_2NH. 145

5.3 Left: Section of the structure of $Li_7(NH_2)_6Br$, displayed to be compared to that for the imide bromide. Right: structure of Li_2NH: in the imide bromide, bromide ions are present evenly distributed on the NH^{2-} sites. Lithium ions are shown as red spheres, nitrogen blue and bromide brown. Unit cells are marked with dotted lines. 146

5.4 Arrhenius plots for $Li_7(NH_2)_6Br$ and $Li_{13}(NH)_6Br$ alongside those for $LiNH_2$, Li_2NH, $Li_7(NH_2)_6Cl$ and $Li_{13}(NH)_6Cl$. 147

5.5 Hydrogen traces of different ratios of lithium amide, lithium hydride and lithium bromide, heated on the TPD-MS. 148

5.6 Hydrogen traces for the amide bromide system heated to different temperatures on the TPD-MS. 150

5.7 Contour plot of the neutron powder diffraction patterns collected during deuterium cycling of $Li_7(NH_2)_6Br$ on the POLARIS beamline. Peaks for the deutero-amide bromide (A), deutero-imide bromide (I) and LiD are labelled, and that of the new phase observed circled. 152

5.8 Linear fit to the lattice parameter, *a* for $Li_7(NH_2)_6Br$ when data was collected under vacuum at 250°C on the POLARIS beamline. 153

5.9 Lattice parameter of the $Li_{13}(NH)_6Br$ during the initial dedeuteration at 275°C on the POLARIS beamline, along with an exponential function fit to the data (left, red, $r^2 = 0.9992$), and the 1D (right, green, $r^2 = 0.9684$) and 3D (right, blue, $r^2 = 0.957$) diffusion models which, in this case, are indistinguishable. 154

5.10 Raman spectra of samples of $Li_7(NH_2)_6Br$ before and after cycling on the POLARIS beamline. 155

5.11 Contour plot of powder synchrotron XRD patterns for 2θ between 5° and 20° during the hydrogen cycling of $Li_{13}(NH)_6Br$ at beamline I11. An orange asterisk marks the peak observed for the unknown phase and ‘a’s label the (101), (110), (012), (021), (12-1) and (122) peaks of the amide bromide. . . 157

5.12 Contour plot of powder synchrotron XRD patterns for 2θ between 15° and 16.5° during the hydrogen cycling of $Li_{13}(NH)_6Br$ at beamline I11 showing how the peak shapes change over time. 159

5.13 Weight percentages of the amide and imide bromide phases during hydrogen cycling on the I11 beamline. 160

5.14 Statistical parameters for the batch QPA of the amide and imide bromide phases during hydrogen cycling on the I11 beamline. 160

5.15 IGA^n data and contour plot of neutron diffraction patterns collected on the POLARIS beamline with peaks for LiD and the deutero-amide bromide (A-Br) labelled. 162

5.16 Sample weight for sample of $Li_7(ND_2)_6Br$ + 6 LiD during dedeuteration on the IGA^n on the POLARIS beamline, along with an exponential function fit to the data (left, red, $r^2 = 0.9994$), and the 3D (right, blue, $r^2 = 0.9955$) diffusion model. 163

5.17 Sample weight for sample of $Li_7(ND_2)_6Br$ + 6 LiD during cycling with D_2 on the IGA^n on the POLARIS beamline. 164

5.18 Hydrogen traces of different ratios of lithium amide, lithium hydride and lithium iodide, heated on the TPD-MS. 168

5.19 Contour plot of synchrotron powder diffraction patterns during hydrogen cycling of $Li_3(NH_2)_2I$ on beamline I11. 170

5.20 Contour plot of synchrotron powder diffraction patterns for 2θ between 12.8° and 13.3° during hydrogen cycling of $Li_3(NH_2)_2I$ on beamline I11 showing the merging of satellite peaks into the imide iodide (110) peak. 171

5.21 Weight percentages of the amide and imide iodide phases present during cycling of $Li_3(NH_2)_2I$ under hydrogen and vacuum on beamline I11. 172

5.22 Statistical parameters for the batch QPA of the amide and imide iodide phases during hydrogen cycling on the I11 beamline. 172

5.23 IGA^n data and contour plot of neutron diffraction data of $Li_3(NH_2)_2I$ collected on the POLARIS beamline. 174

5.24 Sample weight for sample of $Li_3(NH_2)_2I$ during dedeuteration on the IGA^n on the POLARIS beamline, along with an exponential function fit to the data (left, red, r^2 = 0.9965), and the 1D (left, green, r^2 = 0.9784) and 3D (right, blue, r^2 = 0.9983) diffusion models. 175

5.25 Weight percentages of the deutero-amide and deutero-imide iodide phases during hydrogen cycling on the POLARIS beamline during cycling in the IGA^n sample environment. 177

5.26 Statistical parameters for the batch QPA of the deutero-amide and deutero-imide bromide phases during cycling on the POLARIS beamline during cycling in the IGA^n sample environmen. 177

5.27 IGA^n data and contour plot of neutron diffraction data for $Li_3(NH_2)_2I$ collected on the POLARIS beamline. 179

5.28 Scale factor of $Li_3(NH_2)_2I$ during cycling under hydrogen and vacuum on the POLARIS beamline. 180

5.29 Sample weight for sample of $Li_3(NH_2)_2I$ during dedeuteration on the IGA^n on the POLARIS beamline, along with an exponential function fit to the data (left, red, $r^2 = 0.9902$), and the 1D (right, green, $r^2 = 0.9124$) and the 3D (right, blue, $r^2 = 0.9990$) diffusion models. 181

5.30 Hydrogen and ammonia traces for $LiBF_4$ and $NaBF_4$ added to $LiNH_2$ and LiH, collected on the TPD-MS. 183

5.31 TPD-MS hydrogen traces for the reaction of $LiNH_2$ with Li_xF_{1-x} and LiH and LiF mixtures, scaled to the LiH content. 185

List of Tables

1.1 Table showing the US DoE targets for vehicular hydrogen storage.[22] 14

2.1 Crystal systems and Bravais lattices 32

2.2 Point group table for C_{2v} 49

2.3 Observed Raman stretching modes for $LiNH_2$ and Li_2NH 50

3.1 Cubic lithium phases and their unit cell sizes. 74

3.2 Structure of $Li_7(NH_2)_6Cl$ after a preliminary structural refinement with R_{wp} = 11.338, R_{exp} = 5.531. 76

4.1 Phases present after dehydrogenation of $Li_7(NH_2)_6Cl$ with (6 - y) LiH + $\frac{1}{2}$ y MgH_2 as a weight percentage of the non-oxide content. 103

4.2 Phases present after rehydrogenation of the dehydrogenation products of $Li_7(NH_2)_6Cl$ with (6 - y) LiH + $\frac{1}{2}$ y MgH_2 as a weight percentage of the non-oxide content. 104

4.3 Comparison of Raman peak positions for $Li_7(ND)_6Cl$ and $Li_7(NH)_6Cl$ . . . 124

4.4 Mass losses and molar fractions for a sample of $Li_7(ND_2)_6Cl$ + 6 LiD for four dehydrogenation cycles on the IGA^n measured on the POLARIS beamline. 130

4.5 Gradients and calculated activation energies of ionic conduction for pellets of $Li_7(NH_2)_6Cl$ compared to those for $LiNH_2$ and Li_2NH. 134

4.6 Half lives for different stages of cycling of a sample of $Li_{13}(ND)_6Cl$ with D_2. 138

5.1 Distances between the halide ions and nitrogen atoms in the amide ions in the amide halide structures. 143
5.2 Conductivity values at approximately 100°C for $Li_7(NH_2)_6Br$ and $Li_{13}(NH)_6Br$ compared to those for $LiNH_2$ and Li_2NH. 144
5.3 Activation energy of ionic conduction for samples measured in this study. . 147
5.4 Mass losses and molar fractions for a sample of $Li_7(ND_2)_6Br$ + 6 LiD for the dehydrogenation cycles on the IGA^n measured on the POLARIS beamline. 165